Drone Cellular Networks: Fundamentals, Modeling, and Analysis

by

Morteza Banagar

Dissertation submitted to the Faculty of the
Virginia Polytechnic Institute and State University
in partial fulfillment of the requirements for the degree of

Doctor of Philosophy
in
Electrical Engineering

Harpreet S. Dhillon, Chair
R. Michael Buehrer
Walid Saad
Ryan K. Williams
Azim Eskandarian

May 6, 2022
Blacksburg, Virginia

Keywords: Drone, UAV, stochastic geometry, Poisson point process, aerial-terrestrial coexistence, wireless backhaul, mobility, random waypoint, handover, wobbling, hardware impairments, coherence time, coherence bandwidth.

Drone Cellular Networks: Fundamentals, Modeling, and Analysis

Morteza Banagar

(ABSTRACT)

With the increasing maturity of unmanned aerial vehicles (UAVs), also known as drones, wireless ecosystem is experiencing an unprecedented paradigm shift. These aerial platforms are specifically appealing for a variety of applications due to their rapid and flexible deployment, cost-effectiveness, and high chance of forming line-of-sight (LoS) links to the ground nodes. As with any new technology, the benefits of incorporating UAVs in existing cellular networks cannot be characterized without completely exploring the underlying trade space. This requires a detailed system-level analysis of drone cellular networks by taking the unique features of UAVs into account, which is the main objective of this dissertation.

We first focus on a *static* setup and characterize the performance of a three-dimensional (3D) two-hop cellular network in which terrestrial base stations (BSs) coexist with UAVs to serve a set of ground user equipment (UE). In particular, a UE connects either directly to its serving terrestrial BS by an access link or connects first to its serving UAV which is then wirelessly backhauled to a terrestrial BS (joint access and backhaul). We consider realistic antenna radiation patterns for both BSs and UAVs using practical models developed by the third generation partnership project (3GPP). We assume a probabilistic channel model for the air-to-ground transmission, which incorporates both LoS and non-LoS links. Assuming the max-power association policy, we study the performance of the network in both amplify-and-forward (AF) and decode-and-forward (DF) relaying protocols. Using tools from stochastic geometry, we analyze the joint distribution of distance and zenith angle of the closest (and serving) UAV to the origin in a 3D setting. Further, we identify and extensively study key mathematical constructs as the building blocks of characterizing the received signal-to-interference-plus-noise ratio (SINR) distribution. Using these results, we obtain exact mathematical expressions for the coverage probability in both AF and DF relaying protocols. Furthermore, considering the fact that backhaul links could be quite weak because of the downtilted antennas at the BSs, we propose and analyze the addition of a directional uptilted antenna at the BS that is solely used for backhaul purposes. The superiority of having directional antennas with wirelessly backhauled UAVs is further demonstrated via extensive simulations.

Second, we turn our attention to a *mobile* setup and characterize the performance of several canonical mobility models in a drone cellular network in which UAV base stations serve UEs on the ground. In particular, we consider the following four mobility models: (i) straight line (SL), (ii) random stop (RS), (iii) random walk (RW), and (iv) random waypoint (RWP), among which the SL mobility model is inspired by the simulation models used by the 3GPP for the placement and trajectory of UAVs, while the other three are well-known canonical

models (or their variants) that offer a useful balance between realism and tractability. Assuming the nearest-neighbor association policy, we consider two service models for the UEs: (i) UE independent model (UIM), and (ii) UE dependent model (UDM). While the serving UAV follows the same mobility model as the other UAVs in the UIM, it is assumed to fly towards the UE of interest in the UDM and hover above its location after reaching there. We then present a unified approach to characterize the point process of UAVs for all the mobility and service models. Using this, we provide exact mathematical expressions for the average received rate and the session rate as seen by the typical UE. Further, using tools from the calculus of variations, we concretely demonstrate that the simple SL mobility model provides a lower bound on the performance of other general mobility models (including the ones in which UAVs follow *curved* trajectories) as long as the movement of each UAV in these models is independent and identically distributed (i.i.d.).

Continuing our analysis on mobile setups, we analyze the handover probability in a drone cellular network, where the initial positions of the UAVs serving the ground UEs are modeled by a homogeneous Poisson point process (PPP). Inspired by the mobility model considered in the 3GPP studies, we assume that all the UAVs follow the SL mobility model, i.e., move along straight lines in random directions. We further consider two different scenarios for the UAV speeds: (i) same speed model (SSM), and (ii) different speed model (DSM). Assuming nearest-neighbor association policy, we characterize the handover probability of this network for both mobility scenarios. For the SSM, we compute the exact handover probability by establishing equivalence with a single-tier terrestrial cellular network, in which the BSs are static while the UEs are mobile. We then derive a lower bound for the handover probability in the DSM by characterizing the evolution of the spatial distribution of the UAVs over time.

After performing these system-level analyses on UAV networks, we focus our attention on the air-to-ground wireless channel and attempt to understand its unique features. For that, we first study the impact of UAV wobbling on the coherence time of the wireless channel between UAVs and a ground UE, using a Rician multi-path channel model. We consider two different scenarios for the number of UAVs: (i) single UAV scenario (SUS), and (ii) multiple UAV scenario (MUS). For each scenario, we model UAV wobbling by two random processes, i.e., the Wiener and sinusoidal processes, and characterize the channel autocorrelation function (ACF) which is then used to derive the coherence time of the channel. For the MUS, we further show that the UAV-UE channels for different UAVs are uncorrelated from each other. One key observation that is revealed from our analysis is that even for small UAV wobbling, the coherence time of the channel may degrade quickly, which may make it difficult to track the channel and establish a reliable communication link.

Finally, we develop an *impairments-aware air-to-ground unified channel model* that incorporates the effect of both wobbling and hardware impairments, where the former is caused by random physical fluctuations of UAVs, and the latter by intrinsic radio frequency (RF) nonidealities at both the transmitter and receiver, such as phase noise, in-phase/quadrature

(I/Q) imbalance, and power amplifier (PA) nonlinearity. The impact of UAV wobbling is modeled by two stochastic processes, i.e., the canonical Wiener process and the more realistic sinusoidal process. On the other hand, the *aggregate* impact of all hardware impairments is modeled as two multiplicative and additive distortion noise processes, which is a well-accepted model. For the sake of generality, we consider both wide-sense stationary (WSS) and nonstationary processes for the distortion noises. We then rigorously characterize the ACF of the wireless channel, using which we provide a comprehensive analysis of four key channel-related metrics: (i) power delay profile (PDP), (ii) coherence time, (iii) coherence bandwidth, and (iv) power spectral density (PSD) of the distortion-plus-noise process. Furthermore, we evaluate these metrics with reasonable UAV wobbling and hardware impairment models to obtain useful insights. Similar to our observation above, this work again demonstrates that the coherence time severely degrades at high frequencies even for small UAV wobbling, which renders air-to-ground channel estimation very difficult at these frequencies.

Drone Cellular Networks: Fundamentals, Modeling, and Analysis

Morteza Banagar

(GENERAL AUDIENCE ABSTRACT)

With the increasing maturity of unmanned aerial vehicles (UAVs), also known as drones, wireless ecosystem is changing dramatically. Owing to their ease of deployment and high chance of forming direct line-of-sight (LoS) links with the other UAVs and ground users, they are very appealing for numerous wireless applications. As with any new technology, exploring the full extent of the benefits of UAVs requires careful exploration of the underlying trade space. Therefore, in this dissertation, our main focus is on the analysis of such aerial networks, their interplay with the current terrestrial networks, and the unique features of UAVs that make them different from conventional ground nodes.

One important aspect of aerial communication systems is their integration into our current cellular networks. Clearly, the addition of these new aerial components has the potential of benefiting both the ground users (such as mobile users watching a concert who need cellular connectivity to share the moments) and the cellular base station (BS). Therefore, careful analysis of these "aerial-terrestrial" networks is of utmost importance. In the first phase of this dissertation, we perform this analysis by interpreting the network as a combination of one-hop (from the BS to the user) and two-hop (from the BS to the UAV and then from the UAV to the UE) links. Since the locations of BSs, UAVs, and users are irregular in general, we use tools from stochastic geometry to carry out our analysis, which is a field of mathematics that studies random shapes and patterns. Also, because existing terrestrial BSs are primarily designed to serve the "ground", we propose the addition of a separate set of antennas at the BS site that is solely used to serve the "air", i.e., to communicate with the UAVs, and demonstrate the benefits of this additional infrastructure in detail.

One of our assumptions in the first phase of this dissertation was that the considered network was *static*, i.e., the UAVs were hovering in the air and the BSs/users were also not moving. In the second phase, on the other hand, we explore the benefits and challenges of a *mobile* network of UAVs and characterize the performance of several canonical mobility models in a drone cellular network. In particular, one of the models that we studied extensively is the so-called straight line (SL) mobility model, which was inspired by the simulation models used by the third generation partnership project (3GPP) for the placement and trajectory of UAVs. Since the locations of UAVs could be assumed random in general, we use tools from stochastic geometry and present a unified approach to characterize the point process of UAVs, using which we obtained exact mathematical expressions for the average received rate (i.e., throughput) as seen by the users. Continuing our analysis on mobile setups and using the SL mobility model, we also analyze the handover probability in a drone cellular

network, which is defined as the event when the serving UAV of a user changes. By establishing equivalence between our aerial setup with a terrestrial cellular network, we compute the exact handover probability in drone cellular networks.

In the final phase of this dissertation, we focus our attention on the air-to-ground wireless channel and attempt to understand its unique features. For that, we propose an *impairments-aware unified channel model* for an air-to-ground wireless communication system and extensively analyze the link between a hovering UAV in the air and a static user on the ground. In particular, we consider two different types of impairments: (i) UAV wobbling, and (ii) hardware impairments, where the former is caused by random physical fluctuations, and the latter by intrinsic radio frequency (RF) nonidealities at both the transmitter and receiver. Using appropriate models for each type of impairment, we rigorously characterize the autocorrelation function (ACF) of the wireless channel, using which we provide a comprehensive analysis of key channel-related metrics, such as coherence time and coherence bandwidth. One key observation that is revealed from our analysis is that even for small UAV wobbling and low hardware impairment levels, the coherence time of the channel may degrade quickly at high frequencies, which could make it difficult to track the channel and establish a reliable communication link at these frequencies.

Dedication

To my love, Behnaz, and my family Maman, Baba, Iliya, Samaneh, and Behnam.

Acknowledgments

Before starting the Ph.D. journey, I was kind of hesitant and thought it is going to be very difficult with lots of long nights in the lab! But working with such a great advisor, Dr. Harpreet S. Dhillon, who is more like a big brother/friend to me than an academic advisor, made things much easier for me than what I expected. Apart from being a fantastic teacher and researcher, he taught me how to behave respectfully with everyone. I am very happy (and lucky) to be one of Harpreet's advisees :)

I would like to thank all my committee members, Dr. Mike Buehrer, Dr. Walid Saad, Dr. Ryan Williams, and Dr. Azim Eskandarian for their invaluable feedback and support. I have learned a lot from Dr. Buehrer by taking "four" of his graduate courses at VT! I want to also thank Dr. Andy Molisch from the University of Southern California (USC) for his collaboration on one of our papers. Furthermore, I would like to thank my M.Sc. and B.Sc. advisors, Dr. Behrouz Maham and Dr. Ali Olfat, from whom I learned the alphabets of digital communications. I am also grateful to the National Science Foundation (NSF) for supporting this research through grants CNS-1617896 and CNS-1923807. Last but not the least, I want to sincerely thank Hilda Reynolds at the office of Wireless@VT, who was always very helpful and attentive. I wish her a happy and healthy life.

I had zillion interesting discussions with my cohorts at VT, which made me a better researcher, and in some ways, a better person. I would like to cordially thank all of them. Let me name each and every one of them, as they are all important to me: Mehrnaz, Mohammad, and Atieh, who introduced me to the lab in the first days of 2018 when I joined VT and knew nothing about the new environment, Vishnu, who was the silent and sweet guy in the lab and my only peer co-author from our research group, Chiranjib, who helped me a lot in my very first paper and also took many nice photos of me and Behnaz during our fifth anniversary, Kartheek, who was a very good friend and we had many nice technical discussions, Priyabrata, who was the father of MIMO! Chris, the amazing guy who I wish I knew him much sooner, Praful, who gave me useful hints for my first journal paper, Mohamed, who is the epitome of a wonderful researcher, Mustafa, who helped me a lot even after his graduation, Solmaz, who was truly a good and supportive friend, Tolga, the chess master who introduced me to the amazing anime world and changed my life forever! Anish, who followed Tolga's path! Keerthana, who was among the smartest students I have ever seen, Raghu, which words cannot describe him! Avik, who was always polite and helpful, and Xiangliu and Haozhou, who are going to be wonderful researchers later on.

Having a friendly and supporting community outside the lab is very important for a healthy graduate life. I was very lucky to have so many supportive friends (both in the U.S. and Iran)

that always tried to cherish me. Here is a short list: Ali and Maede, Amirsina and Somayeh, Farshad and Nastaran, Hossein and Fatemeh, Amer and Sare, Masoud and Leyla, Aidin and Mimosa, MH and Zahra, Mohammadreza and Behnoosh, Mohsen and Esmat, Ali Hosseini, Mammad Karim, Safoura, Nooshin, Alireza and Fatemeh, Kian and Kate, Keyvan, Javad, Shahan, Ali and Kiana, Mehran and Hoda, Boyook and Morva, Mohamad and Zahra, Hadi and Ayda, Hamed and Banafsheh, Mohammadhossein, Hossein, Saman and Zahra, Meysam, and Vahid.

I want to close this section by a heartfelt thanks to my and Behnaz's wonderful families, Maman, Baba, Iliya, Samaneh, Behnam, Maman, Baba, Aghajoon, Madar, Amin, and Fatemeh, who endured my lack of presence for the past four years so that I could continue my Ph.D. Finally, I would like to warmly appreciate my best friend and lovely wife, Behnaz, without whom I would have been lost so many times for the past nine years of my life. Thank you Behnaz :)

Contents

List of Figures xv

List of Tables xviii

1 Introduction 1

1.1 Background and Motivation . . . 1

1.2 Selected Prior Works . . . 2

1.3 Contributions . . . 5

1.3.1 3D Two-Hop Networks with Wireless Backhauled UAVs . . . 5

1.3.2 Mobility and Handover in Drone Cellular Networks . . . 6

1.3.3 Impairments-Aware Air-to-Ground Wireless Communications . . . 7

1.4 Organization . . . 7

1.5 List of Publications . . . 8

2 3D Two-Hop Cellular Networks with Wireless Backhauled UAVs: Modeling and Fundamentals 10

2.1 Introduction . . . 10

2.1.1 Related Works . . . 10

2.1.2 Contributions . . . 12

2.2 System Model . . . 14

2.2.1 Spatial Setup . . . 14

2.2.2 Antenna Pattern . . . 14

2.2.3 Channel Model . . . 17

2.2.4 Service Model and Association Policy . . . 20

2.2.5 Relaying Protocols and Metrics . . . 20

2.3 Mathematical Constructs . . . 21

2.3.1 Useful Lemmas for the Two-Hop Setting . . . 21
2.3.2 Relative Distance and Angle Distributions in the 3D Setting . . . 24
2.4 Performance Analysis . . . 27
2.4.1 Conditional Laplace Transform of Interference . . . 27
2.4.2 Coverage Probability . . . 29
2.5 Simulation Results . . . 31
2.5.1 Intermediate Results . . . 32
2.5.2 Impact of Relaying Protocols, UAV Height, and Density . . . 34
2.5.3 Impact of Environments and Antenna Models . . . 35
2.6 Chapter Summary . . . 36

3 Performance Characterization of Canonical Mobility Models in Drone Cellular Networks 39

3.1 Introduction . . . 39
3.1.1 Related Works . . . 39
3.1.2 Contributions . . . 41
3.2 System Model . . . 42
3.2.1 Spatial Setup . . . 42
3.2.2 Service and Mobility Models . . . 43
3.2.3 Channel Model . . . 45
3.2.4 Metrics of Interest . . . 45
3.2.5 Methodology of Analysis . . . 45
3.3 Point Process of Interferers . . . 46
3.4 RW and RWP Mobility Models . . . 50
3.5 Average and Session Rates . . . 56
3.6 Simulation Results . . . 57
3.6.1 Distribution of $L(t)$ in RW and RWP . . . 58
3.6.2 Point Process of Interferers . . . 58
3.6.3 Impact of Fading and Height . . . 61

3.6.4 Impact of Mobility Models . . . 63
3.7 Chapter Summary . . . 64

4 Handover Probability in Drone Cellular Networks 65
4.1 Introduction . . . 65
4.2 System Model . . . 66
4.3 Handover Probability . . . 67
4.3.1 Handover Analysis in the SSM . . . 67
4.3.2 Handover Analysis in the DSM . . . 69
4.4 Simulation Results . . . 70
4.5 Chapter Summary . . . 72

5 Impact of UAV Wobbling on the Air-to-Ground Wireless Channel 73
5.1 Introduction . . . 73
5.2 System Model . . . 74
5.3 Channel Autocorrelation Function . . . 77
5.3.1 ACF Analysis in the SUS . . . 78
5.3.2 ACF Analysis in the MUS . . . 81
5.4 Simulation Results . . . 82
5.5 Chapter Summary . . . 85

6 Fundamentals of Wobbling and Hardware Impairments-Aware Air-to-Ground Channel Model 87
6.1 Introduction . . . 87
6.1.1 Related Works . . . 87
6.1.2 Contributions . . . 89
6.2 System Model . . . 92
6.2.1 Spatial Setup . . . 92
6.2.2 Impairments . . . 92
6.2.3 Metrics . . . 93

6.3 Impairments-Aware Unified Channel Model . . . 94
6.3.1 Preliminaries . . . 94
6.3.2 Unified Channel Model . . . 96
6.3.3 Metrics: General Results . . . 97
6.3.4 Metrics: Evaluations for Some Case Studies . . . 103
6.4 Simulation Results . . . 109
6.4.1 PDP . . . 110
6.4.2 Coherence Time . . . 110
6.4.3 Coherence Bandwidth . . . 113
6.4.4 PSD of Distortion-Plus-Noise . . . 113
6.5 Chapter Summary . . . 115

7 Conclusion and Future Works **118**
7.1 Conclusion . . . 118
7.2 Future Works . . . 120

Bibliography **122**

Appendices **134**

Appendix A Proofs of Lemmas and Theorems of Chapter 2 **135**
A.1 Proof of Lemma 2.3 . . . 135
A.2 Proof of Lemma 2.4 . . . 136
A.3 Proof of Lemma 2.5 . . . 137
A.4 Proof of Lemma 2.11 . . . 137
A.5 Proof of Lemma 2.12 . . . 138
A.6 Proof of Lemma 2.13 . . . 138
A.7 Proof of Lemma 2.14 . . . 139
A.8 Proof of Theorem 2.15 . . . 139
A.9 Proof of Theorem 2.16 . . . 140

Appendix B Proofs of Lemmas and Theorems of Chapter 3 **142**

B.1 Proof of Lemma 3.9 142

B.2 Proof of Theorem 3.13 144

B.3 Proof of Lemma 3.16 145

B.4 Proof of Lemma 3.17 146

B.5 Proof of Proposition 3.20 146

B.6 Proof of Proposition 3.23 147

B.7 Proof of Proposition 3.24 148

Appendix C Proofs of Lemmas and Theorems of Chapter 4 **151**

C.1 Proof of Lemma 4.2 151

C.2 Proof of Theorem 4.4 152

C.3 Proof of Lemma 4.6 153

C.4 Proof of Theorem 4.7 154

C.5 Proof of Corollary 4.8 155

List of Figures

2.1 An illustration of the system model. Desired and interfering signals to the typical UE are denoted by solid green and dotted red lines, and the access and backhaul links to the typical UE are shown as solid green and blue lines, respectively. 13

2.2 The 3D network setting when the closest UAV is at distance r from $\mathbf{o}$ for (a) $h_{\mathrm{D,m}} \leq r \leq h_{\mathrm{D,M}}$, and (b) $r > h_{\mathrm{D,M}}$. 24

2.3 Comparison between the cdfs of T_1, T_2, and the joint cdf of T_1 and T_3 ($a = 1$, $b = 4$, $I = 2$, $m = 2$, and $g = 1$). 32

2.4 The joint pdf of $r_{\mathrm{D}_0,\mathrm{L}}$ and $\theta_{\mathrm{D}_0,\mathrm{L}}$ (suburban, $\lambda_{\mathrm{D}} = 10^{-6}$, $h_{\mathrm{D,m}} = 100$ m, and $h_{\mathrm{D,M}} = 300$ m). 33

2.5 Coverage probability as a function of the mean UAV height for both AF and DF and different τ's (urban, $\lambda_{\mathrm{D}} = 10^{-8}$, $m = 1$, $h_{\mathrm{D,M}} - h_{\mathrm{D,m}} = 100$ m). . . . 33

2.6 Coverage probability as a function of the maximum UAV height for both AF and DF and different τ's (urban, $\lambda_{\mathrm{D}} = 10^{-8}$, $m = 1$, $h_{\mathrm{D,m}} = 50$ m). 34

2.7 Coverage probability as a function of UAV density for both AF and DF and different τ's (urban, $m = 1$, $h_{\mathrm{D,m}} = 100$ m, $h_{\mathrm{D,M}} = 300$ m). 35

2.8 Coverage probability as a function of τ for the AF protocol at different environments ($\lambda_{\mathrm{D}} = 10^{-8}$, $m = 2$, $h_{\mathrm{D,m}} = 100$ m, $h_{\mathrm{D,M}} = 300$ m). 36

2.9 Coverage probability as a function of τ for the DF protocol using different BS antenna models (urban, $\lambda_{\mathrm{D}} = 10^{-8}$, $m = 2$, $h_{\mathrm{D,m}} = 100$ m, $h_{\mathrm{D,M}} = 300$ m). 37

3.1 (a) An illustration of the system model, and (b) top view of the two service models. Note the difference between the movement direction of the serving DBS in the UDM and the UIM. 42

3.2 Network density in different regions for the SL mobility model. Green and black stars, red circles, and black squares represent serving DBS, displaced serving DBS, interfering DBSs, and displaced interfering DBSs, respectively. (a) Serving DBS is moving towards $\mathbf{o}'$, and (b) serving DBS is hovering at $\mathbf{o}'$. 48

3.3 A realization of the RW mobility model. 51

3.4 Distribution of $L(t)$ in the RW and RWP mobility models for $t \in \{50, 100, 300\}$ s. As t increases, the pdf of $L(t)$ in both the RW and RWP models converges to the Rayleigh distribution. 58

3.5 Density of the network of interfering DBSs for the UDM with the SL and RS mobility models. Serving distance is $u_0 = 500$ m and the density is given at $t \in \{20, 40, 50, 200\}$ s. 59

3.6 Density of the network of interfering DBSs for the UDM with the RW and RWP mobility models. Serving distance is $u_0 = 500$ m and the flights are Rayleigh distributed with mean 500 m. 60

3.7 Comparison of the average rate for the UDM with the SL mobility model for different Nakagami-m parameters with $\alpha = 3$ and $h = 100$ m. 61

3.8 Comparison of the average rate for both the UIM and the UDM with the SL mobility model at different heights with $\alpha = 3$ and $m_0 = m_{\mathbf{x}} = 1$. 62

3.9 Comparison of the average rate for the UDM with different mobility models. Other parameters are $\alpha = 3$, $h = 100$ m, and $m_0 = m_{\mathbf{x}} = 1$. 62

3.10 Comparison of the session rate for the UDM with different mobility models. Other parameters are $\alpha = 3$, $h = 100$ m, and $m_0 = m_{\mathbf{x}} = 1$. 63

4.1 Density of non-serving DBSs for the DSM with Rayleigh distributed speed. . 71

4.2 Handover probability for both mobility scenarios. 71

5.1 An illustration of the system model. The green solid lines represent the LoS links from the UAV transceiver to the UE at times 0 and t and the red dotted lines represent the MPCs from the scatterers. 75

5.2 The channel ACF for different random processes. The parameters are $f_{\mathrm{c}} = 6$ GHz and $\theta_{\mathrm{m}} = 5°$. 83

5.3 The channel ACF when $\theta(t)$ follows the sinusoidal process with varying carrier frequencies and $\theta_{\mathrm{m}} = 5°$. 84

5.4 The channel ACF when $\theta(t)$ follows the sinusoidal process with varying maximum pitch angles and $f_{\mathrm{c}} = 2.4$ GHz. 85

6.1 Spatial setup where the UAV platform wobbles and the UAV transceiver suffers from various hardware impairments. 91

6.2 PDP for ideal and impaired hardware scenarios. Assumptions: $N = 20$, $K = 11.5$, and $\kappa^2_{\chi_{\mathrm{T}}} = \kappa^2_{\chi_{\mathrm{R}}} = 0.5$ W. HI stands for hardware impairment. . . . 110

6.3 Coherence time: Normalized channel ACF for different random processes. Assumptions: $N = 20$, $K = 11.5$, $f_{\mathrm{c}} = 6$ GHz, $\theta_{\mathrm{m}} = 5°$, and $l_{\chi_{\mathrm{T}}} = l_{\chi_{\mathrm{R}}} = 0.05$ s. 111

6.4 Coherence time: Normalized channel ACF for different random processes and impairment levels. Assumptions: $N = 20$, $K = 11.5$, $f_{\mathrm{c}} = 6$ GHz, and $\theta_{\mathrm{m}} = 5°$. 111

6.5 Coherence time: Normalized channel ACF for different f_{c}. Assumptions: $K = 11.5$, $\theta_{\mathrm{m}} = 5°$, and $l_{\chi_{\mathrm{T}}} = l_{\chi_{\mathrm{R}}} = 0.05$ s. 112

6.6 Coherence time: Normalized channel ACF for different θ_{m}. Assumptions: $K = 11.5$, $f_{\mathrm{c}} = 2.4$ GHz, and $l_{\chi_{\mathrm{T}}} = l_{\chi_{\mathrm{R}}} = 0.05$ s. 112

6.7 Coherence bandwidth: Normalized channel ACF for different impairment models and times t. Assumptions: $N = 20$ and $K = 11.5$. 114

6.8 Coherence bandwidth: Normalized channel ACF for different Rician K factors. Assumptions: WSS hardware impairments and $N = 20$. 114

6.9 PSD of $n(t)$ for different impairment levels. Assumptions: Wiener wobbling, WSS hardware impairments, $N = 20$, $K = 11.5$, $f_{\mathrm{c}} = 2.4$ GHz, and $\theta_{\mathrm{m}} = 5°$. 115

6.10 PSD of $n(t)$ for different impairment levels. Assumptions: Sinusoidal wobbling, WSS hardware impairments, $N = 20$, $K = 11.5$, $f_{\mathrm{c}} = 2.4$ GHz, and $\theta_{\mathrm{m}} = 5°$. 116

6.11 PSD of $n(t)$ for different θ_{m}. Assumptions: WSS hardware impairments, $N = 20$, $K = 11.5$, $f_{\mathrm{c}} = 2.4$ GHz, $\kappa^2_{\eta_{\mathrm{T}}} = \kappa^2_{\eta_{\mathrm{R}}} = \kappa^2_{\chi_{\mathrm{R}}} = 1$ W, and $l_{\eta_{\mathrm{T}}} = l_{\eta_{\mathrm{R}}} = l_{\chi_{\mathrm{R}}} = 0.01$ s. 116

B.1 An illustration for the proof of Lemma 3.9. The red circle and the green dotted circles indicate $\mathcal{X}$ and $\mathcal{A}$, respectively. 143

B.2 An illustration for the proof of Lemma 3.16 showing the geometrical interpretations of Δ and Δ' in an RW. 145

C.1 Trajectories of D_0 and D_1. Arrows denote the direction of movements of DBSs. 152

C.2 Movement of the reference UE. Triangles and squares denote BSs and the reference UE, respectively. 153

C.3 Movement of the DBSs. Triangles and the square denote DBSs and the typical UE, respectively. 154

List of Tables

2.1 Exclusion zone radius for different interfering and serving UAV channel conditions. 28

3.1 A comparison between different mobility models. 63

List of Abbreviations

2D Two-Dimensional

3D Three-Dimensional

3GPP Third Generation Partnership Project

5G Fifth Generation

ACF AutoCorrelation Function

AF Amplify-and-Forward

AoD Angle-of-Departure

AWGN Additive White Gaussian Noise

BPP Binomial Point Process

BS Base Station

ccdf complementary cumulative distribution function

cdf cumulative distribution function

cf characteristic function

CLT Central Limit Theorem

CoMP Coordinated MultiPoint

D2D Device-to-Device

DBS Drone Base Station

DF Decode-and-Forward

DSM Different Speed Model

i.i.d. independent and identically distributed

I/Q In-phase/Quadrature

ITU International Telecommunication Union

LAP Low Altitude Platform

LoS Line-of-Sight

LTV Linear Time-Variant

MC Monte Carlo

mgf moment generating function

MIMO Multiple-Input Multiple-Output

MISO Multiple-Input Single-Output

mmWave millimeter Wave

MPC Multi-Path Component

MUS Multiple UAV Scenario

NLoS Non-Line-of-Sight

NOMA Non-Orthogonal Multiple Access

NonSI Non-Stationary-Increments

NonSt Non-Stationary

PA Power Amplifier

pdf probability density function

PDP Power Delay Profile

pgfl probability generating functional

PPP Poisson Point Process

PSD Power Spectral Density

RF Radio Frequency

rms root-mean-square

RS Random Stop

RW Random Walk

RWP Random WayPoint

SI Stationary-Increments

SINR Signal-to-Interference-plus-Noise Ratio

SIR Signal-to-Interference Ratio

SL Straight Line

SNR Signal-to-Noise Ratio

SSM Same Speed Model

SUS Single UAV Scenario

UAV Unmanned Aerial Vehicle

UDM UE Dependent Model

UE User Equipment

UIM UE Independent Model

ULA Uniform Linear Array

US Uncorrelated Scattering

WSS Wide-Sense Stationary

Chapter 1

Introduction

1.1 Background and Motivation

With the increasing maturity of unmanned aerial vehicle (UAV) technology, also known as drone [1], wireless networks are all set to undergo a major transformation from predominantly terrestrial networks to the ones that will have an elaborate and dynamic aerial component in the form of drone networks [1]. In principle, a UAV can act either as an aerial user equipment (UE), or a relay to assist serving the ground UEs, or even a base station (BS), also known as a drone base station (DBS) [2]. UAVs possess several advantages over their conventional terrestrial counterparts due to their mobility, ease of deployment, cost-effectiveness, and a high likelihood of line-of-sight (LoS) link to the ground. In particular, DBSs and UAV-relays extend the coverage of cellular networks by providing connectivity to locations which are beyond the service zones of terrestrial cellular BSs. Moreover, DBSs play a crucial role in providing connectivity in times of natural disasters and emergencies, as the terrestrial networks may be completely incapacitated [3]. Further, the ease of deployment of DBSs has made them an effective solution for providing network access in scenarios where there is a short-term need for network resources, such as sporting events or concerts [4]. Unsurprisingly, the third generation partnership project (3GPP) has recently included the support for UAV communications as part of the fifth generation (5G) standard [5, 6]. Despite the numerous advantages offered by the UAVs, this new technology comes with its own unprecedented challenges. For instance, one important challenge of incorporating UAVs into our current cellular networks is the provision of *wireless backhaul* support for them, as they are supposed to move/hover freely in the sky. Note that without a reliable backhaul link to the rest of the network, we may lose many advantages of aerial networks, such as their high LoS probability to the ground. In addition to providing wireless backhaul for the UAVs, note that UAVs could be *mobile* while serving the ground UEs or being served by the terrestrial BSs. This unique mobility feature, especially when UAVs act as DBSs, adds an entirely new dimension to the system design which needs to be properly understood. For example, one of the key consequences of the mobility of DBSs is the occurrence of *handovers*, even if the ground UEs are static. Since handovers result in signaling overhead, it is highly desirable to carefully understand the handover behavior in this new operational regime. Another important and unique challenge of these aerial components arises from the lack

[1] We use the terms 'UAV' and 'drone' interchangeably in this dissertation.

of fixed and stable infrastructure and various environmental issues, such as bad weather conditions or wind gusts, which make UAVs experience *random wobbling* while hovering at a specific location in the air [7]. Although this wobbling is typically small, it could severely affect the quality of wireless channel because of the large values of the carrier frequencies (especially in millimeter wave (mmWave) and higher frequencies). The fundamental objective of this dissertation is to address such challenges and provide useful insights in drone cellular networks.

1.2 Selected Prior Works

Air-to-Ground Channel Modeling. Since UAVs are typically deployed at much higher altitudes than the terrestrial BSs and UEs, the propagation characteristics of the air-to-ground links of UAVs differ significantly from those of the terrestrial links [2, 8, 9]. Following the mathematical model suggested by the international telecommunication union (ITU) [10], perhaps the first work that established a meaningful yet simple relation between the LoS probability and the elevation angle in an aerial-terrestrial setup for low altitude platforms (LAPs) was [11], where the authors fitted a modified Sigmoid function to the LoS probability. Extensive measurement campaigns have also been conducted to obtain specific air-to-ground channel models for different environments (over-water [12], hilly and mountainous [13], and suburban and near-urban [14]). In these papers, the authors characterized different metrics related to the air-to-ground channels, such as path loss, Ricean K factor of the small-scale fading, and delay spread of the channel. Another relatively recent measurement campaign was conducted in [15], where the authors extracted channel impulse responses from the received data, using which they obtained key characteristics of the channel, such as path loss and shadow fading. In [16], the authors proposed an air-to-ground channel model for UAV base stations flying at high altitudes and moving periodically in circular curves. Considering ultrawideband signals, the authors in [17] conducted measurements for air-to-ground wireless channels and developed stochastic path-loss and multi-path channel models for ultrawideband propagation channels. Furthermore, the 3GPP has also provided a detailed channel model, including the LoS probability and path-loss and fading models, in different environments in its technical report on cellular support for UAVs [5].

Stochastic Geometry. As is the case in any wireless setting, the system-level performance analysis of drone cellular networks can, in principle, be carried out by simulation-based approaches. However, since these approaches are often prone to errors and not easily scalable to larger network sizes, it is important to further develop analytical approaches to complement the simulations. Given the irregularity in the locations of UAVs and UEs, the use of tools from *stochastic geometry* is a natural choice for modeling and analysis of aerial communication networks. The main idea in this approach is to endow the locations of wireless nodes with appropriate distributions and then analytically characterize key performance metrics such as coverage and data rate by leveraging the properties of these distributions [18, 19].

In [20], the authors considered a finite network of DBSs distributed as a uniform binomial point process (BPP) [21] and derived the coverage probability of the network. Along similar lines, the authors of [22] investigated the coexistence of BSs and DBSs using probabilistic LoS and NLoS propagation models, where the locations of BSs and DBSs are modeled as a superposition of a Poisson point process (PPP) and a BPP. The work presented in [23] considered a network of DBSs modeled as a PPP serving ground UEs. In particular, incorporating LoS and NLoS propagation models, the authors derived approximations for the coverage probability and the received rate in the network. In [24], the coexistence between a single DBS and an underlaid device-to-device (D2D) network has been analyzed in terms of coverage probability and rate. As UAVs often coexist with terrestrial cellular networks in practice, the coverage probability has been computed for the typical user in a multi-tier heterogeneous network in [25, 26], where the locations of UAVs and terrestrial BSs are modeled by independent homogeneous PPPs.

Wireless Backhaul for UAVs. Given the growing number of BSs in the forms of terrestrial (macro or small cell) and aerial units, providing strong fiber backhaul for all of these BSs is an extremely difficult, if not impossible, task. Therefore, it is inevitable that some of the BSs in a cellular network are wirelessly backhauled to the core network [27, 28, 29, 30]. This is specifically the case for most UAVs, as they are supposed to hover and move freely in the sky, unless being tethered to a building rooftop [31]. In [32], the impact of UAV mmWave backhauling is considered in an aerial-terrestrial cellular network using tools from stochastic geometry. Along similar lines, the authors in [33] studied the success probability of establishing a wireless backhaul network using directional antenna patterns for the UAVs. In [34], the authors used tools from graph theory to solve a three-dimensional (3D) UAV placement problem, where UAVs serve the ground UEs and are also wirelessly backhauled to the terrestrial BSs. Optimal 3D path planning problem for a UAV is investigated in [35] considering both backhaul constraint and realistic antenna patterns. The main idea was to change the UAV height during the course of its path to improve the backhaul link quality using dynamic programming. Considering link blockages in mmWave frequencies, the authors in [36] studied the use of UAVs as relays in a flexible backhaul architecture for dynamically rerouting to alternative paths. Chapter 2 of this dissertation is devoted to the coexistence problem of aerial and terrestrial networks, where we conduct a comprehensive analysis of 3D UAV-assisted backhaul-aware cellular networks using practical antenna and channel models.

Mobile UAV Networks. In order to design efficient application-oriented protocols, it is imperative to understand the performance of drone cellular networks by accounting for the mobility of UAVs. Two key performance metrics that are directly related to the mobility of nodes in cellular networks are the handover probability and the handover rate. Furthermore, as the spatial distribution of UAVs is affected by their mobility, it is also of interest to investigate the temporal evolution of SINR-based performance metrics, such as coverage probability and achievable data rate. Building further on the finite network model of DBSs considered in [20], two classes of trajectory processes were proposed in [37] to reduce the

average fade duration while ensuring the same coverage performance as that of static DBSs. The performance gains achieved in terms of spectral efficiency by dynamically deploying DBSs have been demonstrated in [38]. Using the random walk (RW) and random waypoint (RWP) mobility models for the horizontal and vertical displacements in a finite 3D network of DBSs, the authors in [39, 40] derived the coverage probability for a reference ground UE. Using tools from stochastic geometry, we study the performance of several canonical mobility models in drone cellular networks in Chapter 3. We also analyze the handover probability in mobile drone cellular networks in Chapter 4.

UAV Wobbling. One unique feature of aerial wireless communications, which can be viewed as an impairment, is the fact that UAVs may experience wobbling, i.e., typically small and random fluctuations of the UAV platform due to various reasons, such as wind gusts and lack of fixed infrastructure [41]. Since this area of research is still at its nascent stage, there are only a handful of works that incorporate UAV wobbling [42, 43, 44, 45]. For instance, the authors in [42] provided a stochastic model for the UAV wobbling and then studied a resource allocation problem in UAV-assisted cellular networks. Considering directional antennas, the antenna gain mismatch problem due to random UAV wobbling for an air-to-air network was studied in [44], where the authors also provided closed-form statistical channel models for the air-to-air links. In [46], the authors proposed a novel aerial network design of coordinated multipoint (CoMP) which benefits from both interference mitigation and UAV mobility. Specifically, they considered a Rician fading channel model where the LoS path has a random phase component due to the random UAV wobbling. Apart from analytical results, measurement campaigns have also reported the impact of wobbling as an important source of error in establishing a strong connection in aerial wireless networks [47, 48]. In particular, in [47], the authors used a channel sounder to investigate an air-to-ground wireless link, from which they observed that the variations of the received power from a completely static UAV is much less than that of a hovering UAV. Although these works address important problems related to UAV wobbling, its impact on the wireless communication channel still remains an open problem, which is the main focus of Chapter 5.

Hardware Impairments. Apart from wobbling, which is unique to UAV communications, implementing an actual UAV communication system requires careful consideration of other types of impairments as well, such as intrinsic hardware impairments. The unfavorable impact of radio frequency (RF) imperfections, also known as hardware impairments, on various aspects of communication systems has been studied extensively during the past decades. Perhaps one of the most comprehensive books on this subject is [49], where the authors describe in detail three fundamental hardware impairments, i.e., phase noise, I/Q imbalance, and PA nonlinearity, along with a general error model that characterizes the effect of all three impairments on the received signal in a wireless channel. This general error model [49, Ch. 7] motivated many researchers to redefine and solve fundamental communication-theoretic problems under a more realistic impairment-aware channel model [50, 51, 52, 53, 54, 55, 56, 57, 58]. For instance, the authors in [50] quantified the aggregate

effect of hardware impairments on two-hop relaying systems [34, 59, 60] and obtained closed-form expressions for the outage probability in these networks. In [51], the authors analytically proved that the capacity of a multiple-input multiple-output (MIMO) channel will be limited when hardware impairments are assumed, which signifies the fundamental impact of these impairments on the wireless channel. The problem of MIMO transmission with residual RF impairments on the transmitter side was studied in [52], where the authors showed that such hardware impairments substantially degrade the performance of MIMO detection algorithms. In [53], the authors incorporated hardware impairments in the analysis of massive MIMO systems, and demonstrated the existence of an upper bound on the capacity of each UE. Another interesting work that studies the impact of hardware impairments on massive MIMO systems is [54], where the authors perform various simulations considering both additive and multiplicative stochastic impairment models, as well as more accurate deterministic behavioral models. Although sparse, there are a few works that study the impact of hardware impairments in UAV communications [61, 62]. For example, the authors in [61] studied a UAV-aided non-orthogonal multiple access (NOMA) relaying network, where both the UAV-relay and terrestrial UEs suffer from residual hardware impairments. Quite surprisingly, none of the recent literature consider the impact of hardware impairments along with UAV wobbling. In Chapter 6, we analyze the joint impact of hardware impairments and UAV wobbling on the wireless channel and provide a unified impairment-aware air-to-ground channel model.

1.3 Contributions

The contributions of this dissertation are summarized as follows along with the related publications. More elaborate technical contributions are provided under the "Contributions" section of each chapter.

1.3.1 3D Two-Hop Networks with Wireless Backhauled UAVs

In the second chapter of this dissertation, we characterize the performance of a 3D two-hop cellular network in which terrestrial BSs coexist with UAVs to serve ground UEs. In particular, a UE connects either directly to its serving terrestrial BS by an access link or connects first to its serving UAV which is then wirelessly backhauled to a terrestrial BS (joint access and backhaul). We consider realistic antenna radiation patterns for both BSs and UAVs using practical models developed by the 3GPP. We assume a probabilistic channel model for the air-to-ground transmission, which incorporates both LoS and non-LoS (NLoS) links. Assuming the max-power association policy, we study the performance of the network in both amplify-and-forward (AF) and decode-and-forward (DF) relaying protocols. Using tools from stochastic geometry, we analyze the joint distribution of distance and zenith angle of the closest (and serving) UAV to the origin in a 3D setting. Further,

we identify and extensively study key mathematical constructs as the building blocks of characterizing the received signal-to-interference-plus-noise ratio (SINR) distribution. Using these results, we obtain exact mathematical expressions for the coverage probability in both AF and DF relaying protocols. Furthermore, considering the fact that backhaul links could be quite weak because of the downtilted antennas at the BSs, we propose and analyze the addition of a directional uptilted antenna at the BS that is solely used for backhaul purposes. The superiority of having directional antennas with wirelessly backhauled UAVs is further demonstrated via simulation. More details of our contributions in this part of the dissertation can be found in Section 2.1.2.

1.3.2 Mobility and Handover in Drone Cellular Networks

In Chapter 3, we characterize the performance of several canonical mobility models in a drone cellular network in which DBSs serve a set of UEs on the ground. In particular, we consider the following four mobility models: (i) straight line (SL), (ii) random stop (RS), (iii) RW, and (iv) RWP, among which the SL mobility model is inspired by the simulation models used by the 3GPP for the placement and trajectory of drones, while the other three are well-known canonical models (or their variants) that offer a useful balance between realism and tractability. Assuming the nearest-neighbor association policy, we consider two service models for the UEs: (i) UE independent model (UIM), and (ii) UE dependent model (UDM). While the serving DBS follows the same mobility model as the other DBSs in the UIM, it is assumed to fly towards the UE of interest in the UDM and hover above its location after reaching there. The main contribution of this chapter is a unified approach to characterize the point process of DBSs for all the mobility and service models. Using this, we provide exact mathematical expressions for the average received rate and the session rate as seen by the typical UE. Further, using tools from the calculus of variations, we concretely demonstrate that the simple SL mobility model provides a lower bound on the performance of other general mobility models (including the ones in which drones follow *curved* trajectories) as long as the movement of each drone in these models is independent and identically distributed (i.i.d.).

We analyze the handover probability in a drone cellular network in Chapter 4, where the initial positions of the DBSs serving the ground UEs are modeled by a homogeneous PPP. Similar to Chapter 3 and inspired by the mobility model considered in the 3GPP studies, we assume that all the DBSs move along straight lines in random directions. We further consider two different scenarios for the DBS speeds: (i) same speed model (SSM), and (ii) different speed model (DSM). Assuming nearest-neighbor association policy for the UEs on the ground, we characterize the handover probability of this network for both mobility scenarios. For the SSM, we compute the exact handover probability by establishing equivalence with a single-tier terrestrial cellular network, in which the BSs are static while the UEs are mobile. We then derive a lower bound for the handover probability in the DSM by characterizing the evolution of the spatial distribution of the DBSs over time. More details of our

contributions in this part of the dissertation can be found in Sections 3.1.2 and 4.1.

1.3.3 Impairments-Aware Air-to-Ground Wireless Communications

Chapter 5 of this dissertation is dedicated to the impact of random physical fluctuations of UAVs, also known as UAV wobbling, on the coherence time of the wireless channel between UAVs and a ground UE, using a Rician multi-path channel model. We consider two different scenarios for the number of UAVs: (i) *single UAV scenario* (SUS), and (ii) *multiple UAV scenario* (MUS). For each scenario, we model UAV wobbling by two random processes, i.e., the Wiener and sinusoidal processes, and characterize the channel autocorrelation function (ACF) which is then used to derive the coherence time of the channel. For the MUS, we further show that the UAV-UE channels for different UAVs are uncorrelated from each other. A key observation in this chapter is that even for small UAV wobbling, the coherence time of the channel may degrade quickly, which may make it more challenging to estimate the channel and establish a reliable communication link.

In Chapter 6, we develop an impairments-aware air-to-ground unified channel model that incorporates the effect of both wobbling and hardware impairments, where the former is caused by random physical fluctuations of UAVs, and the latter by intrinsic RF nonidealities at both the transmitter and receiver, such as phase noise, in-phase/quadrature (I/Q) imbalance, and power amplifier (PA) nonlinearity. The impact of UAV wobbling is modeled by two stochastic processes, i.e., the canonical Wiener process and the more realistic sinusoidal process. On the other hand, the *aggregate* impact of all hardware impairments is modeled as two multiplicative and additive distortion noise processes, which is a well-accepted model. For the sake of generality, we consider both wide-sense stationary (WSS) and nonstationary processes for the distortion noises. We then rigorously characterize the ACF of the wireless channel, using which we provide a comprehensive analysis of four key channel-related metrics: (i) power delay profile (PDP), (ii) coherence time, (iii) coherence bandwidth, and (iv) power spectral density (PSD) of the distortion-plus-noise process. Furthermore, we evaluate these metrics with reasonable UAV wobbling and hardware impairment models to obtain useful insights. Similar to our observation in the previous chapter, we demonstrate that the coherence time severely degrades at high frequencies even for small UAV wobbling, which renders air-to-ground channel estimation very difficult at these frequencies. More details of our contributions in this part of the dissertation can be found in Sections 5.1 and 6.1.2.

1.4 Organization

The rest of this dissertation is organized as follows. Considering 3D deployment of UAVs and following realistic antenna and channel models, we study the coexistence of UAVs with terrestrial BSs in Chapter 2, where BSs provide wireless backhaul to the UAVs in a two-hop

setting. In Chapter 3, we study various canonical mobility models in drone cellular networks and analyze the average received rate at the typical UE. Chapter 4 is devoted to the analysis of handover probability in drone cellular networks using different scenarios for drone speeds. Impact of UAV wobbling on the air-to-ground wireless channel is investigated in Chapter 5 and we propose and extensively study an impairment-aware unified channel model for the air-to-ground wireless communications in Chapter 6. We conclude the dissertation with a discussion on the potential future works in Chapter 7.

1.5 List of Publications

This dissertation had led to one book chapter and several journal and conference papers as listed below.

Book Chapters

[BC1] **M. Banagar**, V. V. Chetlur, and H. S. Dhillon, "Stochastic Geometry-Based Performance Analysis of Drone Cellular Networks," in *UAV Communications for 5G and Beyond*, chapter 9, pp. 231–254, John Wiley & Sons, Ltd, Dec. 2020.

Journal Publications

[J1] **M. Banagar** and H. S. Dhillon, "3D two-hop cellular networks with wireless backhauled UAVs: Modeling and fundamentals," *IEEE Trans. Wireless Commun.*, to appear.

[J2] **M. Banagar** and H. S. Dhillon, "Performance characterization of canonical mobility models in drone cellular networks," *IEEE Trans. Wireless Commun.*, vol. 19, no. 7, pp. 4994–5009, Jul. 2020.

[J3] **M. Banagar**, V. V. Chetlur, and H. S. Dhillon, "Handover probability in drone cellular networks," *IEEE Wireless Commun. Lett.*, vol. 9, no. 7, pp. 933–937, Jul. 2020.

[J4] **M. Banagar**, H. S. Dhillon, and A. F. Molisch, "Impact of UAV wobbling on the air-to-ground wireless channel," *IEEE Trans. Veh. Technol.*, vol. 69, no. 11, pp. 14025–14030, Nov. 2020.

[J5] **M. Banagar** and H. S. Dhillon, "Fundamentals of wobbling and hardware impairments-aware air-to-ground channel model," submitted, May 2022.

Conference Proceedings

[C1] **M. Banagar** and H. S. Dhillon, "Fundamentals of 3D two-hop cellular networks analysis with wireless backhauled UAVs," in *Proc. IEEE Global Commun. Conf.*, Dec. 2021.

[C2] **M. Banagar** and H. S. Dhillon, "3GPP-inspired stochastic geometry-based mobility model for a drone cellular network," in *Proc. IEEE Global Commun. Conf.*, Dec. 2019.

[C3] **M. Banagar** and H. S. Dhillon, "Fundamentals of drone cellular network analysis under random waypoint mobility model," in *Proc. IEEE Global Commun. Conf.*, Dec. 2019.

[C4] **M. Banagar** and H. S. Dhillon, "Wobbling and impairments-aware channel model and its implications on high-frequency UAV links," submitted to *IEEE Global Commun. Conf.*, May 2022.

Chapter 2

3D Two-Hop Cellular Networks with Wireless Backhauled UAVs: Modeling and Fundamentals

2.1 Introduction

Owing to their unique deployment advantages, such as agility, cost-effectiveness, and high probability of LoS, UAVs are widely regarded as an indispensable component of modern wireless networks [2, 63, 64]. Specifically, UAVs can act as aerial UEs, BSs, or even relays to expand the coverage or capacity of a terrestrial network or to establish a temporary wireless network in case of natural disasters. Since most UAV platforms are able to move freely in the sky and do not have any wired connection to the ground, they will naturally need to establish *wireless backhaul* connections with fiber-backhauled BSs on the ground. Since terrestrial BSs are downtilted, these wireless backhaul connections may be established through BS antenna sidelobes, which may limit their capacity [65, 66]. Given the 3D nature of this network and the intricate dependencies of access and backhaul links in this setup, it is not straightforward to quantify the performance of this network. Tackling this important challenge, this chapter develops a comprehensive framework with foundations in stochastic geometry to study the end-to-end performance of this 3D two-hop network in which the UE on the ground may be served by a UAV, which, in turn, is wirelessly backhauled to a terrestrial BS. Crucially, our analysis is cognizant of the performance limiting characteristics of the UAV networks, such as the realistic antenna patterns of BSs. Going further, we also characterize the performance gains obtained by deploying dedicated uptilted antennas at the terrestrial BSs specifically for the backhaul purposes.

2.1.1 Related Works

This chapter lies at the intersection of the following three research directions: (i) relaying in cellular networks, (ii) stochastic geometry for UAV networks, and (iii) wirelessly backhauled UAVs. We discuss each of the above lines of research next.

Relaying in Cellular Networks. The idea of using relays for improving the performance of cellular networks, such as increasing the coverage area or offering higher throughput to the UEs, is well-established in wireless communications [67, 68, 69, 70, 71, 72]. Two major cooperative signaling methods, i.e., AF and DF, have been extensively studied in the literature [67]. For instance, the authors in [68] studied the information-theoretic aspects of both AF and DF relaying schemes along with their variants. End-to-end performance of cooperative relay networks over Rayleigh and Nakagami fading channels has been analyzed in several works, such as in [69, 70, 72], where the authors obtained mathematical expressions for the end-to-end signal-to-noise ratio (SNR) of each relaying protocol. Moving forward to the past decade, interference has become a non-negligible factor in determining the performance of wireless networks due to a dramatic increase in the number of nodes and bandwidth scarcity. Taking the impact of interference into account, the authors in [73] studied the outage performance of a multi-hop AF communication system where the relays were exposed to a Poisson field of interferes. Using tools from stochastic geometry and optimization theory, the authors in [74] provided a system-level analysis of two-hop DF networks and showed that the benefits of relays could be negligible if the system is not appropriately designed. In recent years and with the emergence of UAVs as potential wireless nodes, there has been a lot of interest in using UAVs as relays [75, 76, 77, 78]. For example, the authors in [75] considered the problem of joint power and trajectory optimization for an AF relay network consisting of a single UAV as a relay. The problem of using either only one UAV or multiple UAVs as relays is studied in [76], where the placement of UAVs is optimized by maximizing the end-to-end SNR for both AF and DF relaying protocols. The optimal placement of a UAV-relay for maximum reliability is considered in [77], where the UAV altitude is also optimized for both static and mobile UAVs.

Stochastic Geometry for UAV Networks. Given the irregular locations of transmitters and receivers in modern wireless networks, it is reasonable to consider the random network viewpoint for the system-level analysis of such networks using ideas from stochastic geometry [19, 79, 80]. This is particularly relevant for UAV networks, where the UAVs could act either as BSs, UEs, or relays with random placements and movements [81, 82, 83, 84, 85, 86]. Considering a finite network of UAVs distributed as a binomial point process (BPP), the authors in [20] studied the coverage probability of the network for the cases of with and without fading. Motivated by this work, the problem of designing stochastic trajectory processes for mobile UAVs was investigated in [37] and the same coverage trends as in [20] were observed. Modeling the locations of UAVs as a BPP, the authors in [22] studied the coexistence problem of UAVs with a network of BSs distributed as a Poisson point process (PPP) on the ground. They have also considered probabilistic LoS/NLoS channel model to further leverage the benefits of using UAVs. Along similar lines, the authors in [87] and [88] analyzed the received rate for a terrestrial and aerial UE, respectively, in a vertical heterogeneous network, comprising of terrestrial BSs and UAVs acting as BSs. Using probabilistic channel model and realistic antenna pattern at the BS site, the problem of finding the optimal spectrum sharing strategy for UAV-to-UAV communications is studied in [89]. Considering Poisson cluster processes, the authors in [90] investigated the impact of different UAV placement

strategies, which could be either independent of or dependent on the UE locations on the ground.

Wirelessly Backhauled UAVs. Given the growing number of BSs in the forms of terrestrial (macro or small cell) and aerial units, providing strong fiber backhaul for all of these BSs is a challenging task. Therefore, it is inevitable that some of the BSs in a cellular network are wirelessly backhauled to the core network [28, 29, 30]. This is specifically the case for most UAVs, as they are supposed to hover and move freely in the sky, unless being tethered to a building rooftop [31]. In [32], the impact of UAV millimeter-wave (mmWave) backhauling is considered in an aerial-terrestrial cellular network using tools from stochastic geometry. Along similar lines, the authors in [33] studied the success probability of establishing a wireless backhaul network using directional antenna patterns for the UAVs. In [34], the authors used tools from graph theory to solve a 3D UAV placement problem, where UAVs serve the ground UEs and are also wirelessly backhauled to the terrestrial BSs. Optimal 3D path planning problem for a UAV is investigated in [35] considering both backhaul constraint and realistic antenna patterns. The main idea was to change the UAV height during the course of its path to improve the backhaul link quality using dynamic programming. Considering link blockages in mmWave frequencies, the authors in [36] studied the use of UAVs as relays in a flexible backhaul architecture for dynamically rerouting to alternative paths.

Taking full advantage of UAVs for wireless backhaul support requires considering UAV-specific criteria, such as 3D deployment [91], realistic antenna patterns (both at the UAV and BS sites) [66, 92], and a high probability of LoS transmission. In this work, we present the first stochastic geometry-based analysis of 3D UAV-assisted two-hop cellular networks using realistic antenna and channel models. Our key contributions are summarized next.

2.1.2 Contributions

This chapter provides a comprehensive analysis of downlink transmission in a two-hop UAV-assisted 3D communication system using realistic antenna and channel models. In particular, we model the fiber-backhauled BSs as a two-dimensional (2D) homogeneous PPP at a constant height that serve the ground UEs. UAVs are wirelessly backhauled to the BSs and are modeled as a 3D homogeneous PPP hovering between two permissible heights. We assume realistic antenna patterns for the BSs and UAVs based on 3GPP studies [93] and also consider a probabilistic LoS/NLoS channel model for the air-to-ground communication links. Using the max-power association policy for selecting the serving BS and UAV, we consider both AF and DF relaying protocols and adopt a hybrid scheme where a UE is either served directly by a one-hop access link from the serving terrestrial BS or by a two-hop link consisting of an access link from the serving UAV to the UE and a backhaul link from the terrestrial BS to that UAV. Selection between one-hop or two-hop connection is made based on the received SINR [71]. In both cases, we will term the terrestrial BS as the *serving BS*, where it serves the UE directly in the one-hop connection and the serving UAV over the backhual link in

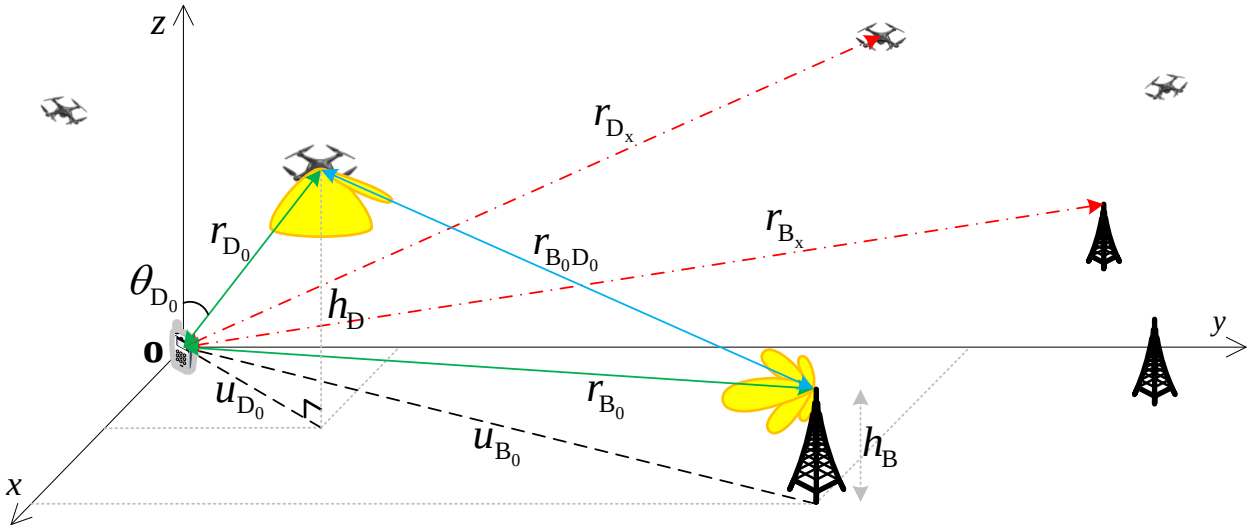

Figure 2.1: An illustration of the system model. Desired and interfering signals to the typical UE are denoted by solid green and dotted red lines, and the access and backhaul links to the typical UE are shown as solid green and blue lines, respectively.

the two-hop connection. For this setup, we highlight our key contributions next.

Mathematical Constructs for 3D Relay-Assisted Communication Networks

We derive the distribution of several random variables that are the building blocks for the analysis of two-hop AF and DF relaying protocols. Furthermore, considering the 3D PPP of UAVs and the probabilistic channel model, we obtain the LoS/NLoS association probabilities and derive the joint distribution of the distance and zenith angle of the serving UAV to the typical UE. We also provide asymptotic results for these distributions.

Coverage Performance in Backhaul-Aware Communication Networks

We develop a general framework for analyzing the coverage probability in backhaul-aware two-hop communication networks. For a specific serving UAV channel condition, we derive the conditional Laplace transform of interference for both LoS and NLoS interfering UAVs. Using this Laplace transform along with the distributional results described above, we characterize the coverage probability for both AF and DF relaying protocols.

Design Insights with Directional Antenna Models

Inspired by 3GPP documents [6, Section 5.8], we propose a novel method to increase the coverage probability of the network by adding a dedicated uptilted directional antenna at

the BS site, which is only used for backhaul purposes. This is the first work that considers uptilted antennas at the BS sites for improving aerial coverage. As a baseline, we also consider canonical isotropic antennas, which are vastly used in the literature, and demonstrate the superiority of using directional antennas over them in the simulation results.

2.2 System Model

2.2.1 Spatial Setup

We consider a 3D setting where BSs and UAVs coexist to serve UEs on the ground. We assume that BSs have a constant height of h_{B} and the projection of BS locations onto the ground follows a homogeneous PPP Φ_{B} with density λ_{B}. Independently from Φ_{B}, UAVs are distributed based on a 3D homogeneous PPP Φ_{D} with density λ_{D} in the space enclosed between heights $h_{\mathrm{D,m}}$ and $h_{\mathrm{D,M}}$, which represent the minimum and maximum allowable UAV heights, respectively. The ground UEs are distributed as another homogeneous PPP Φ_{U} independently from Φ_{B} and Φ_{D}. In this setup, we consider the ground to be aligned with the xy-plane of the 3D coordinate system, and without loss of generality, we perform the analysis for the *typical UE* placed at the origin $\mathbf{o} = (0, 0, 0)$. As shown in Fig. 2.1, we represent the 3D distances from a BS and a UAV located at $\mathrm{B}_{\mathbf{x}} \in \Phi_{\mathrm{B}}$ and $\mathrm{D}_{\mathbf{x}} \in \Phi_{\mathrm{D}}$ to $\mathbf{o}$ by $r_{\mathrm{B}_{\mathbf{x}}} = \sqrt{u_{\mathrm{B}_{\mathbf{x}}}^2 + h_{\mathrm{B}}^2}$ and $r_{\mathrm{D}_{\mathbf{x}}} = \sqrt{u_{\mathrm{D}_{\mathbf{x}}}^2 + h_{\mathrm{D}}^2}$, respectively, where $u_{\mathrm{B}_{\mathbf{x}}}$ and $u_{\mathrm{D}_{\mathbf{x}}}$ are the 2D (i.e., horizontal) distances from $\mathrm{B}_{\mathbf{x}}$ and $\mathrm{D}_{\mathbf{x}}$ to $\mathbf{o}$, respectively. In this chapter, we use subscript '0' for denoting the serving BS and UAV. Therefore, the locations of the serving BS and UAV are denoted by B_0 and D_0, respectively[1], and the 3D and 2D distances from B_0 (resp. D_0) to $\mathbf{o}$ are denoted by $r_{\mathrm{B}_0} = \sqrt{u_{\mathrm{B}_0}^2 + h_{\mathrm{B}}^2}$ and u_{B_0} (resp. $r_{\mathrm{D}_0} = \sqrt{u_{\mathrm{D}_0}^2 + h_{\mathrm{D}_0}^2}$ and u_{D_0}), respectively, where h_{D_0} is the serving UAV height. We represent the 3D distance between B_0 and D_0 by $r_{\mathrm{B}_0\mathrm{D}_0}$. More details on the serving BS and UAV are given in Section 2.2.4.

Remark 2.1. Since the UAVs should be able to hover at any location, we require them to be rotary-wing drones in this chapter.

2.2.2 Antenna Pattern

We adopt realistic antenna radiation patterns [93] for BSs, UAVs, and UEs, as explained next.

[1]With a slight abuse of notation, we represent both the location of the serving BS and the serving BS itself by B_0. The same goes with D_0 as well.

BS

We consider two different antenna models at the BSs: (i) omnidirectional antenna[2], and (ii) a combination of omnidirectional and directional antennas. Although our main focus in this chapter is on realistic antenna patterns, we will also study the canonical isotropic antenna pattern, which has the same radiation pattern in *all* directions, as a baseline for comparison.

Downtilted Omnidirectional In this model proposed by 3GPP, we consider a uniform linear array (ULA) that is vertically installed at each BS. The ULA has N_{B} elements, equally separated by $\lambda/2$, where $\lambda = \mathrm{c}/f$ is the wavelength of the operating frequency f and c is the speed of light. The *normalized array factor* for this ULA can be written as [94, Sec. 8.3.2]

$$f_{\mathrm{A}}(\theta, \theta_{\mathrm{B}}) = \frac{\sin\left(N_{\mathrm{B}} \frac{\pi}{2}[\cos(\theta) - \cos(\theta_{\mathrm{B}})]\right)}{N_{\mathrm{B}} \sin\left(\frac{\pi}{2}[\cos(\theta) - \cos(\theta_{\mathrm{B}})]\right)}, \tag{2.1}$$

where θ and θ_{B} are, respectively, the zenith angle and the direction of the BS antenna mainlobe, both measured from the z-axis of the 3D coordinate system. Note that since the primary objective of terrestrial BSs is to serve the ground UEs, their antenna mainlobes are tilted downward to the ground, which means that $\pi/2 < \theta_{\mathrm{B}} < \pi$. Each element of the ULA is an omnidirectional antenna that has a normalized vertical radiation power pattern (in dB) of

$$G_{\mathrm{E,V}}(\theta) = -\min\left\{12\left(\frac{\theta - \pi/2}{\theta_{\mathrm{3dB}}}\right)^2,\ \mathrm{SLA}_{\mathrm{V}}\right\},$$

where $\theta_{\mathrm{3dB}} = 65°$ is the vertical 3dB beamwidth and $\mathrm{SLA}_{\mathrm{V}} = 30$ dB is the sidelobe attenuation limit [93]. Note that this antenna is omnidirectional along the horizontal direction with a normalized gain of $G_{\mathrm{E,H}}(\phi) = 0$ dB, where ϕ is the azimuthal angle measured from the x-axis in the xy-plane. Furthermore, we assume the maximum gain of each antenna element is $G_{\mathrm{E}}^{\max} = 8$ dBi [93]. Therefore, we write the *3D element pattern* as

$$\begin{aligned} G_{\mathrm{E,3D}}(\theta, \phi) &= G_{\mathrm{E}}^{\max} + G_{\mathrm{E,V}}(\theta) + G_{\mathrm{E,H}}(\phi) \\ &= G_{\mathrm{E}}^{\max} + G_{\mathrm{E,V}}(\theta) \\ &:= G_{\mathrm{E}}(\theta). \end{aligned}$$

The complete gain of the BS antenna array along direction θ for all ϕ can now be written in dBi as [94, Sec. 8.4]

$$G_{\mathrm{B}}^{\mathrm{OmniD}}(\theta, \theta_{\mathrm{B}}) = G_{\mathrm{E}}(\theta) + 20\log(|f_{\mathrm{A}}(\theta, \theta_{\mathrm{B}})|), \tag{2.2}$$

where the superscript OmniD stands for "downtilted omnidirectional".

[2] In antenna theory terminology, "omnidirectional" refers to constant radiation pattern only in the *horizontal* direction [94].

Downtilted Omnidirectional and Uptilted Directional Looking closely at the previous model, we observe that UAVs are mostly served by the BS antenna sidelobes, which is a major drawback of this model since sidelobe peak gain is usually much lower than the mainlobe peak gain. For instance, the sidelobe level for a ULA with a large number of antenna elements is about -13.3 dB [94, Sec. 8.3.1]. Furthermore, UAVs may be in the null direction of the BS antenna array, which could cause an outage in the UAV-BS link. As discussed in 3GPP TR 22.829 [6, Section 5.8], one way to combat these effects and improve the backhaul link is to deploy a separate *uptilted* directional antenna along with the aforementioned downtilted omnidirectional antenna array at the BS. Note that this newly added directional antenna is merely used for backhaul purposes, i.e., communicating with the UAVs. It is worth mentioning that while this work was under review, other researchers have also used the idea of adding equipment at the BS sites to better accommodate UAVs, see e.g., [95, 96]. In both these works, the authors try to optimize the tilt angle of the BS uptilted antenna to avoid aerial coverage holes and guarantee reliable communications.

Similar to the downtilted omnidirectional antenna model, we use the 3GPP-based antenna pattern here as well, which can be either mechanically or electrically steered toward the UAV locations. More specifically, when directed toward (θ_0, ϕ_0), this antenna has normalized vertical, horizontal, and 3D radiation power patterns (in dB) of

$$G_{\mathrm{V}}(\theta, \theta_0) = -\min\left\{12\left(\frac{\theta-\theta_0}{\theta_{3\mathrm{dB}}}\right)^2,\ \mathrm{SLA}_{\mathrm{V}}\right\},$$
$$G_{\mathrm{H}}(\phi, \phi_0) = -\min\left\{12\left(\frac{\phi-\phi_0}{\phi_{3\mathrm{dB}}}\right)^2,\ A_{\mathrm{m}}\right\},$$
$$G_{\mathrm{3D}}(\theta, \phi, \theta_0, \phi_0) = -\min\left\{-G_{\mathrm{V}}(\theta, \theta_0) - G_{\mathrm{H}}(\phi, \phi_0),\ A_{\mathrm{m}}\right\},$$

respectively, where $\theta_{3\mathrm{dB}} = 10^\circ$ and $\phi_{3\mathrm{dB}} = 10^\circ$ are the vertical and horizontal 3dB beamwidths and $A_{\mathrm{m}} = 30$ dB is the front-back ratio [93]. Note that we used narrower beamwidths than those in the downtilted omnidirectional antenna to reduce interference. Furthermore, since this antenna is tilted upward, we require that $0 < \theta_0 < \pi/2$. Hence, the gain of this antenna along direction (θ, ϕ) in dBi becomes

$$G_{\mathrm{B}}^{\mathrm{DirU}}(\theta, \phi, \theta_0, \phi_0) = G^{\max} + G_{\mathrm{3D}}(\theta, \phi, \theta_0, \phi_0),$$

where $G^{\max} = 8$ dBi is the maximum gain of this antenna and the superscript DirU stands for "uptilted directional".

UAV

We assume UAVs are equipped with two sets of antennas, one for the backhaul connection and the other for the access link (see Fig. 2.1). The backhaul antenna is directional and has the same pattern as the uptilted directional antenna at the BS described earlier in Section

2.2.2, with the only difference that its main beam is not necessarily tilted upward. In fact, since the height of the UAVs are usually higher than that of the BSs, the UAV backhaul antenna is usually downtilted. Hence, we write the gain of this antenna as

$$G_{\mathrm{D}}^{\mathrm{BH}}(\theta,\phi,\theta_0,\phi_0) = G_{\mathrm{B}}^{\mathrm{DirU}}(\theta,\phi,\theta_0,\phi_0),$$

where $\pi/2 < \theta_0 < \pi$ and the superscript BH stands for "backhaul". On the other hand, the access antenna is assumed to be downtilted omnidirectional with the following features: (i) static (non-steerable), so the mainlobe direction cannot change, (ii) tilted completely toward the ground with $\theta_0 = \pi$, and (iii) has a wider beam than the backhaul antenna to serve the UEs and we set $\theta_{3\mathrm{dB}} = 120°$. Thus, the UAV access antenna gain can be written in dBi as

$$G_{\mathrm{D}}^{\mathrm{AC}}(\theta) = G^{\max} - \min\left\{12\left(\frac{\theta-\pi}{\theta_{3\mathrm{dB}}}\right)^2,\ \mathrm{SLA}\right\}, \tag{2.3}$$

where $G^{\max} = 8$ dBi, SLA = 30 dB [93], and the superscript AC stands for "access".

UE

Each UE is equipped with an isotropic antenna with gain $G_{\mathrm{U}} = 0$ dBi in all directions.

Remark 2.2. As mentioned earlier, the antenna mainlobe directions for both the BS omnidirectional and the UAV access antennas are static, while the BS directional antenna (which is used only for backhaul) and the UAV backhaul antenna have both steerable mainlobe directions. As for the UAV and the terrestrial BS to which it is backhauled, we assume that their backhaul antennas are steered exactly toward each other, while the antenna directions of interfering BSs and UAVs are chosen uniformly at random.

2.2.3 Channel Model

LoS and NLoS Channel Conditions

One of the major advantages of employing UAVs in wireless communications is their superior channel conditions as compared to their terrestrial counterparts. In fact, since UAVs usually fly at high altitudes, they are expected to have a high probability of LoS, which results in low attenuation in the received signal [5]. To capture this unique feature of aerial networks, we consider a mixture of LoS and NLoS links for the channel model. Specifically, a UAV establishes an LoS link with the typical UE with probability [11]

$$p_{\mathrm{L}}(\theta) = \frac{1}{1 + c_1 \mathrm{e}^{-c_2(90-\theta-c_1)}}, \tag{2.4}$$

and an NLoS link with probability $p_{\mathrm{N}}(\theta) = 1 - p_{\mathrm{L}}(\theta)$, where θ is the zenith angle measured from the z-axis in degrees ($90 - \theta$ is the elevation angle), and c_1 and c_2 are two positive environment-dependent parameters. From (2.4), we observe that as the UAV height increases, θ decreases, and thus, $p_{\mathrm{L}}(\theta)$ will increase. Note that we use this model only for the UAV-UE channels. Since the BS heights are usually comparable to those of buildings in urban or rural environments, we assume that BS-UAV and BS-UE links are always in LoS and NLoS conditions, respectively.

Received Powers

We assume that BSs and UAVs transmit with constant powers P_{B} and P_{D}, respectively. For consistency, we represent the antenna gains of the BSs and UAVs toward the typical UE (access) by G and toward each other and among themselves (backhaul) by g. Since the BS-UE link is in an NLoS condition, the received power at the typical UE from the serving BS can be written as $P^{\mathrm{Rx}}_{\mathrm{B}_0} = P_{\mathrm{B}} G_{\mathrm{B}_0} G_{\mathrm{U}} f_{\mathrm{B}_0} r_{\mathrm{B}_0}^{-\alpha_{\mathrm{N}}} \eta_{\mathrm{N}}^{-1}$, where G_{B_0} is the serving BS antenna gain along the direction of the typical UE, G_{U} is the typical UE antenna gain, f_{B_0} is the small-scale fading power between the serving BS and the typical UE, and α_{N} and η_{N} are the path-loss exponent and the mean excessive path-loss for NLoS transmission, respectively [11]. On the other hand, the BS-UAV link is in an LoS condition, and thus, we write the received power at the serving UAV from the serving BS as $P^{\mathrm{Rx}}_{\mathrm{B}_0\mathrm{D}_0} = P_{\mathrm{B}} g_{\mathrm{B}_0} g_{\mathrm{D}_0} f_{\mathrm{B}_0\mathrm{D}_0} r_{\mathrm{B}_0\mathrm{D}_0}^{-\alpha_{\mathrm{L}}} \eta_{\mathrm{L}}^{-1}$, where g_{B_0} is the serving BS antenna gain along the direction of the serving UAV, g_{D_0} is the serving UAV antenna gain along the direction of the serving BS, $f_{\mathrm{B}_0\mathrm{D}_0}$ is the small-scale fading power between the serving BS and the serving UAV, and α_{L} and η_{L} are the path-loss exponent and the mean excessive path-loss for LoS transmission, respectively. Since the UAV-UE link may experience both channel conditions, we write the received power at the typical UE from the serving UAV for the LoS and NLoS conditions, respectively, as $P^{\mathrm{Rx}}_{\mathrm{D}_0,\mathrm{L}} = P_{\mathrm{D}} G_{\mathrm{D}_0} G_{\mathrm{U}} f_{\mathrm{D}_0} r_{\mathrm{D}_0,\mathrm{L}}^{-\alpha_{\mathrm{L}}} \eta_{\mathrm{L}}^{-1}$ and $P^{\mathrm{Rx}}_{\mathrm{D}_0,\mathrm{N}} = P_{\mathrm{D}} G_{\mathrm{D}_0} G_{\mathrm{U}} f_{\mathrm{D}_0} r_{\mathrm{D}_0,\mathrm{N}}^{-\alpha_{\mathrm{N}}} \eta_{\mathrm{N}}^{-1}$, where G_{D_0} is the serving UAV antenna gain along the direction of the typical UE, f_{D_0} is the small-scale fading power between the serving UAV and the typical UE, and $r_{\mathrm{D}_0,\mathrm{L}}$ and $r_{\mathrm{D}_0,\mathrm{N}}$ are the serving UAV distances to the typical UE in LoS and NLoS conditions, respectively. Note that we have $\alpha_{\mathrm{L}} < \alpha_{\mathrm{N}}$ and $\eta_{\mathrm{L}} < \eta_{\mathrm{N}}$.

Let us now define interference at the typical UE and the serving UAV, which are of interest for the downlink analysis. We represent the set of interfering BSs and UAVs by $\Phi'_{\mathrm{B}} \coloneqq \Phi_{\mathrm{B}} \backslash \mathrm{B}_0$ and $\Phi'_{\mathrm{D}} \coloneqq \Phi_{\mathrm{D}} \backslash \mathrm{D}_0$, respectively, and write the received power at the typical UE and the serving UAV from the interfering BSs (I_{BU} and I_{BD}) and the received power at the serving UAV from the interfering UAVs (I_{DD}) as $I_{\mathrm{BU}} = \sum_{\mathrm{B}_{\mathbf{x}} \in \Phi'_{\mathrm{B}}} P_{\mathrm{B}} G_{\mathrm{B}_{\mathbf{x}}} G_{\mathrm{U}} f_{\mathrm{B}_{\mathbf{x}}} r_{\mathrm{B}_{\mathbf{x}}}^{-\alpha_{\mathrm{N}}} \eta_{\mathrm{N}}^{-1}$, $I_{\mathrm{BD}} = \sum_{\mathrm{B}_{\mathbf{x}} \in \Phi'_{\mathrm{B}}} P_{\mathrm{B}} g_{\mathrm{B}_{\mathbf{x}}} g_{\mathrm{D}_0} f_{\mathrm{B}_{\mathbf{x}}\mathrm{D}_0} r_{\mathrm{B}_{\mathbf{x}}\mathrm{D}_0}^{-\alpha_{\mathrm{L}}} \eta_{\mathrm{L}}^{-1}$, and $I_{\mathrm{DD}} = \sum_{\mathrm{D}_{\mathbf{x}} \in \Phi'_{\mathrm{D}}} P_{\mathrm{D}} g_{\mathrm{D}_{\mathbf{x}}} g_{\mathrm{D}_0} f_{\mathrm{D}_{\mathbf{x}}\mathrm{D}_0} r_{\mathrm{D}_{\mathbf{x}}\mathrm{D}_0}^{-\alpha_{\mathrm{L}}} \eta_{\mathrm{L}}^{-1}$, respectively, where the parameters $G_{\mathrm{B}_{\mathbf{x}}}$, $f_{\mathrm{B}_{\mathbf{x}}}$, $g_{\mathrm{B}_{\mathbf{x}}}$, $f_{\mathrm{B}_{\mathbf{x}}\mathrm{D}_0}$, $g_{\mathrm{D}_{\mathbf{x}}}$, and $f_{\mathrm{D}_{\mathbf{x}}\mathrm{D}_0}$ are defined similarly as in the serving BS/UAV parameters described earlier. As for the received power at the typical UE from the interfering UAVs, we first partition the set of all UAVs in two disjoint sets of LoS ($\Phi_{\mathrm{D,L}}$) and NLoS ($\Phi_{\mathrm{D,N}}$) UAVs. Using thinning theorem for the PPP Φ_{D}, we observe that $\Phi_{\mathrm{D,L}}$ and $\Phi_{\mathrm{D,N}}$ are two independent inhomogeneous PPPs with densities $\lambda_{\mathrm{D}} p_{\mathrm{L}}(\theta)$ and

$\lambda_{\mathrm{D}} p_{\mathrm{N}}(\theta)$, respectively [19]. The point process of interfering UAVs in LoS and NLoS conditions can now be defined as $\Phi'_{\mathrm{D,L}} \coloneqq \Phi_{\mathrm{D,L}} \backslash \mathrm{D}_0$ and $\Phi'_{\mathrm{D,N}} \coloneqq \Phi_{\mathrm{D,N}} \backslash \mathrm{D}_0$. Finally, we define the received power at the typical UE from each set as $I_{\mathrm{DU,L}} = \sum_{\mathrm{D}_{\mathbf{x}} \in \Phi'_{\mathrm{D,L}}} P_{\mathrm{D}} G_{\mathrm{D}_{\mathbf{x}}} G_{\mathrm{U}} f_{\mathrm{D}_{\mathbf{x}}} r_{\mathrm{D}_{\mathbf{x}}}^{-\alpha_{\mathrm{L}}} \eta_{\mathrm{L}}^{-1}$ and $I_{\mathrm{DU,N}} = \sum_{\mathrm{D}_{\mathbf{x}} \in \Phi'_{\mathrm{D,N}}} P_{\mathrm{D}} G_{\mathrm{D}_{\mathbf{x}}} G_{\mathrm{U}} f_{\mathrm{D}_{\mathbf{x}}} r_{\mathrm{D}_{\mathbf{x}}}^{-\alpha_{\mathrm{N}}} \eta_{\mathrm{N}}^{-1}$, where the parameters $G_{\mathrm{D}_{\mathbf{x}}}$ and $f_{\mathrm{D}_{\mathbf{x}}}$ are defined similarly as before. We also represent the total interference from the UAVs at the typical UE by $I_{\mathrm{DU}} = I_{\mathrm{DU,L}} + I_{\mathrm{DU,N}}$, and the total interference from both the BSs and UAVs at the typical UE by $I_{\mathrm{U}} = I_{\mathrm{BU}} + I_{\mathrm{DU}}$. The received SINR at the typical UE from the serving BS, the received SINR at the typical UE from the serving UAV, and the received SINR at the serving UAV from the serving BS are defined, respectively, as

$$\mathrm{SINR}_{\mathrm{BU},q} = \frac{P^{\mathrm{Rx}}_{\mathrm{B}_0}}{I_{\mathrm{U}} + P^{\mathrm{Rx}}_{\mathrm{D}_0,q} + N_0}, \tag{2.5}$$

$$\mathrm{SINR}_{\mathrm{DU},q} = \frac{P^{\mathrm{Rx}}_{\mathrm{D}_0,q}}{I_{\mathrm{U}} + P^{\mathrm{Rx}}_{\mathrm{B}_0} + N_0}, \tag{2.6}$$

$$\mathrm{SINR}_{\mathrm{BD}} = \frac{P^{\mathrm{Rx}}_{\mathrm{B}_0\mathrm{D}_0}}{I_{\mathrm{BD}} + I_{\mathrm{DD}} + N_0}, \tag{2.7}$$

where $q = \{\mathrm{L}, \mathrm{N}\}$ denotes the LoS or NLoS channel conditions and N_0 is the noise power.

Assumption 1. For *non-isotropic* antennas, the total interference at the serving UAV from other BSs (I_{BD}) and UAVs (I_{DD}) is negligible and assumed to be 0 in this chapter. Therefore, we have $\mathrm{SINR}_{\mathrm{BD}} \approx \mathrm{SNR}_{\mathrm{BD}} = \frac{P^{\mathrm{Rx}}_{\mathrm{B}_0\mathrm{D}_0}}{N_0}$, where $\mathrm{SNR}_{\mathrm{BD}}$ is the SNR at the serving UAV from the serving BS.

Fading

We consider Nakagami-m fading model for both the LoS and NLoS channels since it captures a wide variety of fading environments[3]. Hence, the channel fading powers f_{B_0}, f_{D_0}, $f_{\mathrm{B}_0\mathrm{D}_0}$, $f_{\mathrm{B}_{\mathbf{x}}}$, $f_{\mathrm{D}_{\mathbf{x}}}$, $f_{\mathrm{B}_{\mathbf{x}}\mathrm{D}_0}$, and $f_{\mathrm{D}_{\mathbf{x}}\mathrm{D}_0}$ are all gamma distributed with probability density function (pdf) and cumulative distribution function (cdf) of $f_X(x) = \frac{m^m}{\Gamma(m)} x^{m-1} \mathrm{e}^{-mx}$ and $F_x(x) = \frac{1}{\Gamma(m)} \gamma(m, mx)$, respectively, where $\gamma(s, x) = \int_0^x t^{s-1} \mathrm{e}^{-t}\, \mathrm{d}t$ is the lower incomplete gamma function and $\Gamma(s) = \gamma(s, \infty)$ is the gamma function. For mathematical tractability, we assume that m is integer and the serving and interfering links have the same m values.

[3]The most natural choice for modeling small-scale fading in UAV-assisted communications is Rician fading, which makes a clear distinction between the direct and scattered paths. This is mainly due to the high probability of LoS in aerial networks [11]. However, the Rician pdf does not lend itself to further analysis since it entails modified Bessel function. Because of this, we use the Nakagami-m fading model instead of the Rician model, which is quite common in the literature for system-level analysis thanks to its mathematical tractability. Furthermore, using the moment matching technique, it is well-known that the Rician distribution with factor K can be well approximated with the Nakagami-m distribution using the relation $m = \frac{(K+1)^2}{2K+1}$.

2.2.4 Service Model and Association Policy

We assume BSs have strong and reliable fiber backhaul connections to the core network, while UAVs are wirelessly backhauled to the BSs. To connect UEs to the core network, we consider the following two service models: (i) access only, where the UEs connect directly to the BSs via access links, and (ii) joint access and backhaul, where the UEs use UAVs as relays for connecting to the BSs. In the second service model, UAV-UE and BS-UAV links are regarded as the access and backhaul links, respectively. In this chapter, we use a *hybrid* scheme where the UEs can be served either directly by the BS-UE links or indirectly by a two-hop connection consisting of the BS-UAV and UAV-UE links. The selection between the one-hop and two-hop connections is made based on the SINR [71]. Using the maximum received power association policy, we write the association rules as

$$\mathrm{B}_0 = \underset{\mathrm{B}_{\mathbf{x}}\in\Phi_{\mathrm{B}}}{\arg\max}\, P^{\mathrm{Rx}}_{\mathrm{B}_{\mathbf{x}}} = \underset{\mathrm{B}_{\mathbf{x}}\in\Phi_{\mathrm{B}}}{\arg\max}\, r^{-\alpha_{\mathrm{N}}}_{\mathrm{B}_{\mathbf{x}}} = \underset{\mathrm{B}_{\mathbf{x}}\in\Phi_{\mathrm{B}}}{\arg\min}\, r_{\mathrm{B}_{\mathbf{x}}}, \tag{2.8}$$

$$\mathrm{D}_0 = \underset{q\in\{\mathrm{L},\mathrm{N}\},\, \mathrm{D}_{\mathbf{x}}\in\Phi_{\mathrm{D},q}}{\arg\max}\, P^{\mathrm{Rx}}_{\mathrm{D}_{\mathbf{x}},q} = \underset{q\in\{\mathrm{L},\mathrm{N}\},\, \mathrm{D}_{\mathbf{x}}\in\Phi_{\mathrm{D},q}}{\arg\max}\, r^{-\alpha_q}_{\mathrm{D}_{\mathbf{x}}}\eta_q^{-1}, \tag{2.9}$$

where the impact of antenna gains is absorbed into η_q for simplicity. Note that since all the BSs experience the NLoS channel condition when connecting to the typical UE, the maximum average received power and the nearest neighbor association policies are equivalent for the BSs. However, this is not the case for the UAVs, as a farther UAV to the typical UE may have better channel conditions than a nearer one, and thus, be regarded as the serving UAV.

2.2.5 Relaying Protocols and Metrics

We adopt both AF and DF relaying protocols in this chapter. Considering AF downlink transmission, the received signal from the source (BS) at the relay (UAV) is multiplied by a gain G before being forwarded to the destination (UE). Note that the choice of the relay gain G defines the overall performance of the AF relaying protocol [68, 70]. Assuming $G = 1/(P^{\mathrm{Rx}}_{\mathrm{B}_0\mathrm{D}_0} + I_{\mathrm{BD}} + I_{\mathrm{DD}} + N_0)$, the AF end-to-end SINR for the UAV-UE channel condition q can be written as

$$\mathrm{SINR}^{\mathrm{AF}}_{\mathrm{e2e},q} = \frac{\mathrm{SINR}_{\mathrm{BD}}\mathrm{SINR}_{\mathrm{DU},q}}{\mathrm{SINR}_{\mathrm{BD}} + \mathrm{SINR}_{\mathrm{DU},q} + 1}. \tag{2.10}$$

In the DF protocol, the received signal is first decoded and then forwarded to the destination. Since both the relay and destination nodes must decode the source signal without error for a successful transmission [68], we write the DF end-to-end SINR for channel condition q as

$$\mathrm{SINR}^{\mathrm{DF}}_{\mathrm{e2e},q} = \min\left\{\mathrm{SINR}_{\mathrm{BD}}, \mathrm{SINR}_{\mathrm{DU},q}\right\}. \tag{2.11}$$

We can easily show that the DF protocol always outperforms the AF protocol. In fact, we have

$$\mathrm{SINR}^{\mathrm{DF}}_{\mathrm{e2e},q} > \left(\mathrm{SINR}_{\mathrm{BD}}{}^{-1} + \mathrm{SINR}_{\mathrm{DU},q}{}^{-1}\right)^{-1} > \mathrm{SINR}^{\mathrm{AF}}_{\mathrm{e2e},q}.$$

We represent the received SINR at the typical UE by $\mathrm{SINR}^{\mathrm{AF}}$ and $\mathrm{SINR}^{\mathrm{DF}}$ for the AF and DF relaying protocols, respectively, and define them for specific channel condition q using the aforementioned hybrid scheme as

$$\mathrm{SINR}_q^{\mathrm{AF}} = \max\left\{\mathrm{SINR}_{\mathrm{BU},q}, \mathrm{SINR}_{\mathrm{e2e},q}^{\mathrm{AF}}\right\}, \tag{2.12}$$

$$\mathrm{SINR}_q^{\mathrm{DF}} = \max\left\{\mathrm{SINR}_{\mathrm{BU},q}, \mathrm{SINR}_{\mathrm{e2e},q}^{\mathrm{DF}}\right\}. \tag{2.13}$$

To evaluate the network performance, we introduce coverage probability as our main metric, which is defined as the probability that the received SINR at the typical UE exceeds a predetermined constant threshold τ, i.e., $P_{\mathrm{Cov}}^{\mathrm{AF}} = \mathbb{P}[\mathrm{SINR}^{\mathrm{AF}} \geq \tau]$ and $P_{\mathrm{Cov}}^{\mathrm{DF}} = \mathbb{P}[\mathrm{SINR}^{\mathrm{DF}} \geq \tau]$ for the AF and DF relaying protocols, respectively.

2.3 Mathematical Constructs

In this section, we provide some important intermediate results that help us analyze the coverage probability in 3D UAV-assisted communication networks.

2.3.1 Useful Lemmas for the Two-Hop Setting

Conditioned on knowing B_0 and D_0, one can represent the SINR values given in (2.5)–(2.7) as

$$\mathrm{SINR}_{\mathrm{BU},q} = \frac{aX}{bY + I}, \tag{2.14}$$

$$\mathrm{SINR}_{\mathrm{DU},q} = \frac{bY}{aX + I}, \tag{2.15}$$

$$\mathrm{SINR}_{\mathrm{BD}} = \frac{cZ}{N_0}, \tag{2.16}$$

where $a = P_{\mathrm{B}} G_{\mathrm{B}_0} r_{\mathrm{B}_0}^{-\alpha_{\mathrm{N}}} \eta_{\mathrm{N}}^{-1}$, $b = P_{\mathrm{D}} G_{\mathrm{D}_0} r_{\mathrm{D}_0,q}^{-\alpha_q} \eta_q^{-1}$, $c = P_{\mathrm{B}} g_{\mathrm{B}_0} g_{\mathrm{D}_0} r_{\mathrm{B}_0\mathrm{D}_0}^{-\alpha_{\mathrm{L}}} \eta_{\mathrm{L}}^{-1}$, $I = I_{\mathrm{U}} + N_0$, $X = f_{\mathrm{B}_0}$, $Y = f_{\mathrm{D}_0}$, $Z = f_{\mathrm{B}_0\mathrm{D}_0}$, and we used Assumption 1 in writing $\mathrm{SINR}_{\mathrm{BD}}$. Since we assumed the Nakagami-m fading model, X, Y, and Z are distributed as gamma random variables. In the next three lemmas, we will characterize the statistics of some functions of these gamma random variables that are useful for analyzing the performance of UAV-assisted two-hop relay networks.

Lemma 2.3. *Let X and Y be two independent gamma random variables with integer-valued shape and rate parameters both equal to m, and let a, b, and I be given non-negative constants. Then the cdf of $T_1 = \frac{aX}{bY+I}$ can be written as*

$$F_{T_1}(\tau) = 1 - \sum_{i=0}^{m-1} \sum_{k=0}^{i} \frac{(k+m-1)!}{k!(m-1)!(i-k)!} \frac{a^m (b\tau)^k}{(a+b\tau)^{m+k}} \left(\frac{m\tau}{a} I\right)^{i-k} \mathrm{e}^{-\frac{m\tau}{a} I}. \tag{2.17}$$

Proof. See Appendix A.1. □

Lemma 2.4. *Let X and Y be two independent gamma random variables with integer-valued shape and rate parameters both equal to m, and let a, b, and I be given non-negative constants. Then the cdf of $T_2 = \frac{\max\{aX,bY\}}{\min\{aX,bY\}+I}$ can be written as*

$$\begin{aligned} F_{T_2}(\tau) = &\sum_{i=0}^{m-1} \frac{\gamma\left(m+i, \left(\frac{1}{a}+\frac{1}{b}\right)\frac{m\tau}{|1-\tau|\mathbf{1}(\tau<1)}I\right)}{i!(m-1)!} \frac{a^m b^i + a^i b^m}{(a+b)^{m+i}} \\ &- \sum_{i=0}^{m-1}\sum_{k=0}^{i} \frac{\gamma\left(m+k, \left(\frac{\tau}{a}+\frac{1}{b}\right)\frac{m\tau}{|1-\tau|\mathbf{1}(\tau<1)}I\right)}{k!(m-1)!(i-k)!} \frac{a^m(b\tau)^k}{(a+b\tau)^{m+k}} \left(\frac{m\tau}{a}I\right)^{i-k} \mathrm{e}^{-\frac{m\tau}{a}I} \\ &- \sum_{i=0}^{m-1}\sum_{k=0}^{i} \frac{\gamma\left(m+k, \left(\frac{1}{a}+\frac{\tau}{b}\right)\frac{m\tau}{|1-\tau|\mathbf{1}(\tau<1)}I\right)}{k!(m-1)!(i-k)!} \frac{(a\tau)^k b^m}{(a\tau+b)^{k+m}} \left(\frac{m\tau}{b}I\right)^{i-k} \mathrm{e}^{-\frac{m\tau}{b}I}, \end{aligned} \tag{2.18}$$

where $\mathbf{1}(.)$ is the indicator function.

Proof. See Appendix A.2. □

The following lemma characterizes a joint cdf that will be used in analyzing the coverage probability in the AF relaying protocol.

Lemma 2.5. *Let X and Y be two independent gamma random variables with integer-valued shape and rate parameters both equal to m, and let a, b, I, and g be given non-negative constants. Then the joint cdf of $T_1 = \frac{aX}{bY+I}$ and $T_3 = \frac{bY}{aX+I+g(aX+bY+I)}$ when $\tau < \frac{1}{g}$ can be written as*

$$\begin{aligned} F_{T_1,T_3}(\tau,\tau) = &\sum_{i=0}^{m-1} \frac{\gamma\left(m+i, \left(\frac{1}{a(1+g)}+\frac{1}{b}\right)\frac{m\tau(1+g)}{|1-\tau(1+g)|\mathbf{1}(\tau<\frac{1}{1+g})}I\right)}{i!(m-1)!} \frac{(a(1+g))^m b^i + (a(1+g))^i b^m}{(a(1+g)+b)^{m+i}} \\ &- \sum_{i=0}^{m-1}\sum_{k=0}^{i} \frac{\gamma\left(m+k, \left(\frac{\tau}{a}+\frac{1}{b}\right)\frac{m\tau(1+g)}{|1-\tau(1+g)|\mathbf{1}(\tau<\frac{1}{1+g})}I\right)}{k!(m-1)!(i-k)!} \frac{a^m(b\tau)^k}{(a+b\tau)^{m+k}} \left(\frac{m\tau}{a}I\right)^{i-k} \mathrm{e}^{-\frac{m\tau}{a}I} \\ &- \sum_{i=0}^{m-1}\sum_{k=0}^{i} \frac{\gamma\left(m+k, \left(\frac{1}{a(1+g)}+\frac{\tau}{b(1-\tau g)}\right)\frac{m\tau(1+g)}{|1-\tau(1+g)|\mathbf{1}(\tau<\frac{1}{1+g})}I\right)}{k!(m-1)!(i-k)!} \\ &\times \frac{(a\tau(1+g))^k (b(1-\tau g))^m}{(a\tau(1+g)+b(1-\tau g))^{k+m}} \left(\frac{m\tau(1+g)}{b(1-\tau g)}I\right)^{i-k} \mathrm{e}^{-\frac{m\tau(1+g)}{b(1-\tau g)}I}, \end{aligned} \tag{2.19}$$

and when $\tau \geq \frac{1}{g}$, we have $F_{T_1,T_3}(\tau,\tau) = F_{T_1}(\tau)$, where $F_{T_1}(\tau)$ is given in Lemma 2.3.

Proof. See Appendix A.3. □

Remark 2.6. From the previous lemmas, we observe the following special cases:

- $\tau = 0$. All the cdfs tend to 0. For T_1, all the terms in the double summation are 0, except for $i = k = 0$, which is 1, making $F_{T_1}(0) = 0$. For T_2, since $\gamma(s, 0) = 0$ for all s, we have $F_{T_2}(0) = 0$. The same reasoning applies to the joint cdf of T_1 and T_3, giving $F_{T_1,T_3}(0, 0) = 0$.

- $\tau \to \infty$. All the cdfs tend to 1. For T_1, the double summation will be 0, making $F_{T_1}(\infty) = 1$. For T_2, note that the double summations are both 0, while the single summation is equal to 1. This can be shown as follows:

$$\begin{aligned}
&\sum_{i=0}^{m-1} \binom{m+i-1}{i} \frac{a^m b^i + a^i b^m}{(a+b)^{m+i}} \\
&= \frac{1}{(a+b)^{2m-1}} \sum_{i=0}^{m-1} \binom{m+i-1}{i} (a^m b^i + a^i b^m)(a+b)^{m-1-i} \\
&= \frac{\sum_{i=0}^{m-1} \sum_{k=0}^{i} \binom{2(m-1)-i}{m-1} \binom{i}{k} (a^{m+k} b^{m-1-k} + a^{m-1-i+k} b^{m+i-k})}{\sum_{l=0}^{2m-1} \binom{2m-1}{l} a^l b^{2m-1-l}},
\end{aligned} \tag{2.20}$$

  where in the last equality we expanded $(a+b)^{m-1-i}$ and used the change of variables $m-1-i \mapsto i$ in the numerator. To prove the last equation is unity, we need to show that the coefficients of $a^l b^{2m-1-l}$ for $0 \le l \le 2m-1$ are equal in the numerator and denominator of (2.20), which can be verified using the following binomial identity [97, Eq. (1.78)]:

$$\sum_{k=0}^{n} \binom{\alpha+k}{k} \binom{r+n-k}{n-k} = \binom{\alpha+r+n+1}{n}, \quad \forall \alpha, r.$$

  Hence, $F_{T_2}(\infty) = 1$. As for the joint cdf of T_1 and T_3, we have $F_{T_1,T_3}(\infty, \infty) = F_{T_1}(\infty) = 1$.

- $g = 0$. The joint cdf of T_1 and T_3 is equivalent to the cdf of T_2.

- $g \to \infty$. The joint cdf of T_1 and T_3 is equivalent to the cdf of T_1, since $T_3 \to 0$.

In case of Rayleigh fading, the fading powers will have exponential distribution, which is a special case of the gamma distribution. Corollary 2.7 gives the results of the previous lemmas for Rayleigh fading, which has a straightforward proof by setting $m = 1$ in (2.17), (2.18), and (2.19).

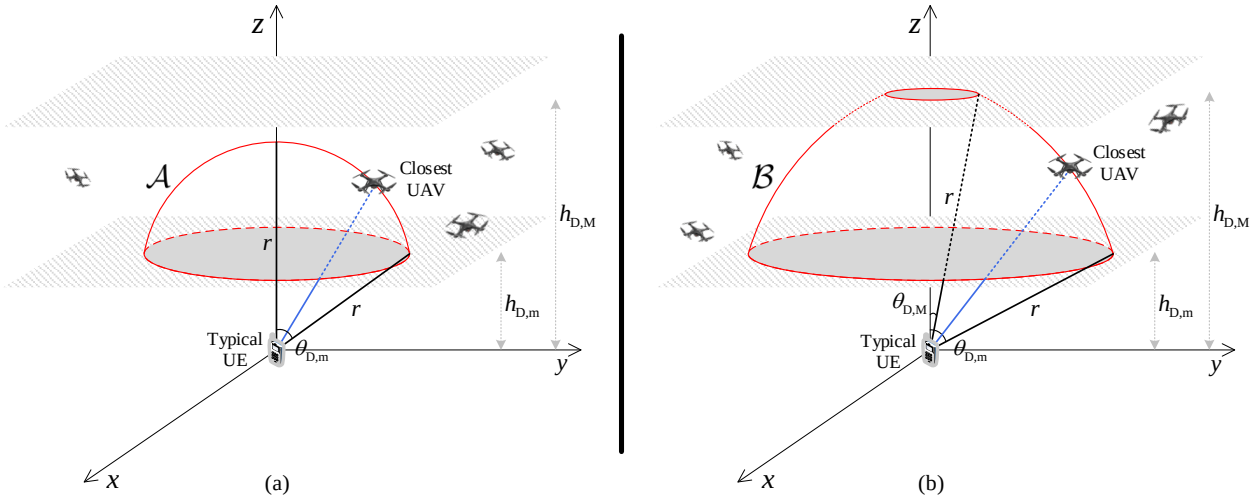

Figure 2.2: The 3D network setting when the closest UAV is at distance r from $\mathbf{o}$ for (a) $h_{\mathrm{D,m}} \leq r \leq h_{\mathrm{D,M}}$, and (b) $r > h_{\mathrm{D,M}}$.

Corollary 2.7. *Let X and Y be two independent exponential random variables with unity mean, and let a, b, I, and g be given non-negative constants. Then the cdfs of T_1 and T_2, and the joint cdf of T_1 and T_3 are given, respectively, as*

$$F_{T_1}(\tau) = 1 - \frac{a}{a+b\tau}\,\mathrm{e}^{-\frac{\tau}{a}I}, \tag{2.21}$$

$$F_{T_2}(\tau) = 1 - \frac{a}{a+b\tau}\,\mathrm{e}^{-\frac{\tau}{a}I} - \frac{b}{b+a\tau}\,\mathrm{e}^{-\frac{\tau}{b}I} + \frac{ab(1+\tau)(1-\tau)}{(a+b\tau)(b+a\tau)}\,\mathrm{e}^{-\left(\frac{1}{a}+\frac{1}{b}\right)\frac{\tau}{|1-\tau|\mathbf{1}(\tau<1)}I}, \tag{2.22}$$

$$\begin{aligned} F_{T_1,T_3}(\tau,\tau) = 1 &- \frac{a}{a+b\tau}\,\mathrm{e}^{-\frac{\tau}{a}I} - \frac{b(1-\tau g)}{b(1-\tau g)+a\tau(1+g)}\mathrm{e}^{-\frac{\tau(1+g)}{b|1-\tau g|\mathbf{1}(\tau<\frac{1}{g})}I} \\ &+ \frac{ab(1+\tau)(1-\tau(1+g))}{(a+b\tau)(b(1-\tau g)+a\tau(1+g))}\mathrm{e}^{-\left(\frac{1}{a(1+g)}+\frac{1}{b}\right)\frac{\tau(1+g)}{|1-\tau(1+g)|\mathbf{1}(\tau<\frac{1}{1+g})}I}. \end{aligned} \tag{2.23}$$

2.3.2 Relative Distance and Angle Distributions in the 3D Setting

Let $\tilde{r}_{\mathrm{B}_0}$, $\tilde{r}_{\mathrm{D}_0,\mathrm{L}}$, and $\tilde{r}_{\mathrm{D}_0,\mathrm{N}}$ be the distances of the closest BS, LoS UAV, and NLoS UAV to the typical UE, and also let $\tilde{\theta}_{\mathrm{D}_0,\mathrm{L}}$ and $\tilde{\theta}_{\mathrm{D}_0,\mathrm{N}}$ be the zenith angles of the closest LoS and NLoS UAVs to the typical UE, respectively. We start by providing the distance distribution of the closest BS to the typical UE in the following lemma, where the proof follows directly from the null probability of a PPP [19] and is omitted here for brevity.

Lemma 2.8. *The cdf and pdf of the closest BS distance to the origin, i.e., $\tilde{r}_{\mathrm{B}_0}$, can be written*

as

$$F_{\tilde{r}_{\mathrm{B}_0}}(r) = 1 - \mathrm{e}^{-\pi\lambda_{\mathrm{B}}(r^2 - h_{\mathrm{B}}^2)}, \tag{2.24}$$

$$f_{\tilde{r}_{\mathrm{B}_0}}(r) = 2\pi\lambda_{\mathrm{B}} r \mathrm{e}^{-\pi\lambda_{\mathrm{B}}(r^2 - h_{\mathrm{B}}^2)}. \tag{2.25}$$

As mentioned earlier in Section 2.2.4, since all BSs are in the NLoS channel condition and have the same height, the closest BS to the typical UE is also regarded as its serving BS. Hence, we have $r_{\mathrm{B}_0} = \tilde{r}_{\mathrm{B}_0}$, and thus, the serving BS distance distribution to the typical UE will be $f_{r_{\mathrm{B}_0}}(r) = f_{\tilde{r}_{\mathrm{B}_0}}(r)$. We now provide the relative distance and angle distributions in 3D aerial networks in the following lemmas. First, we derive the distance distribution of the closest UAV to the typical UE for the LoS and NLoS channel conditions in Lemma 2.9. Using this result, we obtain the *joint distance and angle* distribution of the closest UAV to the typical UE in Lemma 2.10. We will then determine the association probabilities for each channel condition in Lemma 2.11. Finally, we derive the joint distribution of the distance and angle of the *serving* UAV to the typical UE for both channel conditions in Lemma 2.12.

Lemma 2.9. *The cdf and pdf of the closest UAV distance to the origin for channel condition* $q = \{\mathrm{L}, \mathrm{N}\}$*, i.e.,* $\tilde{r}_{\mathrm{D}_0,q}$*, can be written, respectively, as*

$$F_{\tilde{r}_{\mathrm{D}_0,q}}(r) = 1 - \mathrm{e}^{-\pi\lambda_{\mathrm{D}}\beta_q(r)}, \tag{2.26}$$

$$f_{\tilde{r}_{\mathrm{D}_0,q}}(r) = 2\pi\lambda_{\mathrm{D}} r^2 \left(\int_{\theta_{\mathrm{D,M}}(r)}^{\theta_{\mathrm{D,m}}(r)} \sin(\omega) p_q(\omega)\, \mathrm{d}\omega \right) \mathrm{e}^{-\pi\lambda_{\mathrm{D}}\beta_q(r)}, \tag{2.27}$$

where $p_q(.)$ *is given in* (2.4) *and*

$$\theta_{\mathrm{D,m}}(r) = \cos^{-1}\left(\frac{h_{\mathrm{D,m}}}{r}\right),$$

$$\theta_{\mathrm{D,M}}(r) = \cos^{-1}\left(\min\left\{\frac{h_{\mathrm{D,M}}}{r}, 1\right\}\right),$$

$$\beta_q(r) = \frac{2}{3}\int_0^{\theta_{\mathrm{D,m}}(r)} \left(\min\{h_{\mathrm{D,M}}^3, r^3\cos^3(\theta_1)\} - h_{\mathrm{D,m}}^3\right) \frac{\sin(\theta_1)}{\cos^3(\theta_1)} p_q(\theta_1)\, \mathrm{d}\theta_1.$$

Proof. Consider the 3D setting in Fig. 2.2, where the typical UE is located at the origin and the UAVs are distributed as a 3D homogeneous PPP in the region enclosed between heights $h_{\mathrm{D,m}}$ and $h_{\mathrm{D,M}}$. Depending on where the closest UAV resides, an *exclusion zone* is formed, where no other UAVs are allowed to enter. This exclusion zone is a spherical cap when $h_{\mathrm{D,m}} \leq \tilde{r}_{\mathrm{D}_0,q} \leq h_{\mathrm{D,M}}$ (see Fig. 2.2 (a)) and a spherical segment when $\tilde{r}_{\mathrm{D}_0,q} > h_{\mathrm{D,M}}$ (see

Fig. 2.2 (b)). Therefore, we can write the cdf of $\tilde{r}_{\mathrm{D}_0,q}$ as

$$\begin{aligned}
F_{\tilde{r}_{\mathrm{D}_0,q}}(r) &= \mathbb{P}[\tilde{r}_{\mathrm{D}_0,q} \le r] = 1 - \mathbb{P}[\text{No UAV in } \mathcal{A} \text{ or } \mathcal{B}] \\
&= 1 - \mathrm{e}^{-\Lambda(\mathcal{A})}\mathbf{1}(h_{\mathrm{D,m}} \le r \le h_{\mathrm{D,M}}) - \mathrm{e}^{-\Lambda(\mathcal{B})}\mathbf{1}(r > h_{\mathrm{D,M}}) \\
&\overset{(a)}{=} 1 - \begin{cases}
\exp\Big[- \int_0^{2\pi} \int_0^{\cos^{-1}(\frac{h_{\mathrm{D,m}}}{r})} \int_{\frac{h_{\mathrm{D,m}}}{\cos(\theta_1)}}^{r} \lambda_{\mathrm{D}} p_q(\theta_1) r_1^2 \sin(\theta_1)\, \mathrm{d}r_1\, \mathrm{d}\theta_1\, \mathrm{d}\phi_1 \Big], & r \le h_{\mathrm{D,M}} \\
\exp\Big[- \int_0^{2\pi} \int_0^{\cos^{-1}(\frac{h_{\mathrm{D,M}}}{r})} \int_{\frac{h_{\mathrm{D,m}}}{\cos(\theta_1)}}^{\frac{h_{\mathrm{D,M}}}{\cos(\theta_1)}} \lambda_{\mathrm{D}} p_q(\theta_1) r_1^2 \sin(\theta_1)\, \mathrm{d}r_1\, \mathrm{d}\theta_1\, \mathrm{d}\phi_1 \\
\qquad - \int_0^{2\pi} \int_{\cos^{-1}(\frac{h_{\mathrm{D,m}}}{r})}^{\cos^{-1}(\frac{h_{\mathrm{D,M}}}{r})} \int_{\frac{h_{\mathrm{D,m}}}{\cos(\theta_1)}}^{r} \lambda_{\mathrm{D}} p_q(\theta_1) r_1^2 \sin(\theta_1)\, \mathrm{d}r_1\, \mathrm{d}\theta_1\, \mathrm{d}\phi_1 \Big], & r > h_{\mathrm{D,M}},
\end{cases}
\end{aligned}$$

where $\Lambda(\mathcal{S})$ is the intensity measure of set $\mathcal{S}$ and (r_1, θ_1, ϕ_1) is the spherical coordinate triplet. Note that in (a) we derived the null probability of 3D PPP $\Phi_{\mathrm{D},q}$ by integrating its density (i.e., $\lambda_{\mathrm{D}} p_q(\theta_1)$) over the spherical cap $\mathcal{A}$ for $h_{\mathrm{D,m}} \le r \le h_{\mathrm{D,M}}$ and the spherical segment $\mathcal{B}$ for $r > h_{\mathrm{D,M}}$. Evaluating these integrals and taking their derivatives with respect to r, we end up with the cdf and pdf of $\tilde{r}_{\mathrm{D}_0,q}$ as given in (2.26) and (2.27), respectively. □

Lemma 2.10. *The joint pdf of the distance and zenith angle of the closest UAV to the origin for channel condition q, i.e., $\tilde{r}_{\mathrm{D}_0,q}$ and $\tilde{\theta}_{\mathrm{D}_0,q}$, respectively, can be written as*

$$f_{\tilde{r}_{\mathrm{D}_0,q},\tilde{\theta}_{\mathrm{D}_0,q}}(r,\theta) = 2\pi\lambda_{\mathrm{D}} r^2 \int_{\theta_{\mathrm{D,M}}(r)}^{\theta_{\mathrm{D,m}}(r)} \sin(\omega) p_q(\omega)\, \mathrm{d}\omega \frac{\mathrm{e}^{-\pi\lambda_{\mathrm{D}}\beta_q(r)} \sin(\theta)\mathbf{1}(\theta_{\mathrm{D,M}}(r) \le \theta \le \theta_{\mathrm{D,m}}(r))}{\cos(\theta_{\mathrm{D,M}}(r)) - \cos(\theta_{\mathrm{D,m}}(r))}, \tag{2.28}$$

where $\theta_{\mathrm{D,m}}(r)$, $\theta_{\mathrm{D,M}}(r)$, and $\beta_q(r)$ are as given in Lemma 2.9.

Proof. To obtain the joint pdf of $\tilde{r}_{\mathrm{D}_0,q}$ and $\tilde{\theta}_{\mathrm{D}_0,q}$, we first derive the conditional pdf $f_{\tilde{\theta}_{\mathrm{D}_0,q}|\tilde{r}_{\mathrm{D}_0,q}}(\theta|r)$. Conditioned on $\tilde{r}_{\mathrm{D}_0,q} = r$, the closest UAV is distributed uniformly on the surface of the spherical cap $\mathcal{A}$ or the spherical segment $\mathcal{B}$. Since the differential element of solid angle Ω for a sphere is given by $\mathrm{d}\Omega = r^2 \sin(\theta)\mathrm{d}r\mathrm{d}\theta\mathrm{d}\phi = -r^2\mathrm{d}r\mathrm{d}(\cos(\theta))\mathrm{d}\phi$, we conclude that $\cos(\theta)$ should be uniformly distributed between $\cos(\theta_{\mathrm{D,M}}(r))$ and $\cos(\theta_{\mathrm{D,m}}(r))$. Hence, we have

$$f_{\tilde{\theta}_{\mathrm{D}_0,q}|\tilde{r}_{\mathrm{D}_0,q}}(\theta|r) = \frac{\sin(\theta) \times \mathbf{1}(\theta_{\mathrm{D,M}}(r) \le \theta \le \theta_{\mathrm{D,m}}(r))}{\cos(\theta_{\mathrm{D,M}}(r)) - \cos(\theta_{\mathrm{D,m}}(r))}.$$

Now, using $f_{\tilde{r}_{\mathrm{D}_0,q},\tilde{\theta}_{\mathrm{D}_0,q}}(r,\theta) = f_{\tilde{\theta}_{\mathrm{D}_0,q}|\tilde{r}_{\mathrm{D}_0,q}}(\theta|r) f_{\tilde{r}_{\mathrm{D}_0,q}}(r)$ and the previous lemma, we arrive at (2.28). □

The random variables $\tilde{r}_{\mathrm{D}_0,q}$ and $\tilde{\theta}_{\mathrm{D}_0,q}$ are clearly dependent. However, this dependency becomes less significant as $h_{\mathrm{D,m}} \to 0$ and $h_{\mathrm{D,M}} \to \infty$. In fact, when UAVs are distributed as a PPP in the half-space $z \ge 0$, $\tilde{r}_{\mathrm{D}_0,q}$ and $\tilde{\theta}_{\mathrm{D}_0,q}$ are independent from each other and we have

$$\begin{aligned}
f_{\tilde{r}_{\mathrm{D}_0,q}}(r) &= 2\pi\lambda_{\mathrm{D}} b_q r^2\, \mathrm{e}^{-\frac{2}{3}\pi\lambda_{\mathrm{D}} b_q r^3}, \\
f_{\tilde{\theta}_{\mathrm{D}_0,q}}(\theta) &= \sin(\theta)\mathbf{1}\left(0 \le \theta \le \frac{\pi}{2}\right),
\end{aligned}$$

where $b_q = \int_0^{\frac{\pi}{2}} \sin(\omega) p_q(\omega)\, \mathrm{d}\omega$.

Lemma 2.11. *The probability that the typical UE is associated with an NLoS UAV is given as*

$$A_{\mathrm{N}} = \int_{h_{\mathrm{D,m}}}^{\infty} \int_{\theta_{\mathrm{D,M}}(r)}^{\theta_{\mathrm{D,m}}(r)} 2\pi\lambda_{\mathrm{D}} r^2 \sin(\theta) p_{\mathrm{N}}(\theta) \mathrm{e}^{-\pi\lambda_{\mathrm{D}}\left(\beta_{\mathrm{N}}(r)+\beta_{\mathrm{L}}\left(\left(\frac{\eta_{\mathrm{N}}}{\eta_{\mathrm{L}}}\right)^{\frac{1}{\alpha_{\mathrm{L}}}} r^{\frac{\alpha_{\mathrm{N}}}{\alpha_{\mathrm{L}}}}\right)\right)} \mathrm{d}\theta\, \mathrm{d}r \tag{2.29}$$

where $\theta_{\mathrm{D,m}}(r)$, $\theta_{\mathrm{D,M}}(r)$, $\beta_{\mathrm{N}}(r)$, and $\beta_{\mathrm{L}}(r)$ are as given in Lemma 2.9. Furthermore, the probability that the typical UE is associated with an LoS UAV is $A_{\mathrm{L}} = 1 - A_{\mathrm{N}}$.

Proof. See Appendix A.4. □

Lemma 2.12. *Given that the typical UE is associated with UAV D_0 with channel condition q, the joint pdf of the serving distance and angle between D_0 and the typical UE can be written as*

$$f_{r_{\mathrm{D}_0,q},\theta_{\mathrm{D}_0,q}}(r,\theta) = \frac{1}{A_q} f_{\tilde{r}_{\mathrm{D}_0,q},\tilde{\theta}_{\mathrm{D}_0,q}}(r,\theta) \exp\left[-\pi\lambda_{\mathrm{D}}\beta_{\bar{q}}\left(\max\left\{h_{\mathrm{D,m}}, \left(\frac{\eta_q}{\eta_{\bar{q}}}\right)^{\frac{1}{\alpha_{\bar{q}}}} r^{\frac{\alpha_q}{\alpha_{\bar{q}}}}\right\}\right)\right], \tag{2.30}$$

where $\bar{q} = \{\mathrm{L},\mathrm{N}\} \setminus q$ and $f_{\tilde{r}_{\mathrm{D}_0,\mathrm{L}},\tilde{\theta}_{\mathrm{D}_0,\mathrm{L}}}(r)$ and $\beta_q(r)$ are given in Lemmas 2.10 and 2.9, respectively.

Proof. See Appendix A.5. □

2.4 Performance Analysis

In this section, we will first derive the conditional Laplace transform of the interference imposed at the typical UE by both the BSs and the UAVs. Using this result along with the results of the previous section, we will be ready to analyze the coverage probability.

2.4.1 Conditional Laplace Transform of Interference

The Laplace transform of random variable X at point s is defined as $\mathcal{L}_X(s) = \mathbb{E}[\mathrm{e}^{-sX}]$. Assuming $X = I_{\mathrm{U}}$, i.e., the total interference at the typical UE, our goal is to derive the Laplace transform of I_{U} conditioned on knowing the locations of the serving BS and UAV, i.e., B_0 and D_0, respectively. Since the channel condition of the serving UAV affects the total interference, we further condition the Laplace transform on the serving UAV being in LoS or NLoS conditions. Since I_{BU}, $I_{\mathrm{DU,L}}$, and $I_{\mathrm{DU,N}}$ are independent from each other given B_0 and D_0, we have

$$\mathcal{L}_{I_{\mathrm{U}|q}}(s|\mathrm{B}_0,\mathrm{D}_0) = \mathcal{L}_{I_{\mathrm{BU}}}(s|\mathrm{B}_0)\mathcal{L}_{I_{\mathrm{DU,L}|q}}(s|\mathrm{D}_0)\mathcal{L}_{I_{\mathrm{DU,N}|q}}(s|\mathrm{D}_0), \tag{2.31}$$

Table 2.1: Exclusion zone radius for different interfering and serving UAV channel conditions.

Interfering UAVs	Serving UAV	Exclusion zone radius
LoS	LoS	$r_{\mathrm{L}\vert\mathrm{L}} = r$
LoS	NLoS	$r_{\mathrm{L}\vert\mathrm{N}} = \left(\frac{\eta_{\mathrm{N}}}{\eta_{\mathrm{L}}}\right)^{\frac{1}{\alpha_{\mathrm{L}}}} r^{\frac{\alpha_{\mathrm{N}}}{\alpha_{\mathrm{L}}}}$
NLoS	LoS	$r_{\mathrm{N}\vert\mathrm{L}} = \left(\frac{\eta_{\mathrm{L}}}{\eta_{\mathrm{N}}}\right)^{\frac{1}{\alpha_{\mathrm{N}}}} r^{\frac{\alpha_{\mathrm{L}}}{\alpha_{\mathrm{N}}}}$
NLoS	NLoS	$r_{\mathrm{N}\vert\mathrm{N}} = r$

where $q = \{\mathrm{L}, \mathrm{N}\}$ represents the serving UAV channel condition.

As mentioned in Section 2.2.3, Φ'_{B} is an inhomogeneous PPP with density λ_{B} for $u_{\mathrm{B}_{\mathbf{x}}} \geq u_{\mathrm{B}_0}$ and 0 otherwise. Since all BSs experience the NLoS channel condition, there is an exclusion zone $\mathcal{X}_{\mathrm{B}} = b(\mathbf{o}, u_{\mathrm{B}_0})$ for the projection of interfering BSs onto the ground, where $b(\mathbf{o}, r)$ is a disc of radius r centered at $\mathbf{o}$. Next, we derive the conditional Laplace transform of I_{BU}.

Lemma 2.13. *The Laplace transform of interference from the BSs at the typical UE conditioned on knowing the location of the serving BS (with 2D distance u_{B_0} to $\mathbf{o}$) can be written as* $\mathcal{L}_{I_{\mathrm{BU}}}(s|\mathrm{B}_0) =$

$$\exp\left[-2\pi\lambda_{\mathrm{B}}\int_{u_{\mathrm{B}_0}}^{\infty}\left[1-\left(1+\frac{sP_{\mathrm{B}}}{m\eta_{\mathrm{N}}}\frac{G_{\mathrm{B}}^{\mathrm{OmniD}}\left(\pi-\tan^{-1}(\frac{u_{\mathrm{B}_{\mathbf{x}}}}{h_{\mathrm{B}}}),\theta_{\mathrm{B}}\right)}{\left(u_{\mathrm{B}_{\mathbf{x}}}^2+h_{\mathrm{B}}^2\right)^{\frac{\alpha_{\mathrm{N}}}{2}}}\right)^{-m}\right]u_{\mathrm{B}_{\mathbf{x}}}\mathrm{d}u_{\mathrm{B}_{\mathbf{x}}}\right], \quad (2.32)$$

where $G_{\mathrm{B}}^{\mathrm{OmniD}}(\theta, \theta_{\mathrm{B}})$ is the downtilted BS antenna gain along direction θ given in (2.2).

Proof. See Appendix A.6. □

Since UAVs experience both LoS and NLoS channel conditions, the exclusion zone for the interfering UAVs, i.e., $\mathcal{X}_{\mathrm{D}}$, depends on the channel conditions of both the serving UAV and the interfering UAVs. Assuming that the serving UAV has distance r to the origin, $\mathcal{X}_{\mathrm{D}}$ will either be a spherical cap or a spherical segment with radius $r_{q_1|q_2}$, where $q_1, q_2 = \{\mathrm{L}, \mathrm{N}\}$ denote the channel condition of the interfering UAVs and the serving UAV, respectively. Note that $\mathcal{X}_{\mathrm{D}}$ is a spherical cap when $h_{\mathrm{D,m}} \leq r_{q_1|q_2} \leq h_{\mathrm{D,M}}$ and a spherical segment when $r_{q_1|q_2} > h_{\mathrm{D,M}}$. The exclusion zone radii for different values of q_1 and q_2 are given in Table 2.1, using which we derive the conditional Laplace transform of $I_{\mathrm{DU},q_1|q_2}$ in the next lemma.

Lemma 2.14. *The Laplace transform of interference from the UAVs with channel condition q_1 at the typical UE conditioned on knowing the location and channel condition of the serving UAV (with 3D distance r_{D_0,q_2} to $\mathbf{o}$, where q_2 is the serving UAV channel condition) can be*

written as $\mathcal{L}_{I_{\mathrm{DU},q_1|q_2}}(s|\mathrm{D}_0) =$

$$\exp\Bigg[-2\pi\lambda_{\mathrm{D}}\int_{\theta_{\mathrm{D,M}}}^{\theta_{\mathrm{D,m}}}\int_{r_{q_1|q_2}}^{\frac{h_{\mathrm{D,M}}}{\cos(\theta)}}\left[1-\left(1+\frac{sP_{\mathrm{D}}}{m\eta_{q_1}}\frac{G_{\mathrm{D}}^{\mathrm{AC}}(\pi-\theta)}{r^{\alpha_{q_1}}}\right)^{-m}\right]p_{q_1}(\theta)r^2\sin(\theta)\mathrm{d}r\mathrm{d}\theta$$
$$-2\pi\lambda_{\mathrm{D}}\int_{\theta_{\mathrm{D,m}}}^{\frac{\pi}{2}}\int_{\frac{h_{\mathrm{D,m}}}{\cos(\theta)}}^{\frac{h_{\mathrm{D,M}}}{\cos(\theta)}}\left[1-\left(1+\frac{sP_{\mathrm{D}}}{m\eta_{q_1}}\frac{G_{\mathrm{D}}^{\mathrm{AC}}(\pi-\theta)}{r^{\alpha_{q_1}}}\right)^{-m}\right]p_{q_1}(\theta)r^2\sin(\theta)\mathrm{d}r\mathrm{d}\theta\Bigg], \quad (2.33)$$

where $\theta_{\mathrm{D,m}} = \cos^{-1}(\frac{h_{\mathrm{D,m}}}{r_{q_1|q_2}})$, $\theta_{\mathrm{D,M}} = \cos^{-1}\left(\min\left\{\frac{h_{\mathrm{D,M}}}{r_{q_1|q_2}},1\right\}\right)$, *and* $G_{\mathrm{D}}^{\mathrm{AC}}(\theta)$ *is the UAV access antenna gain along direction* θ *given in* (2.3).

Proof. See Appendix A.7. □

Using the results of Lemmas 2.13 and 2.14, we end up with the conditional Laplace transform of interference at the typical UE given the serving UAV has channel condition q as in (2.31).

2.4.2 Coverage Probability

In this section, we derive the coverage probability for the typical UE considering both AF and DF relaying protocols. Since we assumed a hybrid scheme in this chapter, the received SINR at the typical UE is the maximum of the BS-UE SINR and the relay-aided end-to-end SINR, as given in (2.12)–(2.13). The following two theorems provide the main results of this chapter.

Theorem 2.15. *The network coverage probability for the AF protocol can be written as* $P_{\mathrm{Cov}}^{\mathrm{AF}} = A_{\mathrm{L}}P_{\mathrm{Cov,L}}^{\mathrm{AF}} + A_{\mathrm{N}}P_{\mathrm{Cov,N}}^{\mathrm{AF}}$, *where* A_q *is the probability that the typical UE is associated with a UAV with channel condition* q *as given in Lemma 2.11, and* $P_{\mathrm{Cov},q}^{\mathrm{AF}}$ *is the ccdf of* $\mathrm{SINR}_q^{\mathrm{AF}}$, *given as*

$$P_{\mathrm{Cov},q}^{\mathrm{AF}} = \sum_{i=1}^{3}\int\cdots\int_{\mathcal{R}\cap\hat{\mathcal{R}}_i} W_i f_Z(z) f_{r_{\mathrm{B}_0}}(r_{\mathrm{B}_0}) f_{r_{\mathrm{D}_{0,q}},\theta_{\mathrm{D}_{0,q}}}(r_{\mathrm{D}_{0,q}},\theta_{\mathrm{D}_{0,q}}) f_{\phi_{\mathrm{B}_0\mathrm{D}_0}}(\phi_{\mathrm{B}_0\mathrm{D}_0})$$
$$\times\,\mathrm{d}z\,\mathrm{d}r_{\mathrm{B}_0}\,\mathrm{d}\theta_{\mathrm{D}_{0,q}}\,\mathrm{d}r_{\mathrm{D}_{0,q}}\,\mathrm{d}\phi_{\mathrm{B}_0\mathrm{D}_0}, \quad (2.34)$$

where $Z = f_{\mathrm{B}_0\mathrm{D}_0} \sim \mathrm{Gamma}(m,m)$, $f_{r_{\mathrm{B}_0}}(r)$ *and* $f_{r_{\mathrm{D}_{0,q}},\theta_{\mathrm{D}_{0,q}}}(r,\theta)$ *are given in Lemmas 2.8 and 2.12, respectively,* $\phi_{\mathrm{B}_0\mathrm{D}_0} \sim U[0,2\pi)$ *is the azimuthal angle between* B_0 *and* D_0, $\mathcal{R} = \{0 \le z < \infty, h_{\mathrm{B}} \le r_{\mathrm{B}_0} < \infty, \theta_{\mathrm{D,M}}(r) \le \theta_{\mathrm{D}_{0,q}} \le \theta_{\mathrm{D,m}}(r), h_{\mathrm{D,m}} \le r_{\mathrm{D}_{0,q}} < \infty, 0 \le \phi_{\mathrm{B}_0\mathrm{D}_0} < 2\pi\}$,

$\hat{\mathcal{R}}_1 = \{\frac{1}{g} \le \tau\}$, $\hat{\mathcal{R}}_2 = \{\frac{1}{1+g} \le \tau < \frac{1}{g}\}$, $\hat{\mathcal{R}}_3 = \{\tau < \frac{1}{1+g}\}$, *and* W_i*'s are defined as follows:*

$$W_1 = \sum_{i=0}^{m-1}\sum_{k=0}^{i}\binom{k+m-1}{k}\mu\left(\begin{matrix}a, b\tau\\ m, k\end{matrix}\middle|\begin{matrix}s_1, s_1\\ i-k\end{matrix}\right),$$

$$W_2 = W_1 + \sum_{i=0}^{m-1}\sum_{k=0}^{i}\binom{k+m-1}{k}\mu\left(\begin{matrix}a\tau(1+g), b(1-\tau g)\\ k, m\end{matrix}\middle|\begin{matrix}s_2, s_2\\ i-k\end{matrix}\right),$$

$$W_3 = W_2 + \sum_{i=0}^{m-1}\sum_{j=0}^{i+m-1}\binom{i+m-1}{i}\left[\mu\left(\begin{matrix}a(1+g), b\\ m, i\end{matrix}\middle|\begin{matrix}s_3, s_3\\ j\end{matrix}\right) + \mu\left(\begin{matrix}a(1+g), b\\ i, m\end{matrix}\middle|\begin{matrix}s_3, s_3\\ j\end{matrix}\right)\right]$$
$$- \sum_{i=0}^{m-1}\sum_{k=0}^{i}\sum_{j=0}^{k+m-1}\binom{k+m-1}{k}\binom{j+i-k}{j}\left[\left(\frac{\tau(1+g)}{1-\tau(1+g)}\right)^j \mu\left(\begin{matrix}a, b\tau\\ m, k-j\end{matrix}\middle|\begin{matrix}s_1, s_3\\ j+i-k\end{matrix}\right)\right.$$
$$\left. + \left(\frac{\tau}{1-\tau(1+g)}\right)^j \mu\left(\begin{matrix}a\tau(1+g), b(1-\tau g)\\ k-j, m\end{matrix}\middle|\begin{matrix}s_2, s_3\\ j+i-k\end{matrix}\right)\right],$$

$$\mu\left(\begin{matrix}x, y\\ i, j\end{matrix}\middle|\begin{matrix}r, s\\ k\end{matrix}\right) = \frac{x^i y^j}{(x+y)^{i+j}}\frac{(-r)^k}{k!}\frac{\partial^k}{\partial s^k}\mathrm{e}^{-sN_0}\mathcal{L}_{I_{\mathrm{U}|q}}(s|\mathrm{B}_0, \mathrm{D}_0),$$

$$s_1 = \frac{1}{a}m\tau, \quad s_2 = \frac{1+g}{b(1-\tau g)}m\tau, \quad s_3 = \frac{a(1+g)+b}{ab(1-\tau(1+g))}m\tau, \quad g = \frac{N_0}{cZ},$$

$$a = P_{\mathrm{B}}G_{\mathrm{B}_0}r_{\mathrm{B}_0}^{-\alpha_{\mathrm{N}}}\eta_{\mathrm{N}}^{-1}, \quad b = P_{\mathrm{D}}G_{\mathrm{D}_0}r_{\mathrm{D}_0,q}^{-\alpha_q}\eta_q^{-1}, \quad c = P_{\mathrm{B}}g_{\mathrm{B}_0}g_{\mathrm{D}_0}r_{\mathrm{B}_0\mathrm{D}_0}^{-\alpha_{\mathrm{L}}}\eta_{\mathrm{L}}^{-1},$$

$$G_{\mathrm{D}_0} = G_{\mathrm{D}}^{\mathrm{AC}}(\pi - \theta_{\mathrm{D}_0,q}), \quad g_{\mathrm{D}_0} = G^{\max}, \quad G_{\mathrm{B}_0} = G_{\mathrm{B}}^{\mathrm{OmniD}}(\pi - \cos^{-1}(\frac{h_{\mathrm{B}}}{r_{\mathrm{B}_0}}), \theta_{\mathrm{B}}),$$

$$g_{\mathrm{B}_0} = \begin{cases} G_{\mathrm{B}}^{\mathrm{OmniD}}(\cos^{-1}(\frac{r_{\mathrm{D}_0,q}\cos(\theta_{\mathrm{D}_0,q})-h_{\mathrm{B}}}{r_{\mathrm{B}_0\mathrm{D}_0}}), \theta_{\mathrm{B}}), & \text{BS first antenna model}\\ G^{\max}, & \text{BS second antenna model,}\end{cases}$$

$$r_{\mathrm{B}_0\mathrm{D}_0}^2 = r_{\mathrm{B}_0}^2 + r_{\mathrm{D}_0,q}^2 - 2h_{\mathrm{B}}r_{\mathrm{D}_0,q}\cos(\theta_{\mathrm{D}_0,q}) - 2\sqrt{r_{\mathrm{B}_0}^2 - h_{\mathrm{B}}^2}\, r_{\mathrm{D}_0,q}\sin(\theta_{\mathrm{D}_0,q})\cos(\phi_{\mathrm{B}_0\mathrm{D}_0}),$$

Proof. See Appendix A.8. □

Theorem 2.16. *The network coverage probability for the DF protocol can be written as* $P_{\mathrm{Cov}}^{\mathrm{DF}} = A_{\mathrm{L}}P_{\mathrm{Cov,L}}^{\mathrm{DF}} + A_{\mathrm{N}}P_{\mathrm{Cov,N}}^{\mathrm{DF}}$*, where* A_q *is given in Lemma 2.11 and* $P_{\mathrm{Cov},q}^{\mathrm{DF}}$ *is the ccdf of* $\mathrm{SINR}_q^{\mathrm{DF}}$*, given as*

$$P_{\mathrm{Cov},q}^{\mathrm{DF}} = \int_{\mathcal{R}}\cdots\int W f_Z(z) f_{r_{\mathrm{B}_0}}(r_{\mathrm{B}_0}) f_{r_{\mathrm{D}_0,q},\theta_{\mathrm{D}_0,q}}(r_{\mathrm{D}_0,q}, \theta_{\mathrm{D}_0,q}) f_{\phi_{\mathrm{B}_0\mathrm{D}_0}}(\phi_{\mathrm{B}_0\mathrm{D}_0})$$
$$\times \mathrm{d}z\, \mathrm{d}r_{\mathrm{B}_0}\, \mathrm{d}\theta_{\mathrm{D}_0,q}\, \mathrm{d}r_{\mathrm{D}_0,q}\, \mathrm{d}\phi_{\mathrm{B}_0\mathrm{D}_0}, \tag{2.35}$$

where the region $\mathcal{R}$ *and the joint distribution of* Z, r_{B_0}, $\theta_{\mathrm{D}_0,q}$, $r_{\mathrm{D}_0,q}$, *and* $\phi_{\mathrm{B}_0\mathrm{D}_0}$ *are the same as given in Theorem 2.15, and* $W = V_1 + (1-V_0)(V_2 + V_3\mathbf{1}(\tau < 1))$*, where* $V_0 = \frac{\gamma\left(m, \frac{N_0}{c}m\tau\right)}{(m-1)!}$

and

$$V_1 = \sum_{i=0}^{m-1}\sum_{k=0}^{i}\binom{k+m-1}{k}\mu\left(\begin{matrix}a, b\tau\\ m, k\end{matrix}\middle|\begin{matrix}s_1, s_1\\ i-k\end{matrix}\right),$$

$$V_2 = \sum_{i=0}^{m-1}\sum_{k=0}^{i}\binom{k+m-1}{k}\mu\left(\begin{matrix}a\tau, b\\ k, m\end{matrix}\middle|\begin{matrix}s_2, s_2\\ i-k\end{matrix}\right),$$

$$V_3 = \sum_{i=0}^{m-1}\sum_{j=0}^{i+m-1}\binom{i+m-1}{i}\left[\mu\left(\begin{matrix}a, b\\ m, i\end{matrix}\middle|\begin{matrix}s_3, s_3\\ j\end{matrix}\right)+\mu\left(\begin{matrix}a, b\\ i, m\end{matrix}\middle|\begin{matrix}s_3, s_3\\ j\end{matrix}\right)\right]$$
$$-\sum_{i=0}^{m-1}\sum_{k=0}^{i}\sum_{j=0}^{k+m-1}\binom{k+m-1}{k}\binom{j+i-k}{j}\left(\frac{\tau}{1-\tau}\right)^{j}$$
$$\times\left[\mu\left(\begin{matrix}a, b\tau\\ m, k-j\end{matrix}\middle|\begin{matrix}s_1, s_3\\ j+i-k\end{matrix}\right)+\mu\left(\begin{matrix}a\tau, b\\ k-j, m\end{matrix}\middle|\begin{matrix}s_2, s_3\\ j+i-k\end{matrix}\right)\right],$$

$$s_1 = \frac{1}{a}m\tau, \qquad s_2 = \frac{1}{b}m\tau, \qquad s_3 = \frac{a+b}{ab(1-\tau)}m\tau,$$

and the function μ and parameters a, b, and c are the same as given in Theorem 2.15.

Proof. See Appendix A.9. □

Ignoring noise and using Assumption 1, we have $\mathrm{SINR}_{\mathrm{BD}} \to \infty$, and thus $\mathrm{SINR}^{\mathrm{AF}}_{\mathrm{e2e},q} = \mathrm{SINR}^{\mathrm{DF}}_{\mathrm{e2e},q} = \mathrm{SINR}_{\mathrm{DU},q}$. The following corollary gives the coverage probability in this scenario, where the proof follows by setting $N_0 = 0$ in Theorems 2.15 and 2.16, giving $g = 0$ and $V_0 = 0$.

Corollary 2.17. *The coverage probability for both the AF and DF protocols in an interference-limited network can be written as $P_{\mathrm{Cov}} = A_{\mathrm{L}}P_{\mathrm{Cov,L}} + A_{\mathrm{N}}P_{\mathrm{Cov,N}}$, where $P_{\mathrm{Cov},q}$ is as given in (2.35) with $W = V_1 + V_2 + V_3\mathbf{1}(\tau < 1)$, where V_1, V_2, and V_3 are given in Theorem 2.16 statement.*

2.5 Simulation Results

In this section, we verify our analytical results via numerical simulations and provide several system-level insights of our 3D setup. We assume that the density of BSs is $\lambda_{\mathrm{B}} = 10^{-6}$ (i.e., 1 BS/km^2) and they are located at a constant height of $h_{\mathrm{B}} = 20$ m. The BSs provide wireless backhaul connections for the UAVs, which are distributed as a 3D PPP with density λ_{D} between heights $h_{\mathrm{D,m}}$ and $h_{\mathrm{D,M}}$, where we assume λ_{D} ranges from 10^{-9} to 10^{-6}, and $h_{\mathrm{D,m}}$ and $h_{\mathrm{D,M}}$ take values in $\{50, \ldots, 1000\}$ m. Following [11], we consider the following four urban environments, where the parameters of the LoS probability function (c_1 and c_2)

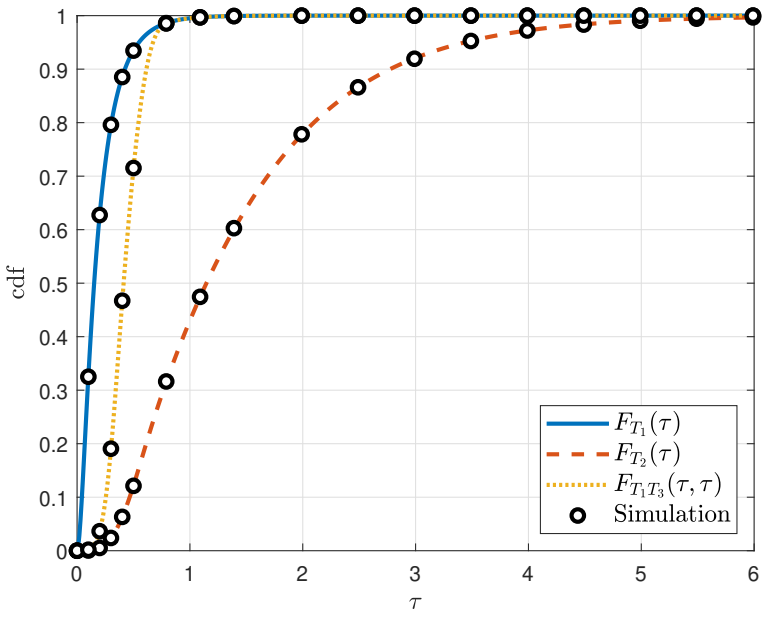

Figure 2.3: Comparison between the cdfs of T_1, T_2, and the joint cdf of T_1 and T_3 ($a = 1$, $b = 4$, $I = 2$, $m = 2$, and $g = 1$).

and the mean excessive path-loss (η_{L} and η_{N}) for each environment are also provided: (i) suburban ($c_1 = 4.88$, $c_2 = 0.43$, $\eta_{\mathrm{L}} = 0.1$ dB, $\eta_{\mathrm{N}} = 21$ dB), (ii) urban ($c_1 = 9.61$, $c_2 = 0.16$, $\eta_{\mathrm{L}} = 1$ dB, $\eta_{\mathrm{N}} = 20$ dB), (iii) dense urban ($c_1 = 12.08$, $c_2 = 0.11$, $\eta_{\mathrm{L}} = 1.6$ dB, $\eta_{\mathrm{N}} = 23$ dB), and (iv) highrise urban ($c_1 = 27.23$, $c_2 = 0.08$, $\eta_{\mathrm{L}} = 2.3$ dB, $\eta_{\mathrm{N}} = 34$ dB). Other parameters are $\alpha_{\mathrm{L}} = 2.5$, $\alpha_{\mathrm{N}} = 4$, $m = \{1, 2\}$, $P_{\mathrm{B}} = 10$ dB, $P_{\mathrm{D}} = 5$ dB, $N_0 = 10^{-8}$, $N_{\mathrm{B}} = 8$, and $\theta_{\mathrm{B}} = 100^{\circ}$ (measured from the z-axis).

2.5.1 Intermediate Results

We begin by focusing on the intermediate results given in Section 2.3. In Fig. 2.3, we compare the analytical results for the cdf of T_1 (Lemma 2.3), T_2 (Lemma 2.4), and the joint cdf of T_1 and T_3 (Lemma 2.5) with numerical simulations using representative parameters $a = 1$, $b = 4$, $I = 2$, $m = 2$, and $g = 1$. Since the coverage probability in the DF and AF relaying protocols is proportional to the ccdf of T_2 and the joint ccdf of T_1 and T_3, respectively, we can clearly observe the performance superiority of the DF over AF in this figure. The joint pdf of the serving distance ($r_{\mathrm{D}_0,\mathrm{L}}$) and zenith angle ($\theta_{\mathrm{D}_0,\mathrm{L}}$) when the serving UAV is in LoS is plotted in Fig. 2.4 for a suburban environment with $\lambda_{\mathrm{D}} = 10^{-6}$, $h_{\mathrm{D,m}} = 100$ m, and $h_{\mathrm{D,M}} = 300$ m. Note that since the excessive path-loss is very high for an NLoS channel condition [11], the NLoS association probability will be low in such realistic environments and the closest LoS UAV to the origin almost always provides higher received power at the

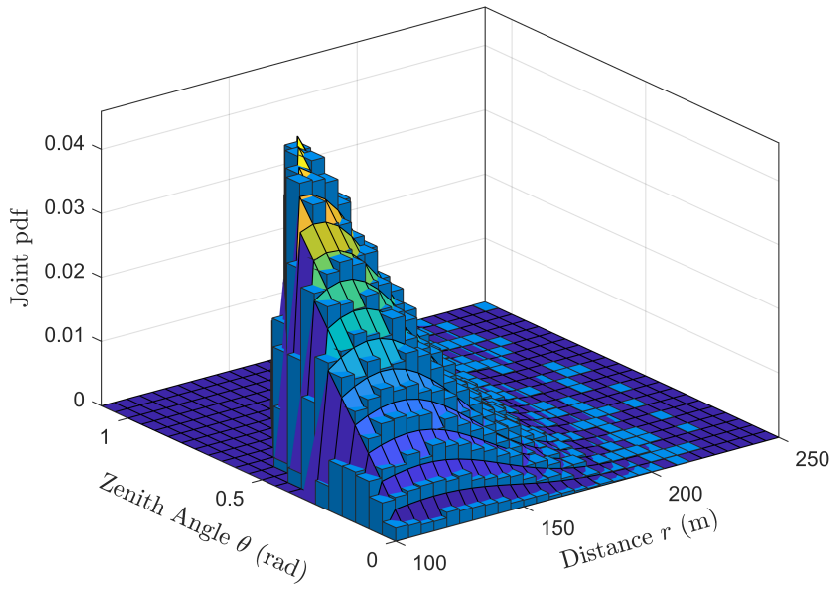

Figure 2.4: The joint pdf of $r_{\mathrm{D}_0,\mathrm{L}}$ and $\theta_{\mathrm{D}_0,\mathrm{L}}$ (suburban, $\lambda_{\mathrm{D}} = 10^{-6}$, $h_{\mathrm{D,m}} = 100$ m, and $h_{\mathrm{D,M}} = 300$ m).

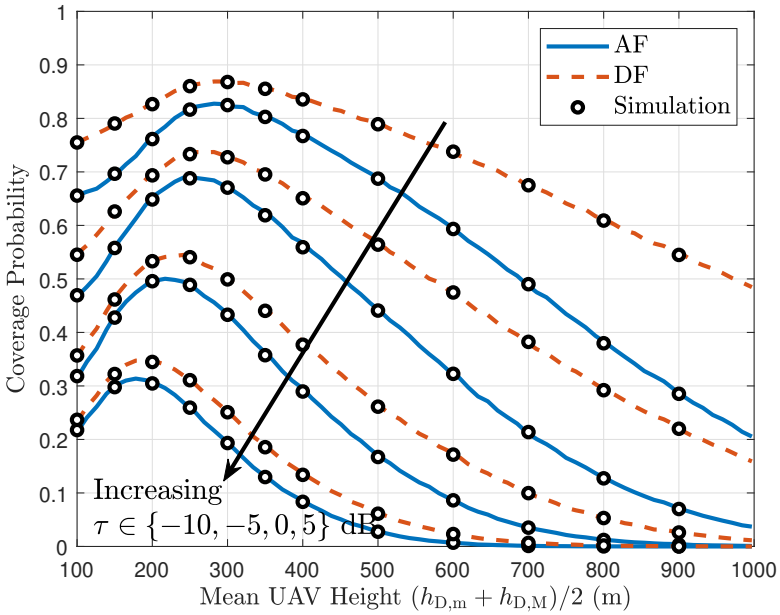

Figure 2.5: Coverage probability as a function of the mean UAV height for both AF and DF and different τ's (urban, $\lambda_{\mathrm{D}} = 10^{-8}$, $m = 1$, $h_{\mathrm{D,M}} - h_{\mathrm{D,m}} = 100$ m).

typical UE than the closest NLoS UAV.

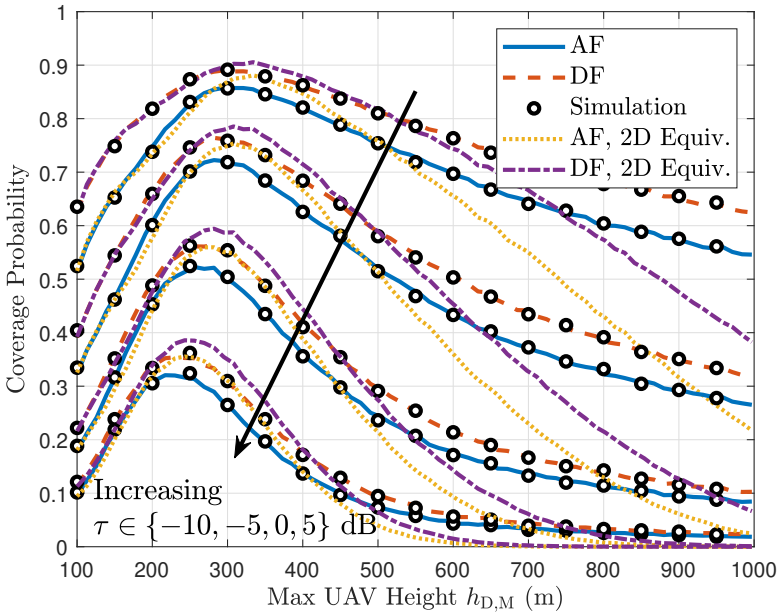

Figure 2.6: Coverage probability as a function of the maximum UAV height for both AF and DF and different τ's (urban, $\lambda_{\mathrm{D}} = 10^{-8}$, $m = 1$, $h_{\mathrm{D,m}} = 50$ m).

2.5.2 Impact of Relaying Protocols, UAV Height, and Density

In Figs. 2.5-2.7, we show the coverage probability as a function of UAV height and density for both AF and DF relaying protocols in an urban environment. In Fig. 2.5, we keep the difference between the maximum and minimum UAV heights constant ($h_{\mathrm{D,M}} - h_{\mathrm{D,m}} = 100$ m) and then increase the mean UAV height from 100 m to 1000 m. On the other hand, in Fig. 2.6, we keep the minimum UAV height constant ($h_{\mathrm{D,m}} = 50$ m) and increase the maximum UAV height from 100 m to 1000 m. In both of these figures, we set $\lambda_{\mathrm{D}} = 10^{-8}$ and $m = 1$. Let us define the equivalent 2D model of a 3D UAV network as a network with the following two properties: (i) all the UAVs are at the same height, which is set to be the mean value of the maximum and minimum UAV heights of the original 3D network, and (ii) the average number of points in the 2D model is the same as that of the 3D network (with the interpretation that all the points in the 3D setup are projected onto the 2D plane). Using this definition, we compare our results for the 3D network with its equivalent 2D model in Fig. 2.6. As seen from this figure, the two networks behave very similarly for small values of the height difference. However, as we increase the height difference, the coverage probability of the equivalent 2D model differs significantly from that of the 3D network. In Fig. 2.7, we assume $m = 1$, $h_{\mathrm{D,m}} = 100$ m, $h_{\mathrm{D,M}} = 300$ m, and obtain the coverage probability by increasing λ_{D} from 10^{-9} to 5×10^{-8}. The following observations can be made from these figures: (i) coverage probability in the DF relaying protocol is higher than that of the AF protocol, which has been theoretically shown in Section 2.2.5 and further pointed out in

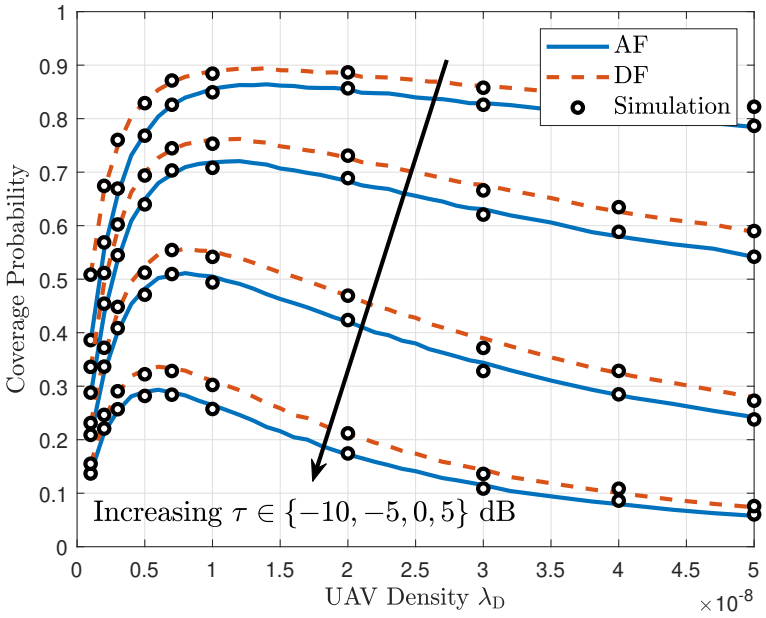

Figure 2.7: Coverage probability as a function of UAV density for both AF and DF and different τ's (urban, $m = 1$, $h_{D,m} = 100$ m, $h_{D,M} = 300$ m).

Fig. 2.3, (ii) coverage probability decreases as the SINR threshold τ increases, which is also clear from the definition, (iii) network performance can significantly benefit from limiting the maximum allowable UAV height, (iv) 3D UAV networks cannot always be accurately modeled using their equivalent 2D models, and (v) there exist mean UAV height h_D^* and UAV density λ_D^* for which the coverage probability is maximized for each SINR threshold τ. Note that although increasing the average UAV height increases the LoS probability and makes the overall channel condition better, the increased UAV-UE distance significantly affects the path-loss and degrades the coverage probability. Furthermore, increasing the average number of UAVs per unit volume beyond λ_D^* increases the overall interference at the typical UE and the serving UAV, which in turn degrades the coverage probability.

2.5.3 Impact of Environments and Antenna Models

We plot the AF coverage probability versus SINR threshold at different environments in Fig. 2.8, where the parameters are $\lambda_D = 10^{-8}$, $m = 2$, $h_{D,m} = 100$ m, and $h_{D,M} = 300$ m. Due to high excessive path-loss and low LoS probability, we observe the worst coverage performance for most SINR thresholds in the highrise urban environment. It is also quite interesting to note that the suburban environment does not demonstrate the best performance. Although we have stronger received power at the typical UE in the suburban environment due to lower path-loss and higher LoS probability, the interference will also be stronger in this

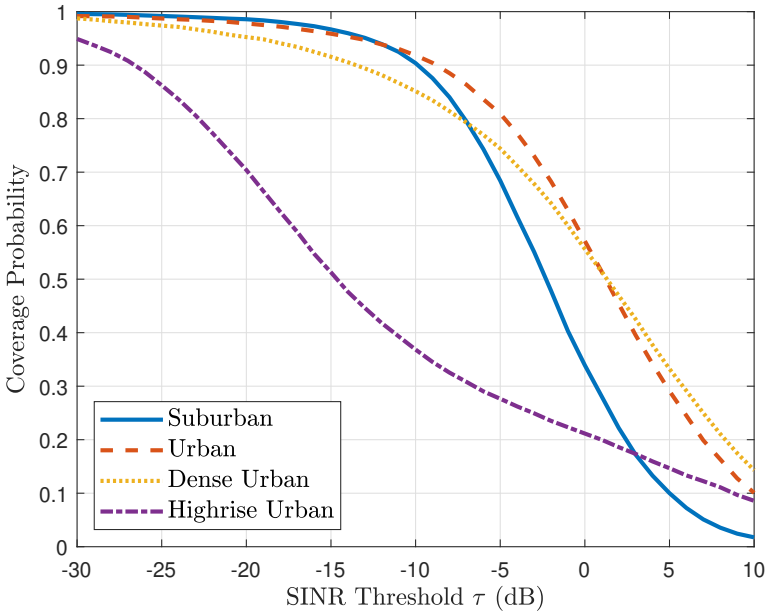

Figure 2.8: Coverage probability as a function of τ for the AF protocol at different environments ($\lambda_{\mathrm{D}} = 10^{-8}$, $m = 2$, $h_{\mathrm{D,m}} = 100$ m, $h_{\mathrm{D,M}} = 300$ m).

case. Therefore, numerical simulations are necessary to compare the coverage performance in different environments. In Fig. 2.9, we show the DF coverage probability of the network in an urban environment for three antenna models: (i) *isotropic*, where we assume all BSs and UAVs are equipped with isotropic antennas, (ii) *omnidirectional*, where we assume each BS is equipped with one downtilted omnidirectional ULA, as described in Section 2.2.2, and (iii) *omnidirectional and directional*, where each BS is equipped with one downtilted omnidirectional ULA and one uptilted directional antenna, as described in Section 2.2.2. The performance superiority of antenna models (ii) and (iii) over the canonical model in (i) is completely clear in this figure. We can also observe the benefit of having an uptilted antenna at the BS site that is solely used for backhaul purposes in this plot. With the antenna model given in (iii), the serving UAV is no longer served by the BS antenna sidelobes, which could be very weak. On the contrary, upon proper antenna orientation, the serving UAV will be served by a strong directional antenna at the serving BS, and thus, the BS-UAV backhaul link will be strong, which results in a better overall coverage performance.

2.6 Chapter Summary

In this chapter, we studied the performance of two-hop backhaul-aware 3D cellular networks, where BSs and UAVs coexist to serve the UEs on the ground. Specifically, each UE either

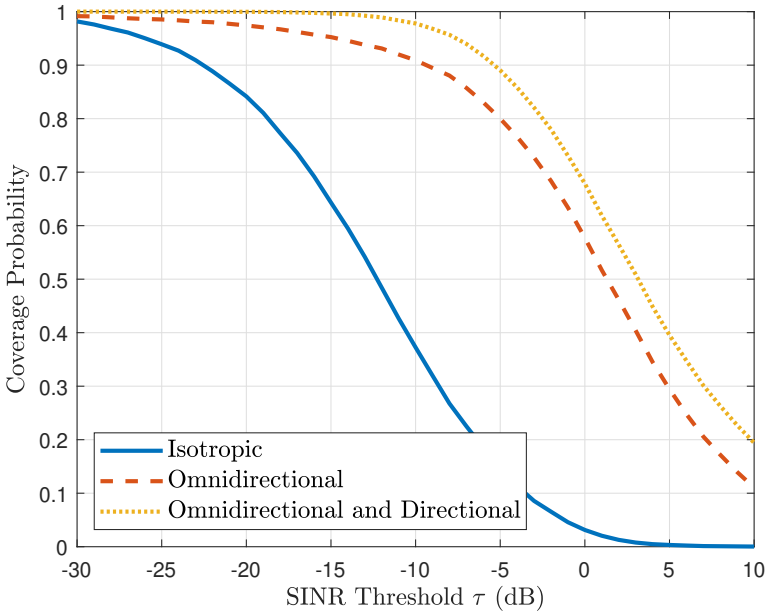

Figure 2.9: Coverage probability as a function of τ for the DF protocol using different BS antenna models (urban, $\lambda_{\mathrm{D}} = 10^{-8}$, $m = 2$, $h_{\mathrm{D,m}} = 100$ m, $h_{\mathrm{D,M}} = 300$ m).

connects directly to a fiber-backhauled terrestrial BS (access link), or connects first to a UAV which is then wirelessly backhauled to a terrestrial BS (joint access and backhaul). Inspired by the 3GPP studies, we used realistic antenna patterns for both BSs and UAVs. Due to the high probability of LoS in air-to-ground wireless communications, we adopted a probabilistic channel model for the UAV-UE links that incorporates both LoS and NLoS channel conditions. Following the max-power association policy, we characterized the network coverage performance for two well-known relaying protocols, i.e., AF and DF, by identifying and analyzing the building blocks of their SINR expressions. We also provided a comprehensive analysis of the joint distribution of distance and zenith angle of the closest and serving UAV to the typical UE in a 3D setting using tools from stochastic geometry. Moreover, since the UAV backhaul link could be much weaker than its access link due to the BS antenna sidelobes and nulls, we analyzed the addition of an uptilted directional antenna at the BS site for improving the UAV backhaul link. To the best of our understanding, this is the first work that offers a comprehensive analysis of 3D cellular networks where BSs provide wireless backhaul to the UAVs using a two-hop relaying scheme. While this work provides insightful results in a two-hop setting, extending its outcomes to a multi-hop scenario would be valuable, especially when coverage in faraway regions is required. Another possible extension of this work is the analysis of the two-hop transmission while incorporating spatial coupling in the placement of UAVs and UEs through the use of Poisson cluster processes [90, 98]. Furthermore, because we considered the joint transmission of BSs and UAVs to the UEs in this chapter, studying their *coordinated* joint transmission [99] is a meaningful

extension of this work. Since the serving BS and UAV do not interfere with each other's transmission in the coordinated scheme, we expect to get better results in terms of average rate and coverage probability.

The analysis in this chapter was carried out on a *static* network of UAVs. In the next two chapters, we will consider a *mobile* network of UAVs and explore the challenges that come with this new framework.

Chapter 3

Performance Characterization of Canonical Mobility Models in Drone Cellular Networks

3.1 Introduction

Owing to their deployment flexibility, drones are currently being considered for a variety of use cases, such as acting as mobile relays to expand the coverage of cellular networks, providing network connectivity for public safety applications, and setting up temporary networks in the times of natural disasters or large social gatherings. While the flexibility offered by the mobility of drones is highly appealing to the network designers, it also adds an entirely new dimension to the system design that was not present in the traditional terrestrial networks. In particular, while mobility is known to have a fundamental impact on the system-level performance of wireless networks, e.g., see [100], the research focus in this direction has traditionally been on the setting in which the UEs are mobile while the BSs are static [101, 102]. This is clearly not the case in drone-assisted communication networks where some mobile drones may act as BSs [2]. Not surprisingly, the support of mobile drones, either as UEs or BSs, has also been recently explored in 3GPP studies [5, 6]. In general, there has been an increasing interest in the community to characterize the effect of drone mobility on the design and performance of drone-assisted cellular networks. Due to the irregularity of the drone placements and their trajectories, it is expected that powerful tools from stochastic geometry and point process theory could be leveraged for accurate modeling and tractable analysis of drone networks. Inspired by this, the main focus of this chapter is to present a unified performance analysis of a DBS network under various mobility models that involves a novel characterization of the underlying point processes as a function of time.

3.1.1 Related Works

This chapter builds on the following two key lines of research: (i) stochastic geometry for drone networks, and (ii) mobility models in wireless networks. Although sparse, there are some works that lie at their intersection and will be discussed below after establishing the prior art for each research direction separately.

Stochastic Geometry for Drone Networks. Owing to its ability to capture irregularity in the placement and movement of drones, stochastic geometry has recently found many applica-

tions in the performance analysis of drone networks [20, 22, 23, 24, 83, 103, 104, 105, 106]. In [20], the authors considered a finite network of DBSs distributed as a uniform BPP [21] and derived the coverage probability of the network. In [104], the problem of spectrum sharing for a network of drone small cells as an underlay to a conventional cellular network has been studied. On the similar lines, the authors of [22] investigated the coexistence of BSs and DBSs using probabilistic LoS and NLoS propagation models [11], where the locations of BSs and DBSs are modeled as a superposition of a PPP and a BPP. The work presented in [23] considered a network of DBSs modeled as a PPP serving ground UEs. In particular, incorporating LoS and NLoS propagation models, the authors derived approximations for the coverage probability and the received rate in the network. In [24], the coexistence between a single DBS and an underlaid D2D network has been analyzed in terms of coverage probability and rate. Motivated by the requirement to provide coverage in a post-disaster scenario, the authors in [105] analyzed the performance of a DBS network serving clustered UEs.

Mobility Models in Wireless Networks. Mobility modeling is a well-established area of research in wireless networks [107, 108, 109, 110]. Perhaps the simplest mobility model is the one in which nodes move along straight lines in random directions at a constant speed. Variants of this simple model have been used extensively in the literature, e.g., see [5, 109, 111, 112, 113]. Although this model may appear simplistic, it is known to provide performance bounds and useful insights in wireless networks [111]. In fact, this model has also been used recently to model drone mobility in 3GPP studies related to drone networks [5]. Among other mobility models that have been studied in wireless networks (such as RW, RWP, random direction, Brownian motion, Levy walk, and Gauss-Markov), RW and RWP mobility models have been more popular because of their tractability [101, 107, 114, 115, 116]. Hence, we also study these two models in this chapter.

In the RW model, the mobile nodes can change their directions [107, 112, 114]. In particular, each node selects a uniformly random direction and a random speed in each time slot and moves along a straight line using the selected direction and speed. Upon arrival at the destination, it repeats this procedure. As a generalization of the RW model, the finite RWP model was proposed in [117] by adding a random pause time between direction and/or speed changes in the RW model. Specifically, the mobility process in the finite RWP model starts with a random pause time at the initial waypoint of a node in a finite region. Then, a destination waypoint is selected randomly in that region and the node moves to this destination waypoint along a straight line with a random speed. Upon its arrival, the node pauses for another random time and repeats this procedure. Due to some major drawbacks of this model, such as the non-uniform distribution of the nodes [101, 118, 119], the authors in [102] extended the finite RWP to an infinite RWP model, where the nodes are allowed to move over the entire plane. In particular, each node first pauses for a random time at its initial waypoint and determines the next waypoint by choosing a uniformly random direction and a random transition distance. It then moves towards the chosen waypoint at a random speed, pauses at this new waypoint for another random time, and repeats this procedure.

Mobile Drone Networks. Among many works on the analysis of drone networks, only a handful of them considered *mobile* drones. Considering a mobile network of DBSs that are initially modeled as a BPP, the authors in [37] used results from [20] to design stochastic trajectory processes for the mobility of DBSs that provide the same coverage as given in [20]. In [39] and [40], the authors modeled the motion of DBSs in a 3D finite network by the finite RWP and RW models, and using the results of [101], derived the coverage probability of the network.

3.1.2 Contributions

This chapter develops a unified approach for the performance analysis of drone cellular networks under several key canonical models. In particular, we model the initial locations of a mobile network of DBSs as a homogeneous PPP operating at a constant height that serves UEs on the ground. The serving DBS is selected based on the nearest-neighbor association policy and all the other DBSs are regarded as interferers. We consider four canonical mobility models for the interfering DBSs, i.e., SL, RS, RW, and RWP, and two service models for the serving DBS: (i) UIM, in which the serving DBS follows the same mobility model as the interfering DBSs, and (ii) UDM, in which the serving DBS moves towards the typical UE at a constant height and keeps hovering above its location after reaching there until its transmission is completed. For this setup, our key contributions are described next.

Distributional Properties of Canonical Mobility Models

We derive various distributional properties for all the mobility models. Most notably, for the RW and RWP, we derive the joint distribution of the net displacement of a DBS and its total traveled distance at each waypoint. Using this joint distribution, we compute the distribution of the net displacement of a DBS at any time t. We also provide insightful asymptotic results for these distributions.

Unified Framework for Characterizing the Point Process of DBSs

We present a novel characterization of the point process of DBSs as seen by the typical UE at any time t for all the service and mobility models. Since the displacement of each DBS is independent of the others, we apply displacement theorem from stochastic geometry along with the net displacement results described above to characterize these point processes. Using this, we characterize the aggregate interference and key performance metrics, such as average and session rates, as seen by the typical UE for all the service and mobility models.

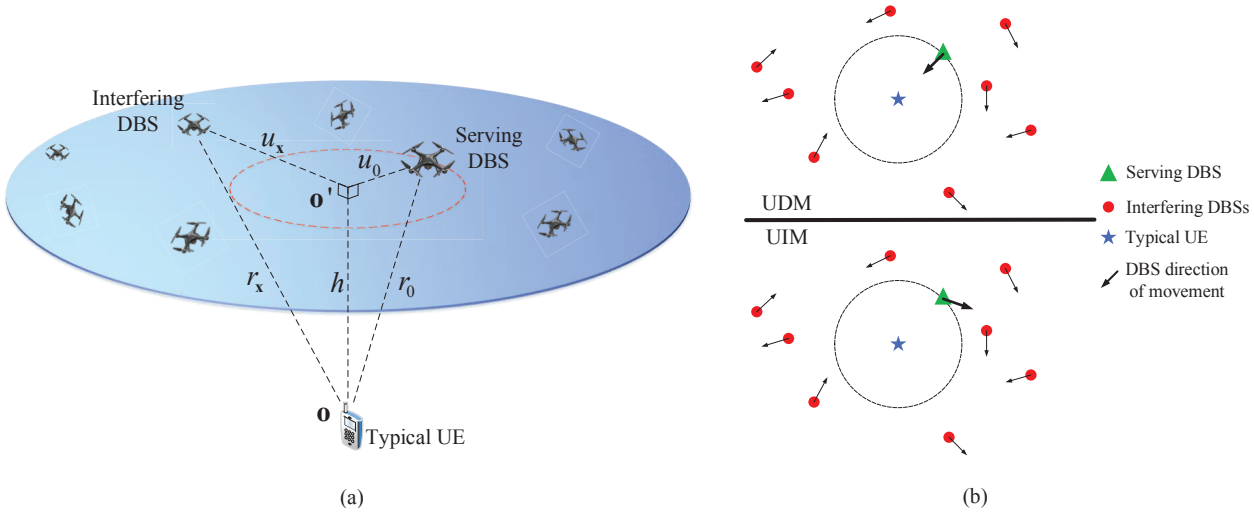

Figure 3.1: (a) An illustration of the system model, and (b) top view of the two service models. Note the difference between the movement direction of the serving DBS in the UDM and the UIM.

Establishing Connections among Mobility Models

Borrowing tools from the calculus of variations, we establish meaningful connections among our mobility models in terms of network performance. Specifically, we prove that the SL mobility model provides a lower bound on the average received rate over the space of all i.i.d. mobility models in which the drones can also follow curved trajectories (as long as they are i.i.d.).

3.2 System Model

3.2.1 Spatial Setup

We consider a network of mobile DBSs serving UEs on the ground. We assume that the DBSs are located at a constant height h from the ground and the temporal evolution of the DBS locations is modeled as the sequence of point processes $\Phi_{\mathrm{D}}(t) \subset \mathbb{R}^2$, indexed by $t \in \mathbb{R}^+$. Further, we assume that the initial locations of the DBSs are distributed as a homogeneous PPP with density λ_0, i.e., $\Phi_{\mathrm{D}}(0) \sim \mathrm{PPP}(\lambda_0)$. Terrestrial UEs are distributed as an independent homogeneous PPP Φ_{U} on the ground. We also assume that the origin $\mathbf{o} = (0, 0, 0)$ of the 3D coordinate system is located on the ground, which is assumed to be aligned with the xy-plane. Throughout the chapter, we refer to the $z = h$ plane as the DBS plane. In this setup, the projection of $\mathbf{o}$ onto the DBS plane is denoted by $\mathbf{o}' = (0, 0, h)$.

Without loss of generality, the analysis will be performed for the *typical UE* placed at $\mathbf{o}$. As shown in Fig. 3.1 (a), the distances of a DBS at time t located at $\mathbf{x}(t) \in \Phi_{\mathrm{D}}(t)$ from $\mathbf{o}'$ and $\mathbf{o}$ are denoted by $u_{\mathbf{x}}(t) = \|\mathbf{x}(t) - \mathbf{o}'\|$ and $r_{\mathbf{x}}(t) = \|\mathbf{x}(t) - \mathbf{o}\| = \sqrt{u_{\mathbf{x}}(t)^2 + h^2}$, respectively. Moreover, the location of the nearest DBS to $\mathbf{o}'$ and its corresponding distance at time t are denoted by $\mathbf{x}_0(t)$ and $u_0(t)$, respectively. Thus, the distance of the closest DBS to $\mathbf{o}$ at time t is $r_0(t) = \sqrt{u_0(t)^2 + h^2}$. For simplicity, we drop the time index t for $u_0(t)$ defined at $t = 0$, i.e., $u_0 \triangleq u_0(0)$, and we drop the time index t for $u_{\mathbf{x}}(t)$ whenever the time index can be clearly understood from the context.

3.2.2 Service and Mobility Models

In this chapter, we assume that each UE connects to its nearest DBS. For the typical UE, this DBS is called the *serving DBS* while all the other DBSs are regarded as *interfering DBSs*. In order to motivate the drone mobility models studied in this chapter, we first take a cue from the mobility model used in the 3GPP studies related to drone networks [5]. In this model, drones start their movement at randomly selected locations in the network and then move at a constant speed and height along straight lines in uniformly random directions, independently of each other, for the entire duration of the simulation. It turns out that this simple enough model is already considered sufficient to capture key effects of drone mobility on the system-level performance. One can, of course, generalize this straight-line mobility model to arrive at classical canonical models, such as RW and RWP, which offer a useful balance between realism and tractability. Since all these models are important in their own right, we will develop a unified approach to analyze their performance jointly. Before that, we formally define the four mobility models considered in this chapter next.

Definition 3.1. *(Mobility Models).* We define the mobility models used in this chapter as follows. Without loss of generality, we choose the x-axis as the reference for measuring all angles.

1. **SL**: DBSs move constantly in random directions $\Theta \sim U[0, 2\pi)$ along straight lines at a constant speed v, independently of each other.
2. **RS**: Each DBS moves a random distance $R \sim f_R(.)$ in a random direction $\Theta \sim U[0, 2\pi)$ along a straight line at a constant speed v, independently of the other DBSs, and then stops and hovers over the stopping location.
3. **RW**: Each DBS selects a random direction $\Theta \sim U[0, 2\pi)$, independently of the other DBSs, and moves a random distance $R \sim f_R(.)$ in this direction at a constant speed v. Upon its arrival, it selects another random direction Θ and distance R and repeats this procedure.
4. **RWP**: In the beginning, each DBS hovers for a random time $T \sim f_T(.)$ at its initial location. It then selects a random direction $\Theta \sim U[0, 2\pi)$, independently of the other

DBSs, and moves a random distance $R \sim f_R(.)$ in this direction at a constant speed v. Upon its arrival, it hovers for another random time T, sampled independently from $f_T(.)$, selects another random direction Θ and distance R, and repeats this procedure.

Remark 3.2. All the mobility models considered in this chapter lie in the space of i.i.d. mobility models, where the drone trajectories are chosen independently of each other from the same common distribution. As will be clear in the sequel, some of our initial results hold for all i.i.d. models (including the ones with curved trajectories).

Remark 3.3. In this chapter, we represent DBSs as "points" in the DBS plane. Hence, the occurrence of a collision, which is defined as the event in which two points arrive at the same location at the same time, is a zero measure event.

Remark 3.4. As mentioned in Definition 3.1, we require our DBSs to be able to hover at specific locations. Hence, we assume that DBSs in this chapter are rotary-winged drones.

Definition 3.5. *(Flight).* In the RW and RWP mobility models, a flight is defined as the distance traveled by a DBS between two consecutive stop points.

As shown in Fig. 3.1 (b), we consider the following two service models for the serving DBS.

1. UIM: The serving DBS follows the same mobility model as the interfering DBSs, independent of the typical UE location.

2. UDM: The serving DBS moves towards $\mathbf{o}'$ in the DBS plane and keeps hovering at this location until its transmission to the typical UE is completed.

The main motivation behind considering the UIM is to have a baseline to evaluate the UDM. In other words, our intention is to see how much we benefit from designing our trajectories based on the UE locations (UDM). Note that in all the aforementioned models, the speeds of the serving and interfering DBSs are assumed to be the same. Moreover, since we are not considering any dependency across the user locations, DBS trajectories will be independent of each other in both the UIM and the UDM.

Remark 3.6. In the UIM, since **all** DBSs move in different directions based on the defined mobility models, handover may occur [82]. On the other hand, in the UDM, no matter what the mobility model is for the interfering DBSs, as long as the interfering DBSs move at the same speed as the serving DBS, the serving DBS will remain the closest DBS to the typical UE. Hence, based on our association policy, the serving DBS will not change in our mobility models, and thus, handover will not occur. Furthermore, UDM can be considered as a best-case model from the perspective of minimizing the distance between the typical UE and its serving DBS.

3.2.3 Channel Model

We assume that all DBSs transmit with the same power level P at all times. The received power at the typical UE from the serving DBS is assumed to be $Ph_0(t)r_0(t)^{-\alpha}$, where $h_0(t)$ represents the small-scale fading power gain between the typical UE and the serving DBS and $\alpha > 2$ is the path loss exponent. Likewise, the interference power is $I(t) = \sum_{\mathbf{x}(t)\in\Phi'_{\mathrm{D}}(t)} Ph_{\mathbf{x}}(t)r_{\mathbf{x}}(t)^{-\alpha}$, where $\Phi'_{\mathrm{D}}(t) \equiv \Phi_{\mathrm{D}}(t)\backslash\mathbf{x}_0(t)$ represents the point process of interfering DBSs and $h_{\mathbf{x}}(t)$ is the small-scale fading power gain between the typical UE and the interfering DBSs. Since the air-to-ground links may experience various fading scenarios, Nakagami-m fading is used here to capture a large class of fading environments. Thus, the channel fading power gains $h_0(t)$ and $h_{\mathbf{x}}(t)$ follow gamma distributions with pdf $f_H(h) = \frac{m^m}{\Gamma(m)}h^{m-1}\mathrm{e}^{-mh}$, where $\Gamma(x) = \int_0^\infty t^{x-1}\mathrm{e}^{-t}\,\mathrm{d}t$ is the gamma function. For the serving and interfering links, we assume $m = m_0$ and $m = m_{\mathbf{x}}$, respectively, and we consider integer values for m_0 and $m_{\mathbf{x}}$ for mathematical tractability.

3.2.4 Metrics of Interest

The received signal-to-interference ratio (SIR) at the typical UE is defined as

$$\mathrm{SIR}(t) = \frac{Ph_0(t)r_0(t)^{-\alpha}}{I(t)}. \tag{3.1}$$

We now define our SIR-based performance metrics as follows.

Average rate: Average received rate is given as $R(t) = \mathbb{E}[\log(1 + \mathrm{SIR}(t))]$, where the expectation is taken over the PPP $\Phi_{\mathrm{D}}(t)$ and the trajectories. This is essentially the average rate experienced by the typical UE at time t across different network and trajectory realizations.

Session rate: This metric is defined as the average received rate by the typical UE at each session of duration T. Mathematically speaking, we have

$$\mathrm{SR}(T) = \frac{1}{T}\int_0^T R(t)\,\mathrm{d}t. \tag{3.2}$$

3.2.5 Methodology of Analysis

In this subsection, we briefly describe the methodology of our analysis in this chapter. In Section III, we will characterize the point process of interferers by deriving the density of the network of interfering DBSs for all service and mobility models. We will then provide some intermediate results for the RW and RWP mobility models in Section IV that are useful in characterizing the distributional properties of these mobility models. Using the results in these two sections, we will finally derive the average and session rates in Section V for all service and mobility models.

3.3 Point Process of Interferers

In this section, we characterize the temporal evolution of the point process of interferers for all the mobility models described in Section 3.2.2. We start our analysis by first considering the UIM in the following lemma.

Lemma 3.7. *Let Φ be a homogeneous PPP with density λ_0. If all the points of Φ are independently displaced based on the four mobility models mentioned in 3.2.2, then the displaced points at every time t form another homogeneous PPP Ψ with the same density λ_0.*

Proof. Based on the displacement theorem [19], we need to argue that the displaced distances of DBSs at every time t are i.i.d. and also independent of their original locations in Φ. For the first two mobility models, this is clear from our model constructions. For the RW and RWP models, note that different flights are independent of the locations of DBSs and the overall displaced distance at time t is a function of these flights. Hence, the overall displacement of DBSs is independent of their locations in the original PPP Φ. Therefore, Ψ is distributed as a homogeneous PPP with density λ_0. This completes the proof. □

In the UIM, the serving DBS and all the interfering DBSs are displaced in uniformly random directions based on our different mobility models. Thus, we can infer from Lemma 3.7 that the network of all DBSs at any time t will remain a homogeneous PPP with density λ_0. As a result, the network of *interfering* DBSs will be distributed as an inhomogeneous PPP in the DBS plane with density

$$\lambda(t; u_{\mathbf{x}}, u_0) = \begin{cases} \lambda_0, & u_{\mathbf{x}} > u_0(t) \\ 0, & u_{\mathbf{x}} \leq u_0(t), \end{cases} \tag{3.3}$$

Note that although the serving distance $u_0(t)$ varies over time, its distribution does not change.

Remark 3.8. The rate performance of a mobile drone network where the service model follows the UIM is equivalent to that of a static drone network since the density of the point process of interferers in a static setting will be also given by (3.3).

In the UDM, it is clear from our construction that $\Phi'_{\mathrm{D}}(0)$ is an inhomogeneous PPP with density given by (3.3), which introduces an *exclusion zone*, $\mathcal{X} = b(\mathbf{o}', u_0)$, for the interfering DBSs in the DBS plane, where $b(\mathbf{o}, r)$ is a disc of radius r centered at $\mathbf{o}$. Using displacement theorem, we observe that $\Phi'_{\mathrm{D}}(t)$ remains an inhomogeneous PPP for the UDM as well. In the next lemma, we provide a mathematical characterization of $\Phi'_{\mathrm{D}}(t)$ in the UDM at every time t.

Lemma 3.9. (Point Process of Interferers). *Consider the UDM with an i.i.d. mobility model. Let $\mathbf{x}(0)$ and $\mathbf{x}(t)$ denote the initial location and the location at time t of an interfering DBS,*

respectively. Define $L(t) = \|\mathbf{x}(0) - \mathbf{x}(t)\|$ *as the net displacement of this interfering DBS until time* t *and denote its cumulative distribution function (cdf) and pdf by* $F_L(l;t)$ *and* $f_L(l;t)$*, respectively. Then the network of interfering DBSs will be an inhomogeneous PPP with density*

$$\lambda(t;u_{\mathbf{x}},u_0)=\lambda_0\begin{cases}1, & u_0+vt\le u_{\mathbf{x}}\\ \beta(t,u_{\mathbf{x}},u_0), & |u_0-vt|\le u_{\mathbf{x}}\le u_0+vt\\ \beta(t,u_{\mathbf{x}},u_0)\mathbf{1}\left(t>\frac{u_0}{v}\right), & 0\le u_{\mathbf{x}}\le |u_0-vt|,\end{cases} \tag{3.4}$$

where $\mathbf{1}(.)$ *is the indicator function and*

$$\beta(t,u_{\mathbf{x}},u_0)=1-F_L(u_0-u_{\mathbf{x}};t)-\int_{|u_{\mathbf{x}}-u_0|}^{\min\{vt,u_{\mathbf{x}}+u_0\}} f_L(l;t)\frac{1}{\pi}\cos^{-1}\left(\frac{l^2+u_{\mathbf{x}}^2-u_0^2}{2lu_{\mathbf{x}}}\right)\mathrm{d}l. \tag{3.5}$$

Proof. See Appendix B.1. □

Remark 3.10. We observe the following directly from Lemma 3.9: (i) (3.4) is continuous at boundaries, i.e., at $u_{\mathbf{x}}=|u_0\pm vt|$, (ii) as $u_0\to 0$, we get $\beta(t,u_{\mathbf{x}},u_0)\to 1$, i.e., the network of interfering DBSs becomes homogeneous, and (iii) as $u_0\to 0$ or $t\to 0$, (3.3) and (3.4) become identical.

The density derived in Lemma 3.9 is valid for all i.i.d. mobility models where DBSs move at the same constant speed. Hence, for mobility models in this chapter, we only need to characterize the distribution of the net displacement of each DBS at every time t. For the SL model, we provide this distribution, and thus, the density of the network of interferers, in the next corollary.

Corollary 3.11. (Point Process of Interferers for the SL Model). *When the interferers move based on the SL mobility model, the network of interferers will be an inhomogeneous PPP with density*

$$\lambda(t;u_{\mathbf{x}},u_0)=\lambda_0\begin{cases}1, & u_0+vt\le u_{\mathbf{x}}\\ \frac{1}{\pi}\cos^{-1}\left(\frac{u_0^2-u_{\mathbf{x}}^2-v^2t^2}{2u_{\mathbf{x}}vt}\right), & |u_0-vt|\le u_{\mathbf{x}}\le u_0+vt\\ \mathbf{1}\left(t>\frac{u_0}{v}\right), & 0\le u_{\mathbf{x}}\le |u_0-vt|,\end{cases} \tag{3.6}$$

Proof. In the SL mobility model, we have $L(t)=vt$, and thus, $f_L(l;t)=\delta(l-vt)$ and $F_L(l;t)=\mathbf{1}(l-vt)$, where $\delta(.)$ is the Dirac delta function. Hence, $\beta(t,u_{\mathbf{x}},u_0)$ can be written as

$$\beta(t,u_{\mathbf{x}},u_0)=1-\mathbf{1}(u_0-u_{\mathbf{x}}-vt)-\int_{|u_{\mathbf{x}}-u_0|}^{\min\{vt,u_{\mathbf{x}}+u_0\}}\delta(l-vt)\frac{1}{\pi}\cos^{-1}\left(\frac{l^2+u_{\mathbf{x}}^2-u_0^2}{2lu_{\mathbf{x}}}\right)\mathrm{d}l. \tag{3.7}$$

We need to consider two cases:

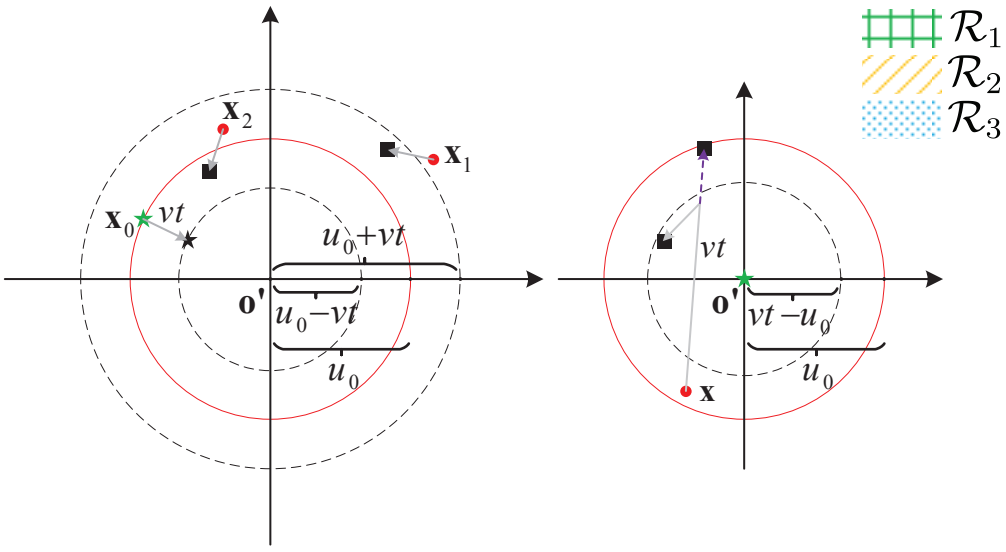

Figure 3.2: Network density in different regions for the SL mobility model. Green and black stars, red circles, and black squares represent serving DBS, displaced serving DBS, interfering DBSs, and displaced interfering DBSs, respectively. (a) Serving DBS is moving towards $\mathbf{o}'$, and (b) serving DBS is hovering at $\mathbf{o}'$.

- $0 \leq u_{\mathbf{x}} \leq |u_0 - vt|$
  In this case, since $\lambda(t; u_{\mathbf{x}}, u_0) = 0$ for $u_0 \geq vt$, we need to only evaluate $\beta(t, u_{\mathbf{x}}, u_0)$ for $u_0 < vt$. This gives $0 \leq u_{\mathbf{x}} \leq vt - u_0$, which makes the integral term in (3.7) zero. Since $u_0 - u_{\mathbf{x}} \leq u_0 + u_{\mathbf{x}} \leq vt$, the term for the indicator function in (3.7) will become zero as well. Hence, $\beta(t, u_{\mathbf{x}}, u_0) = \mathbf{1}\left(t > \frac{u_0}{v}\right)$.

- $|u_0 - vt| \leq u_{\mathbf{x}} \leq u_0 + vt$
  In this case, we have the triangle inequality for the triple $(u_{\mathbf{x}}, u_0, vt)$, which yields $|u_0 - u_{\mathbf{x}}| \leq vt \leq u_0 + u_{\mathbf{x}}$. Hence,

$$\beta(t, u_{\mathbf{x}}, u_0) = 1 - \frac{1}{\pi}\cos^{-1}\left(\frac{v^2t^2 + u_{\mathbf{x}}^2 - u_0^2}{2vtu_{\mathbf{x}}}\right) = \frac{1}{\pi}\cos^{-1}\left(\frac{u_0^2 - u_{\mathbf{x}}^2 - v^2t^2}{2u_{\mathbf{x}}vt}\right).$$

This completes the proof. □

Remark 3.12. We can make sense of (3.6) intuitively by considering the exclusion zone $\mathcal{X}$ and different regions illustrated in Fig. 3.2 as follows: (i) $\mathcal{R}_1 = \{u_{\mathbf{x}} \geq u_0 + vt\}$: No DBS that was initially in $\mathcal{R}_1$ can enter $\mathcal{X}$ within time t, and thus, $\lambda(t; u_{\mathbf{x}}, u_0) = \lambda_0$, (ii) $\mathcal{R}_2 = \{0 \leq u_{\mathbf{x}} \leq u_0 - vt | vt \leq u_0\}$: The serving DBS is in motion towards $\mathbf{o}'$ and since there is no interfering DBS in $\mathcal{R}_2$, we have $\lambda(t; u_{\mathbf{x}}, u_0) = 0$, and (iii) $\mathcal{R}_3 = \{0 \leq u_{\mathbf{x}} \leq vt - u_0 | vt > u_0\}$: In this region, we can use the same method introduced in the proof of Lemma 3.9 as follows.

We first calculate the density contributed by points that would have originally fallen in $\mathcal{X}$ and then subtract it from λ_0 to get the density of the network of interfering DBSs. Since all the DBSs that are initially inside $\mathcal{X}$ will leave $\mathcal{R}_3$ after the displacement of vt, the density contributed by $\mathcal{X}$ in $\mathcal{R}_3$ is 0, which gives $\lambda(t; u_{\mathbf{x}}, u_0) = \lambda_0$. However, for non-linear i.i.d. mobility models, such as RW or RWP, where direction changes are allowed during flights, there is a possibility that some of the DBSs that are initially inside $\mathcal{X}$ do not leave $\mathcal{R}_3$ after the displacement of vt. This fact is highlighted in Fig. 3.2 (b), where a DBS that is initially at $\mathbf{x}$ could possibly fall into $\mathcal{R}_3$ after a displacement of vt with a non-linear i.i.d. mobility model. Hence, the impact of $\mathcal{X}$ is not zero in this case, which implies that the density of interfering DBSs is less than λ_0 in $\mathcal{R}_3$.

It is in fact possible to make a more formal statement about the comparison of SL mobility model with the other models, which is done next.

Theorem 3.13. *The expected number of interferers in the disc $\mathcal{B} = b(\mathbf{o}', u_0 + vt)$ at any time t is maximized over the space of i.i.d. mobility models (including the ones where drones follow curved trajectories) when interferers follow the SL mobility model.*

Proof. See Appendix B.2. □

Remark 3.14. Theorem 3.13 demonstrates that the average number of interferers in any neighborhood of the typical UE is higher in the SL mobility model compared to the other i.i.d. mobility models. Consequently, the average received rate at the typical UE under the SL mobility model is lower compared to the other i.i.d. mobility models.

In the RS mobility model, the net displacement of DBSs until time t is $L(t) = \min\{vt, R\}$, where R is a random variable that determines the displaced distances of DBSs. The following corollary gives the network density for the RS mobility model.

Corollary 3.15. (Point Process of Interferers for the RS Model). *When interfering DBSs move based on the RS mobility model, the network of interfering DBSs will be an inhomogeneous PPP with the same density as given in Lemma 3.9. Furthermore, we have*

$$\beta(t, u_{\mathbf{x}}, u_0) = F_R(u_{\mathbf{x}} - u_0) + (1 - F_R(r)) \frac{1}{\pi} \cos^{-1}\left(\frac{u_0^2 - u_{\mathbf{x}}^2 - r^2}{2u_{\mathbf{x}} r}\right) + \int_{|u_{\mathbf{x}} - u_0|}^{r} f_R(l) \frac{1}{\pi} \cos^{-1}\left(\frac{u_0^2 - u_{\mathbf{x}}^2 - l^2}{2u_{\mathbf{x}} l}\right) \mathrm{d}l, \tag{3.8}$$

where $r = \min\{vt, u_{\mathbf{x}} + u_0\}$.

Proof. Starting with $L(t) = \min\{vt, R\}$, we can write the cdf and pdf of $L(t)$ as

$$F_L(l; t) = \mathbb{P}[\min\{vt, R\} \leq l] = 1 - \mathbb{P}[vt > l, R > l] = F_R(l)\mathbf{1}(vt - l) + \mathbf{1}(l - vt),$$
$$f_L(l; t) = (1 - F_R(vt))\delta(vt - l) + f_R(l)\mathbf{1}(vt - l).$$

Similar to the proof of Corollary 3.11, we consider two cases to derive $\beta(t, u_{\mathbf{x}}, u_0)$ as follows.

- $0 \leq u_{\mathbf{x}} \leq |u_0 - vt|$. We have

$$\beta(t, u_{\mathbf{x}}, u_0) = 1 - F_R(u_0 - u_{\mathbf{x}}) - \int_{|u_{\mathbf{x}}-u_0|}^{u_{\mathbf{x}}+u_0} f_R(l) \frac{1}{\pi} \cos^{-1}\left(\frac{l^2 + u_{\mathbf{x}}^2 - u_0^2}{2lu_{\mathbf{x}}}\right) \mathrm{d}l.$$

- $|u_0 - vt| \leq u_{\mathbf{x}} \leq u_0 + vt$. We have

$$\beta(t, u_{\mathbf{x}}, u_0) = 1 - F_R(u_0 - u_{\mathbf{x}}) - (1 - F_R(vt)) \frac{1}{\pi} \cos^{-1}\left(\frac{v^2t^2 + u_{\mathbf{x}}^2 - u_0^2}{2vtu_{\mathbf{x}}}\right) - \int_{|u_{\mathbf{x}}-u_0|}^{vt} f_R(l) \frac{1}{\pi} \cos^{-1}\left(\frac{l^2 + u_{\mathbf{x}}^2 - u_0^2}{2lu_{\mathbf{x}}}\right) \mathrm{d}l.$$

Combining these equations into a single one, we end up with (3.8) and the proof is complete. □

Note that the SL mobility model is a special case of the RS mobility model when $R \to \infty$, which means that the DBSs never stop. Mathematically speaking, evaluating $\beta(t, u_{\mathbf{x}}, u_0)$ in Corollary 3.15 with $F_R(l) = 0$ and $f_R(l) = \delta(l - \infty) = 0$ for $l < \infty$, we end up with (3.6).

3.4 RW and RWP Mobility Models

In the previous section, we characterized the point process of interferers for both service models, which required the distribution of the net displacement of each DBS as a function of time. As it was shown in Corollaries 3.11 and 3.15, this distribution can be easily derived for the SL and RS mobility models. However, the characterization of this distribution for the RW and RWP mobility models is not straightforward and is the main focus of this section. Note that the distributional results provided here are novel and may be useful in their own right.

As stated in Definition 3.1, we assume that the direction of the i-th movement of a DBS is $\Theta_i \sim U[0, 2\pi)$, which is selected independently of the other DBSs, and the flights R_i are i.i.d. with cdf and pdf of $F_R(.)$ and $f_R(.)$, respectively. Fig. 3.3 shows an example of the RW mobility model. Let $\mathbf{x}(0)$ and $\mathbf{x}(n-1)$ be the initial location of a DBS and its location after $(n-1)$ flights, respectively. Define Z_{n-1} and Ψ_{n-1} as the net displacement of a DBS between $\mathbf{x}(0)$ and $\mathbf{x}(n-1)$ and the angle between the x-axis and the line connecting $\mathbf{x}(0)$ and $\mathbf{x}(n-1)$, respectively. Furthermore, we define S_{n-1} and $L(t)$ as the total distance traveled from $\mathbf{x}(0)$ to $\mathbf{x}(n-1)$ and the net displacement of a DBS until time t, respectively. In order to properly find the distribution of $L(t)$, we need the distributional characteristics of S_{n-1}, Z_{n-1}, and Ψ_{n-1}, which is done next.

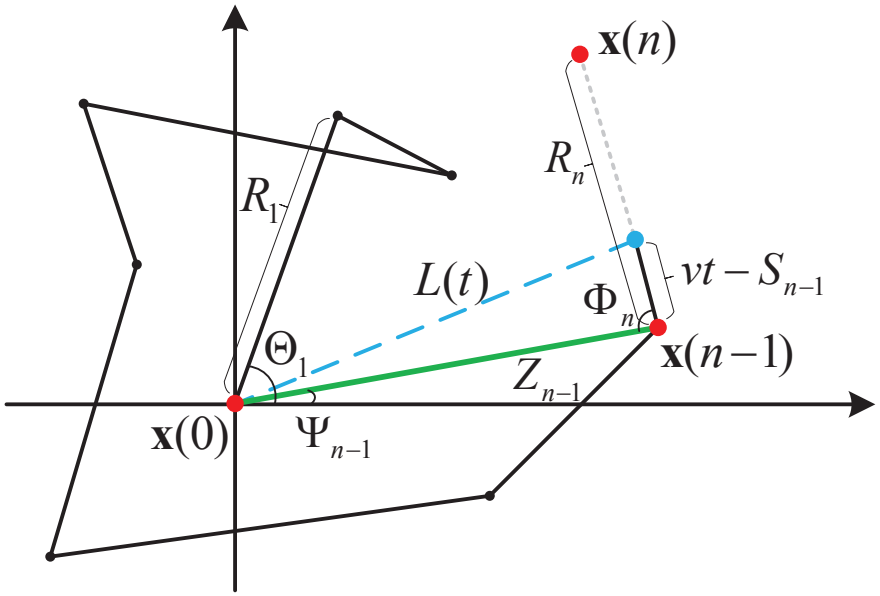

Figure 3.3: A realization of the RW mobility model.

From Fig. 3.3, we can derive the equations for S_{n-1}, Z_{n-1}, and Ψ_{n-1} as

$$S_{n-1} = \sum_{i=1}^{n-1} R_i, \tag{3.9}$$

$$Z_{n-1} = \sqrt{\left(\sum_{i=1}^{n-1} R_i \cos(\Theta_i)\right)^2 + \left(\sum_{i=1}^{n-1} R_i \sin(\Theta_i)\right)^2}, \tag{3.10}$$

$$\Psi_{n-1} = \tan^{-1}\left(\frac{\sum_{i=1}^{n-1} R_i \sin(\Theta_i)}{\sum_{i=1}^{n-1} R_i \cos(\Theta_i)}\right). \tag{3.11}$$

In the next lemma, we derive the distribution of Ψ_n.

Lemma 3.16. *When interfering DBSs move based on the RW mobility model, then irrespective of the flight distribution R, the random variable Ψ_n is distributed uniformly in $[0, 2\pi)$.*

Proof. See Appendix B.3. □

Using the same methodology as in the proof of Lemma 3.16, one can also find the distribution of Z_n. However, it turns out that the $(n-1)$-fold integral that arises in the derivation of the pdf of Z_n does not have a closed-form solution in general. Nevertheless, when the flights are i.i.d. Rayleigh random variables, we can derive the distribution of Z_n in closed form.

Lemma 3.17. *When interfering DBSs move based on the RW mobility model and the flights are Rayleigh distributed with parameter σ, then Z_n is also Rayleigh distributed with parameter $\sigma\sqrt{n}$.*

Proof. See Appendix B.4. □

Lemma 3.17 establishes a useful result for the distribution of Z_n when the flights are Rayleigh distributed. On the other hand, if the flights have a general non-Rayleigh distribution, we can find an asymptotic distribution for Z_n as $n \to \infty$. We present this result in the next lemma.

Lemma 3.18. *When interfering DBSs move based on the RW mobility model and the flights have general non-Rayleigh but i.i.d. distributions with a mean and variance of μ_R and σ_R^2, respectively, then $\frac{Z_n}{\sqrt{n}}$ will have a Rayleigh distribution with parameter $\sqrt{\frac{\mu_R^2+\sigma_R^2}{2}}$ as $n \to \infty$.*

Proof. Define $X = \sum_{i=1}^{n} \frac{1}{\sqrt{n}} R_i \cos(\Theta_i)$ and $Y = \sum_{i=1}^{n} \frac{1}{\sqrt{n}} R_i \sin(\Theta_i)$. Since Θ_i's are i.i.d. with uniform distribution in $[0, 2\pi)$, the central limit theorem (CLT) asserts that as $n \to \infty$, X and Y will have Gaussian distributions. Since R_i and Θ_i are independent of each other, the moments of X can be computed as follows: $\mathbb{E}[X] = \sum_{i=1}^{n} \frac{1}{\sqrt{n}} \mathbb{E}[R_i]\mathbb{E}[\cos(\Theta_i)] = 0$ and $\mathbb{E}[X^2] = \mathbb{E}\left[\sum_{i=1}^{n}\sum_{j=1}^{n} \frac{1}{n} R_i R_j \cos(\Theta_i)\cos(\Theta_j)\right] = \mathbb{E}\left[\sum_{i=1}^{n} \frac{1}{n} R_i^2 \cos^2(\Theta_i)\right] = \frac{\mu_R^2+\sigma_R^2}{2}$. Note that the same is also true for Y. Hence, $X \sim \mathcal{N}(0, \frac{\mu_R^2+\sigma_R^2}{2})$ and $Y \sim \mathcal{N}(0, \frac{\mu_R^2+\sigma_R^2}{2})$. Now since $\mathbb{E}[XY] = 0$, X and Y are uncorrelated, and thus, independent. Therefore, $\frac{Z_n}{\sqrt{n}} = \sqrt{X^2+Y^2}$ is Rayleigh distributed with parameter $\sqrt{\frac{\mu_R^2+\sigma_R^2}{2}}$ as $n \to \infty$. This completes the proof. □

After characterizing Z_n and Ψ_n, we need to find the distribution of S_n as well. Recall that S_n is the sum of n i.i.d. random variables and for a general distribution of R_i, the distribution of S_n is not known. There have been some works that establish the distribution of S_n for different distributions of R_i (see [120] for a comprehensive review). When R_i's are exponentially distributed, the distribution of S_n is known to be Erlang. However, the exact distribution of Z_n is not known for exponentially distributed flights. When R_i's are Rayleigh, the distribution of S_n has been investigated in the literature [121] and the result is given here without proof.

Lemma 3.19. *The pdf of the sum of n i.i.d. Rayleigh random variables with parameter σ can be approximated as*

$$f_{S_n}(s) \approx \frac{(\frac{s}{\sqrt{n}})^{2n-1} \mathrm{e}^{-\frac{s^2}{2nb}}}{2^{n-1} b^n (n-1)!} - \frac{(\frac{s}{\sqrt{n}} - a_2)^{2n-2} \mathrm{e}^{-\frac{a_1(\frac{s}{\sqrt{n}}-a_2)^2}{2b}}}{2^{n-1} b (\frac{b}{a_1})^n (n-1)!} \times a_0 \left[b(2s\sqrt{n} - a_2) - a_1 \frac{s}{\sqrt{n}} (\frac{s}{\sqrt{n}} - a_2)^2 \right], \tag{3.12}$$

where $b = \sigma^2 \frac{\sqrt[n]{(2n-1)!!}}{n}$ and the constants a_0, a_1, and a_2 are derived numerically using a nonlinear curve-fitting least square method based on the trust region reflective algorithm [122].

In order to better understand the distributional properties of the RW mobility model, we also need to find the joint distribution of S_n and Z_n for a given number of flights n. Given S_n, the range of the values for Z_n is upper bounded by the value of S_n, which suggests a dependency between S_n and Z_n. In the next proposition, we characterize this joint distribution.

Proposition 3.20. *The joint pdf of S_n and Z_n for a given number of flights $n \geq 2$ can be written as a $2(n-1)$-fold integral given as*

$$f_{S_n,Z_n}(s,z) = \frac{4z}{(2\pi)^n} \int \cdots \int_{\mathcal{R}} \frac{f_R(s-J_n) \prod_{i=1}^{n-1} f_R(x_i)}{\sqrt{(z^2-(s-J_n-K_n)^2)\,((s-J_n+K_n)^2-z^2)}} \, \mathrm{d}\boldsymbol{x} \, \mathrm{d}\boldsymbol{\xi}, \quad (3.13)$$

where $J_n = \sum_{i=1}^{n-1} x_i$, $K_n = \sqrt{\sum_{i,j=1}^{n-1} x_i x_j \cos(\xi_i - \xi_j)}$, and $\mathcal{R}$ is defined as the region where $0 \leq x_i < \infty$, $0 \leq \xi_i < 2\pi$ for $1 \leq i \leq n-1$, and $|s - J_n - K_n| \leq z \leq s - J_n + K_n$.

Proof. See Appendix B.5. □

Note that for $n = 1$, the random variables S_n and Z_n will become identical and equal to R_1, and thus, their joint distribution will be the same as the distribution of R_1, i.e., $f_R(.)$. For $n = 2$, the result of Proposition 3.20 can be further simplified, which is given in the next corollary.

Corollary 3.21. *The joint pdf between S_2 and Z_2 can be written as*

$$f_{S_2,Z_2}(s,z) = \frac{2z}{\pi\sqrt{s^2-z^2}} \int_{\frac{s-z}{2}}^{\frac{s+z}{2}} \frac{f_R(x) f_R(s-x)}{\sqrt{z^2-(2x-s)^2}} \, \mathrm{d}x, \quad (3.14)$$

for $s > z$ and zero otherwise.

Remark 3.22. As n gets larger, the dependency between S_n and Z_n will become less significant, and thus, we can ignore it for large enough n. Hence, we approximate the joint pdf of S_n and Z_n by assuming them to be independent for $n \geq 3$, thus giving $f_{S_n,Z_n}(s,z) \approx f_{S_n}(s) f_{Z_n}(z)$. Note that $n \geq 3$ is large enough for this result to be reasonably accurate.

Using the results that we have derived for the RW mobility model so far, we can now compute the distribution of $L(t)$, i.e., the distance between the location of a DBS at time t and its original location at time $t = 0$. Fig. 3.3 shows a DBS that is flying in its n-th flight. Note that the distance traveled by the DBS until time t is vt, and thus, the residual distance in the n-th flight will be $vt - S_{n-1}$. We now state the main result in the next proposition.

Proposition 3.23. *When interfering DBSs move based on the RW mobility model, the cdf and pdf of $L(t)$ are given as (3.15) and (3.16) below, respectively, for $l \leq vt$. Otherwise, we*

have $F_L(l;t) = 1$ *and* $f_L(l;t) = 0$.

$$\begin{aligned} F_L(l;t) &= (1 - F_R(vt))\mathbf{1}(l - vt) \\ &\quad + \sum_{n=2}^{\infty} \int_{vt-l}^{vt} \int_{0}^{l-(vt-s)} f_{S_{n-1},Z_{n-1}}(s,z)(1 - F_R(vt-s))\,\mathrm{d}z\,\mathrm{d}s \\ &\quad + \sum_{n=2}^{\infty} \int_{\frac{vt-l}{2}}^{vt} \int_{|l-(vt-s)|}^{\min\{s,\, l+(vt-s)\}} f_{S_{n-1},Z_{n-1}}(s,z)(1 - F_R(vt-s)) \\ &\quad \times \frac{1}{\pi} \cos^{-1}\left(\frac{z^2 + (vt-s)^2 - l^2}{2z(vt-s)}\right) \mathrm{d}z\,\mathrm{d}s, \end{aligned} \tag{3.15}$$

$$\begin{aligned} f_L(l;t) &= (1 - F_R(vt))\delta(l - vt) \\ &\quad + \frac{2l}{\pi} \sum_{n=2}^{\infty} \int_{\frac{vt-l}{2}}^{vt} \int_{|l-(vt-s)|}^{\min\{s,\, l+(vt-s)\}} \frac{f_{S_{n-1},Z_{n-1}}(s,z)(1 - F_R(vt-s))}{\sqrt{[l^2 - (z-(vt-s))^2]\,[(z+(vt-s))^2 - l^2]}}\,\mathrm{d}z\,\mathrm{d}s, \end{aligned} \tag{3.16}$$

Proof. See Appendix B.6. □

For $n = 2$, the double integrals in (3.15) and (3.16) can be written as single integrals since $S_1 = Z_1 = R_1$. Mathematically speaking, for $l < vt$ we have

$$F_L(l;t|n=2) = \int_{\frac{vt-l}{2}}^{\frac{vt+l}{2}} f_R(r)(1 - F_R(vt-r)) \frac{1}{\pi} \cos^{-1}\left(\frac{r^2 + (vt-r)^2 - l^2}{2r(vt-r)}\right) \mathrm{d}r, \tag{3.17}$$

$$f_L(l;t|n=2) = \frac{2l}{\pi\sqrt{v^2t^2 - l^2}} \int_{\frac{vt-l}{2}}^{\frac{vt+l}{2}} \frac{f_R(r)(1 - F_R(vt-r))}{\sqrt{l^2 - (2r - vt)^2}}\,\mathrm{d}r. \tag{3.18}$$

This result will be useful for our further approximations on the distribution of $L(t)$. Applying the results of Proposition 3.23 to Lemma 3.9, we can compute $\beta(t, u_{\mathbf{x}}, u_0)$ in (3.5) and get the density of the network of interfering DBSs for the RW mobility model.

Building on the RW mobility model, we now derive the distribution of $L(t)$ for the RWP mobility model as well. The RWP mobility model is defined by a sequence of quadruples at the i-th flight period: two waypoints $\mathbf{p}_{i-1}$ and $\mathbf{p}_i$ as the starting and destination waypoints, respectively, one transition length R_i, and one waiting time T_i at the destination waypoint. In an infinite network, we can observe that the only difference between the RWP and the RW mobility models is the inclusion of the random variable T_i as the waiting time at the end of each flight. Assuming that the random variables $\{T_i\}$ are i.i.d. with cdf and pdf of $F_T(.)$ and $f_T(.)$, respectively, and also independent of R_i, the following proposition extends the results of Proposition 3.23 to the RWP mobility model. Before stating the main result, we define W_n as the aggregate waiting time until the end of the n-th flight, i.e., $W_n = \sum_{i=0}^{n} T_i$. Note that W_n will be independent of S_n and Z_n. Moreover, we assume that $W_0 = T_0 \neq 0$, which implies that there is an initial random waiting time before the DBSs start to move.

Proposition 3.24. *When interfering DBSs move based on the RWP mobility model, the cdf and pdf of $L(t)$ are given as (3.19) and (3.20) below, respectively, for $l \leq vt$. Otherwise, we have $F_L(l;t) = 1$ and $f_L(l;t) = 0$.*

$$\begin{aligned}
F_L(l;t) = &\int_{t-\frac{l}{v}}^{\infty} \left(1 - F_R(vt - vw)\right) f_T(w)\,\mathrm{d}w \\
&+ \sum_{n=2}^{\infty} \int_0^{vt} \int_0^{\min\{s,l\}} f_{S_{n-1},Z_{n-1}}(s,z) \left(F_{W_{n-2}}(t - \frac{s}{v}) - F_{W_{n-1}}(t - \frac{s}{v})\right) \mathrm{d}z\,\mathrm{d}s \\
&+ \sum_{n=2}^{\infty} \int_{vt-l}^{vt} \int_0^{l-(vt-y)} \int_0^{\frac{y}{v}} f_{W_{n-1}}(w) f_{S_{n-1},Z_{n-1}}(y - vw, z)(1 - F_R(vt - y))\,\mathrm{d}w\,\mathrm{d}z\,\mathrm{d}y \\
&+ \sum_{n=2}^{\infty} \int_{\frac{vt-l}{2}}^{vt} \int_{|l-(vt-y)|}^{\min\{y,\, l+(vt-y)\}} \int_0^{\frac{y}{v}} f_{W_{n-1}}(w) f_{S_{n-1},Z_{n-1}}(y - vw, z)(1 - F_R(vt - y)) \\
&\quad \times \frac{1}{\pi} \cos^{-1}\left(\frac{z^2 + (vt-y)^2 - l^2}{2z(vt-y)}\right) \mathrm{d}w\,\mathrm{d}z\,\mathrm{d}y, \qquad (3.19)
\end{aligned}$$

$$\begin{aligned}
f_L(l;t) = &\frac{1}{v}\left(1 - F_R(l)\right) f_T\left(t - \frac{l}{v}\right) \\
&+ \sum_{n=2}^{\infty} \int_l^{vt} f_{S_{n-1},Z_{n-1}}(s,l) \left(F_{W_{n-2}}(t - \frac{s}{v}) - F_{W_{n-1}}(t - \frac{s}{v})\right) \mathrm{d}s \\
&+ \frac{2l}{\pi} \sum_{n=2}^{\infty} \int_{\frac{vt-l}{2}}^{vt} \int_{|l-(vt-y)|}^{\min\{y,\, l+(vt-y)\}} \int_0^{\frac{y}{v}} f_{W_{n-1}}(w) f_{S_{n-1},Z_{n-1}}(y - vw, z)(1 - F_R(vt - y)) \\
&\quad \times \frac{1}{\sqrt{\left[l^2 - (z - (vt-y))^2\right]\left[(z + (vt-y))^2 - l^2\right]}}\,\mathrm{d}w\,\mathrm{d}z\,\mathrm{d}y, \qquad (3.20)
\end{aligned}$$

Proof. See Appendix B.7. □

As in the RW mobility model, the results can be further simplified for $n = 2$ and $l < vt$ as

$$\begin{aligned}
F_L(l;t|n=2) = &\int_0^{l} f_R(r) \left(F_T(t - \frac{r}{v}) - F_{W_1}(t - \frac{r}{v})\right) \mathrm{d}r \\
&+ \int_{t-\frac{l}{v}}^{t} \int_0^{vt-vw} f_R(r) f_{W_1}(w)(1 - F_R(vt - vw - r))\,\mathrm{d}r\,\mathrm{d}w \\
&+ \int_0^{t-\frac{l}{v}} \int_{\frac{vt-vw-l}{2}}^{\frac{vt-vw+l}{2}} f_R(r) f_{W_1}(w)(1 - F_R(vt - vw - r)) \\
&\quad \times \frac{1}{\pi} \cos^{-1}\left(\frac{r^2 + (vt - vw - r)^2 - l^2}{2r(vt - vw - r)}\right) \mathrm{d}r\,\mathrm{d}w, \qquad (3.21)
\end{aligned}$$

$$f_L(l;t|n=2) = f_R(l)\left(F_T(t-\frac{l}{v}) - F_{W_1}(t-\frac{l}{v})\right) + \frac{2l}{\pi}\int_0^{t-\frac{l}{v}}\int_{\frac{vt-vw-l}{2}}^{\frac{vt-vw+l}{2}} \frac{f_R(r)f_{W_1}(w)(1-F_R(vt-vw-r))}{\sqrt{[(vt-vw)^2-l^2]\,[l^2-(2r-(vt-vw))^2]}}\,\mathrm{d}r\,\mathrm{d}w. \tag{3.22}$$

Similar to the RW scenario, we can apply the distribution of $L(t)$ derived in Proposition 3.24 to Lemma 3.9 and compute the density of the network of interferers for the RWP mobility model.

3.5 Average and Session Rates

In this section, we compute the SIR-based metrics defined in Section 3.2.4 for the typical UE in the network. Equipped with the density of the network of interfering DBSs for each mobility model under both the UIM and the UDM, we first derive the average received rate by the typical UE in the UDM. The following theorem provides this result.

Theorem 3.25. *In the UDM and using any i.i.d. mobility model described in the previous sections, the average received rate by the typical UE at time t is given as*

$$R(t) = \int_0^\infty\int_0^\infty \frac{2\pi\lambda_0 u_0 \mathrm{e}^{-\pi\lambda_0 u_0^2}}{1+\gamma} \times \sum_{k=0}^{m_0-1}\frac{(-s)^k}{k!}\frac{\partial^k}{\partial s^k}\mathcal{L}_{I(t)}(s|\mathbf{x}_0(t))\Big|_{s=m_0\gamma r_0^\alpha(t)}\mathrm{d}u_0\,\mathrm{d}\gamma, \tag{3.23}$$

where $\mathcal{L}_{I(t)}(s|\mathbf{x}_0(t))$ is the conditional Laplace transform of interference given as

$$\mathcal{L}_{I(t)}(s|\mathbf{x}_0(t)) = \exp\left[-2\pi\int_0^\infty u_{\mathbf{x}}(t)\lambda(t;u_{\mathbf{x}},u_0)\Big(1-\big(1+\frac{s\,(u_{\mathbf{x}}^2(t)+h^2)^{-\alpha/2}}{m}\big)^{-m}\Big)\mathrm{d}u_{\mathbf{x}}(t)\right]. \tag{3.24}$$

Proof. We start by writing the complementary cumulative distribution function (ccdf) of $\mathrm{SIR}(t)$ conditioned on $\mathbf{x}_0(t)$ as

$$\begin{aligned}\mathbb{P}\left[\mathrm{SIR}(t)\geq\gamma\big|\mathbf{x}_0(t)\right] &= \mathbb{E}\left[\mathbb{P}\left[h_0(t)\geq\gamma r_0^\alpha(t)I(t)|\mathbf{x}_0(t),I(t)\right]\right]\\ &\overset{(a)}{=}\mathbb{E}\left[\frac{\Gamma(m_0,m_0\gamma r_0^\alpha(t)I(t))}{\Gamma(m_0)}\Big|\mathbf{x}_0(t)\right]\\ &\overset{(b)}{=}\mathbb{E}\left[\sum_{k=0}^{m_0-1}\frac{(m_0\gamma r_0^\alpha(t)I(t))^k}{k!}\mathrm{e}^{-m_0\gamma r_0^\alpha(t)I(t)}\Big|\mathbf{x}_0(t)\right]\\ &= \sum_{k=0}^{m_0-1}\frac{(-s)^k}{k!}\frac{\partial^k}{\partial s^k}\mathcal{L}_{I(t)}(s|\mathbf{x}_0(t))\Big|_{s=m_0\gamma r_0^\alpha(t)},\end{aligned}$$

where in (a) the Nakagami-m fading assumption is used and in (b) we used the definition of the incomplete gamma function for integer values of m_0. The conditional Laplace transform of interference at time t can be computed as

$$\begin{aligned}\mathcal{L}_{I(t)}(s|\mathbf{x}_0(t)) &= \mathbb{E}\left[\mathrm{e}^{-sI(t)}\middle|\mathbf{x}_0(t)\right] \\ &= \mathbb{E}\left[\exp\left[-s\sum_{\mathbf{x}(t)\in\Phi'_{\mathrm{D}}(t)} h_{\mathbf{x}}(t) r_{\mathbf{x}}(t)^{-\alpha}\right]\middle| u_0(t)\right] \\ &\overset{(a)}{=} \mathbb{E}\left[\prod_{\mathbf{x}(t)\in\Phi'_{\mathrm{D}}(t)} \left(1+\frac{s r_{\mathbf{x}}(t)^{-\alpha}}{m}\right)^{-m}\middle| u_0(t)\right] \\ &\overset{(b)}{=} \exp\left[-2\pi\int_0^\infty u_{\mathbf{x}}(t)\lambda(t;u_{\mathbf{x}},u_0)\left(1-\left(1+\frac{s r_{\mathbf{x}}(t)^{-\alpha}}{m}\right)^{-m}\right)\mathrm{d}u_{\mathbf{x}}(t)\right],\end{aligned}$$

where (a) results from the moment generating function (mgf) of the gamma distribution and (b) follows from the probability generating functional (pgfl) of a general PPP. Now, the average rate at time t can be written as

$$\begin{aligned}R(t) &= \mathbb{E}\left[\log\left(1+\mathrm{SIR}(t)\right)\right] \\ &= \int_0^\infty \log(1+\gamma) f_\Gamma(\gamma;t)\,\mathrm{d}\gamma \\ &= \int_0^\infty\int_0^\infty \frac{2\pi\lambda_0 u_0 \mathrm{e}^{-\pi\lambda_0 u_0^2}}{1+\gamma}\mathbb{P}\left[\mathrm{SIR}(t)\geq\gamma\middle|\mathbf{x}_0(t)\right]\mathrm{d}u_0\,\mathrm{d}\gamma,\end{aligned}$$

where $f_\Gamma(\gamma;t)$ is the pdf of $\mathrm{SIR}(t)$ and in the last equation, we used integration by parts and deconditioned the result on $u_0(t)$. Note that in the UDM, we have $u_0(t)=[u_0-vt]^+$, where $[x]^+=x$ if $x\geq 0$ and $[x]^+=0$ otherwise. This completes the proof. □

For the UIM, since the density of the network of interfering DBSs is given in (3.3), the received rate by the typical UE will be given as in (3.23) evaluated at $t=0$. Finally, the session rate at time T is derived by integrating over the average rate w.r.t. t as in (3.2).

3.6 Simulation Results

In this section, we provide numerical simulations to verify our analytical results and provide several useful insights about the system-level performance of the network. We assume that the network density is $\lambda_0 = 1$ DBS/km^2 and DBSs move with a constant speed $v = 45$ km/h using one of the four mobility models defined in Section 3.2. We consider the low altitude platform (LAP) for the flight of DBSs and assume $h \in \{100, 200\}$ m as typical values for the height of drones in the LAP. Furthermore, we assume the path loss exponent is $\alpha = 3$. For

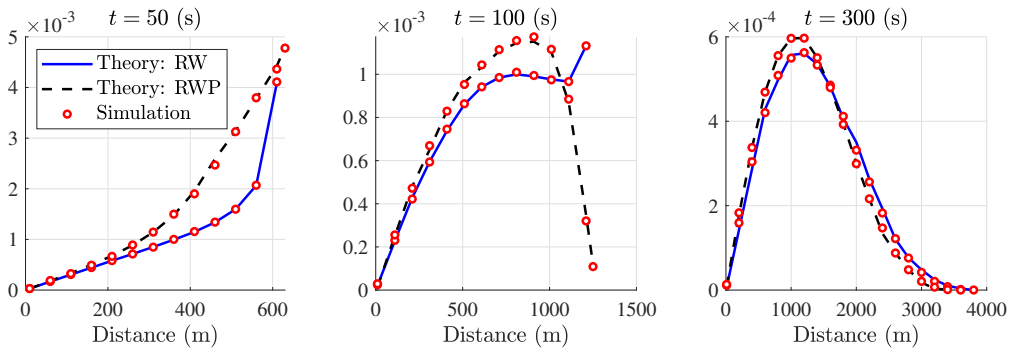

Figure 3.4: Distribution of $L(t)$ in the RW and RWP mobility models for $t \in \{50, 100, 300\}$ s. As t increases, the pdf of $L(t)$ in both the RW and RWP models converges to the Rayleigh distribution.

the RS, RW, and RWP mobility models, we assume that the flight distances are distributed as i.i.d. Rayleigh random variables with mean 500 m. Moreover, in the RWP mobility model, we assume the hovering times follow i.i.d. exponential random variables with mean 5 s. Note that the evaluations of the multiple integrals that occur in the analyses of the RW and RWP mobility models are carried out using the Monte Carlo (MC) integration method.

3.6.1 Distribution of $L(t)$ in RW and RWP

Characterizing the distribution of $L(t)$ for a given time t is essential for the analysis of the RW and RWP mobility models. We derived the exact cdf and pdf of $L(t)$ for the RW and RWP mobility models in Propositions 3.23 and 3.24, respectively. Fig. 3.4 shows the pdf of $L(t)$ for both the RW and RWP mobility models at $t \in \{50, 100, 300\}$ s. Note that as $t \to \infty$, the distance traveled during the n-th flight will be much smaller than Z_{n-1}, and thus, we have $L(t) \approx Z_{n-1}$. Now, according to Lemma 3.18, as $t \to \infty$, the distribution of Z_{n-1} converges to a Rayleigh distribution. Hence, $L(t)$ is also Rayleigh distributed as $t \to \infty$. This trend can also be noticed in Fig. 3.4.

3.6.2 Point Process of Interferers

In Figs. 3.5 and 3.6, we plot the density of the network of interfering DBSs for all the mobility models considered in this chapter at $t \in \{20, 40, 50, 200\}$ s. We assume that the serving DBS follows the UDM and the exclusion zone radius is $u_0 = 500$ m. In the SL mobility model, as also highlighted in Remark 3.12, the density will be divided into two homogeneous parts and one bowl-shaped inhomogeneous part after $t = \frac{u_0}{v}$. Furthermore, the inhomogeneous part will become homogeneous as $t \to \infty$, which ultimately makes the point process of interferers homogeneous. This fact can also be directly inferred from Corollary 3.11 by taking the limit

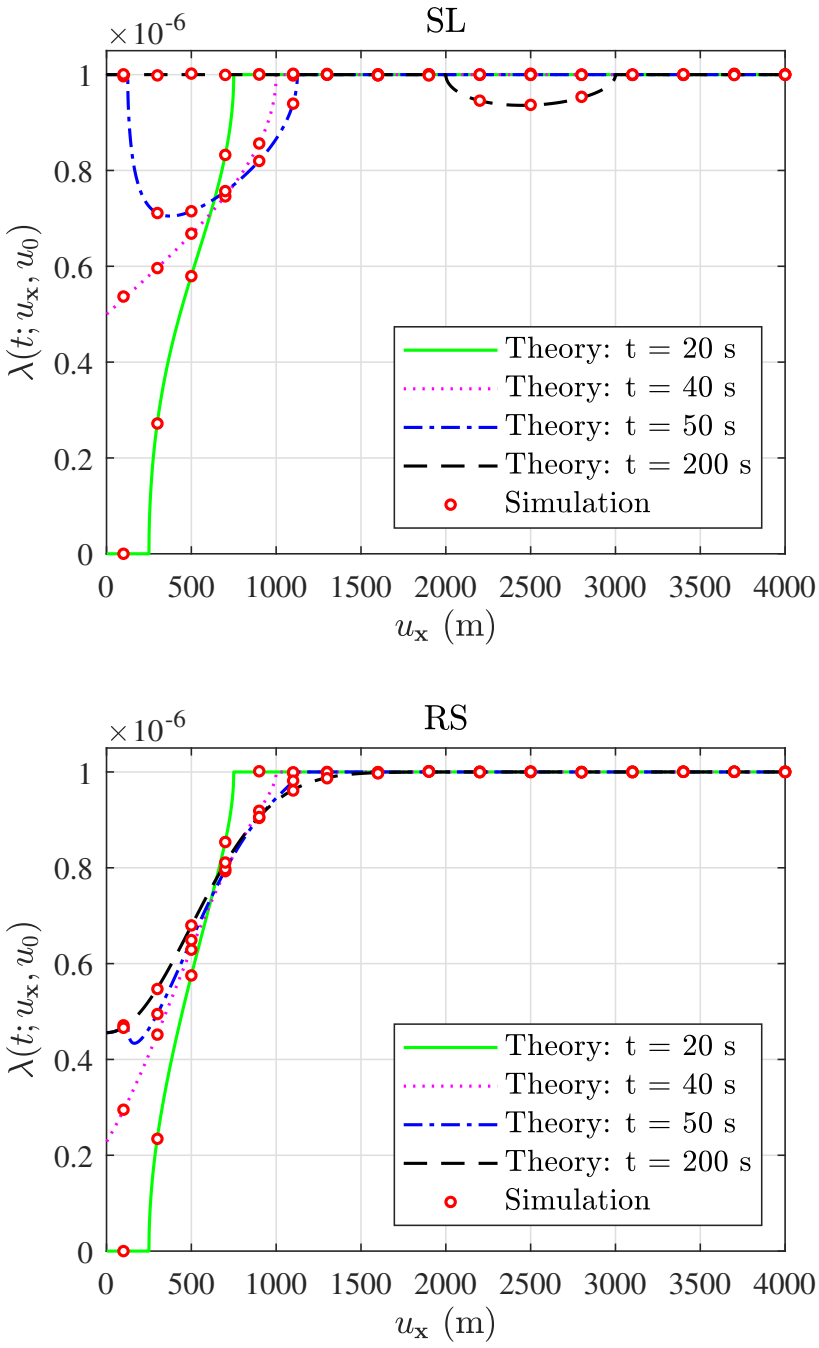

Figure 3.5: Density of the network of interfering DBSs for the UDM with the SL and RS mobility models. Serving distance is $u_0 = 500$ m and the density is given at $t \in \{20, 40, 50, 200\}$ s.

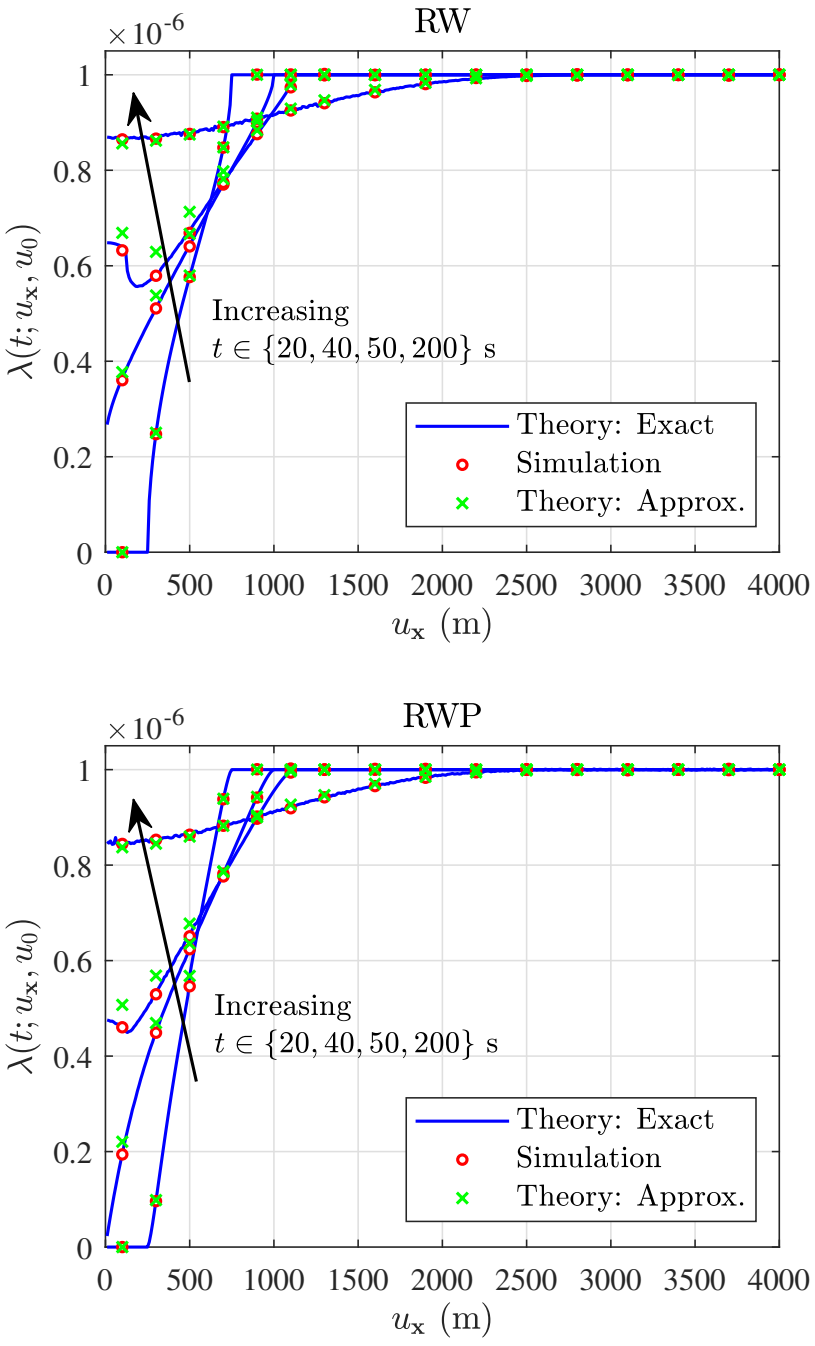

Figure 3.6: Density of the network of interfering DBSs for the UDM with the RW and RWP mobility models. Serving distance is $u_0 = 500$ m and the flights are Rayleigh distributed with mean 500 m.

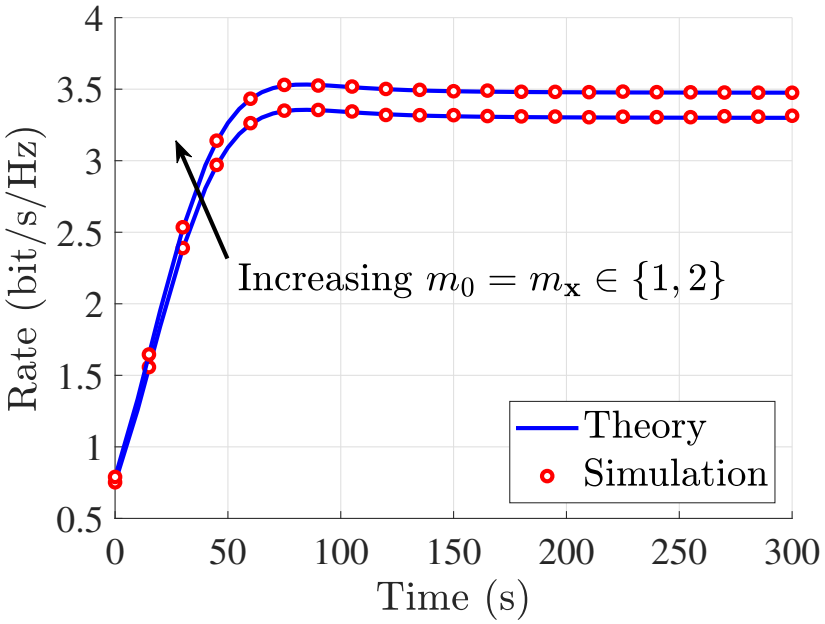

Figure 3.7: Comparison of the average rate for the UDM with the SL mobility model for different Nakagami-m parameters with $\alpha = 3$ and $h = 100$ m.

of (3.6) as $t \to \infty$ and $u_{\mathbf{x}} \to vt$. According to Fig. 3.6, this homogenization happens for the RW and RWP mobility models as well. However, this is not the case in the RS mobility model, since the DBSs "stop" moving after a period of time. Hence, the point process of interferers does not evolve with time, making it inhomogeneous for all time t. In Fig. 3.6, based on Remark 3.22, we also plot the density of the network of interfering DBSs for the RW and RWP mobility models by assuming that S_n and Z_n are independent for $n \geq 3$. Clearly, this approximation is fairly accurate.

3.6.3 Impact of Fading and Height

In order to show the effect of the Nakagami-m fading parameter on the performance of the network, we plot the average rate in the UDM under the SL mobility model for $m_0 = m_{\mathbf{x}} \in \{1, 2\}$ in Fig. 3.7. Since increasing m_0 and $m_{\mathbf{x}}$ decreases the severity of the fading, the average rate will increase as well. Fig. 3.8 depicts the impact of DBS heights on the performance of the network for both service models under the SL mobility model. As is clear in this figure, the average rate increases as height decreases, which can also be observed directly from (3.23) and (3.24).

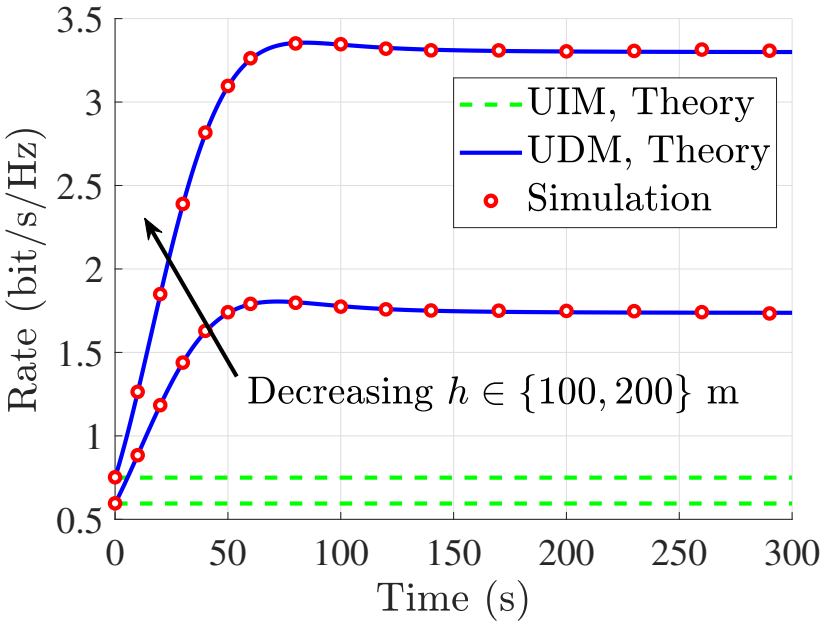

Figure 3.8: Comparison of the average rate for both the UIM and the UDM with the SL mobility model at different heights with $\alpha = 3$ and $m_0 = m_{\mathbf{x}} = 1$.

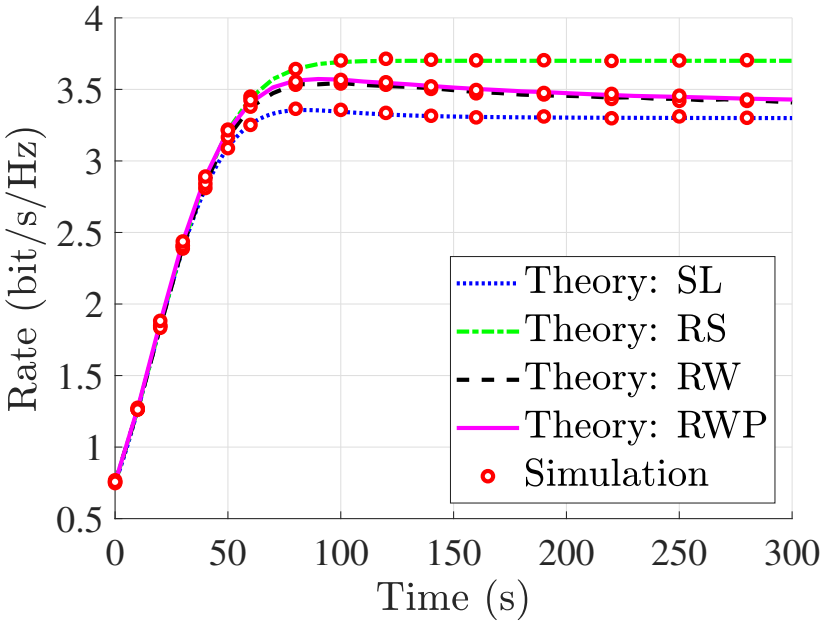

Figure 3.9: Comparison of the average rate for the UDM with different mobility models. Other parameters are $\alpha = 3$, $h = 100$ m, and $m_0 = m_{\mathbf{x}} = 1$.

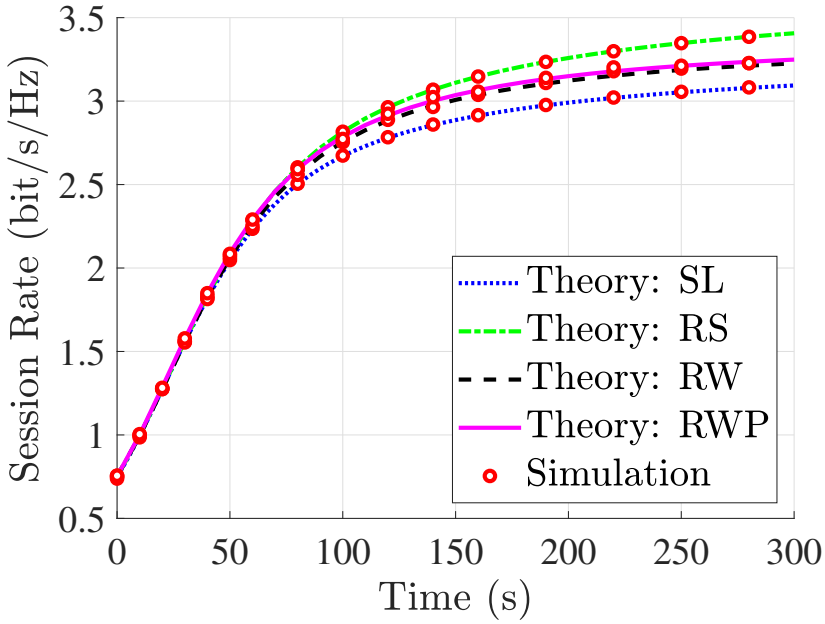

Figure 3.10: Comparison of the session rate for the UDM with different mobility models. Other parameters are $\alpha = 3$, $h = 100$ m, and $m_0 = m_{\mathbf{x}} = 1$.

3.6.4 Impact of Mobility Models

Under the UDM, we compare different mobility models studied in this chapter in terms of the average and session rates in Figs. 3.9 and 3.10, respectively. As can be seen in these figures, the SL mobility model acts as a lower bound on the performance of these models. This result is essentially the one that we proved in Theorem 3.13 by demonstrating that the average number of interferers in the vicinity of the typical UE is higher in the SL mobility model than the other i.i.d. mobility models. Hence, the performance of the network under the SL mobility model will be worse than the other mobility models. In Table 3.1, we provide a brief comparison between the four mobility models studied in this chapter.

Table 3.1: A comparison between different mobility models.

Model	Advantage	Disadvantage
SL	tractable and closed-form solutions	simplistic for some applications
RS	captures limited battery capacity of drones	DBSs do not change their locations after stopping in order to serve other UEs
RW/RWP	more general	less tractable

3.7 Chapter Summary

In this chapter, we presented an in-depth and unified analysis of a mobile drone cellular network operating at a constant height to serve the UEs on the ground. Specifically, we considered four mobility models for the DBSs, i.e., (i) SL, (ii) RS, (iii) RW, and (iv) RWP, and provided several fundamental distributional properties of these models. The use of the SL mobility model for drone networks was inspired by the simulation models used in the 3GPP studies of drone networks, while the others are useful canonical models (or their variants) that have been used extensively in wireless networks and provide a reasonable balance between realism and tractability. The serving DBS is selected based on the nearest-neighbor association policy and moves according to two service models: (i) based on the same mobility model as the interfering DBSs (UIM), and (ii) towards the typical UE at a constant height and keeps hovering above the location of the typical UE (UDM). We proposed a novel characterization of the point process of DBSs for both the UIM and the UDM, using which we analyzed the average received rate and the session rate at the typical UE. Borrowing tools from the calculus of variations, we mathematically showed that the SL mobility model acts as a lower bound on the system-level performance of our mobile drone network over the space of all *i.i.d.* mobility models. To the best of our understanding, this is the first work that offers a unified analysis of canonical mobility models for a drone cellular network in an infinite plane and establishes meaningful connections between them. While this work offers many useful insights in the canonical settings, it will be useful to extend some of these results to more realistic mobility models, including the ones developed from actual mobility traces of drones (as and when they become available). Another direction of future research could be the use of advanced mathematical techniques, such as the stochastic differential equation and the Ornstein-Uhlenbeck process [123], to design more sophisticated drone trajectories. Furthermore, extending the results of this chapter to more general 3D models, such as multi-tier drone cellular networks [124], is a promising future work.

In the next chapter, we will study another important problem in mobile drone cellular networks, which is the occurrence of handover probability.

Chapter 4

Handover Probability in Drone Cellular Networks

4.1 Introduction

One of the key consequences of the mobility of DBSs is the occurrence of handovers, even if the UEs are static on the ground. Since handovers result in signaling overhead, it is highly desirable to carefully understand the handover behavior in this new operational regime. In addition, since handovers have traditionally been studied by assuming mobile UEs and static BSs, it is also natural to wonder whether there is some underlying connection between the statistics of the handovers observed in these two fundamentally different regimes. Inspired by such questions, we present a rigorous analysis of the handover probability in drone cellular networks using tools from stochastic geometry [19].

Prior Art. The handover probability is a well-investigated metric in terrestrial cellular networks with static BSs and mobile UEs [125, 126, 127, 128]. Modeling the locations of BSs as a 2D homogeneous PPP, the authors in [125] derived the probability of the occurrence of the first handover for a reference UE that moves at a constant speed along a straight line. The authors of [126] have also derived this result in the analysis of the joint coverage probability of cellular networks. In [127], the authors analyzed the horizontal and vertical handoff rates in multi-tier heterogeneous networks for arbitrary trajectories of UEs. While these works are useful for designing and optimizing terrestrial networks, they are not directly applicable to drone cellular networks due to the mobility of DBSs. Although several works in the literature were motivated by the mobility of DBSs [37, 39, 84, 85, 129], there have only been a few works that have accounted for handover in drone networks [130, 131]. The authors of [130] proposed an optimal coverage decision algorithm for seamless handover of a 3D drone network. Using the results of [127], the trade-off between average throughput and handover rate in a multi-tier network has been studied in [131]. While these works provide useful insights, the analytical characterization of handover probability in drone networks is still an open problem, which is the main focus of this chapter. More details of our contribution are provided next.

Contributions. We model the initial positions of the DBSs by a homogeneous 2D PPP and assume that they move based on the SL mobility model introduced in the previous chapter. Assuming that the typical UE is served by its closest DBS, we propose two scenarios for the

speed of DBSs, i.e., (i) SSM, where all DBSs move with the same speed, and (ii) DSM, where DBSs move with different speeds. We then analytically characterize the handover probability for both the SSM and the DSM. Specifically, in the SSM, we establish equivalence in the spatial distributions of the mobile DBSs as seen by a static ground UE and of the static terrestrial BSs as seen by a mobile UE. Using this equivalence, we rigorously show that the handover probability in the SSM is the same as that of a mobile UE in a single-tier cellular network studied in [125, 126]. In the DSM, we first characterize the point process of the non-serving DBSs as a function of time and then derive a lower bound on the handover probability. To the best of our knowledge, this is the first work that provides a concrete mathematical treatment of the handover probability in drone cellular networks.

4.2 System Model

We consider a network of mobile DBSs deployed at a constant height h that serves the UEs on the ground. We assume that the ground is aligned with the xy-plane of the Cartesian coordinate system and the DBSs are located in the $z = h$ plane, which will be referred to as the DBS plane in this chapter. We assume that DBSs are initially distributed as a homogeneous PPP $\Phi_{\mathrm{D}}(0)$ with density λ_0 in the DBS plane. UEs are distributed as an independent homogeneous PPP Φ_{U} on the ground. We denote the origin and its projection onto the DBS plane by $\mathbf{o} = (0, 0, 0)$ and $\mathbf{o}' = (0, 0, h)$, respectively. The analysis will be performed for a *typical* UE placed at $\mathbf{o}$. The distance of a DBS located at $\mathbf{x}(t) \in \Phi_{\mathrm{D}}(t)$ at time t from $\mathbf{o}'$ is denoted by $u_{\mathbf{x}}(t) = \|\mathbf{x}(t) - \mathbf{o}'\|$. Moreover, we denote the location of the closest DBS to the origin and its corresponding distance to $\mathbf{o}'$ at time t by $\mathbf{x}^*(t)$ and $u^*(t)$, respectively. For simplicity, we assume $u^* \triangleq u^*(0)$, and we drop t for $u_{\mathbf{x}}(t)$ whenever the time index can be understood from the context.

Following the SL mobility model described in Chapter 3, we assume that each DBS moves along a straight line and in a uniformly random direction, independently of the other DBSs, in the DBS plane. In this chapter, we consider two mobility scenarios for the DBSs, namely (i) SSM, where all DBSs have the same constant speed, and (ii) DSM, where DBSs have different constant speeds. Note that the SSM closely emulates the mobility model used by the 3GPP, where drones are initially placed at uniformly random locations at a constant height and then move in uniformly random directions along straight lines with the *same constant* speed [5, 84]. These simple enough random straight-line mobility scenarios can be regarded as benchmarks for evaluating more sophisticated models. We assume a nearest-neighbor association policy, in which at any time t, the closest DBS to the typical UE is assumed to be the serving DBS and all the other DBSs are regarded as non-serving DBSs. Furthermore, the point process of the non-serving DBSs is denoted by $\Phi'_{\mathrm{D}}(t) \equiv \Phi_{\mathrm{D}}(t) \backslash \mathbf{x}^*(t)$.

A handover is said to occur when the serving DBS of the typical UE changes. The event of

the occurrence of at least one handover until time t can be mathematically expressed as

$$H(t) := \left\{ \exists s < t : \arg\min_{i \in \mathbb{N}} \|\mathbf{x}_i(s)\| \neq \arg\min_{i \in \mathbb{N}} \|\mathbf{x}_i(t)\| \right\}, \tag{4.1}$$

where $i \in \mathbb{N}$ is an arbitrarily assigned index to each DBS. We now define the handover probability $\mathbb{P}[H(t)]$ at time t as the probability that the first handover occurs at or before time t.

4.3 Handover Probability

In this section, we derive the handover probability for both mobility scenarios. To do so, we need to first characterize the point process of the DBSs for both mobility scenarios at any time t. The following lemma is the direct consequence of *displacement theorem* for a PPP, and thus, we state it here without a proof [19].

Lemma 4.1. *Let Φ be a homogeneous PPP with density λ_0. If all the points of Φ are displaced independently of each other with identically distributed displacements, then the displaced points also form a homogeneous PPP with density λ_0.*

4.3.1 Handover Analysis in the SSM

We begin our analysis with the following lemma which is the consequence of having the same speed for all DBSs in the SSM.

Lemma 4.2. *In the SSM, let D_0 be the serving DBS at time $t = t_0$ and a handover occurs at time $t = t_1$, where $t_1 > t_0$, and D_1 becomes the serving DBS. Then, D_0 cannot become the serving DBS again at any time $t > t_1$.*

Proof. See Appendix C.1. □

Once a handover occurs, a DBS that was acting as the serving DBS will be regarded as a non-serving DBS. Lemma 4.2 states that this non-serving DBS cannot become the serving DBS again under the SSM. This fact is also in accordance with single-tier terrestrial cellular networks, where the BSs are static and a reference UE is moving with a constant speed along a straight line in a uniformly random direction. In terrestrial cellular networks, the coverage footprints are characterized by Voronoi cells when the nearest-neighbor association policy is used [79]. Hence, handover occurs when a mobile UE crosses the boundary of a Voronoi cell. Since the Voronoi cells in single-tier terrestrial cellular networks are convex polygons, a reference UE moving along a straight line enters a Voronoi cell only once. An interesting duality between the aerial and terrestrial setups mentioned above is established in the following theorem.

Theorem 4.3. *The handover probabilities of the following two networks are equivalent:*

1. **Terrestrial model**: *A network of static BSs distributed as a homogeneous PPP* Φ_{B} *with density* λ_0. *The reference UE moves along a straight line with speed* v.

2. **Aerial model**: *A network of mobile DBSs initially distributed as a homogeneous PPP* $\Phi_{\mathrm{D}}(0)$ *with density* λ_0, *in which DBSs follow the SSM with speed* v. *The typical UE is static.*

Proof. Let us assume that the reference UE in the terrestrial model moves in a direction $\theta \sim U[0, 2\pi)$ w.r.t. the positive x-axis along a straight line and denote its trajectory by $\mathbf{x}(t)$. Then, the point process of BSs w.r.t. the reference UE can be written as $\Phi_{\mathrm{B}} - \mathbf{x}(t)$. Now, observe that the performance of the reference UE in this terrestrial network is equivalent to that of a *static* typical UE in an aerial network where all the DBSs move along straight lines and in the *same* direction $\pi + \theta$. Denoting this point process by $\tilde{\Phi}_{\mathrm{D}}(t)$, we have $\tilde{\Phi}_{\mathrm{D}}(t) \equiv \Phi_{\mathrm{B}} - \mathbf{x}(t)$. Since Φ_{B} is a homogeneous PPP, it is translation invariant, which gives $\tilde{\Phi}_{\mathrm{D}}(t) \equiv \mathrm{PPP}(\lambda_0)$. Furthermore, Lemma 4.1 states that the DBS locations in our aerial model are distributed as a homogeneous PPP with density λ_0. Hence, as seen from the UE of interest at any time t, the BSs and DBSs in both terrestrial and aerial models follow a homogeneous PPP with density λ_0. Consequently, the two models are equivalent in distribution at any time t. Note that without loss of generality, one can define the handover event "completely" in the DBS plane, and thus, the effect of height is immaterial for the handover calculation.

Now, assume that the serving DBS in the aerial model is initially located at $\mathbf{x}^*(0)$ and moves to $\mathbf{x}^*(t)$ at time t. From Lemma 4.2 and the definition of the handover event in (4.1), we observe that a handover does not occur until time t in the SSM if there is no DBS in $b(\mathbf{o}', \mathbf{x}^*(t))$, where $b(\mathbf{o}, r)$ is a disc of radius r centered at $\mathbf{o}$. Since the probability of this event depends only on the characteristics of the point process of DBSs at time t (and not on its evolution over time), we conclude that the handover probability is the same for both the terrestrial and aerial models. □

From the duality established in Theorem 4.3, it is clear that the handover probability in the SSM is the same as that of a single-tier terrestrial cellular network. Although handover probability for single-tier terrestrial cellular networks has been derived in [125], it is not accurate and a correction has recently been proposed as a part of a tutorial on mobility-aware performance characterization of cellular networks in [110]. In what follows, we state this result and propose a slightly simpler proof.

Theorem 4.4. *In a single-tier terrestrial cellular network, let the BSs be distributed as* $\mathrm{PPP}(\lambda_0)$ *and consider a reference UE that moves along a straight line in a uniformly random direction at a constant speed* v. *Assuming a nearest-neighbor association policy, the handover*

probability as seen by the reference UE at time t can be written as

$$\mathbb{P}[H(t)] = 1 - \frac{1}{2\pi}\int_0^{\infty}\int_0^{2\pi} 2\pi\lambda_0 r \mathrm{e}^{-\lambda_0\left[r^2\left(\pi-\varphi_1+\frac{1}{2}\sin(2\varphi_1)\right)+R^2\left(\pi-\varphi_2+\frac{1}{2}\sin(2\varphi_2)\right)\right]}\,\mathrm{d}\theta\,\mathrm{d}r, \quad (4.2)$$

where $\varphi_1 = \cos^{-1}\left(\frac{v^2t^2+r^2-R^2}{2vtr}\right)$, $\varphi_2 = \cos^{-1}\left(\frac{v^2t^2+R^2-r^2}{2vtR}\right)$, *and* $R = \sqrt{r^2+v^2t^2-2rvt\cos(\theta)}$.

Proof. See Appendix C.2. □

Remark 4.5. To the best of our understanding, this is the first work that establishes the fact that the handover probability in a drone cellular network with mobile DBSs and static UEs is equivalent to that of a terrestrial network with static BSs and mobile UEs. From Theorems 4.3 and 4.4, we conclude that the handover probability for the SSM is as given in (4.2).

4.3.2 Handover Analysis in the DSM

In this subsection, we first characterize the point process of the non-serving DBSs in the DSM. From our construction, it is clear that $\Phi'_{\mathrm{D}}(0)$ is an inhomogeneous PPP with density

$$\lambda(u_{\mathbf{x}}, u^*) = \begin{cases} \lambda_0, & u_{\mathbf{x}} > u^* \\ 0, & u_{\mathbf{x}} \leq u^*, \end{cases} \quad (4.3)$$

Note that the nearest-neighbor association policy introduces an *exclusion zone*, $\mathcal{X} = b(\mathbf{o}', u^*)$, for the non-serving DBSs. Using displacement theorem, we argue that $\Phi'_{\mathrm{D}}(t)$ remains an inhomogeneous PPP and characterize its density in the following lemma.

Lemma 4.6. *In the DSM, let V be a non-negative random variable representing the speed of different DBSs, with the cdf and pdf of $F_V(v)$ and $f_V(v)$, respectively. Then $\Phi'_{\mathrm{D}}(t)$ will be an inhomogeneous PPP with density*

$$\lambda(t; u_{\mathbf{x}}, u^*) = \lambda_0\left[1 - F_V\left(\frac{u^*-u_{\mathbf{x}}}{t}\right) - \int_{\frac{|u^*-u_{\mathbf{x}}|}{t}}^{\frac{u^*+u_{\mathbf{x}}}{t}} f_V(v)\frac{1}{\pi}\cos^{-1}\left(\frac{v^2t^2+u_{\mathbf{x}}^2-u^{*2}}{2vtu_{\mathbf{x}}}\right)\mathrm{d}v\right]. \quad (4.4)$$

Proof. See Appendix C.3. □

It is clear from our setup that the locations of a DBS at two different times t_1 and t_2 are not independent of each other. Therefore, the motion of DBSs will be correlated in time, because of which the exact analysis of the handover probability in the DSM is quite hard. Hence, we provide a lower bound on the handover probability for the DSM using the marginal spatial distribution of non-serving DBSs in the following theorem.

Theorem 4.7. *In the DSM, the handover probability can be lower-bounded as*

$$\mathbb{P}[H(t)] \geq 1 - \frac{1}{2\pi} \int_0^\infty \int_0^\infty \int_0^{2\pi} 2\pi\lambda_0 u^* \mathrm{e}^{-\lambda_0 \pi u^{*2}} f_V(v)\, \mathrm{e}^{-\int_0^R 2\pi u_{\mathbf{x}} \lambda(t;u_{\mathbf{x}},u^*)\,\mathrm{d}u_{\mathbf{x}}}\, \mathrm{d}\theta\, \mathrm{d}u^*\, \mathrm{d}v, \quad (4.5)$$

where $R = \sqrt{u^{*2} + v^2t^2 - 2u^*vt\cos(\theta)}$ *and* $\lambda(t; u_{\mathbf{x}}, u^*)$ *is given by* (4.4).

Proof. See Appendix C.4. □

Note that the SSM is a special case of the DSM, and thus, we can also derive a lower bound on the handover probability in the SSM using Theorem 4.7. However, as shown in the next corollary, the lower bound given by (4.5) is exact for the SSM.

Corollary 4.8. *The handover probability in the SSM is given by*

$$\begin{aligned}\mathbb{P}[H(t)] = 1 &- \frac{1}{2\pi} \int_{vt}^\infty \int_0^{2\pi} 2\pi\lambda_0 u^* \mathrm{e}^{-\lambda_0\left[\pi u^{*2}+Q\right]}\, \mathrm{d}\theta\, \mathrm{d}u^* \\ &- \frac{1}{2\pi} \int_0^{vt} \int_0^{2\pi} 2\pi\lambda_0 u^* \mathrm{e}^{-\lambda_0\left[\pi u^{*2}+\pi(vt-u^*)^2+Q\right]}\, \mathrm{d}\theta\, \mathrm{d}u^*, \end{aligned} \quad (4.6)$$

where $Q = \int_{|vt-u^*|}^R 2\pi u_{\mathbf{x}} \frac{1}{\pi} \cos^{-1}\left(\frac{u^{*2}-u_{\mathbf{x}}^2-v^2t^2}{2u_{\mathbf{x}}vt}\right) \mathrm{d}u_{\mathbf{x}}$ *and* $R = \sqrt{u^{*2} + v^2t^2 - 2u^*vt\cos(\theta)}$.

Proof. See Appendix C.5. □

Note that although the integrands of (4.2) and (4.6) are different, the result of the integrals is the same for all t.

4.4 Simulation Results

In this section, we verify the accuracy of our exact results and the proposed lower bound using Monte Carlo simulations. We assume $\lambda_0 = 1$ DBS/km^2, $v = 45$ km/h, and that the speed in the DSM has Rayleigh or uniform distributions with mean v. In Fig. 4.1, we plot the density of non-serving DBSs for $t \in \{10, 20, 40, 100\}$ s and $u^* = 500$ m in the DSM using Lemma 4.6. Clearly, as $t \to \infty$, the point process of non-serving DBSs becomes homogeneous.

The handover probabilities for both the SSM and the DSM are shown in Fig. 4.2. As evident from this figure, at small values of time, the handover probability is almost the same for both the mobility scenarios and the derived lower bound is tight. As the network evolves with time, we observe that the handover probability in the DSM is smaller than that of the SSM. Note that since we have defined the handover probability in Section 4.2 as the probability of the occurrence of the first handover, this result does not necessarily mean that the *handover rate*, defined as the average number of handovers per unit time, in the DSM will be smaller than that of the SSM.

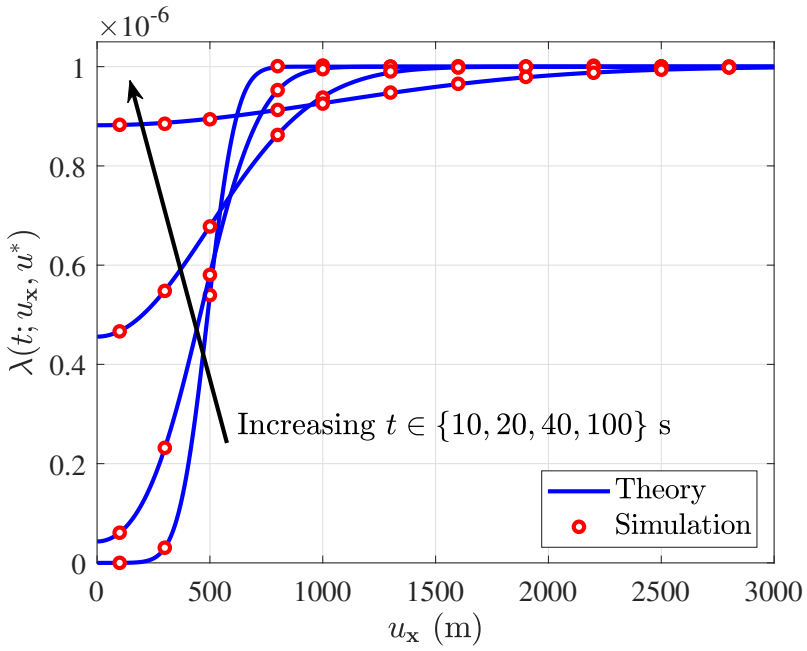

Figure 4.1: Density of non-serving DBSs for the DSM with Rayleigh distributed speed.

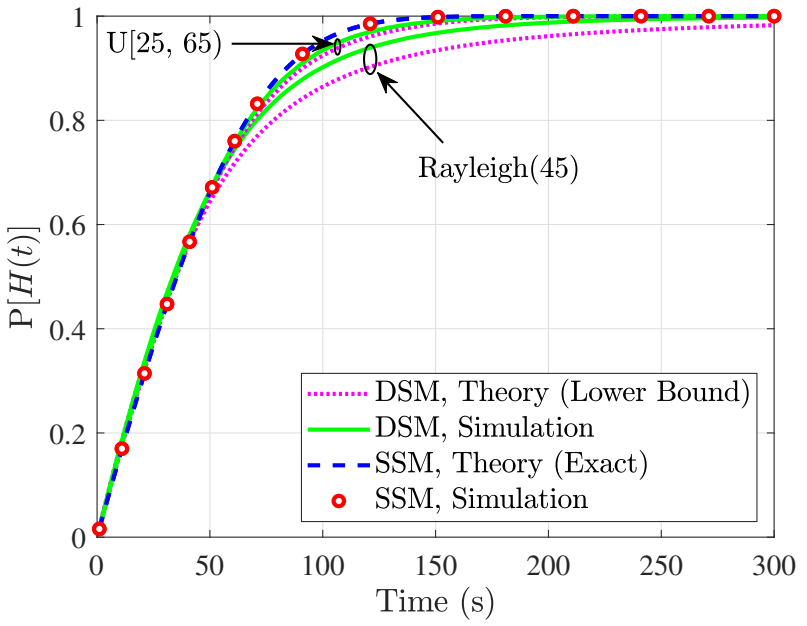

Figure 4.2: Handover probability for both mobility scenarios.

4.5 Chapter Summary

In this chapter, we provided a concrete mathematical treatment of the handover probability in drone cellular networks. Assuming that DBSs move along straight lines and in uniformly random directions, we considered two mobility scenarios for the DBSs: (i) SSM, where all DBSs move with the same speed, and (ii) DSM, where DBSs have different speeds. We then established a duality in terms of the handover probability between the SSM and a terrestrial network where all the BSs are static and a reference UE moves along a straight line. For the DSM, we characterized the point process of non-serving DBSs, using which we derived a lower bound for the handover probability of the network. A meaningful extension of this work could be to characterize the handover rate and other metrics directly affected by the mobility of DBSs. Another direction of research is to consider more sophisticated mobility models, e.g., where the DBSs follow a random waypoint mobility model [64] or a simple cyclical mobility pattern [129].

Up until now, we performed multiple system-level analyses regarding drone cellular networks. In the next two chapters, we will study the air-to-ground channel in more detail and explore the impact of various impairments on the channel.

Chapter 5

Impact of UAV Wobbling on the Air-to-Ground Wireless Channel

5.1 Introduction

After discussing several fundamental system design problems for both static and mobile setups in the previous chapters, we focus on a fundamental question that is specific to air-to-ground wireless links involving UAVs. Due to the lack of fixed and stable infrastructure and various environmental issues, such as bad weather conditions or wind gusts, UAVs may experience random wobbling (also termed fluctuations [44] and jittering [42, 43, 132] in the relevant literature) while hovering at a specific location [7]. Although this wobbling is typically small (less than 10° [41]), it could severely affect the quality of the wireless channel because of the large values of the carrier frequencies (any frequency of the order of or above 1 GHz can be considered "large" in the context of UAV wobbling). Quite remarkably, the impact of UAV wobbling on the properties of the air-to-ground wireless channel, such as its coherence time, has not been quantified yet in the literature, and is the main focus of this chapter.

Prior Art. There has been a lot of recent interest in the analysis and design of UAV-assisted communication networks [20, 64, 82, 83, 84, 85, 133]. However, only a handful of them considered the impact of random wobbling of UAVs on the performance of the UEs. In [44], the authors studied the transmitter-receiver antenna mismatch caused by the random wobbling of hovering UAVs in mmWave wireless communications. The problem of resource allocation in a drone cellular network when the UAVs are equipped with uniform linear antenna arrays and are also wobbling is studied in [132] and further extended to planar antenna arrays in [42]. In these works, the authors designed algorithms to minimize total power consumption in a MISO system by jointly optimizing the UAV trajectory and transmit beamforming vector. Taking UAV wobbling into account, the authors in [43] investigated a wiretap aerial system where the problem of secure and energy-efficient communication between a UAV and a ground UE is analyzed. In [46], the authors proposed a novel aerial network design of CoMP which benefits from both interference mitigation and UAV mobility [64, 83, 84, 85]. Specifically, they considered a Rician fading channel model where the LoS path has a random phase component due to the random UAV wobbling. Although these works address important problems related to UAV wobbling, its impact on the wireless communication

channel still remains an open problem, which is the main focus of this chapter.

Contributions. In this chapter, we assume a Rician multi-path channel model and consider two scenarios for the number of UAVs: (i) SUS, where a single UAV communicates with the UE, and (ii) MUS, where multiple UAVs form a distributed MIMO transceiver to communicate with the ground UE. We then model the wobbling behavior of the UAVs by two random processes, i.e., the Wiener and sinusoidal processes. For the SUS, we rigorously characterize the channel ACF for both random processes and determine the coherence time of the channel. We further derive the channel autocorrelation matrix in the MUS and demonstrate that the channels of different UAVs to the UE are uncorrelated from each other and the coherence time of these channels is the same as that of the SUS. Our analysis demonstrates that the choice of any realistic random process that captures the oscillatory nature of wobbling will result in a non-stationary received signal because of which the notion of channel coherence time needs to be defined carefully for this setting. A key design insight obtained from our analysis is that the coherence time of the channel is highly sensitive to UAV wobbling. Specifically, even for small wobbling of the UAV (w.r.t. the signal wavelength), we observe that the coherence time is not very large, which in turn makes the channel tracking and symbol detection difficult. To the best of our knowledge, this is the first work that characterizes the impact of UAV wobbling on the coherence time of the channel.

5.2 System Model

We use the Cartesian coordinate system to represent the locations of the UAVs, the UE, and scatterers. For the number of UAVs, we consider two different scenarios: (i) SUS, where a single UAV is deployed at some arbitrary location to communicate with the UE, and (ii) MUS, where multiple UAVs are deployed at arbitrary locations to jointly communicate with the UE in a distributed-MIMO fashion. To isolate the effect of the UAV wobbling, the UE is assumed to be static. The UAVs are assumed to be rotary-winged drones that are hovering at their locations. As shown in Fig. 5.1 for the SUS, the UAV is equipped with a single antenna (transceiver) which is located under the UAV platform with an offset of a_{D} meters from its centroid. We assume that the ground is aligned with the xy-plane while the UAV platform is located in the yz-plane and is initially parallel to the xy-plane at height $h = z_{\mathrm{D}}$. The initial location of the transceiver is assumed to be $P_{\mathrm{D}}(0) = (0, 0, z_{\mathrm{D}})$ and the locations of the UE and the n-th scatterer are denoted by $P_{\mathrm{U}} = (x_{\mathrm{U}}, y_{\mathrm{U}}, 0)$ and $P_{\mathrm{S}_n} = (x_{\mathrm{S}_n}, y_{\mathrm{S}_n}, z_{\mathrm{S}_n})$, respectively (with the convention that $P_{\mathrm{S}_0} \equiv P_{\mathrm{U}}$). We represent the UAV-UE, UAV-scatterer, and scatterer-UE distances at time t by $d_0(t)$, $d_n(t)$, and $d_{\mathrm{S}_n,\mathrm{U}}$, respectively. The angle-of-departure (AoD) from the UAV to the UE and from the UAV to the n-th scatterer (measured w.r.t. the z-axis) are denoted by φ_0 and φ_n, respectively. Furthermore, the angle between the x-axis and the line connecting the origin to the projection of P_{S_n} onto the ground is denoted by ω_n.

We assume that the UAV may experience wobbling due to the lack of robust and fixed

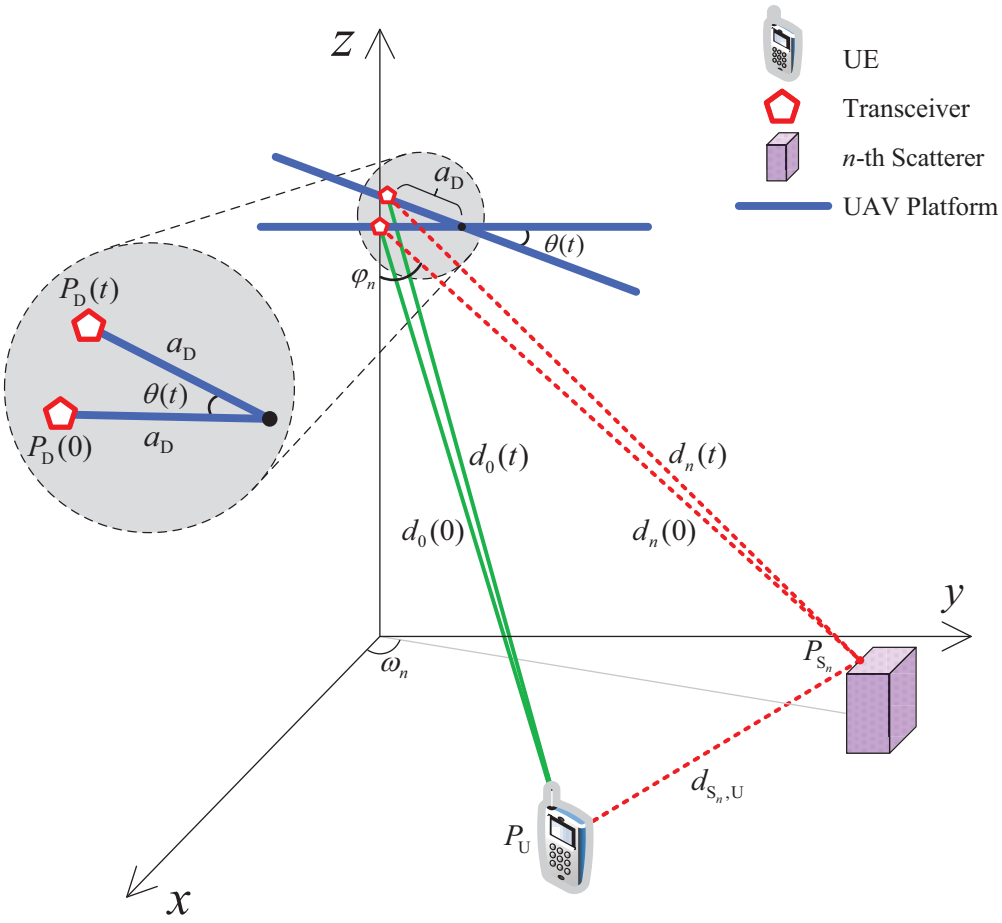

Figure 5.1: An illustration of the system model. The green solid lines represent the LoS links from the UAV transceiver to the UE at times 0 and t and the red dotted lines represent the MPCs from the scatterers.

infrastructure, wind gusts, and the high vibration frequency of its propellers and rotors [7], thus making it wobble. We model this wobbling by random processes and study their impact on the received signal at the UE. Note that because of this wobbling, the UAV platform may rotate in any of its three dimensions: roll, pitch, and yaw. In this chapter, however, we only consider the pitch angle for simplicity as in [42, 132]. This pitch angle is denoted by $\theta(t)$ at time t.

In this chapter, we assume a multi-path channel model where there is one LoS link between the UAV and the UE (the green solid lines in Fig. 5.1) and N multi-path components (MPCs) from scatterers (the red dotted lines for the n-th MPC in Fig. 5.1). In the SUS, we represent the received signal $r(t)$ at time t in the baseband (using the convention $d_{\mathrm{S}_0,\mathrm{U}} = 0$) as [134]

$$r(t) = \sum_{n=0}^{N} \alpha_n \mathrm{e}^{-j\frac{2\pi}{\lambda}(d_n(t)+d_{\mathrm{S}_n,\mathrm{U}})}, \tag{5.1}$$

where $\lambda = \frac{c}{f_\mathrm{c}}$ is the wavelength of the received signal, c is the speed of light, f_c is the carrier frequency, and α_0 and α_n are the amplitudes of the LoS link and the n-th MPC, respectively. Note that α_n and $d_n(t)$ may not be independent from each other in general. Similarly in the MUS, the received signal from the i-th UAV can be written as

$$r_i(t) = \sum_{n=0}^{N} \alpha_{i,n} \mathrm{e}^{-j\frac{2\pi}{\lambda}(d_{i,n}(t)+d_{\mathrm{S}_n,\mathrm{U}})}, \tag{5.2}$$

where $\alpha_{i,n}$ and $d_{i,n}(t)$ are the amplitude and distance from the i-th UAV to the n-th scatterer. The AoD from the i-th UAV to the n-th scatterer is denoted by $\varphi_{i,n}$.

Remark 5.1. For notational ease, we assume that the antenna gain is constant within the range of interest for the angles of the MPCs. For a reasonably smooth amplitude antenna pattern $G(\varphi)$ and assuming small pitch angle, a nonuniform antenna pattern would only require multiplication of α_n with $G(\varphi_n)$.

Remark 5.2. Due to the high carrier frequency of the received signal ($f_\mathrm{c} = 1 \sim 6$ GHz), the wavelength will be in the order of centimeters ($\lambda = 5 \sim 30$ cm). Hence, a small variation in the UAV-UE distance may cause a large phase offset. Note that this effect is even more pronounced at mmWave frequencies.

We now introduce the coherence time (T_C) of the channel as the main metric of interest in this chapter. Coherence time is defined as the time duration over which the impulse response of the channel is almost constant. Writing the channel ACF for the stationary received signal $r(t)$ as $R(\tau) = \mathbb{E}[r(t)r^*(t+\tau)]$, a common way to define the channel coherence time is the first time instant when the normalized ACF ($R(\tau)/\max R(\tau)$) drops below a certain threshold γ [135], i.e.,

$$T_\mathrm{C} = \min\left\{\tau : \frac{R(\tau)}{\max R(\tau)} \leq \gamma\right\}. \tag{5.3}$$

Remark 5.3. When the received signal is non-stationary, the channel ACF becomes a function of both t and τ and will be denoted as $R(t, t+\tau)$. We can define the coherence time in this case by first obtaining $T_C(t)$ from (5.3) using $R(t, t+\tau)$ instead of $R(\tau)$ for all t and then determining $T_C = \min_t T_C(t)$.

5.3 Channel Autocorrelation Function

In this section, we present a comprehensive analysis of the channel ACF for both the SUS and the MUS. We begin our analysis by deriving the relation between the pitch angles at time instants t and $t+\tau$ and the difference between the UAV-scatterer (or UAV-UE) distances at these times in the following lemma.

Lemma 5.4. *For a wobbling UAV, reasonably assuming $a_{\mathrm{D}} \ll d_n(t)$ and $\theta(t) \ll 1$ rad, we have*

$$d_{\mathrm{D},n}(t, t+\tau) := d_n(t+\tau) - d_n(t) \approx a_{\mathrm{D}} \cos(\varphi_n)[\theta(t+\tau) - \theta(t)]. \tag{5.4}$$

Proof. As shown in Fig. 5.1, when the UAV wobbles, the location of the transceiver changes from $P_{\mathrm{D}}(0) = (0, 0, z_{\mathrm{D}})$ to $P_{\mathrm{D}}(t) = (0, a_{\mathrm{D}}(1-\cos(\theta(t))), z_{\mathrm{D}} + a_{\mathrm{D}} \sin(\theta(t)))$. We now write the equations for $d_n(0)$ and $d_n(t)$ as follows:

$$\begin{aligned}
d_n(0) &= \sqrt{x_{\mathrm{S}_n}^2 + y_{\mathrm{S}_n}^2 + (z_{\mathrm{S}_n} - z_{\mathrm{D}})^2}, \\
d_n(t) &= \sqrt{x_{\mathrm{S}_n}^2 + [y_{\mathrm{S}_n} - a_{\mathrm{D}}(1-\cos\theta(t))]^2 + [z_{\mathrm{S}_n} - z_{\mathrm{D}} - a_{\mathrm{D}} \sin\theta(t)]^2} \\
&\overset{(a)}{\approx} \sqrt{x_{\mathrm{S}_n}^2 + y_{\mathrm{S}_n}^2 + (z_{\mathrm{S}_n} - z_{\mathrm{D}})^2 - 2a_{\mathrm{D}}[y_{\mathrm{S}_n}(1-\cos\theta(t)) + (z_{\mathrm{S}_n} - z_{\mathrm{D}}) \sin\theta(t)]} \\
&\overset{(b)}{\approx} d_n(0) - \frac{a_{\mathrm{D}}[y_{\mathrm{S}_n}(1-\cos\theta(t)) + (z_{\mathrm{S}_n} - z_{\mathrm{D}}) \sin\theta(t)]}{d_n(0)},
\end{aligned}$$

where in (a) we used $a_{\mathrm{D}} \ll y_{\mathrm{S}_n}$ and in (b) we used the approximation $\sqrt{1-\beta} \approx 1 - \frac{\beta}{2}$ for small β. Using $d_n(0) = (z_{\mathrm{D}} - z_{\mathrm{S}_n})/\cos(\varphi_n)$, we have

$$\begin{aligned}
d_n(t) - d_n(0) &\approx \frac{a_{\mathrm{D}} \cos(\varphi_n)}{z_{\mathrm{D}} - z_{\mathrm{S}_n}} [(z_{\mathrm{D}} - z_{\mathrm{S}_n}) \sin\theta(t) - y_{\mathrm{S}_n}(1-\cos\theta(t))] \\
&\overset{(a)}{=} a_{\mathrm{D}} \cos(\varphi_n) \sin\theta(t) - a_{\mathrm{D}} \sin(\omega_n) \sin(\varphi_n)(1-\cos\theta(t)) \\
&\approx a_{\mathrm{D}} \cos(\varphi_n)\theta(t) - a_{\mathrm{D}} \sin(\omega_n) \sin(\varphi_n) \frac{\theta^2(t)}{2} \\
&\approx a_{\mathrm{D}} \cos(\varphi_n)\theta(t),
\end{aligned} \tag{5.5}$$

where in (a) we used $y_{\mathrm{S}_n}/(z_{\mathrm{D}} - z_{\mathrm{S}_n}) = \tan(\varphi_n)\sin(\omega_n)$ and the last two steps result from the small-angle approximation of the pitch angle ($\theta(t) \ll 1$ rad). The same approximation is also true for time instant $t+\tau$, i.e., $d_n(t+\tau) - d_n(0) \approx a_{\mathrm{D}} \cos(\varphi_n)\theta(t+\tau)$. Using this result and that in (5.5), the lemma is proved. □

Corollary 5.5. *Assuming $\theta(t)$ to be a random process with stationary increments, i.e., $\theta(t+\tau)-\theta(t)$ has the same distribution as $\theta(\tau)$, the result of Lemma 5.4 can be simplified as $d_{\mathrm{D},n}(\tau) := d_{\mathrm{D},n}(t,t+\tau) \approx a_{\mathrm{D}}\cos(\varphi_n)\theta(\tau)$.*

5.3.1 ACF Analysis in the SUS

We present the main result of this chapter in the following theorem.

Theorem 5.6. *The channel ACF for a wobbling UAV in a multi-path channel is given as*

$$R(t,t+\tau) = \sum_{n=0}^{N} \mathbb{E}\left[|\alpha_n|^2 \mathrm{e}^{j\frac{2\pi}{\lambda}a_{\mathrm{D}}\cos(\varphi_n)[\theta(t+\tau)-\theta(t)]}\right], \tag{5.6}$$

which is a function of both t and τ (non-stationary ACF). However, if $\theta(t)$ has stationary increments, then the channel ACF becomes only a function of τ (stationary ACF):

$$R(\tau) = \sum_{n=0}^{N} \mathbb{E}\left[|\alpha_n|^2 \mathrm{e}^{j\frac{2\pi}{\lambda}a_{\mathrm{D}}\cos(\varphi_n)\theta(\tau)}\right]. \tag{5.7}$$

Proof. We can write the channel ACF using (5.1) as

$$\begin{aligned} R(t,t+\tau) &= \mathbb{E}[r(t)r^*(t+\tau)] \\ &= \mathbb{E}\left[\sum_{m=0}^{N}\sum_{n=0}^{N} \alpha_m\alpha_n^* \mathrm{e}^{j\frac{2\pi}{\lambda}(d_n(t+\tau)-d_m(t))}\mathrm{e}^{j\frac{2\pi}{\lambda}\left(d_{\mathrm{S}_n,\mathrm{U}}-d_{\mathrm{S}_m,\mathrm{U}}\right)}\right] \\ &= \sum_{m=0}^{N}\sum_{\substack{n=0\\n\neq m}}^{N} \mathbb{E}\left[\alpha_m\alpha_n^* \mathrm{e}^{j\frac{2\pi}{\lambda}(d_n(t+\tau)-d_m(t))}\right]\mathbb{E}\left[\mathrm{e}^{j\frac{2\pi}{\lambda}\left(d_{\mathrm{S}_n,\mathrm{U}}-d_{\mathrm{S}_m,\mathrm{U}}\right)}\right] \\ &\quad + \sum_{n=0}^{N} \mathbb{E}\left[|\alpha_n|^2 \mathrm{e}^{j\frac{2\pi}{\lambda}d_{\mathrm{D},n}(t,t+\tau)}\right], \end{aligned} \tag{5.8}$$

where the double summation in the last equality is zero since the random variable defined as $\left[\frac{d_{\mathrm{S}_n,\mathrm{U}}-d_{\mathrm{S}_m,\mathrm{U}}}{\lambda} \bmod 1\right]$ is uniformly distributed from 0 to 1 [28, Lemma 4]. Hence, using Lemma 5.4 and Corollary 5.5, we obtain (5.6) and (5.7), respectively. □

One can compute (5.6) and (5.7) by first conditioning on φ_n, evaluating the resulting expectation, and then deconditioning for a given distribution of φ_n. While the result in (5.6) holds for any angular power spectrum model, it would be instructive to simplify it for a specific model to obtain further insights. For that, we will use the well-accepted Laplacian model for the power of the n-th MPC [134, 136], which is given as $|\alpha_n|^2 = \frac{1}{2\sigma}\mathrm{e}^{-\frac{|\varphi_n-\varphi_0|}{\sigma}}$, $1 \le n \le N$, where σ is the scale parameter of the Laplacian model. In this chapter, we use the Rician

multi-path fading model with factor K to capture the higher probability of LoS in aerial networks. The following corollary simplifies the result of Theorem 5.6 when $\theta(t)$ is a random process with stationary increments (so that ACF is stationary) and $|\alpha_n|^2$ follows a Laplacian model.

Corollary 5.7. *Assuming the Laplacian angular power spectrum with* $|\alpha_0|^2 = K\sum_{n=1}^{N}|\alpha_n|^2 = K\sum_{n=1}^{N}\frac{1}{2\sigma}\mathrm{e}^{-\frac{|\varphi_n-\varphi_0|}{\sigma}}$ *and that* $\theta(t)$ *has stationary increments, the channel ACF can be simplified as*

$$R(t,t+\tau)=R(\tau)=\mathbb{E}\left[|\alpha_0|^2\mathrm{e}^{j\frac{2\pi}{\lambda}a_{\mathrm{D}}\cos(\varphi_0)\theta(\tau)}\right]+\sum_{n=1}^{N}\mathbb{E}\left[\frac{1}{2\sigma}\mathrm{e}^{-\frac{|\varphi_n-\varphi_0|}{\sigma}}\mathrm{e}^{j\frac{2\pi}{\lambda}a_{\mathrm{D}}\cos(\varphi_n)\theta(\tau)}\right]. \quad (5.9)$$

As mentioned in the previous section, due to the UAV wobbling, we model the variations in the pitch angle by random processes. Assuming the wobbling of the pitch angle has stationary increments, i.e., the resulting ACF is a function of the time difference τ only, this wobbling imposes an *effective Doppler shift* of $f_{\mathrm{D}}=\frac{a_{\mathrm{D}}\cos(\varphi_0)\theta(\tau)}{\lambda\tau}$ on the wireless channel. In this chapter, we use two different random processes for this purpose: (i) the Wiener process, and (ii) the sinusoidal process. Note that one can also consider more complex random processes, such as the periodic Brownian bridge or constrained Wiener processes to analyze the coherence time of the channel, however, the coherence time analysis may not even be tractable in the resulting non-stationary settings for these processes.

Remark 5.8. *(No wobbling).* In an ideal setting where the UAV platform is "completely" stable without any wobbling or angular deviations, we have $\theta(t)=0$ which results in a constant value for $R(t,t+\tau)$ for all t and τ. As expected, the coherence time will be infinity in this ideal case.

Wiener Process

The fundamental properties of a Wiener process $W(t)$ can be summarized as follows: (i) $W(0)=0$, (ii) $W(t)$ has independent, stationary, and Gaussian increments, (iii) $W(t)$ is continuous in t. Assuming $\theta(t)$ to be a Wiener process, one can show that it is scale-invariant and its probability density function (pdf) follows a Gaussian distribution with mean zero and variance bt, where b rad^2/s is a proportionality constant which can also be used as a tuning parameter. Hence, following Theorem 5.6, we have

$$R(t,t+\tau)=R(\tau)=\sum_{n=0}^{N}\mathbb{E}\left[|\alpha_n|^2\mathbb{E}\left[\mathrm{e}^{j\frac{2\pi}{\lambda}a_{\mathrm{D}}\cos(\varphi_n)W(\tau)}\right]\right]=\sum_{n=0}^{N}\mathbb{E}\left[|\alpha_n|^2\mathrm{e}^{-\left(\frac{2\pi^2}{\lambda^2}a_{\mathrm{D}}^2\cos^2(\varphi_n)\right)b\tau}\right], \quad (5.10)$$

where the last equality results from the characteristic function (cf) of a Gaussian random variable. Note that since the Wiener process has stationary increments, we were able to

use (5.7) in Theorem 5.6 and the ACF is only a function of the time difference τ. This result shows that the channel ACF becomes an exponentially decaying function of τ when the pitch angle is modeled as a Wiener process, which severely affects the coherence time of the channel.

Sinusoidal Process

In this case, we assume that the pitch angle is given by $\theta(t) = A\sin(2\pi Ft)$, where A and F are independent random variables representing the amplitude and the frequency of the pitch angle variations, respectively. In this chapter, we assume $A \sim U[-\theta_{\mathrm{m}}, \theta_{\mathrm{m}})$ and $F \sim p_F(f)$, where θ_{m} is the maximum pitch angle and $p_F(.)$ is some given pdf. Note that the sinusoidal random process does not have the stationary increment property. Hence, we obtain the channel ACF using Theorem 5.6 as

$$\begin{aligned} R(t,t+\tau) &= \sum_{n=0}^{N} \mathbb{E}\left[|\alpha_n|^2 \mathrm{e}^{j\frac{2\pi}{\lambda} a_{\mathrm{D}}\cos(\varphi_n)A[\sin(2\pi F(t+\tau))-\sin(2\pi Ft)]}\right] \\ &= \sum_{n=0}^{N} \mathbb{E}\left[|\alpha_n|^2 \int_{-\infty}^{\infty} \operatorname{sinc}\left(\frac{2}{\lambda} a_{\mathrm{D}}\cos(\varphi_n)\theta_{\mathrm{m}}\big[\sin(2\pi F(t+\tau)) - \sin(2\pi Ft)\big]\right) p_F(f)\mathrm{d}f\right], \end{aligned} \tag{5.11}$$

where $\operatorname{sinc}(x) = \frac{\sin(\pi x)}{\pi x}$ and in the last equality, we used the cf of the uniform random variable and then took the expectation w.r.t. F. As we will see in Section 5.4, the special case of $t = 0$ gives the lowest coherence time among different values of t. The channel ACF for $t = 0$ is further simplified as

$$R(0,\tau) = \sum_{n=0}^{N} \mathbb{E}\left[|\alpha_n|^2 \int_{-\infty}^{\infty} \operatorname{sinc}\left(\frac{2}{\lambda} a_{\mathrm{D}}\cos(\varphi_n)\theta_{\mathrm{m}}\sin(2\pi f\tau)\right) p_F(f)\mathrm{d}f\right]. \tag{5.12}$$

Note that the channel ACF is not a periodic function of τ due to the random frequency of the pitch angle. However, if we assume a constant F, then the channel ACF will be periodic in τ even with a random pitch angle amplitude A.

Using (5.3), (5.10), and (5.11), one can now derive the coherence time of the channel for each random process. Explicitly for the Wiener process in an LoS channel ($N = 0$) with an arbitrary *non-random* AoD, the channel ACF is given as

$$R(\tau) = \mathbb{E}\left[|\alpha_0|^2 \mathrm{e}^{-\left(\frac{2\pi^2}{\lambda^2} a_{\mathrm{D}}^2 \cos^2(\varphi_0)\right)b\tau}\right] = |\alpha_0|^2 \mathrm{e}^{-\left(\frac{2\pi^2}{\lambda^2} a_{\mathrm{D}}^2 \cos^2(\varphi_0)\right)b\tau}. \tag{5.13}$$

Now since (5.13) is a monotonically decreasing function of τ with its peak at $\tau = 0$, solving $\frac{R(\tau)}{\max R(\tau)} = \gamma$ gives the coherence time of the channel in closed-form as

$$T_{\mathrm{C}} = \frac{\lambda^2}{2b\pi^2 a_{\mathrm{D}}^2 \cos^2(\varphi_0)} \log\left(\frac{1}{\gamma}\right). \tag{5.14}$$

For the sinusoidal process, on the other hand, the closed-form solution is not available and we need to numerically solve (5.12) to obtain the coherence time of the channel.

Remark 5.9. *(Impact of the Rician K-factor).* Using the assumptions and result of Corollary 5.7, we can write the channel ACF as a function of K as

$$R(\tau;K)=K\sum_{n=1}^{N}\mathbb{E}\left[\frac{1}{2\sigma}\mathrm{e}^{-\frac{|\varphi_n-\varphi_0|}{\sigma}}\mathrm{e}^{j\frac{2\pi}{\lambda}a_{\mathrm{D}}\cos(\varphi_0)\theta(\tau)}\right]+\sum_{n=1}^{N}\mathbb{E}\left[\frac{1}{2\sigma}\mathrm{e}^{-\frac{|\varphi_n-\varphi_0|}{\sigma}}\mathrm{e}^{j\frac{2\pi}{\lambda}a_{\mathrm{D}}\cos(\varphi_n)\theta(\tau)}\right].$$

Assuming $\theta(\tau)$ follows the Wiener process, we have

$$\frac{R(\tau;K)}{R(0;K)}=\frac{K}{K+1}\mathrm{e}^{-\left(\frac{2\pi^2}{\lambda^2}a_{\mathrm{D}}^2\cos^2(\varphi_0)\right)b\tau}+\frac{\sum_{n=1}^{N}\mathbb{E}\left[\mathrm{e}^{-\frac{|\varphi_n-\varphi_0|}{\sigma}}\mathrm{e}^{-\left(\frac{2\pi^2}{\lambda^2}a_{\mathrm{D}}^2\cos^2(\varphi_n)\right)b\tau}\right]}{(K+1)\sum_{n=1}^{N}\mathbb{E}\left[\mathrm{e}^{-\frac{|\varphi_n-\varphi_0|}{\sigma}}\right]}. \tag{5.15}$$

Taking the derivative of (5.15) w.r.t. K, we end up with an expression which could be either negative or positive depending on the value of φ_0. Hence, the coherence time of the channel is a function of both K and φ_0, which is neither increasing nor decreasing w.r.t. K.

5.3.2 ACF Analysis in the MUS

In this model, we assume that M UAVs form a distributed MIMO transceiver to jointly communicate with the UE. The channel autocorrelation matrix can be written as

$$\mathbf{R}(t,t+\tau)=[R_{ik}(t,t+\tau)]_{1\leq i,k\leq M}=\mathbb{E}\left[\mathbf{r}(t)\mathbf{r}^{*}(t+\tau)\right],$$

where $\mathbf{r}(t)=[r_1(t),r_2(t),\ldots,r_M(t)]^{\mathrm{T}}$ is the received signal vector, and $R_{ik}(t,t+\tau)$ is the (i,k)-th element of $\mathbf{R}(t,t+\tau)$.

Theorem 5.10. *The channel autocorrelation matrix for M wobbling UAVs that form a distributed MIMO transceiver in an environment with one LoS link for each UAV and N MPCs can be written as*

$$\mathbf{R}(t,t+\tau)=\operatorname{diag}\left\{\sum_{n=0}^{N}\mathbb{E}\left[|\alpha_{i,n}|^2\mathrm{e}^{j\frac{2\pi}{\lambda}a_{\mathrm{D}}\cos(\varphi_{i,n})[\theta(t+\tau)-\theta(t)]}\right]\right\}. \tag{5.16}$$

Proof. For the diagonal elements of $\mathbf{R}(t,t+\tau)$, Theorem 5.6 is directly applied and we have

$$R_{ii}(t,t+\tau)=\mathbb{E}\left[r_i(t)r_i^{*}(t+\tau)\right]=\sum_{n=0}^{N}\mathbb{E}\left[|\alpha_{i,n}|^2\mathrm{e}^{j\frac{2\pi}{\lambda}a_{\mathrm{D}}\cos(\varphi_{i,n})[\theta(t+\tau)-\theta(t)]}\right].$$

On the other hand, for the off-diagonal elements, we can write

$$\begin{aligned}
R_{ik}(t,t+\tau) &= \mathbb{E}\left[r_i(t)r_k^*(t+\tau)\right] \\
&= \mathbb{E}\left[\sum_{m=0}^{N}\sum_{n=0}^{N}\alpha_{i,m}\alpha_{k,n}^* \mathrm{e}^{j\frac{2\pi}{\lambda}\left(d_{k,n}(t+\tau)-d_{i,m}(t)\right)}\mathrm{e}^{j\frac{2\pi}{\lambda}\left(d_{\mathrm{S}_n,\mathrm{U}}-d_{\mathrm{S}_m,\mathrm{U}}\right)}\right] \\
&= \sum_{n=0}^{N}\mathbb{E}\left[\alpha_{i,n}\alpha_{k,n}^* \mathrm{e}^{j\frac{2\pi}{\lambda}\left(d_{k,n}(t+\tau)-d_{k,n}(t)\right)}\right]\mathbb{E}\left[\mathrm{e}^{j\frac{2\pi}{\lambda}\left(d_{k,n}(t)-d_{i,n}(t)\right)}\right] \\
&\quad + \sum_{m=0}^{N}\sum_{\substack{n=0\\ n\neq m}}^{N}\mathbb{E}\left[\alpha_{i,m}\alpha_{k,n}^* \mathrm{e}^{j\frac{2\pi}{\lambda}\left(d_{k,n}(t+\tau)-d_{i,m}(t)\right)}\right]\mathbb{E}\left[\mathrm{e}^{j\frac{2\pi}{\lambda}\left(d_{\mathrm{S}_n,\mathrm{U}}-d_{\mathrm{S}_m,\mathrm{U}}\right)}\right],
\end{aligned}$$

where in the first summation of the last equality we used the fact that the pitch angle wobbling in the location of UAVs is independent of the distances between the UAVs and the scatterers (or the UE). Hence, since the random variable $\left[\frac{d_{k,n}(t)-d_{i,n}(t)}{\lambda} \bmod 1\right]$ is uniformly distributed from 0 to 1 [28, Lemma 4], we conclude that this summation is zero. The second summation is also zero using a similar reasoning as in the proof of Theorem 5.6. □

Corollary 5.11. *Assuming the Laplacian angular power spectrum with Rician fading model, and that $\theta(t)$ has stationary increments, the channel autocorrelation matrix is simplified as*

$$\begin{aligned}
\mathbf{R}(t,t+\tau) = \mathbf{R}(\tau) &= \mathrm{diag}\left\{\mathbb{E}\left[|\alpha_{i,0}|^2 \mathrm{e}^{j\frac{2\pi}{\lambda}a_{\mathrm{D}}\cos(\varphi_{i,0})\theta(\tau)}\right]\right\} \\
&\quad + \sum_{n=1}^{N}\mathrm{diag}\left\{\mathbb{E}\left[\frac{1}{2\sigma}\mathrm{e}^{-\frac{|\varphi_{i,n}-\varphi_{i,0}|}{\sigma}}\mathrm{e}^{j\frac{2\pi}{\lambda}a_{\mathrm{D}}\cos(\varphi_{i,n})\theta(\tau)}\right]\right\}. \qquad (5.17)
\end{aligned}$$

Similar to the SUS, one can model the random process $\theta(t)$ using the Wiener or sinusoidal processes to obtain the channel autocorrelation matrix. The fundamental observation in the MUS is that when multiple UAVs are hovering at some locations to communicate with the UE in a distributed-MIMO fashion, then the channels will be uncorrelated from each other. Using (5.3), (5.6), and (5.16), we conclude that the coherence time of the channel in the MUS is the same as that of the SUS.

5.4 Simulation Results

In this section, we present numerical results to demonstrate the impact of UAV pitch wobbling on the coherence time of the channel. We assume that a single rotary-winged UAV hovers at some arbitrary location and wobbles based on either the Wiener or sinusoidal processes. For the number of scatterers, we assume $N = 20$ and $N = 10$ in the sub-6 GHz and mmWave frequencies, respectively [134]. Following Corollary 5.7, we assume a Laplacian angular power spectrum with $K = 11.5$ [137, Table 1], $\varphi_0 = 20°$ and $\sigma = 1$. For the

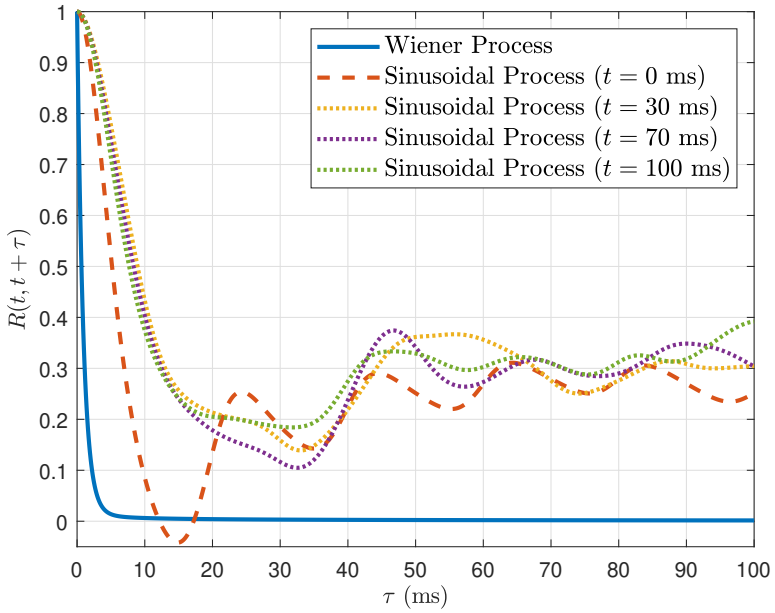

Figure 5.2: The channel ACF for different random processes. The parameters are $f_c = 6$ GHz and $\theta_m = 5°$.

Wiener process, we assume the proportionality constant is $b = 1$ rad^2/s and for the sinusoidal process, we assume that the amplitude and frequency of the pitch angle both follow the uniform distribution, i.e., $A \sim U[-\theta_m, \theta_m)$ and $F \sim U[5, 25)$ Hz. Other parameters are $a_D = 40$ cm, $\theta_m = \{5, 7, 10\}°$ (the maximum pitch angle of 10° is selected based on [41]), and $f_c = \{2.4, 6, 30\}$ GHz (equivalently, $\lambda = \{12.5, 5, 1\}$ cm). Note that the derived values for the channel coherence time should be treated as useful ballpark figures, since they are dependent on the physical characteristics of the UAVs and may vary from one UAV to another.

In Fig. 5.2, we show the impact of UAV pitch angle wobbling on the channel ACF for both random processes where $f_c = 6$ GHz and $\theta_m = 5°$. Note that since the channel ACF is non-stationary in the sinusoidal process, we plotted the ACF at different values of t to understand its behavior. As seen in this figure, the sinusoidal process represents its lowest coherence time at $t = 0$ s. Thus, in the remainder of this section, we use this time instant to calculate the coherence time of the channel for the sinusoidal process. Assuming a normalized threshold of $\gamma = 0.5$, the coherence time of the channel is 642 μs and 5.18 ms for the Wiener and sinusoidal processes, respectively. Note that the observed behavior for the Wiener process is intuitive since the variations in the pitch rotation angle can grow without bounds, and thus, the channel decorrelates with itself rapidly, yielding a very low coherence time. Nevertheless, it is interesting to note that the coherence time for the sinusoidal model is not too high either. Hence, channel tracking and phase estimation for the proper symbol detection become very

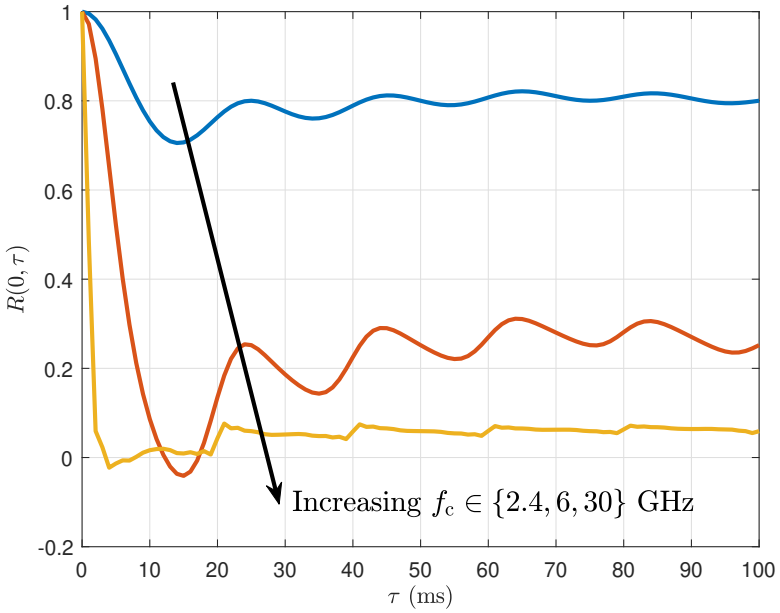

Figure 5.3: The channel ACF when $\theta(t)$ follows the sinusoidal process with varying carrier frequencies and $\theta_m = 5°$.

difficult in both models [138]. Comparing these two random processes, we observe that the Wiener process is tractable and has stationary increments, but suffers from unbounded and non-smooth angular variations. On the other hand, the sinusoidal process is reasonably realistic and has bounded and smoother angular variations at the cost of being relatively less tractable and not having stationary increments. In fact, any reasonably realistic model that captures the oscillatory behavior of the wobbling motion of UAVs is unlikely to possess stationary increments.

In Figs. 5.3 and 5.4, we examine the sinusoidal model more carefully and demonstrate the impact of the carrier frequency and the maximum pitch angle on the channel ACF and the coherence time. From a physical standpoint, since the impulse response of the channel depends on the ratio of the transmitter-receiver distance d and the signal wavelength λ, a higher d/λ translates to a higher channel variation, which in turn results in a lower coherence time. Thus, increasing θ_m (higher d) or increasing f_c (lower λ), gives a lower channel coherence time. Note that increasing the UAV antenna offset a_D would have the same impact on the coherence time of the channel. Furthermore, increasing the range of the UAV pitch wobbling frequency F makes the channel to decorrelate with itself more rapidly, which also yields a lower coherence time. Note that the limiting value of the stationary ACF ($R(\tau)$ as $\tau \to \infty$) also decreases with increasing θ_m or f_c. Assuming a normalized threshold of $\gamma = 0.5$ and $\theta_m = 5°$, we observe from Fig. 5.3 that $T_C = \{\infty, 5.18, 0.97\}$ ms for $f_c = \{2.4, 6, 30\}$ GHz, respectively. As it can be seen in this figure, with the physical parameters

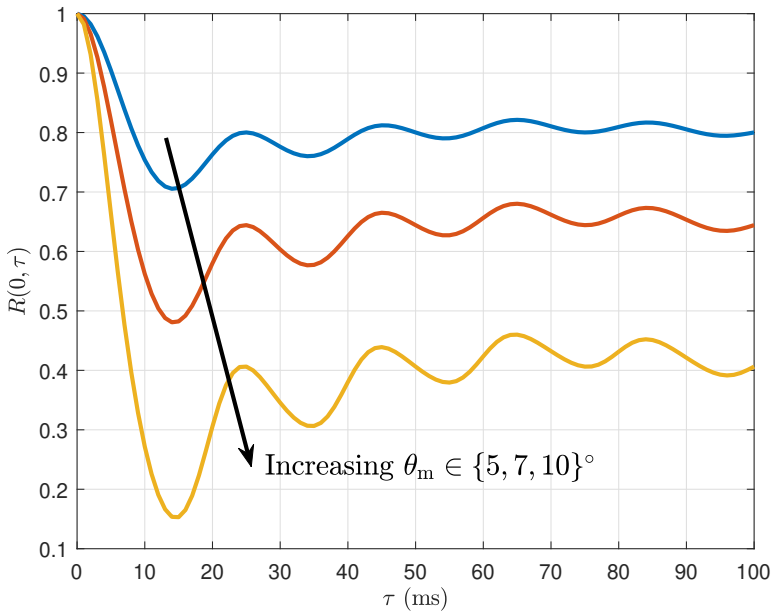

Figure 5.4: The channel ACF when $\theta(t)$ follows the sinusoidal process with varying maximum pitch angles and $f_{\mathrm{c}} = 2.4$ GHz.

[41, 137] mentioned in the beginning of this section, the coherence time of the channel will be in the order of microseconds for mmWave frequencies. Hence, channel tracking and, in turn, communication is very challenging at the mmWave frequencies. From Fig. 5.4, we have $T_{\mathrm{C}} = \{\infty, 12.26, 6.74\}$ ms for $\theta_{\mathrm{m}} = \{5, 7, 10\}^{\circ}$, respectively, when $f_{\mathrm{c}} = 2.4$ GHz. Consequently, when working in higher frequencies or in inclement weather, we require UAVs with robuster stabilizers that guarantee very low angular deviations.

5.5 Chapter Summary

In this chapter, we provided a rigorous mathematical analysis for the coherence time of the channel when UAVs experience random pitch wobbling. Assuming a Rician multi-path channel model, we considered two different scenarios for the number of UAVs communicating with the UE, i.e., SUS and MUS, and modeled the UAV pitch wobbling by random processes. For both the SUS and MUS, we formulated the channel ACF and derived the coherence time of the channel. Specifically in the MUS, we showed that the channels between the UAVs and the UE are uncorrelated from each other and the channel autocorrelation matrix is only determined by its diagonal elements. Our analysis demonstrated that even for small UAV pitch wobbling, the coherence time of the channel could be severely affected, thus making channel tracking and symbol detection difficult. A meaningful extension of this work is to study the impact of UAV wobbling on the fundamental characteristics of the channel when

the UAVs are *mobile*. Another direction for future work is to derive the coherence time of the channel in a centralized MIMO scenario, i.e., having an antenna array instead of a single antenna in the UAV structure [42, 132].

In the next chapter, we continue with the same general theme of understanding the fundamental properties of air-to-ground wireless channels, where we will also incorporate hardware impairments in addition to UAV wobbling. This will result in a unified air-to-ground channel model that is cognizant of both wobbling and hardware impairments and is hence in the general interest of the community.

Chapter 6

Fundamentals of Wobbling and Hardware Impairments-Aware Air-to-Ground Channel Model

6.1 Introduction

Continuing with the same general theme as the previous chapter, this chapter aims to develop a new air-to-ground wireless channel that will incorporate the effect of hardware impairment in addition to wobbling, which was discussed extensively in the previous chapter. In order to make this discussion self-contained, we remind the reader that UAVs may experience physical vibrations due to inclement weather conditions or high vibration frequency of their propellers [7, 86]. These physical vibrations (also known as wobbling [86], jittering [42, 43], and fluctuations [44]) could adversely affect the wireless channel especially at high carrier frequencies. Further, all digital transceivers suffer from RF nonidealities (also known as hardware impairments) that degrade or even severely limit their performance [49, 53]. While the hardware impairments are well-understood in the literature, their interplay with the unique UAV impairments, such as wobbling, has not been studied yet. Motivated by this observation, we consider an aerial-terrestrial setup, where the terrestrial node suffers from hardware impairments, while the aerial node suffers from both hardware impairments and wobbling. For this setup, we develop a unified air-to-ground channel model in this chapter that is cognizant of these impairments and provide a comprehensive analysis of key channel-related metrics. We also discuss the implications of our analysis on operating UAVs at high frequencies.

6.1.1 Related Works

This chapter builds on the following general lines of research: (i) air-to-ground channel model, (ii) UAV wobbling, and (iii) hardware impairments. We explain each research direction next.

Air-to-Ground Channel Model. There have been numerous works that focus on modeling and/or measurement of air-to-ground wireless channels [5, 9, 11, 12, 13, 14, 15, 16, 17, 91]. Air-to-air and air-to-ground channels are inherently different from ground-to-ground

channels due to many reasons, such as the higher probability of LoS in the aerial channels and the mobility of UAVs [2, 8, 9]. Following the mathematical model suggested by the international telecommunication union (ITU) [10], perhaps the first work that established a meaningful yet simple relation between the LoS probability and the elevation angle in an aerial-terrestrial setup for low altitude platforms (LAPs) was [11], where the authors fitted a modified Sigmoid function to the LoS probability. Extensive measurement campaigns were conducted in [12, 13, 14] to obtain specific air-to-ground channel models for different environments (over-water [12], hilly and mountainous [13], and suburban and near-urban [14]). In these papers, the authors characterized different metrics related to the air-to-ground channels, such as path loss, Ricean K factor of the small-scale fading, and delay spread of the channel. Another relatively recent measurement campaign was conducted in [15], where the authors extracted channel impulse responses from the received data, using which they obtained key characteristics of the channel, such as path loss and shadow fading. In [16], the authors proposed an air-to-ground channel model for UAV base stations flying at high altitudes and moving periodically in circular curves. Considering ultrawideband signals, the authors in [17] conducted measurements for air-to-ground wireless channels and developed stochastic path-loss and multi-path channel models for ultrawideband propagation channels. Last but not the least, the third generation partnership project (3GPP) has also provided a detailed channel model, including the LoS probability and path-loss and fading models, in different environments in its technical report on cellular support for UAVs [5].

UAV Wobbling. One unique feature of aerial wireless communications, which can be viewed as an impairment, is the fact that UAVs may experience wobbling, i.e., typically small and random fluctuations of the UAV platform due to various reasons, such as wind gusts and lack of fixed infrastructure [41]. Since this area of research is still at its nascent stage, there are only a handful of works that incorporate UAV wobbling [42, 43, 44, 45, 78, 86]. For instance, the authors in [42] provided a stochastic model for UAV wobbling and then studied a resource allocation problem in UAV-assisted cellular networks. Considering directional antennas, the antenna gain mismatch problem due to random UAV wobbling for an air-to-air network was studied in [44], where the authors also provided closed-form statistical channel models for the air-to-air links. In [86], the authors studied the impact of random UAV wobbling on the air-to-ground wireless channel and obtained the coherence time of the channel under different stochastic wobbling models. Following [86], the authors in [45] studied the Doppler effect at millimeter-wave (mmWave) frequencies for an air-to-ground channel under random UAV wobbling. Apart from analytical results, measurement campaigns have also reported the impact of wobbling as an important source of error in establishing a strong connection in aerial wireless networks [47, 48]. In particular, in [47], the authors used a channel sounder to investigate an air-to-ground wireless link, from which they observed that the variations of the received power from a completely static UAV are much less than that of a hovering UAV. These studies highlight the importance of considering UAV wobbling in aerial wireless communications.

Hardware Impairments. The unfavorable impact of RF imperfections on various aspects of

communication systems has been studied extensively during the past decades. Perhaps one of the most comprehensive books on this subject is [49], where the authors describe in detail three fundamental hardware impairments, i.e., phase noise, I/Q imbalance, and PA nonlinearity, along with a general error model that characterizes the effect of all three impairments on the received signal in a wireless channel. This general error model [49, Ch. 7] motivated many researchers to redefine and solve fundamental communication-theoretic problems under a more realistic impairments-aware channel model [50, 51, 52, 53, 54, 55, 56, 57, 58]. For instance, the authors in [50] quantified the aggregate effect of hardware impairments on two-hop relaying systems [34, 59, 60] and obtained closed-form expressions for the outage probability in these networks. In [51], the authors analytically proved that the capacity of a multiple-input multiple-output (MIMO) channel will be limited when hardware impairments are assumed, which signifies the fundamental impact of these impairments on the wireless channel. The problem of MIMO transmission with residual RF impairments on the transmitter side was studied in [52], where the authors showed that such hardware impairments substantially degrade the performance of MIMO detection algorithms. In [53], the authors incorporated hardware impairments in the analysis of massive MIMO systems, and demonstrated the existence of an upper bound on the capacity of each user equipment (UE). Another interesting work that studied the impact of hardware impairments on massive MIMO systems is [54], where the authors perform two types of simulations considering additive and multiplicative stochastic impairment models, as well as more accurate deterministic behavioral models.

Although sparse, there are a few works that study the impact of hardware impairments in UAV communications [61, 62]. For example, the authors in [61] studied a UAV-aided non-orthogonal multiple access (NOMA) relaying network, where both the UAV-relay and terrestrial UEs suffer from residual hardware impairments. Quite surprisingly, none of the recent works consider the impact of UAV wobbling along with other impairments. In this chapter, we analyze the joint impact of hardware impairments and UAV wobbling on the wireless channel and provide a unified impairments-aware air-to-ground channel model. We summarize our contributions next.

6.1.2 Contributions

This chapter provides a unified model for the air-to-ground wireless channel that suffers from both UAV wobbling and hardware impairments. In particular, we assume that a hovering UAV (transmitter) communicates with a UE on the ground (receiver) in a multi-path environment with Rician fading. Both the UAV and the UE suffer from various hardware impairments, such as phase noise, I/Q imbalance, and PA nonlinearity. Apart from these hardware impairments, we assume that the UAV also suffers from random wobbling, i.e., unpredictable physical fluctuations due to not having a fixed aerial infrastructure. We model UAV wobbling using two different random processes, i.e., the Wiener process and the sinusoidal process, and characterize the properties of each process separately. As for the hardware

impairments, we model the aggregate effect of all of them as two multiplicative and additive distortion processes and study them in both nonstationary and stationary scenarios. Although modeling these hardware impairments is known and well-accepted in the literature, the interplay between hardware impairments and UAV wobbling has not been studied yet. For this setup, our contributions are highlighted next.

Unified Impairments-Aware Wireless Channel Model

We present a unified channel model in a multi-path Rician fading environment that accounts for both UAV wobbling and hardware impairments. Our proposed model consists of a modified channel impulse response and a distortion-plus-noise process, where the former is affected by UAV wobbling and only the multiplicative distortion part of the hardware impairments, while the latter is affected by UAV wobbling and both the multiplicative and additive distortion parts of the hardware impairments.

Derivation and Evaluation of Key Channel Metrics

We rigorously derive channel ACFs for both nonstationary and stationary impairments. Using these results, we extensively study four key metrics that are used to characterize a wireless channel, i.e., (i) PDP, (ii) coherence time, (iii) coherence bandwidth, and (iv) PSD of the distortion-plus-noise process.

Design Insights and Implications on Higher Frequencies

We demonstrate that even with stationary hardware impairments, the received signal could be nonstationary due to the oscillatory nature of UAV wobbling, a phenomenon that could only be observed in air-to-ground wireless communications. The analysis presented in this chapter suggests a high sensitivity of key channel metrics to both UAV wobbling and hardware impairments, especially at higher carrier frequencies. A particularly noteworthy implication of our results is the degradation of channel coherence time at higher carrier frequencies because of these effects. To the best of our knowledge, this is the first work that proposes an impairments-aware unified channel model for UAV communications and characterizes the key metrics associated with the channel.

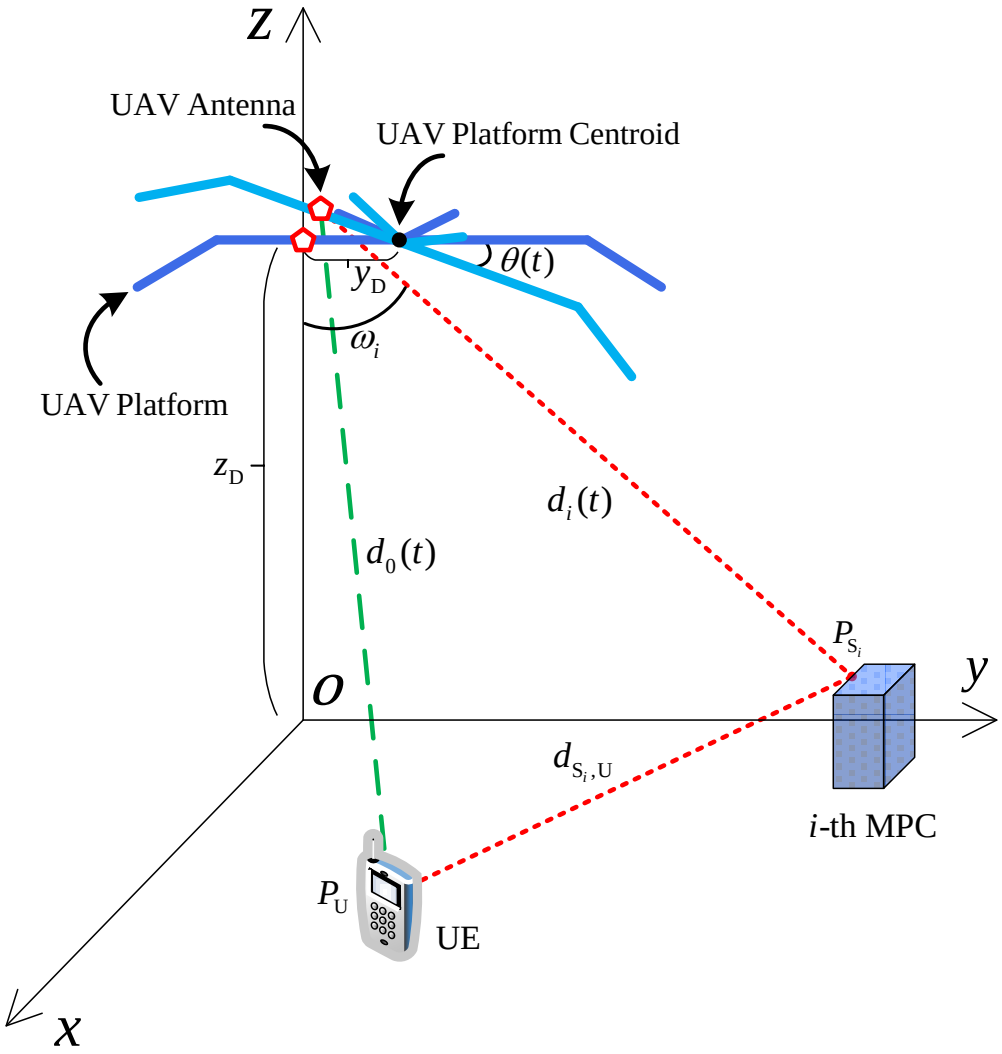

Figure 6.1: Spatial setup where the UAV platform wobbles and the UAV transceiver suffers from various hardware impairments.

6.2 System Model

6.2.1 Spatial Setup

We consider a rotary-winged UAV that is hovering in the air and communicating with a ground UE. We assume that there are N multi-path components (MPCs) from scatterers which contribute to the total received signal at the ground UE. To represent our system model, we use Cartesian coordinate system, where the ground is aligned with the xy-plane and the UAV platform centroid, ground UE, and the i-th scatterer (i.e., the i-th MPC) are located at $P_{\mathrm{D}} = (0, y_{\mathrm{D}}, z_{\mathrm{D}})$, $P_{\mathrm{U}} = (x_{\mathrm{U}}, y_{\mathrm{U}}, 0)$, and $P_{\mathrm{S}_i} = (x_{\mathrm{S}_i}, y_{\mathrm{S}_i}, z_{\mathrm{S}_i})$, respectively. As seen from Fig. 6.1, we assume that the UAV is equipped with an antenna that is located at a distance of y_{D} from the centroid of the UAV platform, so that the initial location of the antenna is $(0, 0, z_{\mathrm{D}})$. Furthermore, for the ease of notation, we use the convention that the UE is the zeroth MPC. The UAV-UE, UAV-MPC, and MPC-UE distances are represented by $d_0(t)$, $d_i(t)$, and $d_{\mathrm{S}_i,\mathrm{U}}$ for the i-th MPC at time t, respectively. Also, the angle-of-departure (AoD) from the UAV to the i-th MPC (measured with respect to the z-axis) is denoted by ω_i.

6.2.2 Impairments

We categorize the nonidealities that degrade reliable aerial-terrestrial communications as *UAV wobbling* and *hardware impairments*, which are introduced next.

UAV Wobbling: The agility of UAVs comes at the price of not having a fixed infrastructure, which could even lead to instability because of wind gusts or bad weather conditions [44]. Considering these natural phenomena and the high vibration frequency of UAVs' propellers, UAVs may experience small random physical vibrations, which are referred to as wobbling in this chapter. Although this wobbling is typically small [41], its impact on the received signals could be non-negligible especially at high carrier frequencies. Furthermore, this impact could be even more severe if the UAV is equipped with a directional antenna instead of an omnidirectional antenna. As shown in Fig. 6.1, we represent the wobbling pitch angle at time t by $\theta(t)$, which shows the deviation of the UAV platform from its initial state. In this chapter, we model $\theta(t)$ using stochastic processes [86] and study the impact of UAV wobbling on different aspects of the wireless channel. More technical discussions are presented in Section 6.3.4.

Hardware Impairments: Because of their inherent physical characteristics, RF transceivers are known to suffer from hardware impairments, such as PA nonlinearity, I/Q imbalance, and phase noise [49, 52]. Although various models for each hardware impairment can be found in the literature [139, 140, 141], we intend to consider the aggregate effect of all such impairments in this work for the sake of generality. The fundamental impact of each of these impairments on the transmitted and received signals usually includes an attenuation

and phase rotation of the original signal (i.e., multiplicative effect) along with a leakage of different carriers or symbols into each other (i.e., additive effect). Due to these factors, the influence of each hardware impairment can be modeled as an affine linear function. Therefore, the combined effect of these hardware impairments can be modeled as two multiplicative and additive distortion noise processes at both the transmitter and receiver [49, Sec. 7.2.2]. Mathematically speaking, the *impaired* transmitted and received signals in complex baseband can be written as

$$s(t) = \chi_{\mathrm{T}}(t)\tilde{s}(t) + \eta_{\mathrm{T}}(t), \qquad r(t) = \chi_{\mathrm{R}}(t)\tilde{r}(t) + \eta_{\mathrm{R}}(t), \tag{6.1}$$

where $\tilde{s}(t)$ and $\tilde{r}(t)$ are the *unimpaired* transmitted and received signals, $s(t)$ and $r(t)$ are their impaired counterparts, and $\chi_{\mathrm{T}}(t)$ and $\eta_{\mathrm{T}}(t)$ (resp. $\chi_{\mathrm{R}}(t)$ and $\eta_{\mathrm{R}}(t)$) are the multiplicative and additive distortion noise processes at the transmitter (resp. receiver), respectively. Note that these RF impairments are nonstationary in nature, and thus, these distortion noises are assumed to be time-dependent in general [49, Sec. 7.2.3]. These four noise processes are characterized by their ACFs, i.e., $A_{\chi_{\mathrm{T}}}(t_1, t_2) = \mathbb{E}\left[\chi_{\mathrm{T}}^*(t_1)\chi_{\mathrm{T}}(t_2)\right]$, $A_{\chi_{\mathrm{R}}}(t_1, t_2) = \mathbb{E}\left[\chi_{\mathrm{R}}^*(t_1)\chi_{\mathrm{R}}(t_2)\right]$, $A_{\eta_{\mathrm{T}}}(t_1, t_2) = \mathbb{E}\left[\eta_{\mathrm{T}}^*(t_1)\eta_{\mathrm{T}}(t_2)\right]$, and $A_{\eta_{\mathrm{R}}}(t_1, t_2) = \mathbb{E}\left[\eta_{\mathrm{R}}^*(t_1)\eta_{\mathrm{R}}(t_2)\right]$. Furthermore, we assume that these four processes are independent from each other and the additive distortions have zero means [49, 50], i.e., $\mathbb{E}\left[\eta_{\mathrm{T}}(t)\right] = \mathbb{E}\left[\eta_{\mathrm{R}}(t)\right] = 0$. Since WSS processes are an important class of random processes, we will also study our channel metrics (described next) when hardware impairments are assumed to be WSS. In that case, the above-mentioned ACFs will only be functions of $t_2 - t_1$.

6.2.3 Metrics

We consider multiple key channel-related metrics in this chapter, which are described next. We represent the channel impulse response by $c(\tau; t)$, where τ is the delay variable and t is the observation time, and define its ACF as $A_{\mathrm{c}}(\tau; t, \Delta t) = \mathbb{E}\left[c^*(\tau; t)c(\tau; t + \Delta t)\right]$. Note that since the channel is assumed to be nonstationary, we present our definitions/results in their general form. Throughout the chapter, we assume that the channel undergoes uncorrelated scattering (US).

PDP

We define PDP in a nonstationary multi-path channel as the average received power at a given multi-path delay τ and a specific observation time t [134, 142]. One way to obtain the PDP is to evaluate the ACF of the channel impulse response at $\Delta t = 0$, i.e., $P_{\mathrm{c}}(\tau; t) = A_{\mathrm{c}}(\tau; t, \Delta t = 0) = \mathbb{E}\left[|c(\tau; t)|^2\right]$. However, as we will see in the next section, the channel impulse response entails a sum of Dirac delta functions (see (6.6) and (6.13)), which introduces a singularity problem (delta squared) into this definition. One way to avoid this issue is to isolate one of the delta functions by writing the channel ACF as $A_{\mathrm{c}}(\tau; t, \Delta t) = P_{\mathrm{c}}(\tau; t)\delta(\Delta t)$, and *redefining* the PDP with only one delta function as $P_{\mathrm{c}}(\tau; t)$ [143].

Coherence Time

Coherence time is defined as the period of time over which the channel remains almost constant, calculated as follows: First, we evaluate the ACF of the channel impulse response, i.e., $A_{\mathrm{c}}(\tau; t, \Delta t)$. Note that for a nonstationary channel, this ACF is a function of τ, t, and Δt. Then, we take the Fourier transform of this ACF with respect to the delay variable τ and represent the new frequency variable by Δf, i.e., $A_{\mathrm{C}}(\Delta f; t, \Delta t) = \mathcal{F}_{\tau}\{A_{\mathrm{c}}(\tau; t, \Delta t)\}$. Now, setting $\Delta f = 0$ and normalizing this ACF, we define coherence time as

$$T_{\mathrm{Coh}}(t) \coloneqq \min\left\{\Delta t : \frac{|A_{\mathrm{C}}(t, \Delta t)|}{\max|A_{\mathrm{C}}(t, \Delta t)|} \leq \gamma_{\mathrm{T}}\right\}, \tag{6.2}$$

where $A_{\mathrm{C}}(t, \Delta t) = A_{\mathrm{C}}(\Delta f = 0; t, \Delta t)$ and γ_{T} is a predefined threshold [86, 135].

Coherence Bandwidth

Coherence bandwidth is defined as the range of frequencies over which the channel remains almost constant, calculated as follows: We first obtain the Fourier transform of the channel ACF as we did in the definition of coherence time, i.e., $A_{\mathrm{C}}(\Delta f; t, \Delta t)$. Then, setting $\Delta t = 0$ and normalizing this ACF, we define coherence bandwidth as

$$B_{\mathrm{Coh}}(t) \coloneqq \min\left\{\Delta f : \frac{|A_{\mathrm{C}}(\Delta f; t)|}{\max|A_{\mathrm{C}}(\Delta f; t)|} \leq \gamma_{\mathrm{B}}\right\}, \tag{6.3}$$

where $A_{\mathrm{C}}(\Delta f; t) = A_{\mathrm{C}}(\Delta f; t, \Delta t = 0)$ and γ_{B} is a predefined threshold.

PSD of Distortion-Plus-Noise

As seen already, UAV wobbling and hardware impairments will cause both multiplicative and additive distortions to the received signal. In this chapter, we treat the additive distortion as noise, and together with additive white Gaussian noise (AWGN), study their PSDs as our last metric of interest. The PSD of nonstationary signal $x(t)$ is defined as the Fourier transform of its time-averaged ACF, i.e., $S_x(f) = \mathcal{F}_{\tau}\{\langle \mathbb{E}[x^*(t)x(t+\Delta t)]\rangle_t\}$, where $\langle y(t)\rangle_t = \lim_{T\to\infty} \frac{1}{2T}\int_{-T}^{T} y(t)\,\mathrm{d}t$ represents averaging $y(t)$ over time [144, Sec. 7.2].

6.3 Impairments-Aware Unified Channel Model

6.3.1 Preliminaries

Before presenting our channel model, we establish a connection between UAV-MPC distances at different times and the wobbling pitch angle, presented next (see Lemma 5.4 from the previous chapter for the proof).

Lemma 6.1. *Assuming that* $y_{\mathrm{D}} \ll d_i(t)$ *and* $\theta(t) \ll 1$ rad *for a wobbling UAV, we have*

$$d_i(t+\Delta t) - d_i(t) \approx y_{\mathrm{D}} \cos(\omega_i)[\theta(t+\Delta t) - \theta(t)]. \tag{6.4}$$

Corollary 6.2. *If* $\theta(t)$ *is a random process with stationary increments, i.e.,* $\theta(t+\Delta t) - \theta(t)$ *and* $\theta(\Delta t)$ *have the same distribution, we have* $d_i(t+\Delta t) - d_i(t) \approx y_{\mathrm{D}} \cos(\omega_i)\theta(\Delta t)$.

Since the distance between the transmitter and receiver changes with time due to UAV wobbling, we observe a Doppler shift in the channel. Specifically, the Doppler phase shift for the i-th MPC can be written using (6.4) as

$$\varphi_{\mathrm{D}_i}(t, \Delta t) = \frac{2\pi}{\lambda} y_{\mathrm{D}} \cos(\omega_i)[\theta(t+\Delta t) - \theta(t)], \tag{6.5}$$

where $\lambda = \frac{c}{f_{\mathrm{c}}}$ is the signal wavelength, c is the speed of light, and f_{c} is the carrier frequency.

We consider a multi-path channel with one LoS and N non-line-of-sight (NLoS) links. In Fig. 6.1, the LoS path from the UAV to the ground UE is represented by a green dashed line and the NLoS path from the UAV to the i-th MPC and then to the ground UE is represented by red dotted lines. Without hardware impairments, the received signal in the complex baseband and the channel impulse response can be written, respectively, as

$$\tilde{r}(t) = \sum_{i=0}^{N} \alpha_i(t) \mathrm{e}^{-\mathrm{j}\varphi_i(t)} \tilde{s}(t - \tau_i(t)) + \tilde{n}(t), \qquad \tilde{c}(\tau; t) = \sum_{i=0}^{N} \alpha_i(t) \mathrm{e}^{-\mathrm{j}\varphi_i(t)} \delta(\tau - \tau_i(t)), \tag{6.6}$$

where $\alpha_i(t)$, $\varphi_i(t)$, and $\tau_i(t)$ are the amplitude, phase, and delay of the i-th MPC, respectively, $\tilde{n}(t)$ is the AWGN, $\tilde{c}(\tau; t)$ is the unimpaired channel impulse response, and $\delta(.)$ is the Dirac delta function. From (6.6), one can easily verify the following convolution integral for the channel, which is considered as a linear time-variant (LTV) system:

$$\tilde{r}(t) = \int_{-\infty}^{\infty} \tilde{c}(\tau; t) \tilde{s}(t - \tau) \, \mathrm{d}\tau + \tilde{n}(t). \tag{6.7}$$

We assume that $\alpha_i(t)$ does not change considerably over the time period of interest, and thus, drop its t argument henceforth. We also consider the well-accepted Laplacian model for $|\alpha_i|^2$ as

$$|\alpha_i|^2 = \frac{1}{2\beta} \mathrm{e}^{-\frac{|\omega_i - \omega_0|}{\beta}}, \qquad 1 \le i \le N, \tag{6.8}$$

where $\beta > 0$ is a scaling parameter [134, 136] and for the AoD we assume that $\omega_i \sim U[0, \frac{\pi}{2})$. Therefore, the power of the i-th MPC is derived as $P_{\alpha_i} \coloneqq \mathbb{E}\left[|\alpha_i|^2\right] = \frac{1}{2\pi}\left(2 - \mathrm{e}^{-\frac{\omega_0}{\beta}} - \mathrm{e}^{-\frac{\pi/2 - \omega_0}{\beta}}\right)$. Furthermore, assuming Rician fading model with factor K, we can write $|\alpha_0|^2 = K \sum_{i=1}^{N} |\alpha_i|^2 =$

$K\sum_{i=1}^{N}\frac{1}{2\beta}\mathrm{e}^{-\frac{|\omega_i-\omega_0|}{\beta}}$, which gives the power of the LoS component as $P_{\alpha_0} \coloneqq \mathbb{E}\left[|\alpha_0|^2\right] = NKP_{\alpha_i}$.

The delay of the i-th MPC can be written as $\tau_i(t) \approx \tau_i(0) = \frac{d_i(0)+d_{\mathrm{S}_i,\mathrm{U}}}{c}$, where we assumed that the delay also does not change significantly over time. In fact, since the UAV-UE distance is in the order of hundreds of meters or even kilometers, the delay will be in the order of microseconds. However, using (6.4), it is clear that the added distance due to UAV wobbling is in the order of centimeters, which makes the corresponding residual delay to be in the order of nanoseconds. Hence, our approximation is valid and we also define $\tau_i \coloneqq \tau_i(0)$ for simplicity. Assuming that the location of the UE (P_{U}) is known and the MPCs are distributed randomly on the ground, the propagation delay of the i-th MPC can be written as $\tau_i = \tau_0 + \tau_{\Delta i}$, where $\tau_0 = \frac{d_0}{\mathrm{c}}$ is the UAV-UE delay and $\tau_{\Delta i}$ is the excess delay of the i-th MPC. We assume that $\tau_{\Delta i}$ is distributed exponentially with parameter ρ_i, which depends on the propagation environment [134, 145]. Therefore, the probability density functions (pdfs) of τ_0 and τ_i can be written as

$$f_{\tau_0}(\tau) = \delta(\tau-\tau_0), \qquad f_{\tau_i}(\tau) = \rho_i \mathrm{e}^{-\rho_i(\tau-\tau_0)}\mathbf{1}(\tau-\tau_0), \tag{6.9}$$

where $\mathbf{1}(.)$ is the indicator function.

As for the phase of the i-th MPC, on the other hand, the small distance variations described earlier become more important since they will be multiplied by the carrier frequency, causing Doppler phase shift. We write the phase of the i-th MPC as

$$\begin{aligned}\varphi_i(t) &= \frac{2\pi}{\lambda}\left(d_i(0)+d_{\mathrm{S}_i,\mathrm{U}}\right) + \frac{2\pi}{\lambda}y_{\mathrm{D}}\cos(\omega_i)[\theta(t)-\theta(0)] \\ &= 2\pi f_{\mathrm{c}}\tau_i + \varphi_{\mathrm{D}_i}(t),\end{aligned} \tag{6.10}$$

where $\varphi_{\mathrm{D}_i}(t) \coloneqq \varphi_{\mathrm{D}_i}(0,t)$ is the Doppler phase shift at time t given in (6.5).

6.3.2 Unified Channel Model

Now, let us revisit (6.6) when there exist hardware impairments. Using (6.1), we can write the received signal in complex baseband as

$$\begin{aligned} r(t) &= \chi_{\mathrm{R}}(t)\left[\sum_{i=0}^{N}\alpha_i(t)\mathrm{e}^{-\mathrm{j}\varphi_i(t)}s(t-\tau_i(t))\right] + \eta_{\mathrm{R}}(t) + \tilde{n}(t) \\ &= \chi_{\mathrm{R}}(t)\left[\sum_{i=0}^{N}\alpha_i(t)\mathrm{e}^{-\mathrm{j}\varphi_i(t)}\Big(\chi_{\mathrm{T}}(t-\tau_i(t))\tilde{s}(t-\tau_i(t)) + \eta_{\mathrm{T}}(t-\tau_i(t))\Big)\right] + \eta_{\mathrm{R}}(t) + \tilde{n}(t) \\ &= \sum_{i=0}^{N}\alpha_i(t)\mathrm{e}^{-\mathrm{j}\varphi_i(t)}\chi_{\mathrm{R}}(t)\chi_{\mathrm{T}}(t-\tau_i(t))\tilde{s}(t-\tau_i(t)) + n(t), \end{aligned} \tag{6.11}$$

where $n(t)$ is the combined effect of AWGN, wobbling, and hardware impairments, given as

$$n(t) = \sum_{i=0}^{N} \alpha_i(t) \mathrm{e}^{-\mathrm{j}\varphi_i(t)} \chi_{\mathrm{R}}(t) \eta_{\mathrm{T}}(t - \tau_i(t)) + \eta_{\mathrm{R}}(t) + \tilde{n}(t). \tag{6.12}$$

From (6.11), we obtain the channel impulse response as

$$c(\tau; t) = \sum_{i=0}^{N} \alpha_i(t) \mathrm{e}^{-\mathrm{j}\varphi_i(t)} \chi_{\mathrm{R}}(t) \chi_{\mathrm{T}}(t - \tau_i(t)) \delta(\tau - \tau_i(t)), \tag{6.13}$$

where the impact of UAV wobbling is hidden in the phase term, i.e., $\varphi_i(t)$ (see (6.10)), while hardware impairments manifest their effect as multiplicative distortion noises, i.e., $\chi_{\mathrm{R}}(t)$ and $\chi_{\mathrm{T}}(t - \tau_i(t))$. This modified channel impulse response together with the new noise term in (6.12), also referred to as the distortion-plus-noise process in this chapter, construct our impairments-aware unified channel model for air-to-ground wireless communications. Completely analogous to the convolution integral for the without-impairment scenario in (6.7), we can write the input-output relation of the new channel (which is also an LTV system) as $r(t) = \int_{-\infty}^{\infty} c(\tau; t) \tilde{s}(t - \tau) \, \mathrm{d}\tau + n(t)$. Note that the input to the channel will still be the unimpaired signal $\tilde{s}(t)$.

6.3.3 Metrics: General Results

In order to further characterize this unified channel model, we obtain the metrics defined in Section 6.2.3 next. The following lemma provides the channel ACF in the time-delay domain.

Lemma 6.3. *For a nonstationary air-to-ground wireless channel with physical nonidealities (due to UAV wobbling) and hardware impairments (due to intrinsic RF components), where the channel impulse response is given by (6.13), the channel ACF can be written as*

$$\begin{aligned} A_{\mathrm{c}}^{\mathrm{NonSt}}(\tau; t, \Delta t) = & \sum_{i=0}^{N} A_{\chi_{\mathrm{R}}}(t, t + \Delta t) A_{\chi_{\mathrm{T}}}(t - \tau, t - \tau + \Delta t) \\ & \times \mathbb{E}\left[|\alpha_i|^2 \exp\left\{ -\mathrm{j} \frac{2\pi}{\lambda} y_{\mathrm{D}} \cos(\omega_i) \left[\theta(t + \Delta t) - \theta(t) \right] \right\} \right] f_{\tau_i}(\tau), \end{aligned} \tag{6.14}$$

where the superscript NonSt *stands for "Non-Stationary" and $f_{\tau_i}(\tau)$ represents the pdf of τ_i.*

Proof. We write the channel ACF as

$$\begin{aligned}
A_{\mathrm{c}}^{\mathrm{NonSt}}(\tau;t,\Delta t) &= \mathbb{E}\left[c^*(\tau;t)c(\tau;t+\Delta t)\right] \\
&= \mathbb{E}\Bigg[\sum_{i=0}^{N}\sum_{k=0}^{N}\alpha_i^*\alpha_k \mathrm{e}^{-\mathrm{j}(\varphi_k(t+\Delta t)-\varphi_i(t))} \\
&\qquad \times \chi_{\mathrm{R}}^*(t)\chi_{\mathrm{R}}(t+\Delta t)\chi_{\mathrm{T}}^*(t-\tau_i)\chi_{\mathrm{T}}(t-\tau_k+\Delta t)\delta(\tau-\tau_i)\delta(\tau-\tau_k)\Bigg] \\
&= \sum_{i=0}^{N}\sum_{\substack{k=0\\k\neq i}}^{N}\mathbb{E}\Big[\alpha_i^*\alpha_k \mathrm{e}^{-\mathrm{j}\frac{2\pi}{\lambda}\left(d_k(0)+d_{\mathrm{S}_k,\mathrm{U}}-d_i(0)-d_{\mathrm{S}_i,\mathrm{U}}\right)}\mathrm{e}^{-\mathrm{j}\left(\varphi_{\mathrm{D}_k}(t+\Delta t)-\varphi_{\mathrm{D}_i}(t)\right)} \\
&\qquad \times \chi_{\mathrm{R}}^*(t)\chi_{\mathrm{R}}(t+\Delta t)\chi_{\mathrm{T}}^*(t-\tau_i)\chi_{\mathrm{T}}(t-\tau_k+\Delta t)\delta(\tau-\tau_i)\delta(\tau-\tau_k)\Big] \\
&\quad + \sum_{i=0}^{N}\mathbb{E}\Big[|\alpha_i|^2\mathrm{e}^{-\mathrm{j}\left(\varphi_{\mathrm{D}_i}(t+\Delta t)-\varphi_{\mathrm{D}_i}(t)\right)} \\
&\qquad \times \chi_{\mathrm{R}}^*(t)\chi_{\mathrm{R}}(t+\Delta t)\chi_{\mathrm{T}}^*(t-\tau_i)\chi_{\mathrm{T}}(t-\tau_i+\Delta t)\delta(\tau-\tau_i)\delta(\tau-\tau_i)\Big].
\end{aligned}$$

Since $d_{\mathrm{S}_k,\mathrm{U}} - d_{\mathrm{S}_i,\mathrm{U}} \gg \lambda$, we observe that $Z_{k,i} = \left[\frac{2\pi}{\lambda}\left(d_{\mathrm{S}_k,\mathrm{U}} - d_{\mathrm{S}_i,\mathrm{U}}\right) \bmod 2\pi\right]$ is a uniformly distributed random variable from 0 to 2π [28, Lemma 4]. Therefore, $\mathbb{E}\left[\mathrm{e}^{-\mathrm{j}Z_{k,i}}\right] = 0$ because of which the double-summation in the last equality is zero. As for the single summation term, we encounter the singularity issue (delta squared) discussed earlier in Sec. 6.2.3. To avoid this singularity problem, we isolate one of the delta functions [143] and rewrite the channel ACF with only one delta function as

$$\begin{aligned}
A_{\mathrm{c}}^{\mathrm{NonSt}}(\tau;t,\Delta t) &= \sum_{i=0}^{N}\mathbb{E}\Big[|\alpha_i|^2\mathrm{e}^{-\mathrm{j}\frac{2\pi}{\lambda}y_{\mathrm{D}}\cos(\omega_i)[\theta(t+\Delta t)-\theta(t)]} \\
&\qquad \times \chi_{\mathrm{R}}^*(t)\chi_{\mathrm{R}}(t+\Delta t)\chi_{\mathrm{T}}^*(t-\tau_i)\chi_{\mathrm{T}}(t-\tau_i+\Delta t)\delta(\tau-\tau_i)\Big] \\
&= \sum_{i=0}^{N}\int_{-\infty}^{\infty}\mathbb{E}\left[|\alpha_i|^2\mathrm{e}^{-\mathrm{j}\frac{2\pi}{\lambda}y_{\mathrm{D}}\cos(\omega_i)[\theta(t+\Delta t)-\theta(t)]}\right] \\
&\qquad \times A_{\chi_{\mathrm{R}}}(t,t+\Delta t)A_{\chi_{\mathrm{T}}}(t-\tau_i,t-\tau_i+\Delta t)\delta(\tau-\tau_i)f_{\tau_i}(\tau_i)\,\mathrm{d}\tau_i,
\end{aligned}$$

which gives the result in (6.14) by applying the sifting property of the delta function. □

The following corollary simplifies (6.14) further by considering WSS hardware impairments.

Corollary 6.4. *Assuming WSS hardware impairments, the channel ACF can be simplified as*

$$A_{\mathrm{c}}^{\mathrm{WSS}}(\tau;t,\Delta t) = \sum_{i=0}^{N}A_{\chi_{\mathrm{R}}}(\Delta t)A_{\chi_{\mathrm{T}}}(\Delta t)\,\mathbb{E}\left[|\alpha_i|^2\mathrm{e}^{-\mathrm{j}\frac{2\pi}{\lambda}y_{\mathrm{D}}\cos(\omega_i)[\theta(t+\Delta t)-\theta(t)]}\right]f_{\tau_i}(\tau). \tag{6.15}$$

Note that the superscript WSS *only pertains to "hardware" impairments, not UAV wobbling. In addition, assuming that $\theta(t)$ is a random process with stationary increments, we have*

$$A_{\mathrm{c}}^{\mathrm{WSS-SI}}(\tau;\Delta t)=\sum_{i=0}^{N}A_{\chi_{\mathrm{R}}}(\Delta t)A_{\chi_{\mathrm{T}}}(\Delta t)\,\mathbb{E}\left[|\alpha_i|^2\mathrm{e}^{-\mathrm{j}\frac{2\pi}{\lambda}y_{\mathrm{D}}\cos(\omega_i)\theta(\Delta t)}\right]f_{\tau_i}(\tau), \tag{6.16}$$

which will not be a function of t anymore. Thus, the channel in this special case becomes stationary. The abbreviation SI *in the superscript stands for "Stationary-Increments".*

The following theorem gives the channel PDP for both nonstationary and WSS impairments.

Theorem 6.5. *The PDP of the air-to-ground wireless channel for the nonstationary and WSS hardware impairments can be formulated, respectively, as*

$$P_{\mathrm{c}}^{\mathrm{NonSt}}(\tau;t)=\sum_{i=0}^{N}P_{\alpha_i}P_{\chi_{\mathrm{R}}(t)}P_{\chi_{\mathrm{T}}(t-\tau)}f_{\tau_i}(\tau),\qquad P_{\mathrm{c}}^{\mathrm{WSS}}(\tau)=\sum_{i=0}^{N}P_{\alpha_i}P_{\chi_{\mathrm{R}}}P_{\chi_{\mathrm{T}}}f_{\tau_i}(\tau), \tag{6.17}$$

where $P_{\chi_{\mathrm{R}}(t)}\coloneqq A_{\chi_{\mathrm{R}}}(t,t)=\mathbb{E}\left[|\chi_{\mathrm{R}}(t)|^2\right]$ and $P_{\chi_{\mathrm{T}}(t-\tau)}\coloneqq A_{\chi_{\mathrm{T}}}(t-\tau,t-\tau)=\mathbb{E}\left[|\chi_{\mathrm{T}}(t-\tau)|^2\right]$ are the powers of the multiplicative distortion noises at the receiver and transmitter at times t and $t-\tau$, respectively. The definitions of their WSS counterparts are similar, i.e., $P_{\chi_{\mathrm{R}}}\coloneqq\mathbb{E}\left[|\chi_{\mathrm{R}}|^2\right]$ and $P_{\chi_{\mathrm{T}}}\coloneqq\mathbb{E}\left[|\chi_{\mathrm{T}}|^2\right]$. Clearly, we also have $P_{\mathrm{c}}^{\mathrm{WSS-SI}}(\tau)=P_{\mathrm{c}}^{\mathrm{WSS}}(\tau)$.

Proof. Setting $\Delta t=0$ in (6.14) and (6.15), we get (6.17). □

Note that UAV wobbling does not play any role in determining the PDP. Further, from (6.17), we observe that the PDP will be proportional to the pdfs of the propagation delays of different MPCs [146, p. 348]. Using Theorem 6.5, we can also determine the average and root-mean-square (rms) delay spreads for nonstationary and WSS hardware impairments, respectively, as

$$\mu^{\mathrm{NonSt}}(t)=\frac{\int_0^\infty\tau P_{\mathrm{c}}(\tau;t)\,\mathrm{d}\tau}{\int_0^\infty P_{\mathrm{c}}(\tau;t)\,\mathrm{d}\tau}=\frac{\sum_{i=0}^{N}P_{\alpha_i}\int_0^\infty\tau P_{\chi_{\mathrm{T}}(t-\tau)}f_{\tau_i}(\tau)\,\mathrm{d}\tau}{\sum_{i=0}^{N}P_{\alpha_i}\int_0^\infty P_{\chi_{\mathrm{T}}(t-\tau)}f_{\tau_i}(\tau)\,\mathrm{d}\tau}, \tag{6.18}$$

$$\sigma^{\mathrm{NonSt}}(t)=\sqrt{\frac{\int_0^\infty(\tau-\mu(t))^2P_{\mathrm{c}}(\tau;t)\,\mathrm{d}\tau}{\int_0^\infty P_{\mathrm{c}}(\tau;t)\,\mathrm{d}\tau}}=\sqrt{\frac{\sum_{i=0}^{N}P_{\alpha_i}\int_0^\infty(\tau-\mu(t))^2P_{\chi_{\mathrm{T}}(t-\tau)}f_{\tau_i}(\tau)\,\mathrm{d}\tau}{\sum_{i=0}^{N}P_{\alpha_i}\int_0^\infty P_{\chi_{\mathrm{T}}(t-\tau)}f_{\tau_i}(\tau)\,\mathrm{d}\tau}}, \tag{6.19}$$

$$\mu^{\mathrm{WSS}}=\frac{\int_0^\infty\tau P_{\mathrm{c}}^{\mathrm{WSS}}(\tau)\,\mathrm{d}\tau}{\int_0^\infty P_{\mathrm{c}}^{\mathrm{WSS}}(\tau)\,\mathrm{d}\tau}=\frac{\sum_{i=0}^{N}P_{\alpha_i}\int_0^\infty\tau f_{\tau_i}(\tau)\,\mathrm{d}\tau}{\sum_{i=0}^{N}P_{\alpha_i}}, \tag{6.20}$$

$$\sigma^{\mathrm{WSS}}=\sqrt{\frac{\int_0^\infty(\tau-\mu^{\mathrm{WSS}})^2P_{\mathrm{c}}^{\mathrm{WSS}}(\tau)\,\mathrm{d}\tau}{\int_0^\infty P_{\mathrm{c}}^{\mathrm{WSS}}(\tau)\,\mathrm{d}\tau}}=\sqrt{\frac{\sum_{i=0}^{N}P_{\alpha_i}\int_0^\infty(\tau-\mu^{\mathrm{WSS}})^2f_{\tau_i}(\tau)\,\mathrm{d}\tau}{\sum_{i=0}^{N}P_{\alpha_i}}}. \tag{6.21}$$

As for the coherence time/bandwidth, we need to first derive the Fourier transform of the channel ACF with respect to the delay variable τ. For nonstationary impairments, we have

$$\begin{aligned} A_{\mathrm{C}}^{\mathrm{NonSt}}(\Delta f; t, \Delta t) &= \mathcal{F}_{\tau}\{A_{\mathrm{c}}^{\mathrm{NonSt}}(\tau; t, \Delta t)\} \\ &= \sum_{i=0}^{N} A_{\chi_{\mathrm{R}}}(t, t+\Delta t)\, \mathbb{E}\left[|\alpha_i|^2 \mathrm{e}^{-\mathrm{j}\frac{2\pi}{\lambda} y_{\mathrm{D}} \cos(\omega_i)[\theta(t+\Delta t)-\theta(t)]}\right] \\ &\quad \times \int_0^{\infty} A_{\chi_{\mathrm{T}}}(t-\tau, t-\tau+\Delta t) f_{\tau_i}(\tau) \mathrm{e}^{-\mathrm{j}2\pi\Delta f \tau}\, \mathrm{d}\tau, \end{aligned} \tag{6.22}$$

while for the WSS hardware impairments, (6.22) can be simplified as

$$\begin{aligned} A_{\mathrm{C}}^{\mathrm{WSS}}(\Delta f; t, \Delta t) &= \sum_{i=0}^{N} A_{\chi_{\mathrm{R}}}(\Delta t) A_{\chi_{\mathrm{T}}}(\Delta t)\, \mathbb{E}\left[|\alpha_i|^2 \mathrm{e}^{-\mathrm{j}\frac{2\pi}{\lambda} y_{\mathrm{D}} \cos(\omega_i)[\theta(t+\Delta t)-\theta(t)]}\right] \\ &\quad \times \int_0^{\infty} f_{\tau_i}(\tau) \mathrm{e}^{-\mathrm{j}2\pi\Delta f \tau}\, \mathrm{d}\tau. \end{aligned} \tag{6.23}$$

Note that when $\theta(t)$ has the stationary-increments property, (6.23) is further simplified as

$$A_{\mathrm{C}}^{\mathrm{WSS-SI}}(\Delta f; \Delta t) = \sum_{i=0}^{N} A_{\chi_{\mathrm{R}}}(\Delta t) A_{\chi_{\mathrm{T}}}(\Delta t)\, \mathbb{E}\left[|\alpha_i|^2 \mathrm{e}^{-\mathrm{j}\frac{2\pi}{\lambda} y_{\mathrm{D}} \cos(\omega_i)\theta(\Delta t)}\right] \int_0^{\infty} f_{\tau_i}(\tau) \mathrm{e}^{-\mathrm{j}2\pi\Delta f \tau}\, \mathrm{d}\tau, \tag{6.24}$$

which is not a function of t anymore. The following two theorems give the coherence time and coherence bandwidth of the channel, respectively.

Theorem 6.6. *The coherence time of the air-to-ground channel can be formulated as in (6.2), where the ACFs for nonstationary and WSS hardware impairments can be written, respectively, as*

$$\begin{aligned} A_{\mathrm{C}}^{\mathrm{NonSt}}(t, \Delta t) &= \sum_{i=0}^{N} A_{\chi_{\mathrm{R}}}(t, t+\Delta t)\, \mathbb{E}\left[|\alpha_i|^2 \mathrm{e}^{-\mathrm{j}\frac{2\pi}{\lambda} y_{\mathrm{D}} \cos(\omega_i)[\theta(t+\Delta t)-\theta(t)]}\right] \\ &\quad \times \int_0^{\infty} A_{\chi_{\mathrm{T}}}(t-\tau, t-\tau+\Delta t) f_{\tau_i}(\tau)\, \mathrm{d}\tau, \end{aligned} \tag{6.25}$$

$$A_{\mathrm{C}}^{\mathrm{WSS}}(t, \Delta t) = \sum_{i=0}^{N} A_{\chi_{\mathrm{R}}}(\Delta t) A_{\chi_{\mathrm{T}}}(\Delta t)\, \mathbb{E}\left[|\alpha_i|^2 \mathrm{e}^{-\mathrm{j}\frac{2\pi}{\lambda} y_{\mathrm{D}} \cos(\omega_i)[\theta(t+\Delta t)-\theta(t)]}\right]. \tag{6.26}$$

Furthermore, when $\theta(t)$ is a random process with stationary increments, we have

$$A_{\mathrm{C}}^{\mathrm{WSS-SI}}(\Delta t) = \sum_{i=0}^{N} A_{\chi_{\mathrm{R}}}(\Delta t) A_{\chi_{\mathrm{T}}}(\Delta t)\, \mathbb{E}\left[|\alpha_i|^2 \mathrm{e}^{-\mathrm{j}\frac{2\pi}{\lambda} y_{\mathrm{D}} \cos(\omega_i)\theta(\Delta t)}\right]. \tag{6.27}$$

Proof. Setting $\Delta f = 0$ in (6.22), (6.23), and (6.24), we end up with the final results. □

Theorem 6.7. *The coherence bandwidth of the air-to-ground channel can be formulated as in (6.3), where the ACFs for nonstationary and WSS hardware impairments can be written, respectively, as*

$$A_{\mathrm{C}}^{\mathrm{NonSt}}(\Delta f; t) = \sum_{i=0}^{N} P_{\alpha_i} P_{\chi_{\mathrm{R}}(t)} \int_0^{\infty} P_{\chi_{\mathrm{T}}(t-\tau)} f_{\tau_i}(\tau) \mathrm{e}^{-\mathrm{j}2\pi\Delta f\tau}\, \mathrm{d}\tau, \tag{6.28}$$

$$A_{\mathrm{C}}^{\mathrm{WSS}}(\Delta f) = \sum_{i=0}^{N} P_{\alpha_i} P_{\chi_{\mathrm{R}}} P_{\chi_{\mathrm{T}}} \int_0^{\infty} f_{\tau_i}(\tau) \mathrm{e}^{-\mathrm{j}2\pi\Delta f\tau}\, \mathrm{d}\tau. \tag{6.29}$$

Clearly, we also have $A_{\mathrm{C}}^{\mathrm{WSS-SI}}(\Delta f) = A_{\mathrm{C}}^{\mathrm{WSS}}(\Delta f)$.

Proof. Setting $\Delta t = 0$ in (6.22) and (6.23), we end up with the final results. □

Remark 6.8. Since only the normalized values of the ACFs matter for the sake of evaluating the coherence bandwidth, we can ignore $P_{\chi_{\mathrm{R}}(t)}$ and $P_{\chi_{\mathrm{R}}} P_{\chi_{\mathrm{T}}}$ in (6.28) and (6.29), respectively, as they are not functions of Δf or the summation dummy variable i.

Remark 6.9. It is interesting to note that hardware impairments, when assumed to be WSS, as well as UAV wobbling do not have any impact on the channel coherence bandwidth.

Up until now, our focus was mainly on the characteristics of the channel, where using the channel impulse response $c(\tau; t)$, we studied the PDP, coherence time, and coherence bandwidth. Note that one can easily obtain other channel-related metrics, such as delay spread and Doppler spread by using the metrics derived in this section. Let us now study the behavior of the effective received noise at the ground UE by analyzing the PSD of the aggregate distortion caused by UAV wobbling and hardware impairments at both the transmitter and receiver plus the AWGN at the receiver, i.e., $n(t)$ defined in (6.12). The following theorem establishes this result.

Theorem 6.10. *The PSD of the distortion-plus-noise process $n(t)$ can be written as*

$$S_n^{\mathrm{NonSt}}(f) = \frac{N_0}{2} + \mathcal{F}_{\Delta t}\{\langle A_{\eta_{\mathrm{R}}}(t, t+\Delta t)\rangle_t\} + \sum_{i=0}^{N} \mathcal{F}_{\Delta t}\Bigg\{\Big\langle A_{\chi_{\mathrm{R}}}(t, t+\Delta t) \times \mathbb{E}\left[|\alpha_i|^2 \mathrm{e}^{-\mathrm{j}\frac{2\pi}{\lambda} y_{\mathrm{D}} \cos(\omega_i)[\theta(t+\Delta t)-\theta(t)]}\right] \int_0^{\infty} A_{\eta_{\mathrm{T}}}(t-\tau_i, t-\tau_i+\Delta t) f_{\tau_i}(\tau_i)\, \mathrm{d}\tau_i \Big\rangle_t\Bigg\}, \tag{6.30}$$

where $\frac{N_0}{2}$ is the AWGN power and $\langle . \rangle_t$ denotes averaging over time.

Proof. We start by writing the ACF of $n(t)$ as

$$\begin{aligned}
A_n^{\mathrm{NonSt}}(t,t+\Delta t) &= \mathbb{E}\left[n^*(t)n(t+\Delta t)\right] \\
&\overset{(a)}{=} \mathbb{E}\left[\tilde{n}^*(t)\tilde{n}(t+\Delta t)\right] + \mathbb{E}\left[\eta_{\mathrm{R}}^*(t)\eta_{\mathrm{R}}(t+\Delta t)\right] \\
&\quad + \mathbb{E}\Bigg[\Bigg(\sum_{i=0}^{N}\alpha_i^*\mathrm{e}^{\mathrm{j}\varphi_i(t)}\chi_{\mathrm{R}}^*(t)\eta_{\mathrm{T}}^*(t-\tau_i(t))\Bigg) \\
&\qquad \times \Bigg(\sum_{i=0}^{N}\alpha_i\mathrm{e}^{-\mathrm{j}\varphi_i(t+\Delta t)}\chi_{\mathrm{R}}(t+\Delta t)\eta_{\mathrm{T}}(t+\Delta t-\tau_i(t+\Delta t))\Bigg)\Bigg] \\
&\overset{(b)}{=} A_{\tilde{n}}(\Delta t) + A_{\eta_{\mathrm{R}}}(t,t+\Delta t) + \mathbb{E}\Bigg[\sum_{i=0}^{N}|\alpha_i|^2\mathrm{e}^{-\mathrm{j}(\varphi_i(t+\Delta t)-\varphi_i(t))} \\
&\quad \times \chi_{\mathrm{R}}^*(t)\chi_{\mathrm{R}}(t+\Delta t)\eta_{\mathrm{T}}^*(t-\tau_i)\eta_{\mathrm{T}}(t-\tau_i+\Delta t)\Bigg] \\
&= A_{\tilde{n}}(\Delta t) + A_{\eta_{\mathrm{R}}}(t,t+\Delta t) + \sum_{i=0}^{N}A_{\chi_{\mathrm{R}}}(t,t+\Delta t) \\
&\quad \times \mathbb{E}\left[|\alpha_i|^2\mathrm{e}^{-\mathrm{j}\frac{2\pi}{\lambda}y_{\mathrm{D}}\cos(\omega_i)[\theta(t+\Delta t)-\theta(t)]}\right]\int_0^{\infty}A_{\eta_{\mathrm{T}}}(t-\tau_i,t-\tau_i+\Delta t)f_{\tau_i}(\tau_i)\,\mathrm{d}\tau_i,
\end{aligned}$$

where in (a) we used the independence between distortion noises and AWGN and the assumption that $\eta_{\mathrm{R}}(t)$ and $\tilde{n}(t)$ have zero means, and in (b) we used the same reasoning as in the proof of Lemma 6.3 to demonstrate that the cross terms in the double-summation are zero, and we also used the approximation $\tau_i(t) \approx \tau_i(0) = \tau_i$. Note that $\tilde{n}(t)$ is a white process, and thus, we have $A_{\tilde{n}}(\Delta t) = \frac{N_0}{2}\delta(\Delta t)$, where $\frac{N_0}{2}$ is the noise power. To obtain the PSD of any nonstationary random process, we need to first average its ACF over time t, and then take its Fourier transform with respect to Δt [144, Sec. 7.2]. Therefore, the PSD of $n(t)$ can be written as in (6.30). □

Corollary 6.11. *The PSD of the distortion-plus-noise process $n(t)$ when hardware impairments are WSS can be written as*

$$\begin{aligned}
S_n^{\mathrm{WSS}}(f) &= \frac{N_0}{2} + \mathcal{F}_{\Delta t}\{A_{\eta_{\mathrm{R}}}(\Delta t)\} \\
&\quad + \sum_{i=0}^{N}\mathcal{F}_{\Delta t}\Bigg\{A_{\chi_{\mathrm{R}}}(\Delta t)A_{\eta_{\mathrm{T}}}(\Delta t)\Big\langle\mathbb{E}\left[|\alpha_i|^2\mathrm{e}^{-\mathrm{j}\frac{2\pi}{\lambda}y_{\mathrm{D}}\cos(\omega_i)[\theta(t+\Delta t)-\theta(t)]}\right]\Big\rangle_t\Bigg\}. \qquad (6.31)
\end{aligned}$$

Also, assuming that $\theta(t)$ is a random process with stationary increments, this result is further simplified as

$$\begin{aligned}
S_n^{\mathrm{WSS-SI}}(f) &= \frac{N_0}{2} + \mathcal{F}_{\Delta t}\{A_{\eta_{\mathrm{R}}}(\Delta t)\} \\
&\quad + \sum_{i=0}^{N}\mathcal{F}_{\Delta t}\Bigg\{A_{\chi_{\mathrm{R}}}(\Delta t)A_{\eta_{\mathrm{T}}}(\Delta t)\mathbb{E}\left[|\alpha_i|^2\mathrm{e}^{-\mathrm{j}\frac{2\pi}{\lambda}y_{\mathrm{D}}\cos(\omega_i)\theta(\Delta t)}\right]\Bigg\}. \qquad (6.32)
\end{aligned}$$

Proof. Following the proof of Theorem 6.10 and assuming WSS hardware impairments, the ACF of $n(t)$ can be simplified as

$$A_n^{\mathrm{WSS}}(t, t+\Delta t) = A_{\tilde{n}}(\Delta t) + A_{\eta_{\mathrm{R}}}(\Delta t) + \sum_{i=0}^{N} A_{\chi_{\mathrm{R}}}(\Delta t) A_{\eta_{\mathrm{T}}}(\Delta t) \mathbb{E}\left[|\alpha_i|^2 \mathrm{e}^{-\mathrm{j}\frac{2\pi}{\lambda} y_{\mathrm{D}} \cos(\omega_i)[\theta(t+\Delta t)-\theta(t)]}\right],$$

which results in (6.31) after averaging over t and taking the Fourier transform with respect to Δt. Moreover, if we assume that $\theta(t)$ is a random process with stationary increments, the process $n(t)$ becomes stationary and we have

$$A_n^{\mathrm{WSS-SI}}(\Delta t) = A_{\tilde{n}}(\Delta t) + A_{\eta_{\mathrm{R}}}(\Delta t) + \sum_{i=0}^{N} A_{\chi_{\mathrm{R}}}(\Delta t) A_{\eta_{\mathrm{T}}}(\Delta t) \mathbb{E}\left[|\alpha_i|^2 \mathrm{e}^{-\mathrm{j}\frac{2\pi}{\lambda} y_{\mathrm{D}} \cos(\omega_i)\theta(\Delta t)}\right],$$

which gives (6.32) after taking its Fourier transform. □

6.3.4 Metrics: Evaluations for Some Case Studies

The results we have derived so far are general and hold for any UAV wobbling model and any distribution of delay and distortion noise processes. However, to gain useful insights, it is instructive to simplify these results for specific case studies. We consider some reasonable models in this section and evaluate the metrics derived in the previous section accordingly.

UAV Wobbling

We consider two different random processes for modeling the UAV pitch angle $\theta(t)$: (i) Wiener process, and (ii) sinusoidal process. Let us review the properties of each process first.

- **Stationary-Increments – Wiener Process**: This canonical model is defined as a process with independent, stationary, and Gaussian increments that is continuous in time t. Furthermore, its value at $t = 0$ is assumed to be zero. Therefore, we have $\theta(t+\Delta t) - \theta(t) \overset{\text{dist.}}{=\!=} \theta(\Delta t) \sim \mathcal{N}(0, \Delta t)$, where $\overset{\text{dist.}}{=\!=}$ stands for equality in distribution. Since Wiener processes are scale-invariant, we can make the variance of $\theta(\Delta t)$ dimensionless by multiplying it with the proportionality constant $b = 1\ \mathrm{s}^{-1}$. Following the characteristic function (cf) of Gaussian random variables, we have

$$\mathbb{E}\left[\mathrm{e}^{\mathrm{j}\omega(\theta(t+\Delta t)-\theta(t))}\right] = \mathbb{E}\left[\mathrm{e}^{\mathrm{j}\omega\theta(\Delta t)}\right] = \mathrm{e}^{-\frac{\omega^2}{2}\Delta t}. \tag{6.33}$$

- **Non-Stationary-Increments – Sinusoidal Process**: This model is motivated by the random *oscillatory* behavior of wobbling. We assume that $\theta(t) = L\sin(2\pi Q t)$,

where $L \sim U[-\theta_{\rm m}, \theta_{\rm m})$ and $Q \sim f_Q(q)$ are the amplitude and frequency of the variations of the UAV pitch angle, respectively, with $\theta_{\rm m}$ and $f_Q(.)$ being the maximum UAV pitch angle and some given pdf, respectively. We also assume that L and Q are independent. Clearly, the independent and stationary-increments property does not hold for this process. Following the cf of uniform random variables, we have

$$\mathbb{E}\left[\mathrm{e}^{\mathrm{j}\omega(\theta(t+\Delta t)-\theta(t))}\right] = \int_{-\infty}^{\infty} \mathrm{sinc}\left(\frac{\omega}{\pi}\theta_{\rm m}\left(\sin(2\pi q(t+\Delta t)) - \sin(2\pi q t)\right)\right) f_Q(q)\,\mathrm{d}q, \quad (6.34)$$

where $\mathrm{sinc}(x) = \frac{\sin(\pi x)}{\pi x}$.

Using (6.8), (6.33), and (6.34), we introduce and evaluate the following relations which will be used extensively in our derivations:

$$\begin{aligned} G_i^{\rm SI}(\Delta t) &= \mathbb{E}\left[|\alpha_i|^2 \mathrm{e}^{-\mathrm{j}\frac{2\pi}{\lambda} y_{\rm D}\cos(\omega_i)\theta(\Delta t)}\right] \\ &= \begin{cases} \int_0^{\pi/2} \frac{1}{\pi\beta} \mathrm{e}^{-\frac{|\omega_i-\omega_0|}{\beta}} \mathrm{e}^{-\frac{2\pi^2}{\lambda^2} y_{\rm D}^2 \cos^2(\omega_i)\Delta t}\,\mathrm{d}\omega_i, & i \neq 0 \\ 2NKP_{\alpha_1} \mathrm{e}^{-\frac{2\pi^2}{\lambda^2} y_{\rm D}^2 \cos^2(\omega_0)\Delta t}, & i = 0, \end{cases} \end{aligned} \quad (6.35)$$

$$\begin{aligned} G_i^{\rm NonSI}(t,\Delta t) &= \mathbb{E}\left[|\alpha_i|^2 \mathrm{e}^{-\mathrm{j}\frac{2\pi}{\lambda} y_{\rm D}\cos(\omega_i)[\theta(t+\Delta t)-\theta(t)]}\right] \\ &= \begin{cases} \int_0^{\pi/2} \int_{-\infty}^{\infty} \frac{1}{\pi\beta} \mathrm{e}^{-\frac{|\omega_i-\omega_0|}{\beta}} f_Q(q) \\ \quad \times \mathrm{sinc}\left(\frac{2}{\lambda}\theta_{\rm m} y_{\rm D}\cos(\omega_i)\left(\sin(2\pi q(t+\Delta t)) - \sin(2\pi q t)\right)\right) \mathrm{d}q\,\mathrm{d}\omega_i, & i \neq 0 \\ 2NKP_{\alpha_1} \int_{-\infty}^{\infty} f_Q(q) \\ \quad \times \mathrm{sinc}\left(\frac{2}{\lambda}\theta_{\rm m} y_{\rm D}\cos(\omega_0)\left(\sin(2\pi q(t+\Delta t)) - \sin(2\pi q t)\right)\right) \mathrm{d}q, & i = 0, \end{cases} \end{aligned} \quad (6.36)$$

where the superscript NonSI stands for "Non-Stationary-Increments". Note that the functions $G_i^{\rm NonSI}(t,\Delta t),\ 1 \le i \le N$ are all equal to each other. The same is also true for the functions $G_i^{\rm SI}(\Delta t),\ 1 \le i \le N$.

Distortion Noises

As for the additive distortion noise, we assume WSS Gaussian processes both at the transmitter and receiver, which is backed by measurements and theoretical studies [49, 50]. Although various models are available for the covariance function of Gaussian processes [147], we consider the squared exponential model in this chapter. Hence, the ACFs for the additive distortion noises can be written as

$$A_{\eta_{\rm T}}(\Delta t) = \kappa_{\eta_{\rm T}}^2 \mathrm{e}^{-\frac{(\Delta t)^2}{2l_{\eta_{\rm T}}^2}}, \qquad A_{\eta_{\rm R}}(\Delta t) = \kappa_{\eta_{\rm R}}^2 \mathrm{e}^{-\frac{(\Delta t)^2}{2l_{\eta_{\rm R}}^2}}, \quad (6.37)$$

where $\kappa_{\eta_{\rm T}}^2$ ($\kappa_{\eta_{\rm R}}^2$) and $l_{\eta_{\rm T}}$ ($l_{\eta_{\rm R}}$) are design parameters, which represent the maximum power and the characteristic length-scale of the additive distortion noise process at the transmitter

(receiver), respectively. On the other hand, the research on representative models for the multiplicative distortion noise processes is scarce. As also pointed out in [49, p. 261], researchers usually ignore the time-dependence and randomness of these distortion processes and assume deterministic multiplicative errors. In this chapter, we study two representative models based on random processes (WSS and nonstationary) for these multiplicative errors listed below:

- **WSS – Gaussian Process**: Similar to the additive distortion noise, we assume the canonical Gaussian process for the WSS multiplicative distortion noises. The ACFs in this case can be written as

$$A_{\chi_{\mathrm{T}}}(\Delta t) = \kappa^2_{\chi_{\mathrm{T}}} \mathrm{e}^{-\frac{(\Delta t)^2}{2l^2_{\chi_{\mathrm{T}}}}}, \qquad A_{\chi_{\mathrm{R}}}(\Delta t) = \kappa^2_{\chi_{\mathrm{R}}} \mathrm{e}^{-\frac{(\Delta t)^2}{2l^2_{\chi_{\mathrm{R}}}}}, \tag{6.38}$$

  where $\kappa^2_{\chi_{\mathrm{T}}}$, $\kappa^2_{\chi_{\mathrm{R}}}$, $l_{\chi_{\mathrm{T}}}$, and $l_{\chi_{\mathrm{R}}}$ are defined similar as before.

- **Nonstationary – Sinusoidal Process**: As a canonical nonstationary model, we again use the sinusoidal process in this case that was also used to model UAV wobbling above. In particular, we define $\chi_{\mathrm{T}}(t) = L_{\mathrm{T}} \sin(2\pi Q_{\mathrm{T}} t)$ and $\chi_{\mathrm{R}}(t) = L_{\mathrm{R}} \sin(2\pi Q_{\mathrm{R}} t)$, where L_{T} (L_{R}) and Q_{T} (Q_{R}) are the amplitude and frequency of variations of $\chi_{\mathrm{T}}(t)$ ($\chi_{\mathrm{R}}(t)$), respectively. Therefore, we can write their ACFs as

$$A_{\chi_{\mathrm{T}}}(t, t+\Delta t) = P_{L_{\mathrm{T}}} \int_{-\infty}^{\infty} \sin(2\pi q t) \sin(2\pi q (t+\Delta t)) f_{Q_{\mathrm{T}}}(q)\, \mathrm{d}q, \tag{6.39}$$

$$A_{\chi_{\mathrm{R}}}(t, t+\Delta t) = P_{L_{\mathrm{R}}} \int_{-\infty}^{\infty} \sin(2\pi q t) \sin(2\pi q (t+\Delta t)) f_{Q_{\mathrm{R}}}(q)\, \mathrm{d}q, , \tag{6.40}$$

  where $P_{L_{\mathrm{T}}} = \mathbb{E}\left[|L_{\mathrm{T}}|^2\right]$, $P_{L_{\mathrm{R}}} = \mathbb{E}\left[|L_{\mathrm{R}}|^2\right]$, and $f_{Q_{\mathrm{T}}}(.)$ and $f_{Q_{\mathrm{R}}}(.)$ are the pdfs of Q_{T} and Q_{R}, respectively. Further discussion about the choice of different parameters for this model will be provided in Section 6.4.

Remark 6.12. In the nonstationary setup, one could also assume a Wiener process for the multiplicative distortion noise processes. However, since the ACF of the Wiener process $W(t)$ is simply the minimum value of its observation times, i.e., $A_W(t, t+\Delta t) = t$ for non-negative Δt, all of our metrics will quickly diverge using this model. Hence, the Wiener process is not a suitable model for the multiplicative distortion noise.

Using these models for UAV wobbling and distortion noise processes, we will now evaluate the metrics derived in Section 6.3.3.

PDP: Using Theorem 6.5, we obtain the PDP for nonstationary and WSS hardware im-

pairments, respectively, as

$$P_{\mathrm{c}}^{\mathrm{NonSt}}(\tau;t) = P_{\alpha_1} P_{L_{\mathrm{R}}} P_{L_{\mathrm{T}}} \int_{-\infty}^{\infty} \sin^2(2\pi q t) f_{Q_{\mathrm{R}}}(q)\,\mathrm{d}q \int_{-\infty}^{\infty} \sin^2(2\pi q(t-\tau)) f_{Q_{\mathrm{T}}}(q)\,\mathrm{d}q \times \left(NK\delta(\tau-\tau_0) + \sum_{i=1}^{N} \rho_i \mathrm{e}^{-\rho_i(\tau-\tau_0)} \mathbf{1}(\tau-\tau_0) \right), \tag{6.41}$$

$$P_{\mathrm{c}}^{\mathrm{WSS}}(\tau) = P_{\alpha_1} \kappa_{\chi_{\mathrm{R}}}^2 \kappa_{\chi_{\mathrm{T}}}^2 \left(NK\delta(\tau-\tau_0) + \sum_{i=1}^{N} \rho_i \mathrm{e}^{-\rho_i(\tau-\tau_0)} \mathbf{1}(\tau-\tau_0) \right), \tag{6.42}$$

where we used the relations $P_{\alpha_i} = P_{\alpha_1} = \frac{1}{2\pi}\left(2 - \mathrm{e}^{-\frac{\omega_0}{\beta}} - \mathrm{e}^{-\frac{\pi/2-\omega_0}{\beta}}\right)$, $1 \le i \le N$, and $P_{\alpha_0} = NKP_{\alpha_1}$. From (6.20) and (6.21), we obtain the average and rms delay spreads for WSS hardware impairments, respectively, as

$$\mu^{\mathrm{WSS}} = \tau_0 + \frac{1}{N(K+1)} \sum_{i=1}^{N} \frac{1}{\rho_i}, \tag{6.43}$$

$$\sigma^{\mathrm{WSS}} = \sqrt{\frac{2}{N(K+1)} \sum_{i=1}^{N} \frac{1}{\rho_i^2} - \frac{1}{N^2(K+1)^2} \left(\sum_{i=1}^{N} \frac{1}{\rho_i} \right)^2}. \tag{6.44}$$

Coherence Time: From Theorem 6.6, (6.35), and (6.36), one can obtain the coherence time of the channel for different impairment scenarios. Since the equations become quite intricate in all cases, we need to perform numerical integration to calculate the coherence time. However, when hardware impairments are WSS, the final equations could be simplified further. Using the predefined functions $G_i^{\mathrm{NonSI}}(t,\Delta t)$ and $G_i^{\mathrm{SI}}(\Delta t)$, we can simplify the ACFs as

$$A_{\mathrm{C}}^{\mathrm{WSS}}(t,\Delta t) = \kappa_{\chi_{\mathrm{R}}}^2 \kappa_{\chi_{\mathrm{T}}}^2 \mathrm{e}^{-\left(\frac{1}{2l_{\chi_{\mathrm{R}}}^2} + \frac{1}{2l_{\chi_{\mathrm{T}}}^2}\right)(\Delta t)^2} \left(G_0^{\mathrm{NonSI}}(t,\Delta t) + NG_1^{\mathrm{NonSI}}(t,\Delta t) \right),$$

$$A_{\mathrm{C}}^{\mathrm{WSS-SI}}(\Delta t) = \kappa_{\chi_{\mathrm{R}}}^2 \kappa_{\chi_{\mathrm{T}}}^2 \mathrm{e}^{-\left(\frac{1}{2l_{\chi_{\mathrm{R}}}^2} + \frac{1}{2l_{\chi_{\mathrm{T}}}^2}\right)(\Delta t)^2} \left(G_0^{\mathrm{SI}}(\Delta t) + NG_1^{\mathrm{SI}}(\Delta t) \right),$$

where we used the fact that $G_i^{\mathrm{NonSI}}(t,\Delta t) = G_1^{\mathrm{NonSI}}(t,\Delta t)$, $1 \le i \le N$, and $G_i^{\mathrm{SI}}(\Delta t) = G_1^{\mathrm{SI}}(\Delta t)$, $1 \le i \le N$. Note that the maximum value for both ACFs is $2\kappa_{\chi_{\mathrm{R}}}^2 \kappa_{\chi_{\mathrm{T}}}^2 N(K+1)P_{\alpha_1}$, which occurs at $\Delta t = 0$. Therefore, the coherence time for WSS hardware impairments when $\theta(t)$ does not and does have the stationary-increments property can be written, respectively,

as

$$T_{\text{Coh}}^{\text{WSS}}(t) = \min\left\{\Delta t : \frac{\mathrm{e}^{-\left(\frac{1}{2l_{\chi_{\text{R}}}^2}+\frac{1}{2l_{\chi_{\text{T}}}^2}\right)(\Delta t)^2}\left|G_0^{\text{NonSI}}(t,\Delta t)+NG_1^{\text{NonSI}}(t,\Delta t)\right|}{2N(K+1)P_{\alpha_1}} \leq \gamma_{\text{T}}\right\}, \quad (6.45)$$

$$T_{\text{Coh}}^{\text{WSS-SI}} = \min\left\{\Delta t : \frac{\mathrm{e}^{-\left(\frac{1}{2l_{\chi_{\text{R}}}^2}+\frac{1}{2l_{\chi_{\text{T}}}^2}\right)(\Delta t)^2}\left|G_0^{\text{SI}}(\Delta t)+NG_1^{\text{SI}}(\Delta t)\right|}{2N(K+1)P_{\alpha_1}} \leq \gamma_{\text{T}}\right\}, \quad (6.46)$$

which needs to be solved numerically for Δt.

Coherence Bandwidth: We use Theorem 6.7 along with (6.38), (6.39), and (6.40) to derive the coherence bandwidth of the channel. Following Remark 6.8, we do not need to evaluate $P_{\chi_{\text{R}}(t)}$ and $P_{\chi_{\text{R}}}P_{\chi_{\text{T}}}$ in (6.28) and (6.29), respectively, as they will be canceled out when normalizing the ACF. Let us start with simplifying the channel ACF when hardware impairments are nonstationary. Setting $\Delta t = 0$ and $t \mapsto t-\tau$ in (6.39), and swapping the integrals in (6.28), we can write

$$\begin{aligned}
A_{\text{C}}^{\text{NonSt}}(\Delta f;t) &= P_{\alpha_1}P_{\chi_{\text{R}}(t)}P_{L_{\text{T}}}\Bigg[NK\int_{-\infty}^{\infty} f_{Q_{\text{T}}}(q)\int_{0}^{\infty}\sin^2(2\pi q(t-\tau))\delta(\tau-\tau_0)\mathrm{e}^{-\mathrm{j}2\pi\Delta f\tau}\,\mathrm{d}\tau\,\mathrm{d}q \\
&\quad + \sum_{i=1}^{N}\int_{-\infty}^{\infty} f_{Q_{\text{T}}}(q)\int_{\tau_0}^{\infty}\sin^2(2\pi q(t-\tau))\rho_i\mathrm{e}^{-\rho_i(\tau-\tau_0)}\mathrm{e}^{-\mathrm{j}2\pi\Delta f\tau}\,\mathrm{d}\tau\,\mathrm{d}q\Bigg] \\
&= P_{\alpha_1}P_{\chi_{\text{R}}(t)}P_{L_{\text{T}}}\mathrm{e}^{-\mathrm{j}2\pi\Delta f\tau_0}\left[H_0(t)+\sum_{i=1}^{N}H_i(\Delta f;t)\right],
\end{aligned}$$

where

$$\begin{aligned}
H_0(t) &= NK\int_{-\infty}^{\infty} f_{Q_{\text{T}}}(q)\sin^2(2\pi q(t-\tau_0))\,\mathrm{d}q, \\
H_i(\Delta f;t) &= \frac{\rho_i}{2(\rho_i+\mathrm{j}2\pi\Delta f)} - \int_{-\infty}^{\infty} f_{Q_{\text{T}}}(q)\left(\frac{\rho_i\mathrm{e}^{\mathrm{j}4\pi q(t-\tau_0)}}{4(\rho_i+\mathrm{j}2\pi\Delta f+\mathrm{j}4\pi q)} + \frac{\rho_i\mathrm{e}^{-\mathrm{j}4\pi q(t-\tau_0)}}{4(\rho_i+\mathrm{j}2\pi\Delta f-\mathrm{j}4\pi q)}\right)\mathrm{d}q.
\end{aligned}$$

Taking the absolute value of $A_{\text{C}}^{\text{NonSt}}(\Delta f;t)$, we can write the coherence bandwidth as

$$B_{\text{Coh}}^{\text{NonSt}}(t) = \min\left\{\Delta f : \frac{\left|H_0(t)+\sum_{i=1}^{N}H_i(\Delta f;t)\right|}{\max\left|H_0(t)+\sum_{i=1}^{N}H_i(\Delta f;t)\right|} \leq \gamma_{\text{B}}\right\}, \quad (6.47)$$

which needs to be solved numerically for Δf. On the other hand, for WSS hardware impair-

ments, the channel ACF can be further simplified as

$$A_{\mathrm{C}}^{\mathrm{WSS}}(\Delta f) = P_{\alpha_1} P_{\chi_{\mathrm{R}}} P_{\chi_{\mathrm{T}}} \left[NK \int_0^{\infty} \delta(\tau - \tau_0) \mathrm{e}^{-\mathrm{j}2\pi\Delta f \tau} \, \mathrm{d}\tau + \sum_{i=1}^{N} \int_{\tau_0}^{\infty} \rho_i \mathrm{e}^{-\rho_i(\tau-\tau_0)} \mathrm{e}^{-\mathrm{j}2\pi\Delta f \tau} \, \mathrm{d}\tau \right]$$
$$= P_{\alpha_1} P_{\chi_{\mathrm{R}}} P_{\chi_{\mathrm{T}}} \mathrm{e}^{-\mathrm{j}2\pi\Delta f \tau_0} \left[NK + \sum_{i=1}^{N} \frac{\rho_i}{\rho_i + \mathrm{j}2\pi\Delta f} \right],$$

which gives the coherence bandwidth as

$$B_{\mathrm{Coh}}^{\mathrm{WSS}} = \min \left\{ \Delta f : \frac{\left| K + \frac{1}{N} \sum_{i=1}^{N} \frac{\rho_i}{\rho_i + \mathrm{j}2\pi\Delta f} \right|}{K+1} \leq \gamma_{\mathrm{B}} \right\}. \tag{6.48}$$

Observe that the coherence bandwidth is not a function of UAV wobbling or hardware impairments in this case (see Remark 6.9).

PSD of Distortion-Plus-Noise: Theorem 6.10 gives the PSD of the distortion-plus-noise process $n(t)$ for the general case where hardware impairments are nonstationary and UAV wobbling does not necessarily have the stationary-increments property. One could use (6.34), (6.37), and (6.40) to obtain an equation for the PSD of $n(t)$, but as is clear from the form of these equations, this derivation quickly becomes intractable. Therefore, for the sake of simplicity, we only analytically evaluate the PSD of the distortion-plus-noise process when hardware impairments are WSS. Let us first analyze the PSD of $n(t)$ when UAV wobbling has the stationary-increments property. Following (6.32) in Corollary 6.11, we have

$$S_n^{\mathrm{WSS-SI}}(f) = \frac{N_0}{2} + \mathcal{F}_{\Delta t} \left\{ \kappa_{\eta_{\mathrm{R}}}^2 \mathrm{e}^{-\frac{(\Delta t)^2}{2l_{\eta_{\mathrm{R}}}^2}} \right\} + \sum_{i=0}^{N} \mathcal{F}_{\Delta t} \left\{ \kappa_{\chi_{\mathrm{R}}}^2 \mathrm{e}^{-\frac{(\Delta t)^2}{2l_{\chi_{\mathrm{R}}}^2}} \kappa_{\eta_{\mathrm{T}}}^2 \mathrm{e}^{-\frac{(\Delta t)^2}{2l_{\eta_{\mathrm{T}}}^2}} G_i^{\mathrm{SI}}(\Delta t) \right\}$$
$$= \frac{N_0}{2} + \mathcal{F}_{\Delta t} \left\{ \kappa_{\eta_{\mathrm{R}}}^2 \mathrm{e}^{-\frac{(\Delta t)^2}{2l_{\eta_{\mathrm{R}}}^2}} \right\} + \mathcal{F}_{\Delta t} \left\{ \kappa^2 \mathrm{e}^{-\frac{(\Delta t)^2}{2l^2}} 2NKP_{\alpha_1} \mathrm{e}^{-u^2 \cos^2(\omega_0)\Delta t} \right\}$$
$$+ N\mathcal{F}_{\Delta t} \left\{ \kappa^2 \mathrm{e}^{-\frac{(\Delta t)^2}{2l^2}} \int_0^{\pi/2} \frac{1}{\pi\beta} \mathrm{e}^{-\frac{|\omega_i - \omega_0|}{\beta}} \mathrm{e}^{-u^2 \cos^2(\omega_i)\Delta t} \, \mathrm{d}\omega_i \right\}$$
$$= \frac{N_0}{2} + \kappa_{\eta_{\mathrm{R}}}^2 \sqrt{2\pi l_{\eta_{\mathrm{R}}}^2} \mathrm{e}^{-2\pi^2 l_{\eta_{\mathrm{R}}}^2 f^2} + \kappa^2 \sqrt{2\pi l^2} \mathrm{e}^{-2\pi^2 l^2 f^2} \Bigg(2P_{\alpha_0} \mathrm{e}^{\frac{1}{2} l^2 u^4 \cos^4(\omega_0)} \mathrm{e}^{\mathrm{j}2\pi l^2 u^2 \cos^2(\omega_0) f}$$
$$+ N \int_0^{\pi/2} \frac{1}{\pi\beta} \mathrm{e}^{-\frac{|\omega_i - \omega_0|}{\beta}} \mathrm{e}^{\frac{1}{2} l^2 u^4 \cos^4(\omega_i)} \mathrm{e}^{\mathrm{j}2\pi l^2 u^2 \cos^2(\omega_i) f} \, \mathrm{d}\omega_i \Bigg), \tag{6.49}$$

where we defined the parameters $\kappa^2 = \kappa_{\chi_{\mathrm{R}}}^2 \kappa_{\eta_{\mathrm{T}}}^2$, $l^{-2} = l_{\chi_{\mathrm{R}}}^{-2} + l_{\eta_{\mathrm{T}}}^{-2}$, and $u^2 = \frac{2\pi^2}{\lambda^2} y_{\mathrm{D}}^2$ to simplify the equations, and in the last equality we used the Fourier transform of a Gaussian function, i.e., $\mathcal{F}_x \left\{ \mathrm{e}^{-ax^2} \right\} = \sqrt{\frac{\pi}{a}} \mathrm{e}^{-\frac{\pi^2}{a} f^2}$. As for the case where UAV wobbling does not have the stationary-increments property (see (6.31) in Corollary 6.11), we need to first average $G_i^{\mathrm{NonSI}}(t, \Delta t)$ over

time t. Following the same procedure as above, we can write the PSD of $n(t)$ as

$$\begin{aligned} S_n^{\mathrm{WSS}}(f) &= \frac{N_0}{2} + \mathcal{F}_{\Delta t}\left\{\kappa_{\eta_{\mathrm{R}}}^2 \mathrm{e}^{-\frac{(\Delta t)^2}{2l_{\eta_{\mathrm{R}}}^2}}\right\} + \sum_{i=0}^{N} \mathcal{F}_{\Delta t}\left\{\kappa_{\chi_{\mathrm{R}}}^2 \mathrm{e}^{-\frac{(\Delta t)^2}{2l_{\chi_{\mathrm{R}}}^2}} \kappa_{\eta_{\mathrm{T}}}^2 \mathrm{e}^{-\frac{(\Delta t)^2}{2l_{\eta_{\mathrm{T}}}^2}} \left\langle G_i^{\mathrm{NonSI}}(t,\Delta t)\right\rangle_t\right\} \\ &= \frac{N_0}{2} + \kappa_{\eta_{\mathrm{R}}}^2 \sqrt{2\pi l_{\eta_{\mathrm{R}}}^2} \mathrm{e}^{-2\pi^2 l_{\eta_{\mathrm{R}}}^2 f^2} + 2P_{\alpha_0} \lim_{T\to\infty} \frac{1}{T} \int_0^T \int_{-\infty}^{\infty} \int_{-\infty}^{\infty} \kappa^2 \mathrm{e}^{-\frac{(\Delta t)^2}{2l^2}} f_Q(q) \\ &\quad \times \operatorname{sinc}\left(\frac{2}{\lambda}\theta_{\mathrm{m}} y_{\mathrm{D}} \cos(\omega_0)\left(\sin(2\pi q(t+\Delta t)) - \sin(2\pi q t)\right)\right) \mathrm{e}^{-\mathrm{j}2\pi f \Delta t}\, \mathrm{d}q\, \mathrm{d}\Delta t\, \mathrm{d}t \\ &\quad + N \lim_{T\to\infty} \frac{1}{T} \int_0^T \int_{-\infty}^{\infty} \int_0^{\frac{\pi}{2}} \int_{-\infty}^{\infty} \kappa^2 \mathrm{e}^{-\frac{(\Delta t)^2}{2l^2}} \frac{1}{\pi\beta} \mathrm{e}^{-\frac{|\omega_i - \omega_0|}{\beta}} f_Q(q) \\ &\quad \times \operatorname{sinc}\left(\frac{2}{\lambda}\theta_{\mathrm{m}} y_{\mathrm{D}} \cos(\omega_i)\left(\sin(2\pi q(t+\Delta t)) - \sin(2\pi q t)\right)\right) \mathrm{e}^{-\mathrm{j}2\pi f \Delta t}\, \mathrm{d}q\, \mathrm{d}\omega_i\, \mathrm{d}\Delta t\, \mathrm{d}t, \end{aligned} \tag{6.50}$$

where in the last equality we used the definition of Fourier transform and swapped the order of limit and integral.

6.4 Simulation Results

In this section, we provide numerical results to obtain further insights on the impact of UAV wobbling and hardware impairments on the key performance metrics of wireless channels. We assume that a rotary-winged UAV hovers in the air and communicates with a UE on the ground in a multi-path channel. The parameters of the channel used in this chapter are as follows: Number of MPCs $N \in \{20, 10\}$ for sub-6 GHz and mmWave frequencies, respectively, carrier frequency $f_{\mathrm{c}} \in \{2.4, 6, 30\}$ GHz (thus, signal wavelength $\lambda \in \{12.5, 5, 1\}$ cm), UAV-UE distance $d_0 = 300$ m (thus, UAV-UE delay $\tau_0 = 1$ μs), UAV-UE AoD $\omega_0 = 20°$, reciprocal of the mean excess delay of the i-th MPC $\rho_i \sim U[10^7, 10^8)$ s^{-1}, Rician K factor $K \in \{0, 1, 5, 11.5\}$ [137, Table 1] (note that $K = 0$ represents the Rayleigh channel), scaling parameter of the Laplacian angular power spectrum $\beta = 1$, and noise power $\frac{N_0}{2} = 5 \times 10^{-9}$ W. The UAV antenna is placed at a distance of $y_{\mathrm{D}} = 40$ cm from the UAV platform centroid. Due to many reasons discussed earlier, the UAV may wobble, which is modeled using two random processes, i.e., the Wiener and sinusoidal processes. The UAV pitch angle in the latter case is bounded to $\theta_{\mathrm{m}} \in \{5, 7, 10\}°$ [41] with a frequency of variations that is uniformly distributed between 5 and 25 Hz. Both the UAV and the UE suffer from hardware impairments as well, and the parameters defined in this chapter for modeling the hardware impairments are as follows: Maximum power and the characteristic length-scale of the WSS additive/multiplicative distortion noise processes at the transmitter/receiver are $\{\kappa_{\eta_{\mathrm{T}}}^2, \kappa_{\eta_{\mathrm{R}}}^2, \kappa_{\chi_{\mathrm{T}}}^2, \kappa_{\chi_{\mathrm{R}}}^2\} \in \{0.1, 0.5, 1\}$ W and $\{l_{\eta_{\mathrm{T}}}, l_{\eta_{\mathrm{R}}}, l_{\chi_{\mathrm{T}}}, l_{\chi_{\mathrm{R}}}\} \in \{0.01, 0.05, 0.1\}$ s, respectively, and power of amplitude and frequency of variations of nonstationary multiplicative distortion

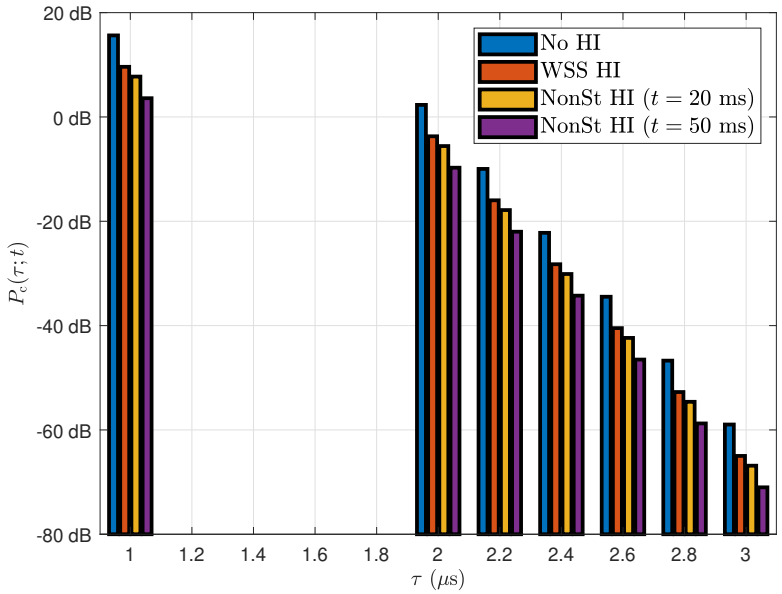

Figure 6.2: PDP for ideal and impaired hardware scenarios. Assumptions: $N = 20$, $K = 11.5$, and $\kappa^2_{\chi_{\mathrm{T}}} = \kappa^2_{\chi_{\mathrm{R}}} = 0.5$ W. HI stands for hardware impairment.

noise process at the transmitter/receiver are $P_{L_{\mathrm{T}}} = P_{L_{\mathrm{R}}} = 0.5$ W and $\{Q_{\mathrm{T}}, Q_{\mathrm{R}}\} \sim U[5, 15)$ Hz, respectively.

6.4.1 PDP

In Fig. 6.2, we plot the PDP for different scenarios. In particular, we highlight the impact of hardware impairments on the PDP by comparing the ideal case (no hardware impairment) with those of impaired scenarios. The gap in the power of the received signal between the ideal and impaired cases is clear in this figure, which is around 6 dB for WSS hardware impairments with $\kappa^2_{\chi_{\mathrm{T}}} = \kappa^2_{\chi_{\mathrm{R}}} = 0.5$ W. As shown before, note that UAV wobbling has no impact on the PDP. It can also be observed that the difference between the WSS and nonstationary hardware impairments in terms of their respective PDPs is not very high. This observation further motivates the use of WSS processes for modeling hardware impairments as they are more tractable than nonstationary models, which are otherwise more realistic [49, Sec. 7.2.3].

6.4.2 Coherence Time

We show the impact of UAV wobbling and hardware impairments on the channel coherence time in Figs. 6.3-6.6. The general trends of the normalized channel ACF for the Wiener

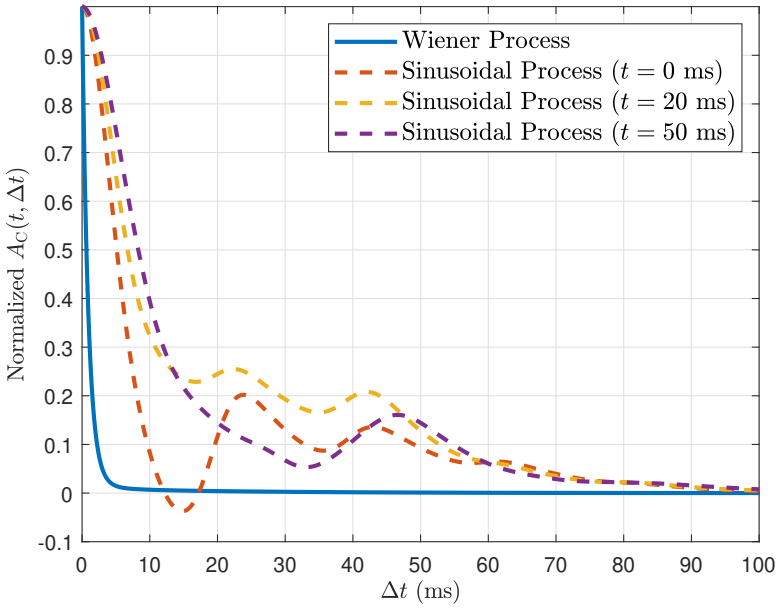

Figure 6.3: Coherence time: Normalized channel ACF for different random processes. Assumptions: $N = 20$, $K = 11.5$, $f_c = 6$ GHz, $\theta_m = 5°$, and $l_{\chi T} = l_{\chi R} = 0.05$ s.

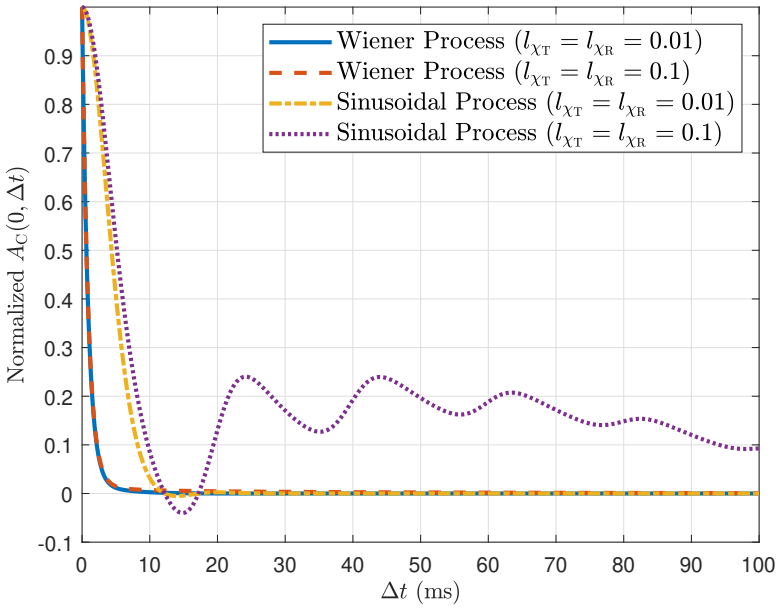

Figure 6.4: Coherence time: Normalized channel ACF for different random processes and impairment levels. Assumptions: $N = 20$, $K = 11.5$, $f_c = 6$ GHz, and $\theta_m = 5°$.

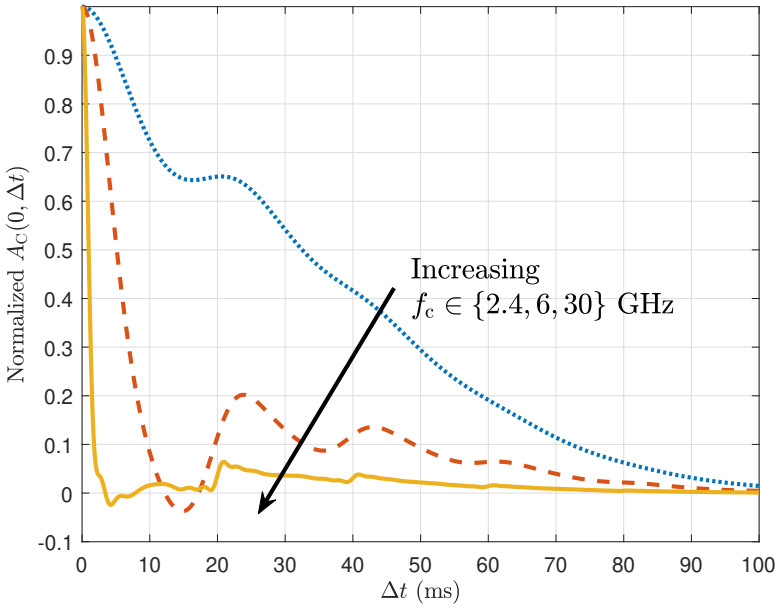

Figure 6.5: Coherence time: Normalized channel ACF for different f_c. Assumptions: $K = 11.5$, $\theta_m = 5°$, and $l_{\chi_T} = l_{\chi_R} = 0.05$ s.

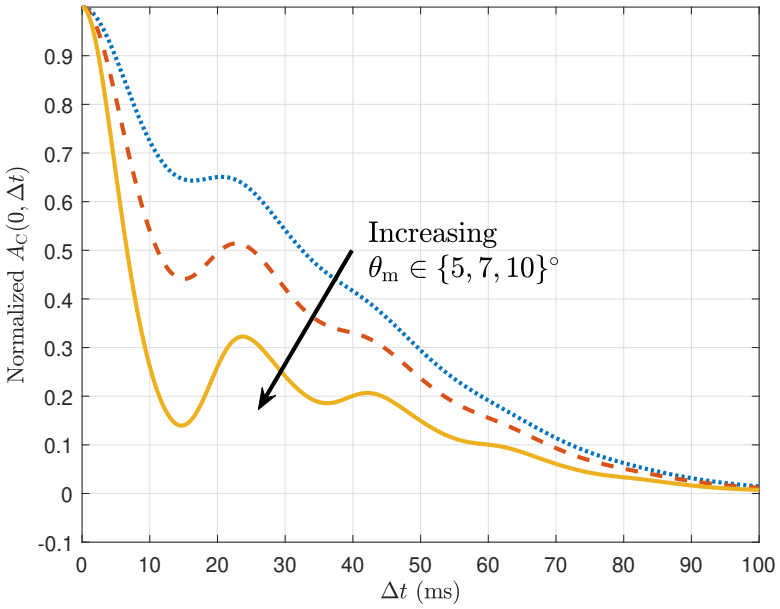

Figure 6.6: Coherence time: Normalized channel ACF for different θ_m. Assumptions: $K = 11.5$, $f_c = 2.4$ GHz, and $l_{\chi_T} = l_{\chi_R} = 0.05$ s.

and sinusoidal processes are depicted in Fig. 6.3. Note that we used the WSS hardware impairment model to obtain these figures. Since the channel ACF becomes nonstationary for the sinusoidal process, we plotted it at different time instants to show its progression over time. Also, from this figure, we observe that channel coherence time is minimized at $t = 0$ s, and thus, we use this time instant as a representative one to determine the channel coherence time. Assuming that $\gamma_{\mathrm{T}} = 0.5$, we find that $T_{\mathrm{Coh}}^{\mathrm{WSS}}(0) = 5.13$ ms and $T_{\mathrm{Coh}}^{\mathrm{WSS-SI}} = 643$ μs, which makes sense intuitively, as the variations in $\theta(t)$ for the Wiener process can grow without bounds. In Fig. 6.4, we compare the normalized channel ACF for different random processes and impairment levels. As seen in this figure, hardware impairments do not have any noticeable effect on the channel ACF when $\theta(t)$ follows the Wiener process. Although this was expected, we observe that hardware impairments do not severely degrade coherence time for the sinusoidal process either. In particular, we have $T_{\mathrm{Coh}}^{\mathrm{WSS-SI}} = \{639, 643\}$ μs and $T_{\mathrm{Coh}}^{\mathrm{WSS}}(0) = \{4.36, 5.16\}$ ms for $l_{\chi_{\mathrm{T}}} = l_{\chi_{\mathrm{R}}} = \{0.01, 0.1\}$ s. The impact of carrier frequency and maximum UAV pitch angle on the coherence time for the sinusoidal process is depicted in Figs. 6.5 and 6.6. From (6.10) and (6.11), we observe that the channel phase directly depends on the UAV-UE distance and the carrier frequency. Therefore, increasing θ_{m} (thus, the UAV-UE distance) or f_{c} results in higher channel variations, which, in turn, decreases the channel coherence time. Numerically speaking, we have $T_{\mathrm{Coh}}^{\mathrm{WSS}}(0) = \{32.52, 5.13, 0.98\}$ ms for $f_{\mathrm{c}} = \{2.4, 6, 30\}$ GHz and $\theta_{\mathrm{m}} = 5^{\circ}$ and $T_{\mathrm{Coh}}^{\mathrm{WSS}}(0) = \{32.52, 11.13, 6.63\}$ ms for $\theta_{\mathrm{m}} = \{5, 7, 10\}^{\circ}$ and $f_{\mathrm{c}} = 2.4$ GHz. As is clear from these numbers, channel coherence time is heavily degraded at high frequencies due to UAV wobbling and hardware impairments (less than 1 ms at $f_{\mathrm{c}} = 30$ GHz), which renders channel estimation and tracking very challenging.

6.4.3 Coherence Bandwidth

In Figs. 6.7 and 6.8, we plot the normalized channel ACF as a function of Δf to investigate the impact of different impairments on the channel coherence bandwidth. From (6.48), we observe for WSS hardware impairments that the normalized ACF monotonically goes from 1 to $\frac{K}{K+1}$ as Δf goes from 0 to ∞. Interestingly, Fig. 6.7 shows that this is also the case for nonstationary hardware impairments as long as $t > \tau_0$. Assuming that $\gamma_{\mathrm{B}} = 0.95$, we have $B_{\mathrm{Coh}}^{\mathrm{WSS}} = 10.75$ MHz and $B_{\mathrm{Coh}}^{\mathrm{NonSt}}(t) = \{0.51, 12.21, 11.21\}$ MHz at $t = \{\tau_0, 2\tau_0, 4\tau_0\}$. Note that the behavior of the nonstationary hardware impairments quickly converges to that of the WSS one. In Fig. 6.8, we show the channel ACF at time instant $t = 0$ s for different Rician K factors. As the power of the LoS link increases with respect to the powers of other MPCs, we expect to have lower delay spreads, and thus, higher coherence bandwidths.

6.4.4 PSD of Distortion-Plus-Noise

We provide numerical results for the PSD of $n(t)$ in Figs. 6.9-6.11. Assuming both Wiener and sinusoidal models for UAV wobbling, we plot the PSD of $n(t)$ for different hardware

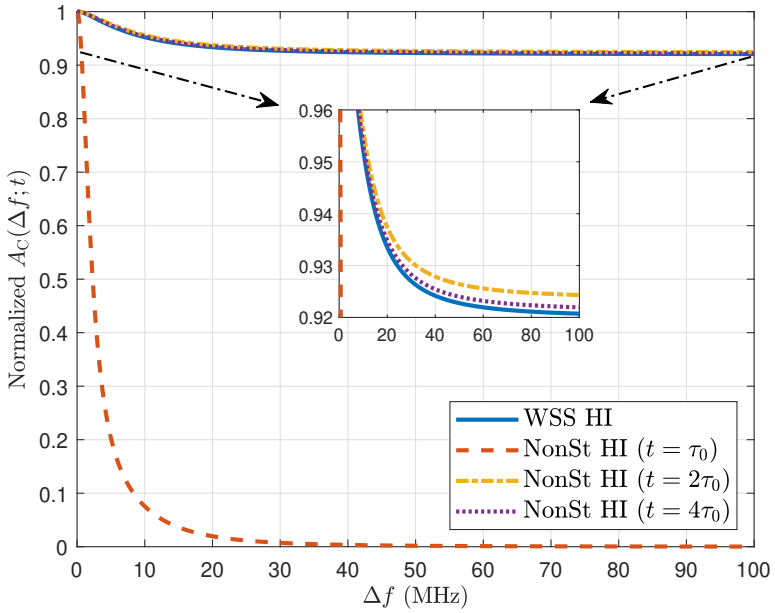

Figure 6.7: Coherence bandwidth: Normalized channel ACF for different impairment models and times t. Assumptions: $N = 20$ and $K = 11.5$.

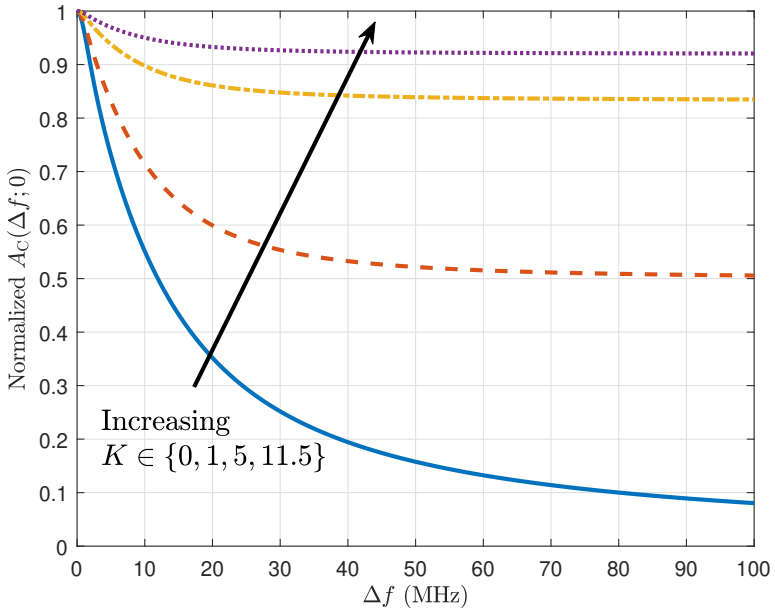

Figure 6.8: Coherence bandwidth: Normalized channel ACF for different Rician K factors. Assumptions: WSS hardware impairments and $N = 20$.

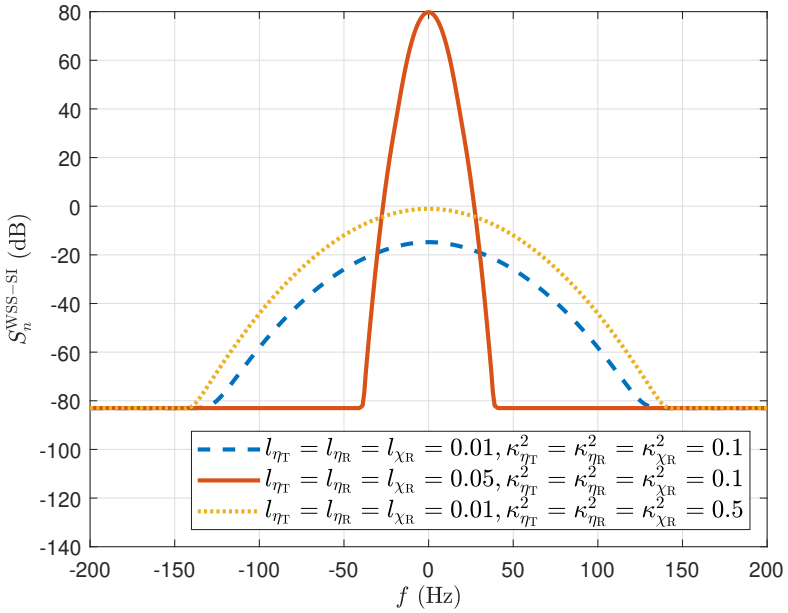

Figure 6.9: PSD of $n(t)$ for different impairment levels. Assumptions: Wiener wobbling, WSS hardware impairments, $N = 20$, $K = 11.5$, $f_{\mathrm{c}} = 2.4$ GHz, and $\theta_{\mathrm{m}} = 5°$.

impairment levels in Figs. 6.9 and 6.10, respectively. We observe that increasing the maximum power of the WSS hardware impairment model (κ^2 parameters, e.g., $\kappa^2_{\eta_{\mathrm{T}}}$) while keeping the characteristic length-scale of this model (l parameters, e.g., $l_{\eta_{\mathrm{T}}}$) constant simply shifts the PSD upward (in dB), which means that the total power of $n(t)$ (integral of its PSD) increases. On the other hand, increasing the l parameters while keeping the κ^2 parameters constant squeezes the PSD curve toward the 0 Hz frequency, which could either increase or decrease the total distortion-plus-noise power depending on the specific values of the l and κ^2 parameters and the wobbling model. In Fig. 6.11, we assume that UAV wobbling follows a sinusoidal model and compare the PSD of $n(t)$ for different values of the maximum UAV pitch angle. As is clear in this figure and assuming realistic values for θ_{m}, the PSD of $n(t)$ is resilient to this impairment and does not degrade noticeably with increasing the maximum UAV pitch angle.

6.5 Chapter Summary

In this chapter, we developed a unified air-to-ground channel model that accounts for multiple impairment types. Specifically, we considered a multi-path Rician channel, where a ground UE receives data from a hovering UAV via one LoS and multiple NLoS paths. Two fundamentally different impairment types have been considered in this chapter, i.e.,

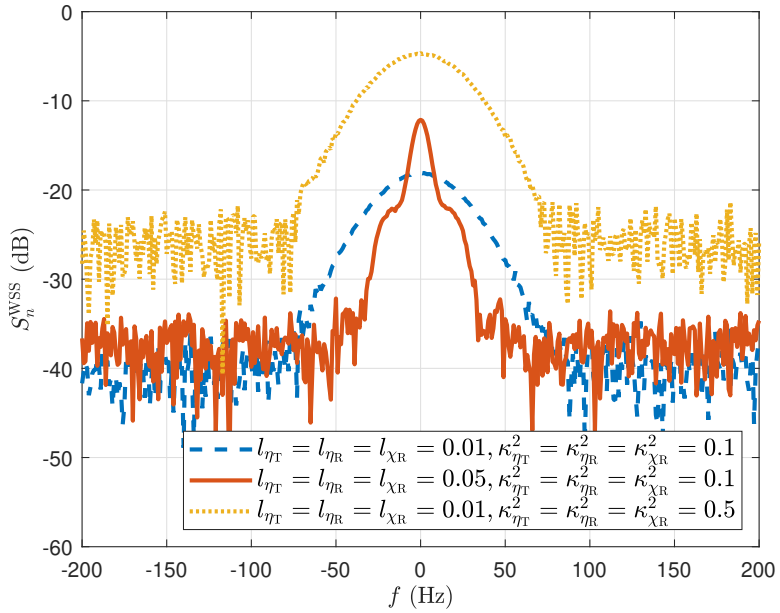

Figure 6.10: PSD of $n(t)$ for different impairment levels. Assumptions: Sinusoidal wobbling, WSS hardware impairments, $N = 20$, $K = 11.5$, $f_\mathrm{c} = 2.4$ GHz, and $\theta_\mathrm{m} = 5°$.

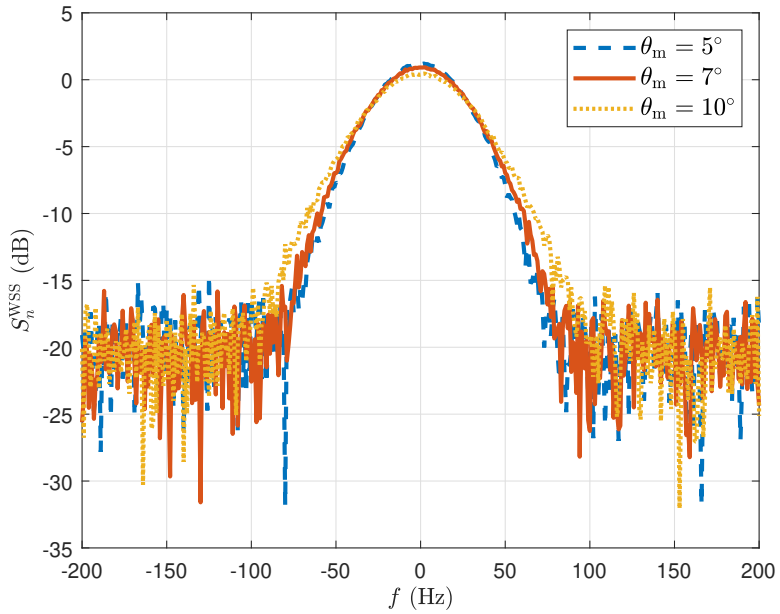

Figure 6.11: PSD of $n(t)$ for different θ_m. Assumptions: WSS hardware impairments, $N = 20$, $K = 11.5$, $f_\mathrm{c} = 2.4$ GHz, $\kappa^2_{\eta_\mathrm{T}} = \kappa^2_{\eta_\mathrm{R}} = \kappa^2_{\chi_\mathrm{R}} = 1$ W, and $l_{\eta_\mathrm{T}} = l_{\eta_\mathrm{R}} = l_{\chi_\mathrm{R}} = 0.01$ s.

UAV wobbling and hardware impairments (RF nonidealities at both the UAV and the UE). We modeled the UAV pitch angle wobbling by two different stochastic processes, one with independent and stationary increments (the Wiener process) and another with bounded fluctuations to represent the oscillatory nature of wobbling (the sinusoidal process). As for the RF nonidealities, we modeled the combined effect of all hardware impairments as two multiplicative and additive distortion noise processes. Using these models, we concretely analyzed the channel ACF and provided easy-to-use equations for four key channel-related metrics, i.e., PDP, coherence time, coherence bandwidth, and PSD of the distortion-plus-noise process. Our results demonstrated a heavy degradation of the channel coherence time at high carrier frequencies due to UAV wobbling and hardware impairments, which effectively makes channel estimation more challenging at mmWave and higher frequencies. To the best of our knowledge, this is the first work that provides a comprehensive analysis of the joint effect of UAV wobbling and hardware impairments on the air-to-ground wireless channel. One meaningful extension of this work is to provide the same analysis when the UAV is mobile, which makes the effective Doppler phase shift even more complicated. Also, analyzing the air-to-ground impairments-aware wireless channel when centralized or distributed MIMO setups are considered (instead of single-antenna transceivers) is another future line of research.

Chapter 7

Conclusion and Future Works

In this dissertation, we studied various fundamental problems related to the idea of UAV-assisted wireless networks. While the mathematical tools and results developed throughout the dissertation are obviously of interest to wireless and stochastic geometry communities in academia, several of our ideas and results are also of current interest to wireless communications industry. For instance, we explored the idea of installing an additional uptilted antenna at the BS site and evaluated its advantages over the conventional downtilted antennas in Chapter 2. This addition is not too costly and increases the coverage probability of the network significantly. We examined the SL mobility model in Chapters 3 and 4, which was inspired by the 3GPP and is used as a baseline for measuring the impact of mobility in UAV networks, and also for comparison with other more advanced mobility models (and we showed it acts as a lower bound in terms of performance). Another important aspect of UAV communications is the fact that UAVs, unlike terrestrial BSs, may wobble randomly, which could have detrimental effects on the received signal. This phenomenon, which is of interest to industrial implementation of the UAVs as well, has been explored in detail in Chapters 5 and 6, and industry researchers and practitioners should be cognizant of this behaviour. In particular, a key implication of our results is the degradation of channel coherence time due to random UAV wobbling, especially at high carrier frequencies, which makes channel tracking very challenging.

In this chapter, we summarize the main contributions of this dissertation and briefly discuss the potential future problems and research directions of drone cellular networks.

7.1 Conclusion

In this dissertation, we have studied various aspects of wireless communications involving UAVs. In particular, wireless backhaul using UAVs in 3D aerial-terrestrial cellular networks was studied in Chapter 2, where the works of this chapter have been published in IEEE journals and conferences [59, 60]. Moving forward to the case of mobile UAVs, we analyzed canonical mobility models and handover probability in drone cellular networks in Chapters 3 and 4, respectively. The results of these chapters have also been published in IEEE journals and conferences [64, 81, 82, 84, 85]. After that, we focused on the wireless channel in Chapters 5 and 6 and studied the impact of UAV wobbling and hardware impairments on

the air-to-ground wireless channel. Some of the works in these chapters have been published and some have been submitted for possible publications in IEEE journals and conferences [86, 148, 149]. More details are provided next.

In Chapter 2, we studied the performance of two-hop backhaul-aware 3D cellular networks, where BSs and UAVs coexist to serve the UEs on the ground. Specifically, each UE either connects directly to a fiber-backhauled terrestrial BS (access link), or connects first to a UAV which is then wirelessly backhauled to a terrestrial BS (joint access and backhaul). Inspired by the 3GPP studies, we used realistic antenna patterns for both BSs and UAVs. Due to the high probability of LoS in air-to-ground wireless communications, we adopted a probabilistic channel model for the UAV-UE links that incorporates both LoS and NLoS channel conditions. Following the max-power association policy, we characterized the network coverage performance for two well-known relaying protocols, i.e., AF and DF, by identifying and analyzing the building blocks of their SINR expressions. We also provided a comprehensive analysis of the joint distribution of distance and zenith angle of the closest and serving UAV to the typical UE in a 3D setting using tools from stochastic geometry. Moreover, since the UAV backhaul link could be much weaker than its access link due to the BS antenna sidelobes and nulls, we analyzed the addition of an uptilted directional antenna at the BS site for improving the UAV backhaul link.

In Chapter 3, we presented an in-depth and unified analysis of a mobile drone cellular network operating at a constant height to serve the UEs on the ground. Specifically, we considered four mobility models for the DBSs, i.e., (i) SL, (ii) RS, (iii) RW, and (iv) RWP, and provided several fundamental distributional properties of these models. The use of the SL mobility model for drone networks was inspired by the simulation models used in the 3GPP studies of drone networks, while the others are useful canonical models (or their variants) that have been used extensively in wireless networks and provide a reasonable balance between realism and tractability. The serving DBS is selected based on the nearest-neighbor association policy and moves according to two service models: (i) based on the same mobility model as the interfering DBSs (UIM), and (ii) towards the typical UE at a constant height and keeps hovering above the location of the typical UE (UDM). We proposed a novel characterization of the point process of DBSs for both the UIM and the UDM, using which we analyzed the average received rate and the session rate at the typical UE. Borrowing tools from the calculus of variations, we mathematically showed that the SL mobility model acts as a lower bound on the system-level performance of our mobile drone network over the space of all i.i.d. mobility models.

In Chapter 4, we provided a concrete mathematical treatment of the handover probability in drone cellular networks. Assuming that DBSs move along straight lines and in uniformly random directions, we considered two mobility scenarios for the DBSs: (i) SSM, where all DBSs move with the same speed, and (ii) DSM, where DBSs have different speeds. We then established a duality in terms of the handover probability between the SSM and a terrestrial network where all the BSs are static and a reference UE moves along a straight line. For the DSM, we characterized the point process of non-serving DBSs, using which we derived

a lower bound for the handover probability of the network.

In Chapter 5, we provided a rigorous mathematical analysis for the coherence time of the channel when UAVs experience random pitch wobbling. Assuming a Rician multi-path channel model, we considered two different scenarios for the number of UAVs communicating with the UE, i.e., SUS and MUS, and modeled the UAV pitch wobbling by random processes. For both the SUS and MUS, we formulated the channel ACF and derived the coherence time of the channel. Specifically in the MUS, we showed that the channels between the UAVs and the UE are uncorrelated from each other and the channel autocorrelation matrix is only determined by its diagonal elements. Our analysis demonstrated that even for small UAV pitch wobbling, the coherence time of the channel could be severely affected, thus making channel estimation and symbol detection difficult.

In Chapter 6, we developed a unified air-to-ground channel model that accounts for multiple physical and hardware impairments. Specifically, we considered a multi-path Rician channel, where a ground UE receives data from a hovering UAV via one LoS and multiple NLoS paths. Two fundamentally different impairment types have been considered in this chapter, i.e., physical impairments (UAV wobbling) and hardware impairments (RF nonidealities at both the UAV and the UE). We modeled the UAV pitch angle wobbling by two different stochastic processes, one with independent and stationary increments (the Wiener process) and another with bounded fluctuations to represent the oscillatory nature of the wobbling (the sinusoidal process). As for the RF nonidealities, we modeled the combined effect of all hardware impairments as two multiplicative and additive distortion noise processes. Using these models, we concretely analyzed the channel ACF and provided easy-to-use equations for four key channel-related metrics, i.e., PDP, coherence time, coherence bandwidth, and PSD of the distortion-plus-noise process. One important observation from our analysis was the high sensitivity of coherence time to both UAV wobbling and hardware impairments, especially at high frequencies, which renders channel tracking very difficult.

7.2 Future Works

We will now discuss some open problems inspired by this dissertation research.

Multi-Hop Aerial-Terrestrial Cellular Networks. We have already studied UAV-assisted aerial-terrestrial wireless backhaul networks in a two-hop setting in Chapter 2. Extending the current two-hop analysis to a multi-hop setting using the nearest neighbor routing policy is an interesting future work. Note that the nearest neighbor routing strategy may not be optimal as it does not solve an optimization problem in essence. Therefore, another future direction in this line of research could be to find the optimal routing strategy in a multi-hop aerial-terrestrial setting using 3GPP-based practical antenna and channel models for both the AF and DF relaying schemes.

Advanced Mobility Models for Drone Cellular Networks. In Chapters 3 and 4,

we extensively studied the performance of drone cellular networks under various canonical mobility models. One promising future direction could be the use of advanced mathematical techniques, such as stochastic differential equations, to design more sophisticated drone trajectories that are fitted to more realistic mobility models. Another interesting future work is to use our insights from Chapter 2 to extend the results of these chapters to more general 3D networks.

Impairment-Aware Channel Model for Mobile Drone Cellular Networks. One of the fundamental assumptions in Chapters 5 and 6 was that both the UAV and the UE were static (*albeit* the UAV was wobbling at it hovering location). As we have seen in the previous chapters, mobility adds a new dimension to the system design, and thus, one meaningful extension of these works is to provide the same analysis when the UAV is mobile, which makes the effective Doppler phase shift even more complicated. Also, analyzing the air-to-ground impairment-aware wireless channel under centralized or distributed MIMO setups (instead of single-antenna transceivers) is another interesting line of future research.

Bibliography

[1] S. Chandrasekharan *et al.*, "Designing and implementing future aerial communication networks," *IEEE Commun. Mag.*, vol. 54, pp. 26–34, May 2016.

[2] M. Mozaffari, W. Saad, M. Bennis, Y. Nam, and M. Debbah, "A tutorial on UAVs for wireless networks: Applications, challenges, and open problems," *IEEE Commun. Surveys Tuts.*, vol. 21, pp. 2334–2360, 3rd Quart. 2019.

[3] A. Merwaday, A. Tuncer, A. Kumbhar, and I. Guvenc, "Improved throughput coverage in natural disasters: Unmanned aerial base stations for public-safety communications," *IEEE Veh. Technol. Mag.*, vol. 11, pp. 53–60, Dec. 2016.

[4] I. Bor-Yaliniz and H. Yanikomeroglu, "The new frontier in RAN heterogeneity: Multi-tier drone-cells," *IEEE Commun. Mag.*, vol. 54, pp. 48–55, Nov. 2016.

[5] 3GPP, "Study on enhanced LTE support for aerial vehicles," Tech. Rep. 36.777, 3rd Generation Partnership Project (3GPP), 01 2018.

[6] 3GPP, "Enhancement for unmanned aerial vehicles," Tech. Rep. 22.829, 3rd Generation Partnership Project (3GPP), 11 2018.

[7] Z. Li *et al.*, "Development and design methodology of an anti-vibration system on micro-UAVs," in *Proc. Int. Micro Air Veh. Conf. Flight Competition (IMAV)*, pp. 223–228, Sep. 2017.

[8] Y. Zeng, Q. Wu, and R. Zhang, "Accessing from the sky: A tutorial on UAV communications for 5G and beyond," *Proc. IEEE*, vol. 107, pp. 2327–2375, Dec. 2019.

[9] W. Khawaja, I. Guvenc, D. W. Matolak, U. C. Fiebig, and N. Schneckenburger, "A survey of air-to-ground propagation channel modeling for unmanned aerial vehicles," *IEEE Commun. Surveys Tuts.*, vol. 21, pp. 2361–2391, 3rd Quart. 2019.

[10] ITU, "Propagation data and prediction methods required for the design of terrestrial broadband radio access systems operating in a frequency range from 3 to 60 GHz," P Series, Radiowave propagation P.1410-5, International Telecommunication Union (ITU), 2 2012.

[11] A. Al-Hourani, S. Kandeepan, and S. Lardner, "Optimal LAP altitude for maximum coverage," *IEEE Wireless Commun. Lett.*, vol. 3, pp. 569–572, Dec. 2014.

[12] D. W. Matolak and R. Sun, "Air-ground channel characterization for unmanned aircraft systems–Part I: Methods, measurements, and models for over-water settings," *IEEE Trans. Veh. Technol.*, vol. 66, pp. 26–44, Jan. 2017.

[13] R. Sun and D. W. Matolak, "Air-ground channel characterization for unmanned aircraft systems–Part II: Hilly and mountainous settings," *IEEE Trans. Veh. Technol.*, vol. 66, pp. 1913–1925, Mar. 2017.

[14] D. W. Matolak and R. Sun, "Air-ground channel characterization for unmanned aircraft systems–Part III: The suburban and near-urban environments," *IEEE Trans. Veh. Technol.*, vol. 66, pp. 6607–6618, Aug. 2017.

[15] X. Cai *et al.*, "An empirical air-to-ground channel model based on passive measurements in LTE," *IEEE Trans. Veh. Technol.*, vol. 68, pp. 1140–1154, Feb. 2019.

[16] J. Liu, H. Zhang, M. Sheng, Y. Su, S. Chen, and J. Li, "High altitude air-to-ground channel modeling for fixed-wing UAV mounted aerial base stations," *IEEE Wireless Commun. Lett.*, vol. 10, pp. 330–334, Feb. 2021.

[17] W. Khawaja, I. Guvenc, and D. Matolak, "UWB channel sounding and modeling for UAV air-to-ground propagation channels," in *Proc. IEEE Global Commun. Conf. (Globecom)*, Dec. 2016.

[18] J. G. Andrews, A. K. Gupta, and H. S. Dhillon, "A primer on cellular network analysis using stochastic geometry," *[Online]. Available: http://arxiv.org/abs/1604.03183*, 2016.

[19] M. Haenggi, *Stochastic Geometry for Wireless Networks*. Cambridge, U.K.: Cambridge University Press, 2012.

[20] V. V. Chetlur and H. S. Dhillon, "Downlink coverage analysis for a finite 3-D wireless network of unmanned aerial vehicles," *IEEE Trans. Commun.*, vol. 65, pp. 4543–4558, Oct. 2017.

[21] M. Afshang and H. S. Dhillon, "Fundamentals of modeling finite wireless networks using binomial point process," *IEEE Trans. Wireless Commun.*, vol. 16, pp. 3355–3370, May 2017.

[22] X. Wang, H. Zhang, Y. Tian, and V. C. M. Leung, "Modeling and analysis of aerial base station-assisted cellular networks in finite areas under LoS and NLoS propagation," *IEEE Trans. Wireless Commun.*, vol. 17, pp. 6985–7000, Oct. 2018.

[23] M. Alzenad and H. Yanikomeroglu, "Coverage and rate analysis for unmanned aerial vehicle base stations with LoS/NLoS propagation," in *Proc. IEEE Global Commun. Conf. (Globecom) Workshops*, Dec. 2018.

[24] M. Mozaffari, W. Saad, M. Bennis, and M. Debbah, "Unmanned aerial vehicle with underlaid device-to-device communications: Performance and tradeoffs," *IEEE Trans. Wireless Commun.*, vol. 15, pp. 3949–3963, June 2016.

[25] M. G. Khoshkholgh, K. Navaie, H. Yanikomeroglu, V. C. M. Leung, and K. G. Shin, "Coverage performance of aerial-terrestrial HetNets," in *Proc. IEEE 89th Veh. Technol. Conf. (VTC'19-Spring)*, Apr. 2019.

[26] M. M. Azari, F. Rosas, A. Chiumento, and S. Pollin, "Coexistence of terrestrial and aerial users in cellular networks," in *Proc. IEEE Global Commun. Conf. (Globecom) Workshops*, Dec. 2017.

[27] M. Polese *et al.*, "Integrated access and backhaul in 5G mmWave networks: Potential and challenges," *IEEE Commun. Mag.*, vol. 58, pp. 62–68, Mar. 2020.

[28] H. S. Dhillon and G. Caire, "Wireless backhaul networks: Capacity bound, scalability analysis and design guidelines," *IEEE Trans. Wireless Commun.*, vol. 14, pp. 6043–6056, Nov. 2015.

[29] M. Jaber *et al.*, "Wireless backhaul: Performance modeling and impact on user association for 5G," *IEEE Trans. Wireless Commun.*, vol. 17, pp. 3095–3110, May 2018.

[30] C. Saha and H. S. Dhillon, "Millimeter wave integrated access and backhaul in 5G: Performance analysis and design insights," *IEEE J. Sel. Areas Commun.*, vol. 37, pp. 2669–2684, Dec. 2019.

[31] M. Kishk, A. Bader, and M. S. Alouini, "Aerial base station deployment in 6G cellular networks using tethered drones: The mobility and endurance tradeoff," *IEEE Veh. Technol. Mag.*, vol. 15, pp. 103–111, Dec. 2020.

[32] N. Kouzayha *et al.*, "Stochastic geometry analysis of hybrid aerial terrestrial networks with mmWave backhauling," in *Proc. IEEE Int. Conf. Commun. (ICC)*, pp. 1–7, June 2020.

[33] B. Galkin, J. Kibilda, and L. A. DaSilva, "Backhaul for low-altitude UAVs in urban environments," in *Proc. IEEE Int. Conf. Commun. (ICC)*, May 2018.

[34] J. Sabzehali, V. K. Shah, Q. Fan, B. Choudhury, L. Liu, and J. H. Reed, "Optimizing number, placement, and backhaul connectivity of multi-UAV networks," *arXiv preprint*, Nov. 2021. [Online]. Available: https://arxiv.org/abs/2111.05457.

[35] M. M. U. Chowdhury, S. J. Maeng, E. Bulut, and I. Guvenc, "3-D trajectory optimization in UAV-assisted cellular networks considering antenna radiation pattern and backhaul constraint," *IEEE Trans. Aerosp. Electron. Syst.*, vol. 56, pp. 3735–3750, Oct. 2020.

[36] M. Gapeyenko *et al.*, "Flexible and reliable UAV-assisted backhaul operation in 5G mmWave cellular networks," *IEEE J. Sel. Areas Commun.*, vol. 36, pp. 2486–2496, Nov. 2018.

[37] S. Enayati, H. Saeedi, H. Pishro-Nik, and H. Yanikomeroglu, "Moving aerial base station networks: A stochastic geometry analysis and design perspective," *IEEE Trans. Wireless Commun.*, vol. 18, pp. 2977–2988, June 2019.

[38] A. Fotouhi, M. Ding, and M. Hassan, "Dynamic base station repositioning to improve performance of drone small cells," in *Proc. IEEE Global Commun. Conf. (Globecom) Workshops*, Dec. 2016.

[39] P. K. Sharma and D. I. Kim, "Coverage probability of 3-D mobile UAV networks," *IEEE Wireless Commun. Lett.*, vol. 8, pp. 97–100, Feb. 2019.

[40] P. K. Sharma and D. I. Kim, "Random 3D mobile UAV networks: Mobility modeling and coverage probability," *IEEE Trans. Wireless Commun.*, vol. 18, pp. 2527–2538, May 2019.

[41] B. Ahmed, H. R. Pota, and M. Garratt, "Flight control of a rotary wing UAV using adaptive backstepping," *Int. J. Robust Nonlinear Control*, vol. 20, pp. 639–658, Apr. 2010.

[42] D. Xu, Y. Sun, D. W. K. Ng, and R. Schober, "Multiuser MISO UAV communications in uncertain environments with no-fly zones: Robust trajectory and resource allocation design," *IEEE Trans. Commun.*, vol. 68, pp. 3153–3172, May 2020.

[43] H. Wu, Y. Wen, J. Zhang, Z. Wei, N. Zhang, and X. Tao, "Energy-efficient and secure air-to-ground communication with jittering UAV," *IEEE Trans. Veh. Technol.*, vol. 69, pp. 3954–3967, Apr. 2020.

[44] M. T. Dabiri, H. Safi, S. Parsaeefard, and W. Saad, "Analytical channel models for millimeter wave UAV networks under hovering fluctuations," *IEEE Trans. Wireless Commun.*, vol. 19, pp. 2868–2883, Apr. 2020.

[45] S. Yang, Z. Zhang, J. Zhang, and J. Zhang, "Impact of rotary-wing UAV wobbling on millimeter-wave air-to-ground wireless channel," *arXiv preprint*, 2021. [Online]. Available: https://arxiv.org/abs/2107.06461.

[46] L. Liu, S. Zhang, and R. Zhang, "CoMP in the sky: UAV placement and movement optimization for multi-user communications," *IEEE Trans. Commun.*, vol. 67, pp. 5645–5658, Aug. 2019.

[47] J. Gomez-Ponce *et al.*, "Air-to-ground directional channel sounder with drone and 64-antenna dual-polarized cylindrical array," in *Proc. IEEE Int. Conf. Commun. (ICC) Workshops*, June 2021.

[48] V. Semkin *et al.*, "Lightweight UAV-based measurement system for air-to-ground channels at 28 GHz," in *Proc. IEEE 32nd Annu. Int. Symp. Pers., Indoor, Mobile Radio Commun. (PIMRC)*, pp. 848–853, Sep. 2021.

[49] T. C. W. Schenk, *RF Imperfections in High-Rate Wireless Systems: Impact and Digital Compensation*. Springer, 2008.

[50] E. Bjornson, M. Matthaiou, and M. Debbah, "A new look at dual-hop relaying: Performance limits with hardware impairments," *IEEE Trans. Commun.*, vol. 61, pp. 4512–4525, Nov. 2013.

[51] E. Bjornson, P. Zetterberg, M. Bengtsson, and B. Ottersten, "Capacity limits and multiplexing gains of MIMO channels with transceiver impairments," *IEEE Commun. Lett.*, vol. 17, pp. 91–94, Jan. 2013.

[52] C. Studer, M. Wenk, and A. Burg, "MIMO transmission with residual transmit-RF impairments," in *Proc. Int. ITG Workshop on Smart Antennas (WSA)*, pp. 189–196, Feb. 2010.

[53] E. Bjornson, J. Hoydis, M. Kountouris, and M. Debbah, "Massive MIMO systems with non-ideal hardware: Energy efficiency, estimation, and capacity limits," *IEEE Trans. Inf. Theory*, vol. 60, pp. 7112–7139, Nov. 2014.

[54] U. Gustavsson *et al.*, "On the impact of hardware impairments on massive MIMO," in *Proc. IEEE Global Commun. Conf. (Globecom) Workshops*, pp. 294–300, Dec. 2014.

[55] O. Taghizadeh, A. C. Cirik, and R. Mathar, "Hardware impairments aware transceiver design for full-duplex amplify-and-forward MIMO relaying," *IEEE Trans. Wireless Commun.*, vol. 17, pp. 1644–1659, Mar. 2018.

[56] O. Taghizadeh, V. Radhakrishnan, A. C. Cirik, R. Mathar, and L. Lampe, "Hardware impairments aware transceiver design for bidirectional full-duplex MIMO OFDM systems," *IEEE Trans. Veh. Technol.*, vol. 67, pp. 7450–7464, Aug. 2018.

[57] V. Radhakrishnan, O. Taghizadeh, and R. Mathar, "Hardware impairments-aware transceiver design for multi-carrier full-duplex MIMO relaying," *IEEE Trans. Veh. Technol.*, vol. 70, pp. 1109–1121, Feb. 2021.

[58] X. Li, J. Li, Y. Liu, Z. Ding, and A. Nallanathan, "Residual transceiver hardware impairments on cooperative NOMA networks," *IEEE Trans. Wireless Commun.*, vol. 19, pp. 680–695, Jan. 2020.

[59] M. Banagar and H. S. Dhillon, "3D two-hop cellular networks with wireless backhauled UAVs: Modeling and fundamentals," *to appear in IEEE Trans. Wireless Commun.*, 2022. [Online]. Available: https://ieeexplore.ieee.org/document/9712177.

[60] M. Banagar and H. S. Dhillon, "Fundamentals of 3D two-hop cellular networks analysis with wireless backhauled UAVs," in *Proc. IEEE Global Commun. Conf. (Globecom)*, Dec. 2021.

[61] X. Li, Q. Wang, Y. Liu, T. A. Tsiftsis, Z. Ding, and A. Nallanathan, "UAV-aided multi-way NOMA networks with residual hardware impairments," *IEEE Wireless Commun. Lett.*, vol. 9, pp. 1538–1542, Sep. 2020.

[62] J. Hou, Z. Yang, and M. Shikh-Bahaei, "Hardware impairment-aware data collection and wireless power transfer using a MIMO full-duplex UAV," in *Proc. IEEE Int. Conf. Commun. (ICC) Workshops*, June 2020.

[63] Y. Zeng, R. Zhang, and T. J. Lim, "Wireless communications with unmanned aerial vehicles: Opportunities and challenges," *IEEE Commun. Mag.*, vol. 54, pp. 36–42, May 2016.

[64] M. Banagar and H. S. Dhillon, "Performance characterization of canonical mobility models in drone cellular networks," *IEEE Trans. Wireless Commun.*, vol. 19, pp. 4994–5009, July 2020.

[65] A. Fakhreddine, C. Bettstetter, S. Hayat, R. Muzaffar, and D. Emini, "Handover challenges for cellular-connected drones," in *Proc. 5th Workshop on Micro Aerial Veh. Netw., Syst., Appl.*, pp. 9–14, June 2019.

[66] R. Amer, W. Saad, B. Galkin, and N. Marchetti, "Performance analysis of mobile cellular-connected drones under practical antenna configurations," in *Proc. IEEE Int. Conf. Commun. (ICC)*, pp. 1–7, June 2020.

[67] A. Nosratinia, T. E. Hunter, and A. Hedayat, "Cooperative communication in wireless networks," *IEEE Commun. Mag.*, vol. 42, pp. 74–80, Oct. 2004.

[68] J. N. Laneman, D. N. C. Tse, and G. W. Wornell, "Cooperative diversity in wireless networks: Efficient protocols and outage behavior," *IEEE Trans. Inf. Theory*, vol. 50, pp. 3062–3080, Dec. 2004.

[69] M. O. Hasna and M. S. Alouini, "Outage probability of multihop transmission over Nakagami fading channels," *IEEE Commun. Lett.*, vol. 7, pp. 216–218, May 2003.

[70] M. O. Hasna and M. S. Alouini, "End-to-end performance of transmission systems with relays over Rayleigh-fading channels," *IEEE Trans. Wireless Commun.*, vol. 2, pp. 1126–1131, Nov. 2003.

[71] J. Cho and Z. J. Haas, "On the throughput enhancement of the downstream channel in cellular radio networks through multihop relaying," *IEEE J. Sel. Areas Commun.*, vol. 22, pp. 1206–1219, Sep. 2004.

[72] D. Senaratne and C. Tellambura, "Unified exact performance analysis of two-hop amplify-and-forward relaying in Nakagami fading," *IEEE Trans. Veh. Technol.*, vol. 59, pp. 1529–1534, Mar. 2010.

[73] V. A. Aalo *et al.*, "Performance analysis of multi-hop amplify-and-forward relaying systems in Rayleigh fading channels with a Poisson interference field," *IEEE Trans. Wireless Commun.*, vol. 13, pp. 24–35, Jan. 2014.

[74] W. Lu and M. Di Renzo, "Stochastic geometry modeling and system-level analysis & optimization of relay-aided downlink cellular networks," *IEEE Trans. Commun.*, vol. 63, pp. 4063–4085, Nov. 2015.

[75] S. Zhang, H. Zhang, Q. He, K. Bian, and L. Song, "Joint trajectory and power optimization for UAV relay networks," *IEEE Commun. Lett.*, vol. 22, pp. 161–164, Jan. 2018.

[76] Y. Chen, N. Zhao, Z. Ding, and M. S. Alouini, "Multiple UAVs as relays: Multi-hop single link versus multiple dual-hop links," *IEEE Trans. Wireless Commun.*, vol. 17, pp. 6348–6359, Sep. 2018.

[77] Y. Chen, W. Feng, and G. Zheng, "Optimum placement of UAV as relays," *IEEE Commun. Lett.*, vol. 22, pp. 248–251, Feb. 2018.

[78] A. Pourranjbar, M. Baniasadi, A. Abbasfar, and G. Kaddoum, "A novel distributed algorithm for phase synchronization in unmanned aerial vehicles," *IEEE Commun. Lett.*, vol. 24, pp. 2260–2264, Oct. 2020.

[79] H. S. Dhillon, R. K. Ganti, F. Baccelli, and J. G. Andrews, "Modeling and analysis of K-tier downlink heterogeneous cellular networks," *IEEE J. Sel. Areas Commun.*, vol. 30, pp. 550–560, Apr. 2012.

[80] H. S. Dhillon and V. V. Chetlur, *Poisson Line Cox Process: Foundations and Applications to Vehicular Networks*. Vermont, USA: Morgan & Claypool Publishers, June 2020.

[81] M. Banagar, V. V. Chetlur, and H. S. Dhillon, *Stochastic Geometry-Based Performance Analysis of Drone Cellular Networks*, ch. 9, pp. 231–254. John Wiley & Sons, Ltd, 2020.

[82] M. Banagar, V. V. Chetlur, and H. S. Dhillon, "Handover probability in drone cellular networks," *IEEE Wireless Commun. Lett.*, vol. 9, pp. 933–937, July 2020.

[83] R. Amer, W. Saad, and N. Marchetti, "Mobility in the sky: Performance and mobility analysis for cellular-connected UAVs," *IEEE Trans. Commun.*, vol. 68, pp. 3229–3246, May 2020.

[84] M. Banagar and H. S. Dhillon, "3GPP-inspired stochastic geometry-based mobility model for a drone cellular network," in *Proc. IEEE Global Commun. Conf. (Globecom)*, Dec. 2019.

[85] M. Banagar and H. S. Dhillon, "Fundamentals of drone cellular network analysis under random waypoint mobility model," in *Proc. IEEE Global Commun. Conf. (Globecom)*, Dec. 2019.

[86] M. Banagar, H. S. Dhillon, and A. F. Molisch, "Impact of UAV wobbling on the air-to-ground wireless channel," *IEEE Trans. Veh. Technol.*, vol. 69, pp. 14025–14030, Nov. 2020.

[87] M. Alzenad and H. Yanikomeroglu, "Coverage and rate analysis for vertical heterogeneous networks (VHetNets)," *IEEE Trans. Wireless Commun.*, vol. 18, pp. 5643–5657, Dec. 2019.

[88] N. Cherif, M. Alzenad, H. Yanikomeroglu, and A. Yongacoglu, "Downlink coverage and rate analysis of an aerial user in vertical heterogeneous networks (VHetNets)," *IEEE Trans. Wireless Commun.*, vol. 20, pp. 1501–1516, Mar. 2021.

[89] M. M. Azari, G. Geraci, A. Garcia-Rodriguez, and S. Pollin, "UAV-to-UAV communications in cellular networks," *IEEE Trans. Wireless Commun.*, vol. 19, pp. 6130–6144, Sep. 2020.

[90] B. Galkin, J. Kibilda, and L. A. DaSilva, "A stochastic model for UAV networks positioned above demand hotspots in urban environments," *IEEE Trans. Veh. Technol.*, vol. 68, pp. 6985–6996, Jul. 2019.

[91] J. Sabzehali, V. K. Shah, H. S. Dhillon, and J. H. Reed, "3D placement and orientation of mmWave-based UAVs for guaranteed LoS coverage," *IEEE Wireless Commun. Lett.*, vol. 10, pp. 1662–1666, Aug. 2021.

[92] R. Amer, W. Saad, and N. Marchetti, "Toward a connected sky: Performance of beamforming with down-tilted antennas for ground and UAV user co-existence," *IEEE Commun. Lett.*, vol. 23, pp. 1840–1844, Oct. 2019.

[93] 3GPP, "Study on 3D channel model for LTE," Tech. Rep. 36.873, 3rd Generation Partnership Project (3GPP), 12 2017.

[94] W. L. Stutzman and G. A. Thiele, *Antenna Theory and Design*. John Wiley & Sons, Inc., May 2012.

[95] S. J. Maeng, M. M. U. Chowdhury, I. Guvenc, A. Bhuyan, and H. Dai, "Base station antenna uptilt optimization for cellular-connected drone corridors," *arXiv preprint*, July 2021. [Online]. Available: https://arxiv.org/abs/2107.00802.

[96] M. M. U. Chowdhury, I. Guvenc, W. Saad, and A. Bhuyan, "Ensuring reliable connectivity to cellular-connected UAVs with uptilted antennas and interference coordination," *arXiv preprint*, Aug. 2021. [Online]. Available: https://arxiv.org/abs/2108.05090.

[97] H. W. Gould, *Combinatorial Identities: Table I: Intermediate Techniques for Summing Finite Series*, vol. 4. May 2010.

[98] C. Saha, M. Afshang, and H. S. Dhillon, "3GPP-inspired HetNet model using Poisson cluster process: Sum-product functionals and downlink coverage," *IEEE Trans. Commun.*, vol. 66, pp. 2219–2234, May 2018.

[99] A. Rajanna and M. Haenggi, "Downlink coordinated joint transmission for mutual information accumulation," *IEEE Wireless Commun. Lett.*, vol. 6, pp. 198–201, Apr. 2017.

[100] M. Grossglauser and D. N. C. Tse, "Mobility increases the capacity of ad hoc wireless networks," *IEEE/ACM Trans. Netw.*, vol. 10, pp. 477–486, Aug. 2002.

[101] C. Bettstetter, G. Resta, and P. Santi, "The node distribution of the random waypoint mobility model for wireless ad hoc networks," *IEEE Trans. Mobile Comput.*, vol. 2, pp. 257–269, July 2003.

[102] X. Lin, R. K. Ganti, P. J. Fleming, and J. G. Andrews, "Towards understanding the fundamentals of mobility in cellular networks," *IEEE Trans. Wireless Commun.*, vol. 12, pp. 1686–1698, Apr. 2013.

[103] V. V. Chetlur and H. S. Dhillon, "Downlink coverage probability in a finite network of unmanned aerial vehicle (UAV) base stations," in *Proc. IEEE 17th Int. Workshop Signal Process. Adv. Wireless Commun. (SPAWC)*, July 2016.

[104] C. Zhang and W. Zhang, "Spectrum sharing for drone networks," *IEEE J. Sel. Areas Commun.*, vol. 35, pp. 136–144, Jan. 2017.

[105] A. M. Hayajneh, S. A. R. Zaidi, D. C. McLernon, M. Di Renzo, and M. Ghogho, "Performance analysis of UAV enabled disaster recovery networks: A stochastic geometric framework based on cluster processes," *IEEE Access*, vol. 6, pp. 26215–26230, June 2018.

[106] M. M. Azari, F. Rosas, and S. Pollin, "Cellular connectivity for UAVs: Network modeling, performance analysis, and design guidelines," *IEEE Trans. Wireless Commun.*, vol. 18, pp. 3366–3381, July 2019.

[107] T. Camp, J. Boleng, and V. Davies, "A survey of mobility models for ad hoc network research," *Wireless Commun. and Mobile Comput.*, vol. 2, no. 5, pp. 483–502, 2002.

[108] F. Bai and A. Helmy, "A survey of mobility models in wireless adhoc networks," in *Wireless Ad Hoc and Sensor Networks*, pp. 1–30, 2004.

[109] Z. Gong and M. Haenggi, "Interference and outage in mobile random networks: Expectation, distribution, and correlation," *IEEE Trans. Mobile Comput.*, vol. 13, pp. 337–349, Feb. 2014.

[110] H. Tabassum, M. Salehi, and E. Hossain, "Fundamentals of mobility-aware performance characterization of cellular networks: A tutorial," *IEEE Commun. Surveys Tuts.*, vol. 21, pp. 2288–2308, 3rd Quart. 2019.

[111] M. J. Neely and E. Modiano, "Capacity and delay tradeoffs for ad hoc mobile networks," *IEEE Trans. Inf. Theory*, vol. 51, pp. 1917–1937, June 2005.

[112] Z. Kong and E. M. Yeh, "On the latency for information dissemination in mobile wireless networks," in *Proc. 9th ACM Int. Symp. Mobile Ad Hoc Netw. Comput.*, pp. 139–148, May 2008.

[113] P. Madadi, F. Baccelli, and G. de Veciana, "Shared rate process for mobile users in Poisson networks and applications," *IEEE Trans. Inf. Theory*, vol. 64, pp. 2121–2141, Mar. 2018.

[114] M. McGuire, "Stationary distributions of random walk mobility models for wireless ad hoc networks," in *Proc. 6th ACM Int. Symp. Mobile Ad Hoc Netw. Comput.*, pp. 90–98, ACM, 2005.

[115] R. Groenevelt, E. Altman, and P. Nain, "Relaying in mobile ad hoc networks: The Brownian motion mobility model," *Wireless Netw.*, vol. 12, pp. 561–571, Sep. 2006.

[116] I. Rhee *et al.*, "On the Levy-walk nature of human mobility," *IEEE/ACM Trans. Netw.*, vol. 19, pp. 630–643, June 2011.

[117] D. B. Johnson and D. A. Maltz, *Dynamic Source Routing in Ad Hoc Wireless Networks*, pp. 153–181. Springer US, 1996.

[118] C. Bettstetter, H. Hartenstein, and X. Perez-Costa, "Stochastic properties of the random waypoint mobility model," *Wireless Netw.*, vol. 10, pp. 555–567, Sep. 2004.

[119] E. Hyytia, P. Lassila, and J. Virtamo, "Spatial node distribution of the random waypoint mobility model with applications," *IEEE Trans. Mobile Comput.*, vol. 5, pp. 680–694, June 2006.

[120] S. Nadarajah, "A review of results on sums of random variables," *Acta Applicandae Mathematicae*, vol. 103, pp. 131–140, Sep. 2008.

[121] J. Hu and N. C. Beaulieu, "Accurate simple closed-form approximations to Rayleigh sum distributions and densities," *IEEE Communications Letters*, vol. 9, pp. 109–111, Feb. 2005.

[122] T. Coleman and Y. Li, "An interior trust region approach for nonlinear minimization subject to bounds," *SIAM J. Optim.*, vol. 6, pp. 418–445, May 1996.

[123] A. Cika, M. Badiu, and J. P. Coon, "Statistical properties of transmissions subject to Rayleigh fading and Ornstein-Uhlenbeck mobility," *IEEE Trans. Mobile Comput.*, pp. 1–1, 2021.

[124] D. Kim, J. Lee, and T. Q. S. Quek, "Multi-layer unmanned aerial vehicle networks: Modeling and performance analysis," *IEEE Trans. Wireless Commun.*, vol. 19, pp. 325–339, Jan. 2020.

[125] S. Sadr and R. S. Adve, "Handoff rate and coverage analysis in multi-tier heterogeneous networks," *IEEE Trans. Wireless Commun.*, vol. 14, pp. 2626–2638, May 2015.

[126] S. Krishnan and H. S. Dhillon, "Spatio-temporal interference correlation and joint coverage in cellular networks," *IEEE Trans. Wireless Commun.*, vol. 16, pp. 5659–5672, Sep. 2017.

[127] W. Bao and B. Liang, "Stochastic geometric analysis of user mobility in heterogeneous wireless networks," *IEEE J. Sel. Areas Commun.*, vol. 33, pp. 2212–2225, Oct. 2015.

[128] R. Arshad, H. ElSawy, S. Sorour, T. Y. Al-Naffouri, and M. S. Alouini, "Velocity-aware handover management in two-tier cellular networks," *IEEE Trans. Wireless Commun.*, vol. 16, pp. 1851–1867, Mar. 2017.

[129] J. Lyu, Y. Zeng, and R. Zhang, "Cyclical multiple access in UAV-aided communications: A throughput-delay tradeoff," *IEEE Wireless Commun. Lett.*, vol. 5, pp. 600–603, Dec. 2016.

[130] K. Park, B. Cho, K. Park, and H. Kim, "Optimal coverage control for net-drone handover," in *Proc. 7th Int. Conf. Ubiquitous Future Netw.*, pp. 97–99, July 2015.

[131] R. Arshad, L. Lampe, H. ElSawy, and M. J. Hossain, "Integrating UAVs into existing wireless networks: A stochastic geometry approach," in *Proc. IEEE Global Commun. Conf. (Globecom) Workshops*, Dec. 2018.

[132] D. Xu, Y. Sun, D. W. K. Ng, and R. Schober, "Robust resource allocation for UAV systems with UAV jittering and user location uncertainty," in *Proc. IEEE Global Commun. Conf. (Globecom) Workshops*, Dec. 2018.

[133] M. Simunek, F. P. Fontan, and P. Pechac, "The UAV low elevation propagation channel in urban areas: Statistical analysis and time-series generator," *IEEE Trans. Antennas Propag.*, vol. 61, pp. 3850–3858, July 2013.

[134] A. F. Molisch, *Wireless Communications*. Wiley-IEEE Press, 2011.

[135] V. Va and R. W. Heath, "Basic relationship between channel coherence time and beamwidth in vehicular channels," in *Proc. IEEE 82nd Veh. Technol. Conf. (VTC'15-Fall)*, Sep. 2015.

[136] K. I. Pedersen, P. E. Mogensen, and B. H. Fleury, "Power azimuth spectrum in outdoor environments," *Electronics Lett.*, vol. 33, pp. 1583–1584, Aug. 1997.

[137] N. Goddemeier and C. Wietfeld, "Investigation of air-to-air channel characteristics and a UAV specific extension to the Rice model," in *Proc. IEEE Global Commun. Conf. (Globecom) Workshops*, 2015.

[138] M. Zhu *et al.*, "Tracking and positioning using phase information from estimated multi-path components," in *Proc. IEEE Int. Conf. Commun. (ICC) Workshops*, pp. 712–717, June 2015.

[139] T. C. W. Schenk, P. F. M. Smulders, and E. R. Fledderus, "Impact of nonlinearities in multiple-antenna OFDM transceivers," in *Symp. Commun. Veh. Technol.*, pp. 53–56, Nov. 2006.

[140] T. C. W. Schenk, E. R. Fledderus, and P. F. M. Smulders, "Performance analysis of zero-IF MIMO OFDM transceivers with IQ imbalance," *J. Commun.*, vol. 2, pp. 9–19, Dec. 2007.

[141] L. Piazzo and P. Mandarini, "Analysis of phase noise effects in OFDM modems," *IEEE Trans. Commun.*, vol. 50, pp. 1696–1705, Oct. 2002.

[142] A. Goldsmith, *Wireless Communications*. Cambridge University Press, 2005.

[143] A. Meijerink and A. F. Molisch, "On the physical interpretation of the Saleh-Valenzuela model and the definition of its power delay profiles," *IEEE Trans. Antennas Propag.*, vol. 62, pp. 4780–4793, Sep. 2014.

[144] J. P. Z. Peebles, *Probability, Random Variables, and Random Signal Principles*. McGraw-Hill series in electrical and computer engineering., McGraw-Hill, Inc., 4 ed., 2001.

[145] C. E. O'Lone, H. S. Dhillon, and R. M. Buehrer, "Characterizing the first-arriving multipath component in 5G millimeter wave networks: TOA, AOA, and non-line-of-sight bias," *IEEE Trans. Wireless Commun.*, vol. 21, pp. 1602–1620, Mar. 2022.

[146] M. Patzold, *Mobile Radio Channels*. John Wiley & Sons, Inc., 2 ed., 2012.

[147] C. E. Rasmussen and C. K. I. Williams, *Gaussian Processes for Machine Learning*. MIT Press, 2006.

[148] M. Banagar and H. S. Dhillon, "Impairment-aware unified channel model for air-to-ground wireless communications," *Submitted to IEEE Trans. Wireless Commun.*

[149] M. Banagar and H. S. Dhillon, "Wobbling and impairments-aware channel model and its implications on high-frequency UAV links," in *Submitted to IEEE Global Commun. Conf. (Globecom)*, 2022.

Appendices

Appendix A

Proofs of Lemmas and Theorems of Chapter 2

A.1 Proof of Lemma 2.3

By definition, we have

$$
\begin{aligned}
F_{T_1}(\tau) &= \mathbb{P}\left[\frac{aX}{bY+I} \leq \tau\right] = \mathbb{P}\left[aX \leq \tau bY + \tau I\right] \\
&\overset{(a)}{=} \int_0^\infty f_Y(y) F_X\left(\frac{\tau by + \tau I}{a}\right) \mathrm{d}y \\
&\overset{(b)}{=} 1 - \sum_{i=0}^{m-1} \frac{m^m}{i!(m-1)!} \left(\frac{m\tau b}{a}\right)^i \mathrm{e}^{-\frac{m\tau I}{a}} \int_0^\infty y^{m-1} \left(y + \frac{I}{b}\right)^i \mathrm{e}^{-\left(m+\frac{m\tau b}{a}\right)y} \mathrm{d}y \\
&\overset{(c)}{=} 1 - \sum_{i=0}^{m-1} \sum_{k=0}^{i} \frac{m^m (k+m-1)!}{i!(m-1)!} \binom{i}{k} \left(\frac{m\tau b}{a}\right)^i \left(\frac{I}{b}\right)^{i-k} \left(m + \frac{m\tau b}{a}\right)^{-m-k} \mathrm{e}^{-\frac{m\tau I}{a}},
\end{aligned}
$$

where in (a) we used the independence of X and Y, in (b) we wrote the cdf of X as the series expansion $F_X(x) = \frac{\gamma(m,mx)}{(m-1)!} = 1 - \sum_{i=0}^{m-1} \frac{(mx)^i}{i!} \mathrm{e}^{-mx}$ for integer m, and in (c) we used the binomial expansion and simplified the resulting integral using the definition of the gamma function. By further mathematical manipulations, we obtain the final result as given in (2.17). □

A.2 Proof of Lemma 2.4

Similar to the proof of Lemma 2.3, we can write

$$
\begin{aligned}
F_{T_2}(\tau) &= \mathbb{P}\left[\frac{\max\{aX, bY\}}{\min\{aX, bY\} + I} \le \tau\right] \\
&= \mathbb{P}\left[\frac{aX}{bY + I} \le \tau, aX \ge bY\right] + \mathbb{P}\left[\frac{bY}{aX + I} \le \tau, aX < bY\right] \\
&= \begin{cases}
\int_0^{\frac{\tau I}{(1-\tau)b}} \int_{\frac{by}{a}}^{\frac{\tau by + \tau I}{a}} f_{X,Y}(x,y)\,\mathrm{d}x\,\mathrm{d}y \\
+ \int_0^{\frac{\tau I}{(1-\tau)a}} \int_{\frac{ax}{b}}^{\frac{\tau ax + \tau I}{b}} f_{X,Y}(x,y)\,\mathrm{d}y\,\mathrm{d}x, & \tau < 1 \\
\int_0^{\infty} \int_{\frac{by}{a}}^{\frac{\tau by + \tau I}{a}} f_{X,Y}(x,y)\,\mathrm{d}x\,\mathrm{d}y \\
+ \int_0^{\infty} \int_{\frac{ax}{b}}^{\frac{\tau ax + \tau I}{b}} f_{X,Y}(x,y)\,\mathrm{d}y\,\mathrm{d}x, & \tau \ge 1.
\end{cases}
\end{aligned}
$$

We now focus our attention to region $\tau < 1$ and denote its first double integral as L_1. We have

$$
\begin{aligned}
L_1 &\overset{(a)}{=} \int_0^{\frac{\tau I}{(1-\tau)b}} \frac{m^m}{(m-1)!} y^{m-1} \mathrm{e}^{-my} \sum_{i=0}^{m-1} \frac{1}{i!} \\
&\quad \times \left[\left(\frac{mb}{a} y\right)^i \mathrm{e}^{-\frac{mb}{a}y} - \left(\frac{m\tau b}{a} y + \frac{m\tau}{a} I\right)^i \mathrm{e}^{-\frac{m\tau b}{a}y - \frac{m\tau}{a}I}\right] \mathrm{d}y \\
&\overset{(b)}{=} \sum_{i=0}^{m-1} \frac{m^m}{i!(m-1)!} \left(\frac{mb}{a}\right)^i \int_0^{\frac{\tau I}{(1-\tau)b}} y^{i+m-1} \mathrm{e}^{-\left(m + \frac{mb}{a}\right)y} \mathrm{d}y \\
&\quad - \sum_{i=0}^{m-1} \frac{m^m}{i!(m-1)!} \left(\frac{m\tau b}{a}\right)^i \mathrm{e}^{-\frac{m\tau}{a}I} \int_0^{\frac{\tau I}{(1-\tau)b}} y^{m-1} \left(y + \frac{I}{b}\right)^i \mathrm{e}^{-\left(m + \frac{m\tau b}{a}\right)y} \mathrm{d}y \\
&\overset{(c)}{=} \sum_{i=0}^{m-1} \frac{\gamma\left(m+i, \left(\frac{1}{a} + \frac{1}{b}\right)\frac{m\tau}{(1-\tau)} I\right)}{i!(m-1)!} \frac{a^m b^i}{(a+b)^{m+i}} \\
&\quad - \sum_{i=0}^{m-1} \sum_{k=0}^{i} \frac{\gamma\left(m+k, \left(\frac{\tau}{a} + \frac{1}{b}\right)\frac{m\tau}{(1-\tau)} I\right)}{k!(m-1)!(i-k)!} \frac{a^m (b\tau)^k}{(a+b\tau)^{m+k}} \left(\frac{m\tau}{a} I\right)^{i-k} \mathrm{e}^{-\frac{m\tau}{a}I},
\end{aligned}
$$

where in (a) we used the independence between X and Y and the series expansion of the cdf of gamma random variables (as given in the proof of Lemma 2.3), in (b) we switched the order of summation and integration, and in (c) we derived the integrals and simplified the resulting expressions using the binomial expansion and the definition of the lower incomplete gamma function. Note that the second double integral is nothing but L_1 with a and b being switched with each other. As for region $\tau \ge 1$, the proof follows the same steps as above,

with the only difference that the upper limits of the outer integrals are ∞ and we end up with gamma functions instead of incomplete gamma functions in the last step. Noting that $\gamma(s,\infty)=\Gamma(s)$, we obtain the final result as given in (2.18). □

A.3 Proof of Lemma 2.5

We start by writing the joint cdf of interest as

$$\begin{aligned} F_{T_1,T_3}(\tau,\tau) &= \mathbb{P}\left[\frac{aX}{bY+I}\le\tau, \frac{bY}{aX+I+g(aX+bY+I)}\le\tau\right] \\ &= \mathbb{P}\left[bY\ge\frac{a}{\tau}X-I, (1-\tau g)bY\le\tau(1+g)aX+\tau(1+g)I\right]. \end{aligned} \tag{A.1}$$

When $\tau\ge\frac{1}{g}$, the second condition in (A.1) always holds since all the constants and random variables on its right-hand side are non-negative. Hence, we have $F_{T_1,T_3}(\tau,\tau)=\mathbb{P}\left[\frac{aX}{bY+I}\le\tau\right]=F_{T_1}(\tau)$ for $\tau\ge\frac{1}{g}$. When $\tau<\frac{1}{g}$, we first find the intersection point of lines $Y=\frac{a}{b\tau}X-\frac{1}{b}I$ and $Y=\frac{a\tau(1+g)}{b(1-\tau g)}X+\frac{\tau(1+g)}{b(1-\tau g)}I$ as $x_0=\frac{\tau I}{a(1-\tau(1+g))}, y_0=\frac{\tau(1+g)I}{b(1-\tau(1+g))}$. Note also that $by_0=(1+g)ax_0$. We can now derive $F_{T_1,T_3}(\tau,\tau)$ by integrating over the region defined in (A.1) as follows:

$$F_{T_1,T_3}(\tau,\tau)=\begin{cases} \int_0^{y_0}\int_{\frac{by}{a(1+g)}}^{\frac{\tau by+\tau I}{a}} f_{X,Y}(x,y)\,\mathrm{d}x\,\mathrm{d}y+\int_0^{x_0}\int_{\frac{(1+g)ax}{b}}^{\frac{\tau(1+g)}{b(1-\tau g)}(ax+I)} f_{X,Y}(x,y)\,\mathrm{d}y\,\mathrm{d}x, \\ \qquad\qquad\qquad\qquad\qquad\qquad\qquad\qquad\qquad\qquad \tau<\frac{1}{1+g} \\ \int_0^{\infty}\int_{\frac{by}{a(1+g)}}^{\frac{\tau by+\tau I}{a}} f_{X,Y}(x,y)\,\mathrm{d}x\,\mathrm{d}y+\int_0^{\infty}\int_{\frac{(1+g)ax}{b}}^{\frac{\tau(1+g)}{b(1-\tau g)}(ax+I)} f_{X,Y}(x,y)\,\mathrm{d}y\,\mathrm{d}x, \\ \qquad\qquad\qquad\qquad\qquad\qquad\qquad\qquad\qquad\qquad \frac{1}{1+g}\le\tau<\frac{1}{g}. \end{cases}$$

This equation can be simplified similarly as in the proof of Lemma 2.4 to obtain (2.19). These steps are skipped here for brevity. This completes the proof. □

A.4 Proof of Lemma 2.11

From (2.9) and for a *specific* channel condition, we observe that among all the UAVs, the closest one to the typical UE provides the highest averaged received power. Hence, the serving UAV will be either the closest LoS UAV or the closest NLoS UAV to the typical UE. We can now write the probability that an NLoS UAV serves the typical UE as

$$\begin{aligned} A_{\mathrm{N}} &= \mathbb{P}\left[P^{\mathrm{Rx}}_{\mathrm{D}_0,\mathrm{N}}\ge P^{\mathrm{Rx}}_{\mathrm{D}_0,\mathrm{L}}\right]=\mathbb{P}\left[\tilde{r}^{-\alpha_{\mathrm{N}}}_{\mathrm{D}_0,\mathrm{N}}\eta_{\mathrm{N}}^{-1}\ge\tilde{r}^{-\alpha_{\mathrm{L}}}_{\mathrm{D}_0,\mathrm{L}}\eta_{\mathrm{L}}^{-1}\right] \\ &\overset{(a)}{=}\int_{h_{\mathrm{D,m}}}^{\infty}\mathbb{P}\left[\tilde{r}_{\mathrm{D}_0,\mathrm{L}}\ge\left(\frac{\eta_{\mathrm{N}}}{\eta_{\mathrm{L}}}\right)^{\frac{1}{\alpha_{\mathrm{L}}}} r^{\frac{\alpha_{\mathrm{N}}}{\alpha_{\mathrm{L}}}}\right] f_{\tilde{r}_{\mathrm{D}_0,\mathrm{N}}}(r)\,\mathrm{d}r, \end{aligned}$$

where in (a) we used the law of total probability by conditioning on $\tilde{r}_{\mathrm{D}_0,\mathrm{N}}$. The final result in (2.29) is derived by applying the complementary cdf (ccdf) and pdf of $\tilde{r}_{\mathrm{D}_0,\mathrm{L}}$ and $\tilde{r}_{\mathrm{D}_0,\mathrm{N}}$, respectively, from (2.26) and (2.27) to the last integral above. Since the typical UE associates with either an LoS UAV or an NLoS UAV, we have $A_{\mathrm{L}} = 1 - A_{\mathrm{N}}$. □

A.5 Proof of Lemma 2.12

Considering the LoS case, we write the joint cdf of $r_{\mathrm{D}_0,\mathrm{L}}$ and $\theta_{\mathrm{D}_0,\mathrm{L}}$ as

$$
\begin{aligned}
F_{r_{\mathrm{D}_0,\mathrm{L}},\theta_{\mathrm{D}_0,\mathrm{L}}}(r,\theta) &= \mathbb{P}\left[\tilde{r}_{\mathrm{D}_0,\mathrm{L}} \le r, \tilde{\theta}_{\mathrm{D}_0,\mathrm{L}} \le \theta \,|\, \mathrm{D}_0 \text{ is an LoS UAV}\right] \\
&\overset{(a)}{=} \frac{1}{A_{\mathrm{L}}}\mathbb{P}\left[\tilde{r}_{\mathrm{D}_0,\mathrm{L}} \le r, \tilde{\theta}_{\mathrm{D}_0,\mathrm{L}} \le \theta, \tilde{r}_{\mathrm{D}_0,\mathrm{L}}^{-\alpha_{\mathrm{L}}}\eta_{\mathrm{L}}^{-1} \ge \tilde{r}_{\mathrm{D}_0,\mathrm{N}}^{-\alpha_{\mathrm{N}}}\eta_{\mathrm{N}}^{-1}\right] \\
&= \frac{1}{A_{\mathrm{L}}}\int_0^{\theta}\int_{h_{\mathrm{D,m}}}^{r} \mathbb{P}\left[\tilde{r}_{\mathrm{D}_0,\mathrm{N}} \ge \left(\frac{\eta_{\mathrm{L}}}{\eta_{\mathrm{N}}}\right)^{\frac{1}{\alpha_{\mathrm{N}}}} r_1^{\frac{\alpha_{\mathrm{L}}}{\alpha_{\mathrm{N}}}}\right] f_{\tilde{r}_{\mathrm{D}_0,\mathrm{L}},\tilde{\theta}_{\mathrm{D}_0,\mathrm{L}}}(r_1,\theta_1)\,\mathrm{d}r_1\,\mathrm{d}\theta_1 \\
&\overset{(b)}{=} \frac{1}{A_{\mathrm{L}}}\int_0^{\theta}\int_{h_{\mathrm{D,m}}}^{\min\{r,r_0\}} f_{\tilde{r}_{\mathrm{D}_0,\mathrm{L}},\tilde{\theta}_{\mathrm{D}_0,\mathrm{L}}}(r_1,\theta_1)\,\mathrm{d}r_1\,\mathrm{d}\theta_1 \\
&\quad + \frac{1}{A_{\mathrm{L}}}\int_0^{\theta}\int_{\min\{r,r_0\}}^{r} \exp\left[-\pi\lambda_{\mathrm{D}}\beta_{\mathrm{N}}\left(\left(\frac{\eta_{\mathrm{L}}}{\eta_{\mathrm{N}}}\right)^{\frac{1}{\alpha_{\mathrm{N}}}} r_1^{\frac{\alpha_{\mathrm{L}}}{\alpha_{\mathrm{N}}}}\right)\right] f_{\tilde{r}_{\mathrm{D}_0,\mathrm{L}},\tilde{\theta}_{\mathrm{D}_0,\mathrm{L}}}(r_1,\theta_1)\,\mathrm{d}r_1\mathrm{d}\theta_1,
\end{aligned}
$$

where $r_0 = (\eta_{\mathrm{N}}/\eta_{\mathrm{L}})^{1/\alpha_{\mathrm{L}}} h_{\mathrm{D,m}}^{\alpha_{\mathrm{N}}/\alpha_{\mathrm{L}}}$, in (a) we used the fact that $A_{\mathrm{L}} = \mathbb{P}\left[\mathrm{D}_0 \text{ is an LoS UAV}\right]$, and in (b) we used $\alpha_{\mathrm{L}} < \alpha_{\mathrm{N}}$, $\eta_{\mathrm{L}} < \eta_{\mathrm{N}}$, and the ccdf of $\tilde{r}_{\mathrm{D}_0,\mathrm{N}}$ from (2.26). Taking the derivative of $F_{r_{\mathrm{D}_0,\mathrm{L}},\theta_{\mathrm{D}_0,\mathrm{L}}}(r,\theta)$ with respect to both r and θ, we obtain the final result as given in (2.30).□

A.6 Proof of Lemma 2.13

By definition, we have

$$
\begin{aligned}
\mathcal{L}_{I_{\mathrm{BU}}}(s|\mathrm{B}_0) &= \mathbb{E}\left[\mathrm{e}^{-s\sum_{\mathrm{B}_{\mathbf{x}}\in\Phi'_{\mathrm{B}}} P_{\mathrm{B}}\eta_{\mathrm{N}}^{-1}G_{\mathrm{B}_{\mathbf{x}}}r_{\mathrm{B}_{\mathbf{x}}}^{-\alpha_{\mathrm{N}}}f_{\mathrm{B}_{\mathbf{x}}}}\middle|\mathrm{B}_0\right] \\
&\overset{(a)}{=} \mathbb{E}\left[\prod_{\mathrm{B}_{\mathbf{x}}\in\Phi'_{\mathrm{B}}}\left(1+\frac{sP_{\mathrm{B}}}{m\eta_{\mathrm{N}}}\frac{G_{\mathrm{B}_{\mathbf{x}}}}{r_{\mathrm{B}_{\mathbf{x}}}^{\alpha_{\mathrm{N}}}}\right)^{-m}\middle|\mathrm{B}_0\right] \\
&\overset{(b)}{=} \exp\left[-2\pi\lambda_{\mathrm{B}}\int_{u_{\mathrm{B}_0}}^{\infty}\left[1-\left(1+\frac{sP_{\mathrm{B}}}{m\eta_{\mathrm{N}}}\frac{G_{\mathrm{B}_{\mathbf{x}}}}{r_{\mathrm{B}_{\mathbf{x}}}^{\alpha_{\mathrm{N}}}}\right)^{-m}\right]u_{\mathrm{B}_{\mathbf{x}}}\mathrm{d}u_{\mathrm{B}_{\mathbf{x}}}\right],
\end{aligned}
$$

where in (a) we took the moment generating function (mgf) of the gamma-distributed $f_{\mathrm{B}_{\mathbf{x}}}$, and in (b) we used the probability generating functional (pgfl) of the PPP Φ'_{B}. Noting that

$r_{\mathrm{B}_\mathbf{x}} = \sqrt{u_{\mathrm{B}_\mathbf{x}}^2 + h_{\mathrm{B}}^2}$ and $G_{\mathrm{B}_\mathbf{x}} = G_{\mathrm{B}}^{\mathrm{OmniD}}(\pi - \theta_{\mathrm{B}_\mathbf{x}}, \theta_{\mathrm{B}})$, where $\theta_{\mathrm{B}_\mathbf{x}} = \tan^{-1}(\frac{u_{\mathrm{B}_\mathbf{x}}}{h_{\mathrm{B}}})$ is the zenith angle of the BS located at $\mathrm{B}_\mathbf{x}$, the final result in (2.32) is obtained. □

A.7 Proof of Lemma 2.14

Similar to the proof of Lemma 2.13, we have

$$\begin{aligned}
\mathcal{L}_{I_{\mathrm{DU},q_1|q_2}}(s|\mathrm{D}_0) &= \mathbb{E}\left[\mathrm{e}^{-s\sum_{\mathrm{D}_\mathbf{x}\in\Phi'_{\mathrm{D},q_1}} P_{\mathrm{D}}\eta_{q_1}^{-1} G_{\mathrm{D}_\mathbf{x}} r_{\mathrm{D}_\mathbf{x}}^{-\alpha_{q_1}} f_{\mathrm{D}_\mathbf{x}}} \middle| \mathrm{D}_0\right] \\
&= \mathbb{E}\left[\prod_{\mathrm{D}_\mathbf{x}\in\Phi'_{\mathrm{D},q_1}} \left(1 + \frac{sP_{\mathrm{D}}}{m\eta_{q_1}} \frac{G_{\mathrm{D}_\mathbf{x}}}{r_{\mathrm{D}_\mathbf{x}}^{\alpha_{q_1}}}\right)^{-m} \middle| \mathrm{D}_0\right] \\
&= \exp\Bigg[-\int_0^{2\pi}\int_{\theta_{\mathrm{D,M}}}^{\theta_{\mathrm{D,m}}}\int_{r_{q_1|q_2}}^{\frac{h_{\mathrm{D,M}}}{\cos(\theta_{\mathrm{D}_\mathbf{x}})}} \left[1 - \left(1 + \frac{sP_{\mathrm{D}}}{m\eta_{q_1}} \frac{G_{\mathrm{D}_\mathbf{x}}}{r_{\mathrm{D}_\mathbf{x}}^{\alpha_{q_1}}}\right)^{-m}\right] \\
&\quad \times \lambda_{\mathrm{D}} p_{q_1}(\theta_{\mathrm{D}_\mathbf{x}}) r_{\mathrm{D}_\mathbf{x}}^2 \sin(\theta_{\mathrm{D}_\mathbf{x}}) \mathrm{d}r_{\mathrm{D}_\mathbf{x}} \mathrm{d}\theta_{\mathrm{D}_\mathbf{x}} \mathrm{d}\phi_{\mathrm{D}_\mathbf{x}} \\
&\quad - \int_0^{2\pi}\int_{\theta_{\mathrm{D,m}}}^{\frac{\pi}{2}}\int_{\frac{h_{\mathrm{D,m}}}{\cos(\theta_{\mathrm{D}_\mathbf{x}})}}^{\frac{h_{\mathrm{D,M}}}{\cos(\theta_{\mathrm{D}_\mathbf{x}})}} \left[1 - \left(1 + \frac{sP_{\mathrm{D}}}{m\eta_{q_1}} \frac{G_{\mathrm{D}_\mathbf{x}}}{r_{\mathrm{D}_\mathbf{x}}^{\alpha_{q_1}}}\right)^{-m}\right] \\
&\quad \times \lambda_{\mathrm{D}} p_{q_1}(\theta_{\mathrm{D}_\mathbf{x}}) r_{\mathrm{D}_\mathbf{x}}^2 \sin(\theta_{\mathrm{D}_\mathbf{x}}) \mathrm{d}r_{\mathrm{D}_\mathbf{x}} \mathrm{d}\theta_{\mathrm{D}_\mathbf{x}} \mathrm{d}\phi_{\mathrm{D}_\mathbf{x}}\Bigg],
\end{aligned}$$

where

$$\theta_{\mathrm{D,m}} = \cos^{-1}\left(\frac{h_{\mathrm{D,m}}}{r_{q_1|q_2}}\right), \quad \theta_{\mathrm{D,M}} = \cos^{-1}\left(\min\left\{\frac{h_{\mathrm{D,M}}}{r_{q_1|q_2}}, 1\right\}\right),$$

and we used the pgfl of the PPP Φ'_{D,q_1} in the last equation. Note that the triple integration is carried out over the region enclosed between the planes $z = h_{\mathrm{D,m}}$ and $z = h_{\mathrm{D,M}}$ minus the exclusion zone $\mathcal{X}_{\mathrm{D}}$ of the interfering UAVs, as explained earlier with details in Table 2.1. Observing that $G_{\mathrm{D}_\mathbf{x}} = G_{\mathrm{D}}^{\mathrm{AC}}(\pi - \theta_{\mathrm{D}_\mathbf{x}})$, where $\theta_{\mathrm{D}_\mathbf{x}}$ is the zenith angle of the UAV located at $\mathrm{D}_\mathbf{x}$, we obtain the final result as given in (2.33). □

A.8 Proof of Theorem 2.15

We start by writing the definition of the coverage probability as

$$\begin{aligned}
P_{\mathrm{Cov}}^{\mathrm{AF}} &= \mathbb{P}\left[\mathrm{SINR}^{\mathrm{AF}} \geq \tau\right] \\
&= \mathbb{P}\left[\mathrm{SINR}^{\mathrm{AF}} \geq \tau \middle| E_{\mathrm{L}}\right] \mathbb{P}\left[E_{\mathrm{L}}\right] + \mathbb{P}\left[\mathrm{SINR}^{\mathrm{AF}} \geq \tau \middle| E_{\mathrm{N}}\right] \mathbb{P}\left[E_{\mathrm{N}}\right] \\
&= \mathbb{P}\left[\mathrm{SINR}_{\mathrm{L}}^{\mathrm{AF}} \geq \tau\right] A_{\mathrm{L}} + \mathbb{P}\left[\mathrm{SINR}_{\mathrm{N}}^{\mathrm{AF}} \geq \tau\right] A_{\mathrm{N}},
\end{aligned}$$

where E_{L} and E_{N} represent the events that the typical UE is associated with an LoS and NLoS UAV, respectively, with probabilities of A_{L} and A_{N}. We now write the ccdf of $\mathrm{SINR}_q^{\mathrm{AF}}$ as

$$\begin{aligned} P_{\mathrm{Cov},q}^{\mathrm{AF}} &\triangleq \mathbb{P}\left[\mathrm{SINR}_q^{\mathrm{AF}} \geq \tau\right] \\ &= 1 - \mathbb{P}\left[\mathrm{SINR}_{\mathrm{BU},q} < \tau, \frac{\mathrm{SINR}_{\mathrm{BD}}\mathrm{SINR}_{\mathrm{DU},q}}{\mathrm{SINR}_{\mathrm{BD}} + \mathrm{SINR}_{\mathrm{DU},q} + 1} < \tau\right]. \end{aligned} \tag{A.2}$$

Recall that conditioned on knowing the locations of the serving BS and UAV, the SINR values in (A.2) can be represented in simpler forms as given in (2.14)–(2.16). Using this representation and by further conditioning on I and Z, we have

$$\begin{aligned} P_{\mathrm{Cov},q}^{\mathrm{AF}} &= 1 - \mathbb{E}\left[\mathbb{P}\left[\frac{aX}{bY+I} < \tau, \frac{bY}{aX + I + g(aX+bY+I)} < \tau \middle| \mathrm{B}_0, \mathrm{D}_0, I, Z\right]\right] \\ &= \mathbb{E}\left[\bar{F}_{T_1,T_3}(\tau,\tau)\right], \end{aligned}$$

where $g = \frac{N_0}{cZ}$ and we used Lemma 2.5 in the last equation. Note that $\bar{F}_{T_1,T_3}(\tau,\tau) = 1 - F_{T_1,T_3}(\tau,\tau)$ is the joint ccdf of T_1 and T_3 conditioned on knowing a, b, g, and I, which entails the incomplete gamma function, and thus, the series expansion $\gamma(s,x) = (s-1)!\left[1 - \sum_{j=0}^{s-1}\frac{x^j}{j!}\mathrm{e}^{-x}\right]$ can be used to obtain $P_{\mathrm{Cov},q}^{\mathrm{AF}}$. Taking the expectation of $\bar{F}_{T_1,T_3}(\tau,\tau)$ over $I = I_{\mathrm{U}} + N_0$, we end up with the derivatives of the Laplace transform of I, where $\mathcal{L}_I(s|\mathrm{B}_0,\mathrm{D}_0) = \mathbb{E}\left[\mathrm{e}^{-s(I_{\mathrm{U}}+N_0)}\middle|\mathrm{B}_0,\mathrm{D}_0\right] = \mathrm{e}^{-sN_0}\mathcal{L}_{I_{\mathrm{U}|q}}(s|\mathrm{B}_0,\mathrm{D}_0)$. Following Remark 2.6, Lemma 2.5, and Lemma 2.3, we denote $\mathbb{E}_I\left[\bar{F}_{T_1,T_3}(\tau,\tau)\right]$ by W_i for region $\hat{\mathcal{R}}_i$, $i \in \{1,2,3\}$, as given in the theorem statement. Since $\hat{\mathcal{R}}_i$ partitions the whole space, we obtain the final result as given in (2.34) by taking the expectation of each W_i over the joint distribution of Z, r_{B_0}, $\theta_{\mathrm{D}_0,q}$, $r_{\mathrm{D}_0,q}$, and $\phi_{\mathrm{B}_0\mathrm{D}_0}$. □

A.9 Proof of Theorem 2.16

Similar to the proof of Theorem 2.15, we only need to derive $P_{\mathrm{Cov},q}^{\mathrm{DF}}$. We have

$$\begin{aligned} P_{\mathrm{Cov},q}^{\mathrm{DF}} &\triangleq \mathbb{P}\left[\mathrm{SINR}_q^{\mathrm{DF}} \geq \tau\right] \\ &= 1 - \mathbb{P}\left[\mathrm{SINR}_{\mathrm{BU},q} < \tau, \min\left\{\mathrm{SINR}_{\mathrm{BD}}, \mathrm{SINR}_{\mathrm{DU},q}\right\} < \tau\right] \\ &= 1 - \mathbb{P}\left[\mathrm{SINR}_{\mathrm{BU},q} < \tau\right] + \mathbb{P}\left[\mathrm{SINR}_{\mathrm{BU},q} < \tau, \mathrm{SINR}_{\mathrm{BD}} \geq \tau, \mathrm{SINR}_{\mathrm{DU},q} \geq \tau\right] \\ &\overset{(a)}{=} 1 - \mathbb{E}\left[\mathbb{P}\left[\mathrm{SINR}_{\mathrm{BU},q} < \tau \middle| \mathrm{B}_0, \mathrm{D}_0, I\right]\right] \\ &\quad + \mathbb{E}\left[\mathbb{P}\left[\mathrm{SINR}_{\mathrm{BU},q} < \tau, \mathrm{SINR}_{\mathrm{DU},q} \geq \tau \middle| \mathrm{B}_0, \mathrm{D}_0, I\right]\mathbb{P}\left[\mathrm{SINR}_{\mathrm{BD}} \geq \tau \middle| \mathrm{B}_0, \mathrm{D}_0\right]\right] \\ &\overset{(b)}{=} 1 - \mathbb{E}\left[\mathbb{P}\left[\frac{aX}{bY+I} < \tau \middle| \mathrm{B}_0, \mathrm{D}_0, I\right]\mathbb{P}\left[\frac{cZ}{N_0} < \tau \middle| \mathrm{B}_0, \mathrm{D}_0\right]\right] \\ &\quad - \mathbb{E}\left[\mathbb{P}\left[\frac{\max\{aX,bY\}}{\min\{aX,bY\}+I} < \tau \middle| \mathrm{B}_0, \mathrm{D}_0, I\right]\mathbb{P}\left[\frac{cZ}{N_0} \geq \tau \middle| \mathrm{B}_0, \mathrm{D}_0\right]\right], \end{aligned}$$

where in (a) we conditioned the probabilities on knowing B_0, D_0, and $I = I_{\mathrm{U}} + N_0$, and in (b) we wrote the SINR values in their simpler forms as in (2.14)–(2.16) and also used the relation $\mathbb{P}[E \cap F] + \mathbb{P}\left[E \cap \bar{F}\right] = \mathbb{P}[E]$, where $E = \mathrm{SINR}_{\mathrm{BU},q}$ and $F = \mathrm{SINR}_{\mathrm{DU},q}$, to further simplify the result. Now, using Lemmas 2.3 and 2.4 and deconditioning similar to the proof of Theorem 2.15, we obtain the final result as given in (2.35). □

Appendix B

Proofs of Lemmas and Theorems of Chapter 3

B.1 Proof of Lemma 3.9

Since we have started with an inhomogeneous PPP with the density given as (3.3) for $t = 0$ in the UDM and the displacements are independent of each other, the network of interfering DBSs will also be an inhomogeneous PPP at every time t due to displacement theorem [19]. According to Lemma 3.7 and defining $\mathcal{X} = b(\mathbf{o}', u_0)$ as the exclusion zone, if there was no $\mathcal{X}$ and DBSs moved independently of each other, as in our mobility models, the network of all DBSs (including the serving DBS) would have remained a homogeneous PPP with density λ_0. Taking $\mathcal{X}$ into account, the resulting density of the network can be partitioned into two sets: (i) density contributed by $\mathcal{X}$ (denoted as $\lambda_1(t; u_{\mathbf{x}}, u_0)$), i.e., due to the points that are initially inside $\mathcal{X}$, and (ii) density of interferers (denoted as $\lambda(t; u_{\mathbf{x}}, u_0)$), i.e., due to the points that are initially outside $\mathcal{X}$. Since the resulting network density is λ_0, we have $\lambda(t; u_{\mathbf{x}}, u_0) = \lambda_0 - \lambda_1(t; u_{\mathbf{x}}, u_0)$. Define $N(t)$ as the average number of points that are initially inside $\mathcal{X}$ and after a displacement of $L(t)$ land on an infinitesimal annulus $\mathcal{A}$ with an inner and outer radii of $u_{\mathbf{x}}$ and $u_{\mathbf{x}} + \mathrm{d}u_{\mathbf{x}}$, respectively. Since the density in this case is rotation-invariant, it is sufficient to consider an annulus centered at $\mathbf{o}'$ for our analysis. By definition, we can write

$$\lambda_1(t; u_{\mathbf{x}}, u_0) = \lim_{\mathrm{d}u_{\mathbf{x}} \to 0} \frac{N(t)}{2\pi u_{\mathbf{x}} \mathrm{d}u_{\mathbf{x}}}, \tag{B.1}$$

where the denominator denotes the area of $\mathcal{A}$. As shown in Fig. B.1, let $\mathbf{x}$, $\mathbf{y}_1$, and $\mathbf{y}_2$ denote a randomly selected point inside $\mathcal{X}$ with distance r from $\mathbf{o}'$ and two intersection points of $b(\mathbf{x}, L(t))$ with $\mathcal{A}$, respectively. Writing the cosine law in triangles $\mathbf{o}'\mathbf{x}\mathbf{y}_1$ and $\mathbf{o}'\mathbf{x}\mathbf{y}_2$, we have

$$u_{\mathbf{x}}^2 = L(t)^2 + r^2 - 2rL(t)\cos(\theta),$$
$$(u_{\mathbf{x}} + \mathrm{d}u_{\mathbf{x}})^2 = L(t)^2 + r^2 - 2rL(t)\cos(\theta + \varphi),$$

where $\theta = \angle\mathbf{o}'\mathbf{x}\mathbf{y}_1$ and $\varphi = \angle\mathbf{y}_1\mathbf{x}\mathbf{y}_2$. Eliminating θ in both of these equations gives

$$\cos(\varphi) = \frac{1}{b^2}\left[a^2 - a\left(\mathrm{d}u_{\mathbf{x}} + \frac{(\mathrm{d}u_{\mathbf{x}})^2}{2u_{\mathbf{x}}}\right) + c\sqrt{c^2 + 2a\left(\mathrm{d}u_{\mathbf{x}} + \frac{(\mathrm{d}u_{\mathbf{x}})^2}{2u_{\mathbf{x}}}\right) - \left(\mathrm{d}u_{\mathbf{x}} + \frac{(\mathrm{d}u_{\mathbf{x}})^2}{2u_{\mathbf{x}}}\right)^2}\right],$$

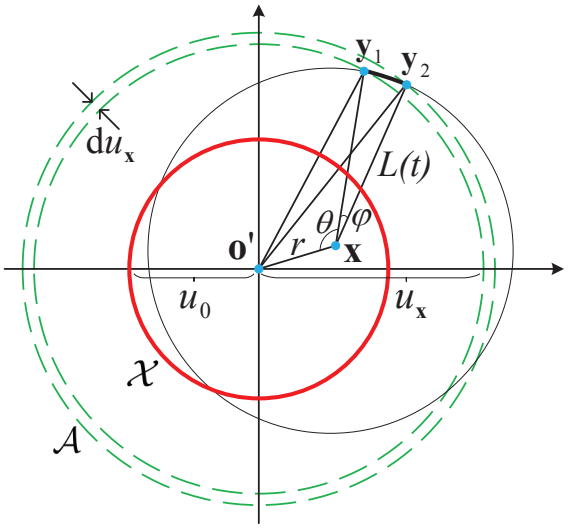

Figure B.1: An illustration for the proof of Lemma 3.9. The red circle and the green dotted circles indicate $\mathcal{X}$ and $\mathcal{A}$, respectively.

where $a = \frac{L(t)^2+r^2-u_{\mathbf{x}}^2}{2u_{\mathbf{x}}}, b = \frac{2rL(t)}{2u_{\mathbf{x}}}, c = \sqrt{b^2-a^2}$. Note that the probability that a DBS at $\mathbf{x}$ lands on $\mathcal{A}$ after a displacement of $L(t)$ is $\frac{2\varphi}{2\pi}$. Hence, we write $N(t)$ by considering all such points $\mathbf{x}$ in $\mathcal{X}$ as $N(t) = \mathbb{E}\left[\int_0^{u_0} \frac{\varphi}{\pi} 2\pi r \lambda_0 \,\mathrm{d}r\right]$, where the expectation is taken over $L(t)$. This gives

$$\lambda_1(t; u_{\mathbf{x}}, u_0) = \frac{\lambda_0}{\pi}\mathbb{E}\left[\int_0^{u_0} \frac{r}{u_{\mathbf{x}}} \lim_{\mathrm{d}u_{\mathbf{x}}\to 0} \frac{\varphi}{\mathrm{d}u_{\mathbf{x}}}\,\mathrm{d}r\right], \tag{B.2}$$

where we have changed the order of limit with the expectation and the integration due to the continuity of the integrand. Representing $\mathrm{d}u_{\mathbf{x}}$ with x for simplicity, we compute the limit as

$$\begin{aligned}\lim_{x\to 0}\frac{\varphi}{x} &= \lim_{x\to 0}\frac{1}{x}\cos^{-1}\left(1-\frac{1}{a^2+c^2}\left[c^2+ax+\frac{a}{2u_{\mathbf{x}}}x^2-c\sqrt{c^2+2ax+\frac{a}{u_{\mathbf{x}}}x^2-\left(x+\frac{x^2}{2u_{\mathbf{x}}}\right)^2}\right]\right)\\ &\overset{(*)}{=} \sqrt{\frac{2}{a^2+c^2}}\lim_{x\to 0}\sqrt{\frac{(a^2+c^2)\left(x^2+\frac{1}{u_{\mathbf{x}}}x^3+\frac{1}{4u_{\mathbf{x}}^2}x^4\right)}{2c^2x^2}}\\ &= \frac{1}{c} = \frac{2u_{\mathbf{x}}}{\sqrt{(u_{\mathbf{x}}^2-(L(t)-r)^2)((L(t)+r)^2-u_{\mathbf{x}}^2)}},\end{aligned} \tag{B.3}$$

where in $(*)$ we used the Taylor series expansion $\cos^{-1}(1-x) = \sqrt{2x} + \Theta(x^{3/2})$ as $x \to 0$, where $f(x) = \Theta(g(x))$ implies that $f(x)$ is asymptotically bounded by $g(x)$ both from above and below. Note that since the triangle inequality holds for the triple $(u_{\mathbf{x}}, r, L(t))$, the result in (B.3) is real and positive, as expected. Plugging (B.3) into (B.2), we have

$$\lambda_1(t; u_{\mathbf{x}}, u_0) = \frac{\lambda_0}{\pi}\int_0^{\infty}\int_{\mathcal{I}_1} \frac{2r f_L(l;t)}{\sqrt{(u_{\mathbf{x}}^2-(l-r)^2)((l+r)^2-u_{\mathbf{x}}^2)}}\,\mathrm{d}r\,\mathrm{d}l, \tag{B.4}$$

where $\mathcal{I}_1 = \{|l - u_{\mathbf{x}}| \leq r \leq l + u_{\mathbf{x}}\} \bigcap \{0 \leq r \leq u_0\}$. Since the net displacement of a DBS at time t cannot exceed its aggregate traveled distance vt, we have $L(t) \leq vt$. Hence, (B.4) simplifies to

$$\lambda_1(t; u_{\mathbf{x}}, u_0) = \frac{\lambda_0}{\pi} \int_0^{vt} \int_{\mathcal{I}_1} f_L(l;t) \frac{2r}{\sqrt{(u_{\mathbf{x}}^2 - (l-r)^2)((l+r)^2 - u_{\mathbf{x}}^2)}} \,\mathrm{d}r \,\mathrm{d}l + \frac{\lambda_0}{\pi}(1 - F_L(vt;t)) \int_{\mathcal{I}_2} \frac{2r}{\sqrt{(u_{\mathbf{x}}^2 - (vt-r)^2)((vt+r)^2 - u_{\mathbf{x}}^2)}} \,\mathrm{d}r,$$

where $\mathcal{I}_2 = \{|vt - u_{\mathbf{x}}| \leq r \leq vt + u_{\mathbf{x}}\} \bigcap \{0 \leq r \leq u_0\}$. Simplifying the last step requires tedious integrations and the details are skipped to maintain brevity. Finally, the density of the network of interfering DBSs is summarized as (3.4) and (3.5) in the lemma statement. □

B.2 Proof of Theorem 3.13

The intensity measure or the expected number of interfering DBSs in the Borel set $\mathcal{B} = b(\mathbf{o}', u_0 + vt)$ is given as $\Lambda(\mathcal{B}) = 2\pi \int_0^{u_0+vt} u_{\mathbf{x}} \lambda(t; u_{\mathbf{x}}, u_0) \,\mathrm{d}u_{\mathbf{x}}$. Defining $\Lambda_1(\mathcal{B})$ and $\Lambda_2(\mathcal{B})$ as the intensity measures for the SL mobility model and a general i.i.d. mobility model, respectively, we need to show that $\Lambda_1(\mathcal{B}) \geq \Lambda_2(\mathcal{B})$. Note that we only prove this for $t \leq \frac{u_0}{v}$ and the proof for $t > \frac{u_0}{v}$ follows on the similar lines. Using (3.4) and (3.5), we have

$$\Lambda_1(\mathcal{B}) - \Lambda_2(\mathcal{B}) = 2\pi\lambda_0 \int_{u_0 - vt}^{u_0+vt} u_{\mathbf{x}} \left[-g(vt, u_{\mathbf{x}}) + F_L(u_0 - u_{\mathbf{x}}; t) + \int_{|u_{\mathbf{x}} - u_0|}^{vt} f_L(l;t) g(l, u_{\mathbf{x}}) \,\mathrm{d}l \right] \mathrm{d}u_{\mathbf{x}}, \tag{B.5}$$

where $g(l, u_{\mathbf{x}}) = \frac{1}{\pi} \cos^{-1}\left(\frac{l^2 + u_{\mathbf{x}}^2 - u_0^2}{2lu_{\mathbf{x}}}\right)$. Denote the integrand in (B.5) by $\mathfrak{L}(u_{\mathbf{x}}, F_L(u_{\mathbf{x}}), f_L(u_{\mathbf{x}}))$, which is a functional with $u_{\mathbf{x}}$ being the independent variable. Note that we also have $F_L(0) = 0$ and $F_L(vt) = 1$ by definition. Using the Euler-Lagrange equation, we show that $\Lambda_1(\mathcal{B}) - \Lambda_2(\mathcal{B})$ attains its minimum at zero. From the calculus of variations, we know that F_L is a critical (extremum) function for the functional $\mathfrak{L}$ if it satisfies the Euler-Lagrange equation: $\frac{\partial \mathfrak{L}}{\partial F_L} - \frac{\mathrm{d}}{\mathrm{d}u_{\mathbf{x}}}\left(\frac{\partial \mathfrak{L}}{\partial f_L}\right) = 0$. We compute the first term as $\frac{\partial \mathfrak{L}}{\partial F_L} = u_{\mathbf{x}} \mathbf{1}(u_0 - u_{\mathbf{x}})$ and the second term as

$$\begin{aligned} \frac{\mathrm{d}}{\mathrm{d}u_{\mathbf{x}}}\left(\frac{\partial \mathfrak{L}}{\partial f_L}\right) &= \frac{\mathrm{d}}{\mathrm{d}u_{\mathbf{x}}}\left(\int_{|u_{\mathbf{x}} - u_0|}^{vt} u_{\mathbf{x}} g(l, u_{\mathbf{x}}) \,\mathrm{d}l\right) \\ &\overset{(a)}{=} u_{\mathbf{x}} \mathbf{1}(u_0 - u_{\mathbf{x}}) + \int_{|u_{\mathbf{x}} - u_0|}^{vt} \frac{\partial}{\partial u_{\mathbf{x}}} \left(u_{\mathbf{x}} g(l, u_{\mathbf{x}})\right) \,\mathrm{d}l, \end{aligned}$$

where in (a) we used the Leibniz integral rule along with $g(|u_{\mathbf{x}} - u_0|, u_{\mathbf{x}}) = \mathbf{1}(u_0 - u_{\mathbf{x}})$. Applying these derivatives to the Euler-Lagrange equation, we get $\int_{|u_{\mathbf{x}} - u_0|}^{vt} \frac{\partial}{\partial u_{\mathbf{x}}} \left(u_{\mathbf{x}} g(l, u_{\mathbf{x}})\right) \,\mathrm{d}l = 0$,

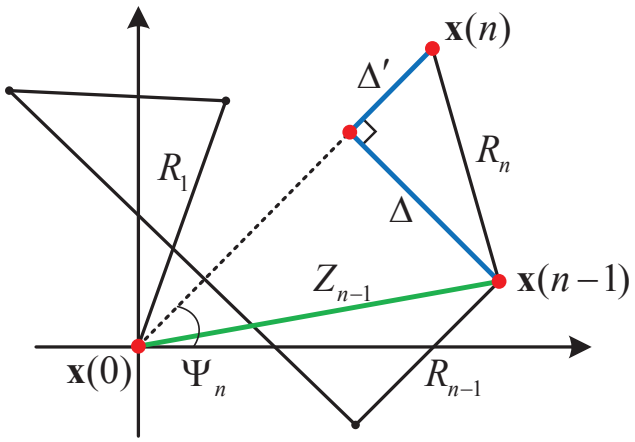

Figure B.2: An illustration for the proof of Lemma 3.16 showing the geometrical interpretations of Δ and Δ' in an RW.

which does not include either F_L or f_L. This means that the original function in (B.5) attains its extremum at the boundaries. We now evaluate $\mathfrak{L}(u_{\mathbf{x}}, F_L(u_{\mathbf{x}}), f_L(u_{\mathbf{x}}))$ at $u_{\mathbf{x}} = u_0 \pm vt$ as

$$u_{\mathbf{x}} = u_0 - vt \rightarrow \mathfrak{L} = -u_{\mathbf{x}} g(vt, u_0 - vt) + u_{\mathbf{x}} F_L(+vt) + 0 = 0$$
$$u_{\mathbf{x}} = u_0 + vt \rightarrow \mathfrak{L} = -u_{\mathbf{x}} g(vt, u_0 + vt) + u_{\mathbf{x}} F_L(-vt) + 0 = 0.$$

Since both of the boundary values are 0, we conclude that the minimum value in (B.5) is 0. □

B.3 Proof of Lemma 3.16

In order to derive the distribution of Ψ_n, we introduce $(n-1)$ auxiliary random variables $\Xi_i = \Theta_i$, $1 \le i \le n-1$, and find the joint pdf of n random variables Ψ_n and Ξ_i, $1 \le i \le n-1$. We then integrate out these auxiliary random variables to find the pdf of Ψ_n. We start by solving the system of n equations (one equation in (3.11) for the definition of Ψ_n and $(n-1)$ equations introduced by the auxiliary random variables) to derive Θ_i's in terms of Ψ_n and Ξ_i's. The result can be written as the following two sets of solutions:

$$\text{Set 1}: \begin{cases} \Theta_i = \Xi_i, & i = 1, 2, \ldots, n-1 \\ \Theta_n = \Xi_{n_1} = \tan^{-1}\left(\frac{-\Delta\cos(\Psi_n) + \Delta'\sin(\Psi_n)}{\Delta\sin(\Psi_n) + \Delta'\cos(\Psi_n)}\right), \end{cases}$$
$$\text{Set 2}: \begin{cases} \Theta_i = \Xi_i, & i = 1, 2, \ldots, n-1 \\ \Theta_n = \Xi_{n_2} = \tan^{-1}\left(\frac{-\Delta\cos(\Psi_n) - \Delta'\sin(\Psi_n)}{\Delta\sin(\Psi_n) - \Delta'\cos(\Psi_n)}\right), \end{cases}$$

where $\Delta = \sum_{i=1}^{n-1} R_i \sin(\Xi_i - \Psi_n)$ and $\Delta' = \sqrt{R_n^2 - \Delta^2}$. In Fig. B.2, we show the geometrical interpretations of Δ and Δ'. Note also that $\Psi_n = \frac{\Xi_{n_1} + \Xi_{n_2}}{2}$. Computing the determinant of

the Jacobian matrix $\mathcal{J}$, we get $|\mathcal{J}| = |\frac{\partial \Theta_n}{\partial \Psi_n}|$ for both solution sets. Hence,

$$\begin{aligned} |\mathcal{J}| &= \frac{\sum_{i=1}^{n}\sum_{j=1}^{n} R_i R_j \cos(\Theta_i - \Theta_j)}{\sum_{i=1}^{n} R_i R_n \cos(\Theta_i - \Theta_n)} \\ &= 1 + \frac{\sum_{i=1}^{n}\sum_{j=1}^{n-1} R_i R_j \cos(\Theta_i - \Theta_j)}{\sum_{i=1}^{n} R_i R_n \cos(\Theta_i - \Theta_n)}. \end{aligned}$$

By some algebraic manipulations, we find that $|\mathcal{J}|\big|_{\Theta_n=\Xi_{n_1}} + |\mathcal{J}|\big|_{\Theta_n=\Xi_{n_2}} = 2$. Now, since $\Theta_i \sim U[0, 2\pi)$, the joint distribution of Ψ_n and Ξ_i's can be written as

$$\begin{aligned} f_{\Psi_n,\boldsymbol{\Xi}}(\psi_n, \boldsymbol{\xi}) &= f_{\boldsymbol{\Theta}}(\boldsymbol{\theta})|\mathcal{J}|\big|_{\Theta_n=\Xi_{n_1}} + f_{\boldsymbol{\Theta}}(\boldsymbol{\theta})|\mathcal{J}|\big|_{\Theta_n=\Xi_{n_2}} \\ &= 2\left(\frac{1}{2\pi}\right)^n, \end{aligned}$$

where the boldface letters represent vector random variables. Integrating out Ξ_i, $1 \le i \le n-1$, the distribution of Ψ_n is derived as $f_{\Psi_n}(\psi_n) = \frac{1}{\pi}$ for $\psi_n \in [-\frac{\pi}{2}, \frac{\pi}{2})$, due to the range of the $\tan^{-1}$ function. Finally, since the actual range of Ψ_n is $[-\pi, \pi)$, we conclude that $f_{\Psi_n}(\psi_n) = \frac{1}{2\pi}$ for $\psi_n \in [-\pi, \pi)$, and the proof is complete. □

B.4 Proof of Lemma 3.17

We consider an RW of two flights F_1 and F_2, where F_1 and F_2 are two independent Rayleigh random variables with parameters σ_1 and σ_2, respectively. Let F be the distance from the start of the first flight to the end of the second flight. We show that F is Rayleigh distributed with parameter $\sigma = \sqrt{\sigma_1^2 + \sigma_2^2}$, which proves the lemma by induction. Since F_1 and F_2 are Rayleigh distributed, they can be written as $F_1 = \sqrt{X_1^2 + Y_1^2}$ and $F_2 = \sqrt{X_2^2 + Y_2^2}$, where $X_1, Y_1 \sim \mathcal{N}(0, \sigma_1^2)$ are $X_2, Y_2 \sim \mathcal{N}(0, \sigma_2^2)$ are independent Gaussian random variables. Note that due to the independence of X_1 and X_2, their sum will also be a Gaussian random variable. Therefore, $X = X_1 + X_2 \sim \mathcal{N}(0, \sigma_1^2 + \sigma_2^2)$. Likewise, $Y = Y_1 + Y_2 \sim \mathcal{N}(0, \sigma_1^2 + \sigma_2^2)$. We can now represent F_1 and F_2 in the abscissa and ordinate axes as $[X_1, Y_1]$ and $[X_2, Y_2]$, respectively. Hence, $F = \sqrt{X^2 + Y^2}$ will have a Rayleigh distribution with parameter $\sigma = \sqrt{\sigma_1^2 + \sigma_2^2}$. This completes the proof. □

B.5 Proof of Proposition 3.20

Similar to the proof of Lemma 3.16, we define $2(n-1)$ auxiliary random variables $X_i = R_i$ and $\Xi_i = \Theta_i$, $1 \le i \le n-1$ and find the joint pdf of these $2n$ random variables. Solving this system of $2n$ equations, we can write R_i and Θ_i, $1 \le i \le n$ in terms of S_n, Z_n, X_i, and Ξ_i, $1 \le i \le n-1$. Note that $(2n-1)$ of these equations have trivial solutions, i.e., $R_i = X_i$ and

$\Theta_i = \Xi_i$ for $1 \leq i \leq n-1$ and $R_n = S_n - \sum_{i=1}^{n-1} X_i$. For Θ_n, we write the governing equation as

$$\sum_{i=1}^{n-1} X_i \cos(\Theta_n - \Xi_i) = \frac{Z_n^2 - R_n^2 - \sum_{i,j=1}^{n-1} X_i X_j \cos(\Xi_i - \Xi_j)}{2R_n}. \tag{B.6}$$

Note that the exact expression for Θ_n will not be required for the derivation of the joint pdf of interest. We then derive the determinant of the Jacobian matrix as

$$|\mathcal{J}| = \left|\frac{\partial \Theta_n}{\partial Z_n}\right| = \frac{Z_n}{R_n \left|\sum_{i=1}^{n-1} X_i \sin(\Theta_n - \Xi_i)\right|}. \tag{B.7}$$

Solving (B.6) and (B.7), we can eliminate R_n and Θ_n to get $|\mathcal{J}|$ only in terms of S_n, Z_n, X_i, and Ξ_i, $1 \leq i \leq n-1$. Hence, we can write the joint distribution of these $2n$ random variables as

$$f_{S_n, Z_n, \boldsymbol{X}, \boldsymbol{\Xi}}(s, z, \boldsymbol{x}, \boldsymbol{\xi}) = \frac{4z}{(2\pi)^n} \frac{f_R(s - J_n) \prod_{i=1}^{n-1} f_R(x_i)}{\sqrt{(z^2 - (s - J_n - K_n)^2)\,((s - J_n + K_n)^2 - z^2)}},$$

where $J_n = \sum_{i=1}^{n-1} x_i$, $K_n = \sqrt{\sum_{i,j=1}^{n-1} x_i x_j \cos(\xi_i - \xi_j)}$. Integrating this pdf $2(n-1)$ times w.r.t. x_i and ξ_i, $1 \leq i \leq n-1$, we end up with (3.13) and the proof is complete. □

B.6 Proof of Proposition 3.23

Considering the RW mobility model at time t, a DBS is either in its first flight, or in its second flight, etc. Hence, initializing $S_0 = 0$, the event $\Omega = \bigcup_{n=1}^{\infty} (S_{n-1} \leq vt < S_n)$ has unit probability. Thus, we can write the cdf of $L(t)$ as

$$\begin{aligned}
F_L(l;t) &= \mathbb{P}[L(t) \leq l] = \mathbb{P}[L(t) \leq l, \Omega] \\
&= \sum_{n=1}^{\infty} \mathbb{P}\left[L(t) \leq l, S_{n-1} \leq vt < S_n\right] \\
&\overset{(a)}{=} \sum_{n=1}^{\infty} \mathbb{P}\left[Z_{n-1}^2 - 2Z_{n-1}(vt - S_{n-1})\cos(\Phi_n) + (vt - S_{n-1})^2 \leq l^2, S_{n-1} \leq vt < S_n\right] \\
&\overset{(b)}{=} \sum_{n=1}^{\infty} \int_0^{vt} \int_0^{s} f_{S_{n-1}, Z_{n-1}}(s, z)(1 - F_R(vt - s)) \\
&\quad \times \mathbb{P}\left[z^2 + (vt - s)^2 - 2z(vt - s)\cos(\Phi_n) \leq l^2\right] \mathrm{d}z\, \mathrm{d}s,
\end{aligned} \tag{B.8}$$

where in (a) we used the cosine law and in (b) we conditioned the probability on knowing S_{n-1} and Z_{n-1}. Note that $\Phi_n = \pi - \Theta_n + \Psi_{n-1}$ is the angle between the direction of Z_{n-1} and the direction of the n-th flight. We now rewrite the probability in (B.8) as $\mathbb{P}\left[\cos(\Phi_n) \geq x\right]$, where

$x = \frac{z^2+(vt-s)^2-l^2}{2z(vt-s)}$. In order for this probability to be non-zero, we have two cases: (i) $x \leq -1$ which gives $z+(vt-s) \leq l$, and (ii) $-1 < x \leq 1$ which gives $|z-(vt-s)| \leq l < z+(vt-s)$, which is the triangle inequality. Note also that it is clear from our setup that $z \leq s \leq vt$. For $l \geq vt$, only the first case will hold and we can write the cdf as

$$\begin{aligned} F_L(l;t) &= \sum_{n=1}^{\infty} \int_0^{vt} \int_0^{s} f_{S_{n-1},Z_{n-1}}(s,z)(1-F_R(vt-s))\,\mathrm{d}z\,\mathrm{d}s \\ &= \sum_{n=1}^{\infty} \int_0^{vt} f_{S_{n-1}}(s)(1-F_R(vt-s))\,\mathrm{d}s \\ &= \sum_{n=1}^{\infty} F_{S_{n-1}}(vt) - F_{S_n}(vt) = 1, \end{aligned}$$

where in the last equality we used the convolution integral that arises in the derivation of the cdf of $S_n = S_{n-1} + R_n$. Hence, $F_L(l;t) = 1$ for $l \geq vt$, as expected. On the other hand, both cases can occur for $l < vt$. For the first case, we have $0 \leq z \leq l-(vt-s)$ and $vt-l \leq s \leq vt$. Similarly, for the second case we have $|l-(vt-s)| \leq z \leq \min\{s,\, l+(vt-s)\}$ and $\frac{vt-l}{2} \leq s \leq vt$ based on the triangle inequality. Now, according to Lemma 3.16, Ψ_{n-1} is uniformly distributed in $[0, 2\pi)$, and since $\Theta_n \sim U[0, 2\pi)$ is independent of Ψ_{n-1}, the random variable Φ_n will have a symmetric triangular distribution. However, since the range of values of Φ_n is between 0 and 2π, we have $\Phi_n \sim U[0, 2\pi)$. Hence, the cdf of $L(t)$ for $l < vt$ can be written as in (3.15). Note that for $n = 1$, we have $L(t) = vt$ and the cdf becomes $\mathbb{P}[vt \leq l, vt < R_1] = (1 - F_R(vt))\mathbf{1}(l - vt)$. Differentiating the derived cdf w.r.t. l using the Leibniz integral rule for two-dimensional integrals, we end up with the pdf of $L(t)$ as in (3.16). □

B.7 Proof of Proposition 3.24

Define $M_n = S_n + vW_{n-1}$ and $Y_n = S_n + vW_n$. Considering the RWP mobility model at time t, a DBS is either in one of its flight states, or in one of its waiting time states. Hence, initializing $S_0 = 0$ and $W_{-1} = 0$, the event $\Omega' = \bigcup_{n=1}^{\infty}(V_{n-1} \cup F_n)$ has unit probability, where $V_n = \{M_n \leq vt < Y_n\}$ and $F_n = \{Y_{n-1} \leq vt < M_n\}$ are the n-th waiting and flight periods, respectively. Thus, we can write the cdf of $L(t)$ as follows.

$$\begin{aligned} F_L(l;t) = \mathbb{P}[L(t) \leq l] = \mathbb{P}[L(t) \leq l, \Omega'] &= \sum_{n=1}^{\infty} \mathbb{P}\left[L(t) \leq l, V_{n-1}\right] + \sum_{n=1}^{\infty} \mathbb{P}\left[L(t) \leq l, F_n\right] \\ &\overset{(a)}{=} \sum_{n=1}^{\infty} \mathbb{P}\left[Z_{n-1} \leq l, V_{n-1}\right] \\ &\quad + \sum_{n=1}^{\infty} \mathbb{P}[Z_{n-1}^2 + (vt - Y_{n-1})^2 - 2Z_{n-1}(vt - Y_{n-1})\cos(\Phi_n) \leq l^2, F_n] \end{aligned}$$

$$
\begin{aligned}
&= \sum_{n=1}^{\infty} \int_0^{vt} \int_0^{\min\{s,l\}} f_{S_{n-1},Z_{n-1}}(s,z) \mathbb{P}\left[s + vW_{n-2} \le vt < s + vW_{n-2} + vT_{n-1}\right] \mathrm{d}z \, \mathrm{d}s \\
&\quad + \sum_{n=1}^{\infty} \int_0^{vt} \int_0^{y} f_{Y_{n-1},Z_{n-1}}(y,z)(1 - F_R(vt-y)) \\
&\quad \times \mathbb{P}\left[z^2 + (vt-y)^2 - 2z(vt-y)\cos(\Phi_n) \le l^2\right] \mathrm{d}z \, \mathrm{d}y \\
&\overset{(b)}{=} \sum_{n=1}^{\infty} \int_0^{vt} \int_0^{\min\{s,l\}} f_{S_{n-1},Z_{n-1}}(s,z) \left(F_{W_{n-2}}(t - \frac{s}{v}) - F_{W_{n-1}}(t - \frac{s}{v})\right) \mathrm{d}z \, \mathrm{d}s \\
&\quad + \sum_{n=1}^{\infty} \int_0^{vt} \int_0^{y} \int_0^{\frac{y}{v}} f_{W_{n-1}}(w) f_{S_{n-1},Z_{n-1}}(y - vw, z)(1 - F_R(vt-y)) \\
&\quad \times \mathbb{P}\left[z^2 + (vt-y)^2 - 2z(vt-y)\cos(\Phi_n) \le l^2\right] \mathrm{d}w \, \mathrm{d}z \, \mathrm{d}y,
\end{aligned}
$$

where in (a) we used the fact that $L(t) = Z_{n-1}$ when a DBS is in its $(n-1)$-th waiting state and $L(t)$ follows the cosine rule when a DBS is in its n-th flight state. In the first summation of (b), we first conditioned the probability in the integrand on knowing T_{n-1} and then used the identity $W_{n-1} = W_{n-2} + T_{n-1}$ to simplify the result. In the second summation of (b), we used the definition of Y_{n-1} to write the joint pdf of Y_{n-1} and Z_{n-1} in terms of the joint pdf of S_{n-1} and Z_{n-1}. Now, with the same reasoning as in the proof of Proposition 3.23, we get the cdf and pdf of $L(t)$ for $l \le vt$ as in (3.19) and (3.20), respectively. Note that for $n = 1$, we have

$$
\begin{aligned}
F_L(l;t|n=1) &= \mathbb{P}[vt \le vW_0] + \mathbb{P}[vt - vW_0 \le l, vW_0 \le vt < R_1 + vW_0] \\
&= \mathbb{P}\left[W_0 \ge t - \frac{\min\{R_1, l\}}{v}\right] \\
&= \int_0^{\infty} \mathbb{P}[\min\{R_1, l\} \ge vt - vw] f_T(w) \, \mathrm{d}w \\
&= \int_{t-\frac{l}{v}}^{\infty} (1 - F_R(vt - vw)) \, f_T(w) \, \mathrm{d}w.
\end{aligned}
$$

For $l > vt$, we can write the cdf as

$$
\begin{aligned}
F_L(l;t) &= \sum_{n=1}^{\infty} \int_0^{vt} f_{S_{n-1}}(s) \left(F_{W_{n-2}}(t - \frac{s}{v}) - F_{W_{n-1}}(t - \frac{s}{v})\right) \mathrm{d}s \\
&\quad + \sum_{n=1}^{\infty} \int_0^{vt} f_{Y_{n-1}}(y)(1 - F_R(vt-y)) \, \mathrm{d}y \\
&\overset{(a)}{=} \sum_{n=1}^{\infty} \int_0^{vt} f_{S_{n-1}}(s) F_{W_{n-2}}(t - \frac{s}{v}) \, \mathrm{d}s - \int_0^{vt} f_{Y_{n-1}}(y) F_R(vt-y) \, \mathrm{d}y \\
&\overset{(b)}{=} \sum_{n=1}^{\infty} F_{M_{n-1}}(vt) - F_{M_n}(vt) = 1,
\end{aligned}
$$

where in (a) we used the definition of Y_{n-1} to get $F_{Y_{n-1}}(vt) = \int_0^{vt} f_{S_{n-1}}(s) F_{W_{n-1}}(t - \frac{s}{v})\,\mathrm{d}s$ and in (b) we used the definition of M_{n-1} and the identity $M_n = Y_{n-1} + R_n$ to get the result. □

Appendix C

Proofs of Lemmas and Theorems of Chapter 4

C.1 Proof of Lemma 4.2

In Fig. C.1, we represent two DBSs D_0 and D_1 and their trajectories in the time interval $[t_0, t_2]$. We denote the location of D_0 (D_1) at times t_0, t_1, and t_2 by A_0 (B_0), A_1 (B_1), and A_2 (B_2), respectively, and its corresponding distance from $\mathbf{o}'$ by a_0 (b_0), a_1 (b_1), and a_2 (b_2), respectively, where we assume that a handover occurs at time $t = t_1$, where $t_0 < t_1 < t_2$. Now, we need to show $a_2 > b_2$ given $a_0 < b_0$ and $a_1 > b_1$. Define $\theta_A = \angle \mathbf{o}' A_0 A_2$, $\varphi_A = \angle \mathbf{o}' A_1 A_2$, $\theta_B = \angle \mathbf{o}' B_0 B_2$, and $\varphi_B = \angle \mathbf{o}' B_1 B_2$. Without loss of generality, we assume that $\pi > \theta_A > \theta_B$. We now consider two cases:

Case 1: $\theta_B > \frac{\pi}{2}$. We first show that $\varphi_A > \varphi_B > \frac{\pi}{2}$. From $\triangle \mathbf{o}' B_0 B_1$, it is clear that $\varphi_B > \theta_B > \frac{\pi}{2}$. Applying the sine law in $\triangle \mathbf{o}' A_0 A_1$ and $\triangle \mathbf{o}' B_0 B_1$, we have

$$\frac{a_0}{\sin(\pi - \varphi_A)} = \frac{a_1}{\sin(\theta_A)},$$
$$\frac{b_0}{\sin(\pi - \varphi_B)} = \frac{b_1}{\sin(\theta_B)}.$$

Since by assumption $\sin(\theta_A) < \sin(\theta_B)$ and $\frac{a_0}{a_1} < \frac{b_0}{b_1}$, we conclude that $\sin(\pi - \varphi_A) < \sin(\pi - \varphi_B)$ which gives $\varphi_A > \varphi_B > \frac{\pi}{2}$. Now writing the cosine law in $\triangle \mathbf{o}' A_1 A_2$ and $\triangle \mathbf{o}' B_1 B_2$, we get $a_2^2 = a_1^2 + d_1^2 - 2a_1 d_1 \cos(\varphi_A)$ and $b_2^2 = b_1^2 + d_1^2 - 2b_1 d_1 \cos(\varphi_B)$. Since $a_1 > b_1$ and $\cos(\varphi_A) < \cos(\varphi_B) < 0$, we end up with $a_2 > b_2$.

Case 2: $\theta_B < \frac{\pi}{2}$. Writing the cosine law in $\triangle \mathbf{o}' A_0 A_1$, $\triangle \mathbf{o}' B_0 B_1$, $\triangle \mathbf{o}' A_0 A_2$, and $\triangle \mathbf{o}' B_0 B_2$, we have

$$\begin{aligned}
a_1^2 &= a_0^2 + d_0^2 - 2a_0 d_0 \cos(\theta_A),\\
b_1^2 &= b_0^2 + d_0^2 - 2b_0 d_0 \cos(\theta_B),\\
a_2^2 &= a_0^2 + (d_0 + d_1)^2 - 2a_0(d_0 + d_1)\cos(\theta_A),\\
b_2^2 &= b_0^2 + (d_0 + d_1)^2 - 2b_0(d_0 + d_1)\cos(\theta_B).
\end{aligned}$$

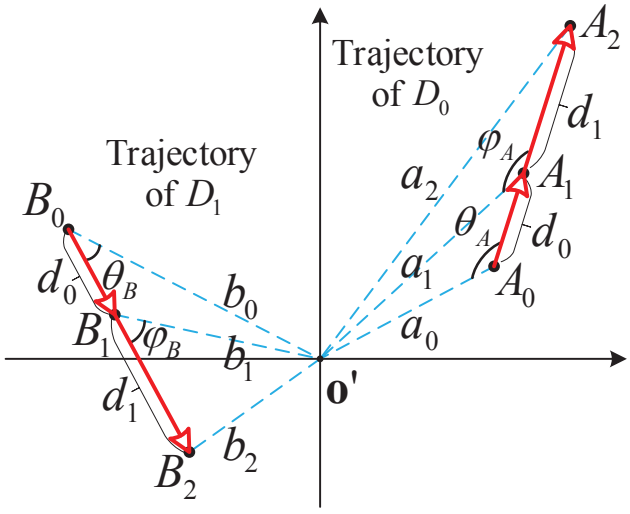

Figure C.1: Trajectories of D_0 and D_1. Arrows denote the direction of movements of DBSs.

Now, to show the inequality $a_2 > b_2$, we can write

$$\begin{aligned} a_2^2 > b_2^2 &\iff a_0^2 - 2a_0(d_0+d_1)\cos(\theta_A) > b_0^2 - 2b_0(d_0+d_1)\cos(\theta_B) \\ &\iff a_1^2 - 2a_0 d_1 \cos(\theta_A) > b_1^2 - 2b_0 d_1 \cos(\theta_B) \\ &\iff (a_1^2 - b_1^2) + 2d_1(b_0\cos(\theta_B) - a_0\cos(\theta_A)) > 0. \end{aligned}$$

The last inequality is valid since $\cos(\theta_B) > \max\{0, \cos(\theta_A)\}$ and $b_0 > a_0$, which gives $b_0\cos(\theta_B) > a_0\cos(\theta_A)$. □

C.2 Proof of Theorem 4.4

Consider the set of BSs and the reference UE in Fig. C.2, where the serving BS is located at $\mathbf{o}$ and the reference UE moves a distance of vt in a uniformly random direction θ from $\mathbf{x}_1$ to $\mathbf{x}_2$. The distance of the reference UE from $\mathbf{o}$ before and after its movement is r and R, respectively. Defining $\mathcal{C}_1 = b(\mathbf{x}_1, r)$ and $\mathcal{C}_2 = b(\mathbf{x}_2, R)$ as two open balls, handover will not occur if there is no BS in $\mathcal{C}_2$. Since $\mathcal{C}_1$ is empty by definition, handover will not occur if there is no BS in $\mathcal{C}_2 \backslash \mathcal{C}_1$ (shaded region in Fig. C.2). Hence, the handover probability can be written by conditioning on r and θ as

$$\begin{aligned} \mathbb{P}[H(t)|r,\theta] &= 1 - \mathbb{P}\left[N(\mathcal{C}_2\backslash\mathcal{C}_1) = 0\right] && \text{(C.1)} \\ &= 1 - \mathbb{P}\left[N(\mathcal{C}_2\backslash(\mathcal{C}_1 \cap \mathcal{C}_2)) = 0\right] \\ &\overset{(*)}{=} 1 - \mathrm{e}^{-\lambda_0|\mathcal{C}_2\backslash(\mathcal{C}_1\cap\mathcal{C}_2)|} && \text{(C.2)} \\ &= 1 - \mathrm{e}^{-\lambda_0(\pi R^2 - \mathcal{S})}, && \text{(C.3)} \end{aligned}$$

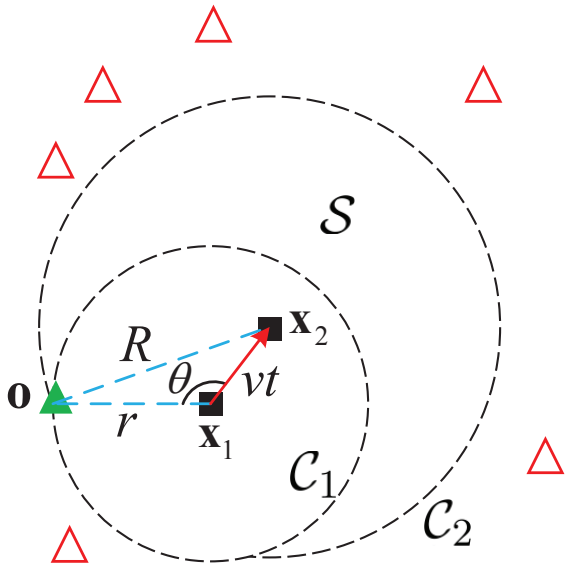

Figure C.2: Movement of the reference UE. Triangles and squares denote BSs and the reference UE, respectively.

where $N(B)$ denotes the number of points in set B, step $(*)$ follows from the null probability of PPP(λ_0), and $\mathcal{S}$ is the intersection area between $\mathcal{C}_1$ and $\mathcal{C}_2$, which can be written from plane geometry as

$$\mathcal{S} = r^2 \left(\varphi_1 - \frac{1}{2}\sin(2\varphi_1) \right) + R^2 \left(\varphi_2 - \frac{1}{2}\sin(2\varphi_2) \right), \tag{C.4}$$

where R, φ_1, and φ_2 are as given in the theorem statement. Substituting (C.4) into (C.1) and deconditioning on r and θ gives the final result for the handover probability as in (4.2). □

C.3 Proof of Lemma 4.6

The non-serving DBSs are initially distributed as an inhomogeneous PPP with density given in (4.3). Since the displacements are independent of each other in the DSM, the resulting network at time t will also be an inhomogeneous PPP because of displacement theorem [19]. Lemma 4.1 asserts that without the exclusion zone $\mathcal{X}$, DBSs will be distributed as PPP(λ_0) at any time t. However, in the presence of $\mathcal{X}$, we can partition the set of non-serving DBSs into two sets: (i) non-serving DBSs initially inside $\mathcal{X}$, and (ii) non-serving DBSs initially outside $\mathcal{X}$. We denote the density due to the former and latter by $\lambda_1(t; u_{\mathbf{x}}, u^*)$ and $\lambda(t; u_{\mathbf{x}}, u^*)$, respectively. Note that $\lambda(t; u_{\mathbf{x}}, u^*)$ is the density of the network of non-serving DBSs and we have $\lambda(t; u_{\mathbf{x}}, u^*) = \lambda_0 - \lambda_1(t; u_{\mathbf{x}}, u^*)$. Using the same treatment as in the proof of Lemma 2

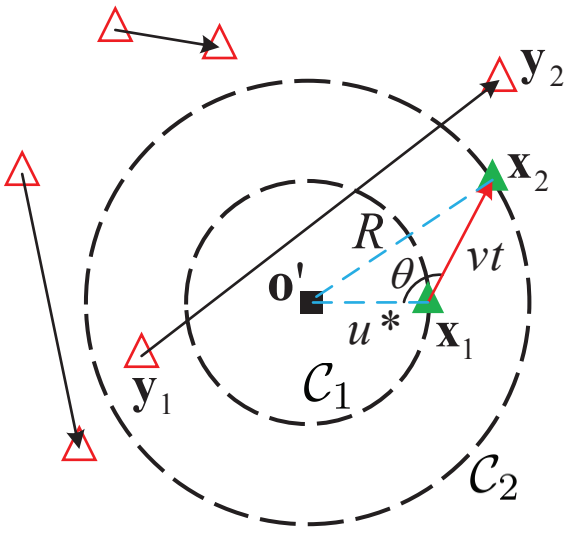

Figure C.3: Movement of the DBSs. Triangles and the square denote DBSs and the typical UE, respectively.

in [64], we get

$$\lambda_1(t;u_{\mathbf{x}},u^*)=\frac{\lambda_0}{\pi}\int_0^{\infty}\int_{\mathcal{R}_1}\frac{2rf_V(v)}{\sqrt{(u_{\mathbf{x}}^2-(vt-r)^2)((vt+r)^2-u_{\mathbf{x}}^2)}}\,\mathrm{d}r\,\mathrm{d}v, \tag{C.5}$$

where $\mathcal{R}_1=\{|vt-u_{\mathbf{x}}|\le r\le vt+u_{\mathbf{x}}\}\bigcap\{0\le r\le u^*\}$. Note that $\mathcal{R}_1$ can be simplified further by considering the relations between u^*, $|vt-u_{\mathbf{x}}|$, and $vt+u_{\mathbf{x}}$. We skip further details for brevity. We finally get

$$\lambda_1(t;u_{\mathbf{x}},u^*)=\lambda_0\left[F_V\left(\frac{u^*-u_{\mathbf{x}}}{t}\right)+\int_{\frac{|u^*-u_{\mathbf{x}}|}{t}}^{\frac{u^*+u_{\mathbf{x}}}{t}}f_V(v)\frac{1}{\pi}\cos^{-1}\left(\frac{v^2t^2+u_{\mathbf{x}}^2-u^{*2}}{2vtu_{\mathbf{x}}}\right)\mathrm{d}v\right], \tag{C.6}$$

which gives the density of non-serving DBSs as in (4.4). □

C.4 Proof of Theorem 4.7

According to Fig. C.3, let $\mathbf{x}_1$ be the initial location of the serving DBS with distance u^* from $\mathbf{o}'$. Assume that the serving DBS moves to a new location $\mathbf{x}_2$ by time t with speed v in direction θ. Let $R=\|\mathbf{o}'\mathbf{x}_2\|$, $\mathcal{C}_1=b(\mathbf{o}',u^*)$, and $\mathcal{C}_2=b(\mathbf{o}',R)$. Defining G as the event that there is no DBS in $\mathcal{C}_2$ and $\bar{H}(t)$ as the event that handover has not been occurred until time t, we have $\bar{H}(t)\subset G$. This is due to different speeds of DBSs and the probable event that a DBS can enter and exit $\mathcal{C}_2$ before time t (see the movement of a non-serving DBS from $\mathbf{y}_1$

to $\mathbf{y}_2$ in Fig. C.3). Hence, $\mathbb{P}[\bar{H}(t)] \leq \mathbb{P}[G]$, which gives

$$\begin{aligned}\mathbb{P}[H(t)] &= 1 - \mathbb{P}[\bar{H}(t)] \\ &\geq 1 - \mathbb{P}[G] \\ &= 1 - \mathbb{P}[N(\mathcal{C}_2) = 0] \\ &= 1 - \exp\left[-\int_0^R 2\pi u_{\mathbf{x}} \lambda(t; u_{\mathbf{x}}, u^*)\, \mathrm{d}u_{\mathbf{x}}\right].\end{aligned}$$

Deconditioning w.r.t. θ, u^*, and v, we end up with (4.5). □

C.5 Proof of Corollary 4.8

In the SSM, since we assume all DBSs have the same speed v, we have $f_V(v') = \delta(v' - v)$. Substituting this equation into (4.5), we end up with (4.6) with some mathematical manipulations. Now based on Lemma 4.2, events G and $\bar{H}(t)$ (defined in Appendix C.4) will become equivalent, i.e., the occurrence of a handover before time t necessitates the existence of a point in $\mathcal{C}_2$. Hence, the derived lower bound in (4.5) becomes exact in (4.6) and the proof is complete. □